TÉCNICO LISBOA

UNIVERSIDADE DE LISBOA

INSTITUTO SUPERIOR TÉCNICO

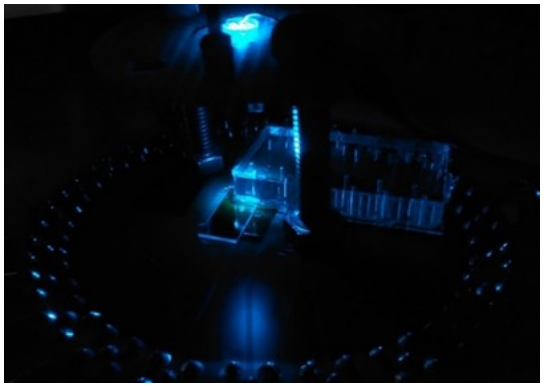

Biocatalysis in microfluidic systems: Biosensing and rapid-screening applications

Eduardo João Silva Brás

Supervisor: Doctor João Pedro Estrela Rodrigues Conde
Co-Supervisor: Doctor Pedro Carlos de Barros Fernandes

Thesis approved in public session to obtain the PhD Degree in

Biotechnology and Biosciences

Jury final classification: Pass with Distinction and Honour

2020

TÉCNICO LISBOA

UNIVERSIDADE DE LISBOA
INSTITUTO SUPERIOR TÉCNICO

Biocatalysis in microfluidic systems: Biosensing and rapid-screening applications

Eduardo João Silva Brás

Supervisor: Doctor João Pedro Estrela Rodrigues Conde

Co-Supervisor: Doctor Pedro Carlos de Barros Fernandes

Thesis approved in public session to obtain the PhD Degree in

Biotechnology and Biosciences

Jury final classification: Pass with Distinction and Honour

Jury

Chairperson: Doctor Duarte Miguel de França Teixeira dos Prazeres, Instituto Superior Técnico, Universidade de Lisboa;

Members of the Committee:

Doctor José António Couto Teixeira, Escola de Engenharia, Universidade do Minho;

Doctor João Pedro Estrela Rodrigues Conde, Instituto Superior Técnico, Universidade de Lisboa;

Doctor Duarte Miguel de França Teixeira dos Prazeres, Instituto Superior Técnico, Universidade de Lisboa;

Doctor Maria Henriques Lourenço Ribeiro, Faculdade de Farmácia, Universidade de Lisboa

Doctor Ana Margarida Nunes da Mata Pires de Azevedo, Instituto Superior Técnico, Universidade de Lisboa.

Doctor Abel Martin Gonzalez Oliva, Instituto de Tecnologia Quimica e Biológica, Universidade Nova de Lisboa

Funding Institutions: Fundação para a Ciência e a Tecnologia

2020

Dedicated to my nephew Tomás Brás Marinho

Acknowledgments

A PhD is not simply a degree, but a journey of self-discovery and self-improvement with some contribution to the scientific landscape along the way. Similar to all great journeys of history, a PHD is not the result of the efforts of a single individual, but are the result obtained by a group of individuals who provide the support necessary for the protagonist to achieve his desired goal. With this in mind there are several individuals who are to thank for their support throughout these tough years.

The first people on this list are my advisors, Professor João Pedro Conde and Professor Pedro Fernandes, which after supervising my MSc. thesis were up to it for a second round. Both of them provided endless support through an unwaivering enthusiasm for science and technology, fruitful discussions and the occasional slap on the wrist to thrive for better outcomes. They have my eternal thank you for all the help provided throughout the years and for cultivating even further my interest for science and technology.

Next are two people that, although are not my formal advisors were always very present throughout my pursuit of a PhD, which are Dr Virginia Chu and Professor Raquel Aires-Barros. Both of them provided interesting discussions concerning the results obtained throughout the years, especially Dr. Chu, as she put up with my countless questions on electronics and material sciences as well as the constant nagging about stuff in the lab.

This thesis would not be possible without the contribution of Professor Margarida Fortes, as she was the driving force behind most, if not all, of the work concerning the monitoring of plant health. Providing always extremely useful insight in the analysis of results obtained in this section of the work.

Next on my list are my parents Fernanda and Antonio Brás, who always provided emotional support when needed and having the patience of putting up with my awkward mannerisms. To my sister and brother (in-law), Celia and Milson, I want to thank the unwaivering support, laughs and curiosity surrounding my work. To my nephew Tomás, an apology to not have being as present as I wished to be.

To my cousin, Cristina Paiva, who introduced me to bioengineering and IST, I extend my gratitude, without her help, I may have ended up as a mathematician, or worse, a biologist.

To the women of my life, Raquel Belo and Inês Godet, I wish to thank you for the staggering support, both emotionally and academically, throughout the years even before my pursuit of a PhD. I am extremely grateful to be able to call you friends, and wish you the best in the upcoming years.

In the years I've been a part of INESC-MN I met a series of amazing people, which certainly made the long hours in the lab more enjoyable and that I'm glad to be able to call friends. At the very top of that list is Dr. Ruben Soares, who was a mentor, companion and friend even prior to my master thesis. Endless discussions with this man significantly improved my approach to research and I will be forever thankful. Next is Dr. Inês Pinto, who was always extremely supportive both inside and outside the lab, thank you for everything.

Next on the list are the idiots who made these years a blast, Dr. Ricardo Fradique and Dr. Rui Pinto. Great adventures were lived both in the lab as well outside of it and abroad! From committing several traffic violations due to my poor navigation skills to the endless lunches and discussions, may

we continue to meet up and discuss how the world will end!

To Catarina Caneira, my eternal gratitude for putting up with my shenanigans and being a true friend since the time of our MSc. thesis! *poke*

Special thanks have to be extended to Dr. Ana Matos, for her companionship and dedication to our small partnership. Several weekends requiring close to 12 h lab sessions were topped with a cold beer, many thanks!

To the rest of the people that I had the pleasure to meet over the years such as Pedro Monteiro, Dr. Denis Santos, Dr. Rita Macedo, Dr Katerina Nikolaidou, Cristiana Domingues, Rita Soares, Debora Alburquerque, Dr. João Mouro, Dr. Veronica Romão, Dr. Ana Silva, Dr. Sofia Martins, Dr. Diana Leitão and Dr. Vânia Silvério, many thanks!

Despite what it may seem on the surface, these years weren't spent entirely in the lab, any form of acknowledgments weren't be complete without extending my gratitude to my closest friends. Marco Figueiredo, Marta Belo and César Belo-Figueiredo, thank you for the dinners, hang-outs and good times throughout the years. I also wish to thank Ricardo Leandro for being a beacon of support during these years, countless football, basketball and pokemon matches were played and viewed throughout these years, still with no major title going to our beloved SCP. I also wish to extend these thanks to my friends, Beatriz Fernandes, Ana Carmo, Alexandre Carnet, Rita Serra, Gonçalo Teodoro, João Fernando, João Coelho, Manuel Sequeira and João Ribeiro.

One can not go without thanking the often unsung heroes behind these projects. I am eternally grateful to Eng. José Bernando, Eng. Fernando Silva and Eng Virginia Soares for the help and training during these years. To the patron saint of IBB, Ricardo Pereira, thank you for all the time expended in helping me with whatever challenge that may have risen.

And finally, a sense of gratitude to those who helped maintain my sanity these years: Corey Taylor, Chester Bennigtnon, Chris Cornell, Serj Tankian, Ozzy Ozborne, Marshal Mathers, James Hetfield, Axl Rose, Bruce Dickinson, Ed Sheeran, Roger Waters, Slash, Andre Young.

Resumo

Esta dissertação de doutoramento visa demonstrar o potêncial da técnologia microfluídica no campo da biotécnologia. O objectivo passa por demonstrar a possibilidade de aplicar a técnologia microfluídica nos campos de: i) reacções enzimáticas de múltiplos passos; ii) ensaios ópticos de biodetecção; iii) e capacidade de cultivar e manipular células animais.

Na primeira parte, foi desenvolvida uma plataforma microfluídica para a optimização de condições para a sintese de L-DOPA e dopamina. Para além dos factores tipicos como o caudal e a concentração do substrato, diferentes geometrias do reactor foram comparadas. O processo de produção de L-DOPA sofreu também um aumento de escala de 780x, mantendo as mesmas condições de transporte de massa, registando-se um rendimento de 0.81 mg_{L-DOPA}/(L.h) para a microescala e de 0.79 mg_{L-DOPA}/(L.h) para a escala maior.

A segunda parte desta dissertação, continua a explorar o uso de enzimas em sistemas microfluídicos, para aplicações de biosensores em plantas. Inicialmente, foi desenvolvido uma plataforma microfluídica para a detecção de ácido azeláico (LOD= 10 μM). Este dispositivo evoluiu posteriormente para ser capaz de detectar também ácido salicilico (LOD= 15 μM) e ácido jasmónico (LOD= 4.4 nM). Foi desenvolvido um leitor portátil para este dispositivo e este foi usado para distinguir uvas infectadas de uvas saudáveis.

A ultima porção desta dissertação foi acerca do uso de tecnologia microfluídica como ferramenta no estudo do cancro. Este trabalho teve três abordagens: i) o desenvolvimento de um biosensor para a detecção d adenilato quinase como forma de monotorização de saúde celular durante o rastreamento de drogas; ii) um sistema de *phage display* para o desenvolvimento de novos agentes terapêuticos; iii) um sistema de co-cultura de células do microambiente tumoral e do baço para o rastreamento de possiveís combinações terapêuticas.

Palavras-chave: Microfluídica, Point-of-need, Bioprocessos, Biosensing, High-throughput

Abstract

In this doctoral thesis, I aim to demonstrate the potential of microfluidics technology for the field of biotechnology. I aim to demonstrate the possibility of integrating, with microfluidic technology: i) multi-stage enzymatic reactions; ii) optically transduced biosensing assays; iii) mammalian cell culture capability and manipulation.

In the first part, a microfluidic platform for the screening of process conditions for the production of L-DOPA and dopamine is presented. In addition to the typical process conditions such as substrate concentration and flowrate, different geometries were also compared. The L-DOPA producing reaction was up-scaled, with an increase of 780-fold, by maintaining similar mass transport properties, resulting in a space-time yield of 0.81 mg_{L-DOPA}/(L.h) for the microfluidic system and 0.79 mg_{L-DOPA}/(L.h) for the larger scale.

The second portion of this thesis, was a continuation of the use of enzymes in microfluidic systems, but this time for biosensing applications in plants. Initially a microfluidic platform for the detection of azelaic acid was developed (LOD= 10 μM). This device later evolved into a multiplexed platform through the inclusion of assays for salicylic acid (LOD= 15 μM) and jasmonic acid (LOD= 4.4 nM). A portable prototype for the readout of this microfluidic device was developed and used to distinguish between infected and healthy grapes.

The final portion of this work revolved around the use of microfluidics for cancer research. This was done in three directions: i) a biosensor for adenylate kinase to monitor cell health during drug screening assays; ii) a phage display system for the development of novel therapeutic agents; iii) a co-culture device containing primary tumor microenvironment cells as well as spleenocytes to assess potential therapeutic combinations.

Keywords: Microfluidics, Point-of-need, Bioprocess, Biosensing, High-throughput

Contents

List of Tables

List of Figures

Glossary

Greek Symbols

α-JA - Anti Jasmonic Acid

ϵ - Voidage of a packed-bed

ϕ - Photon flux

γ - Slope of a photoresponse curve on a log-log plot, proportional to the generation rate

λ - Wavelength

μ - Dynamic viscosity

ρ - Density

σ - Standard deviation

τ_p - Particle velocity response time

Roman Symbols

a-Si:H - Hydrogenated amorphous silicon

AdK - Adenylate kinase

APTES - (3-Aminopropyl)triethoxysilane

ANOVA - Analysis of variance

ATPS - Aqueous two-phase system

AzA - Azelaic acid

AZI - Azelaic acid induced gene

BSA - Bovine serum albumin

C - Concentration

C$_D$- Drag coefficient

CAD - Computer assisted design

CDI - 1,1'-Carbonyldiimidazole

CFD - Computational fluid dynamics

CNC - Computer numeric control

CRC - Colorectal cancer

CVD - Chemical vapor deposition

D - Diffusion coefficient

d$_p$ - Particle diameter

DC - Direct current

DI - Deionized

DMF - Dimethylformamide

DNA - Deoxyribonucleic acid

DSP - Downstream processing

DRIE - Deep reactive ion etching

DTT - Dithiothreitol

DWL- Direct write lithography

E - Energy

E_F - Fermi level energy

ECM - Extra cellular matrix

ELISA - Enzyme linked immunosorbent assay

EWOD - Electrowetting on dielectric

F - Force

F_D - Drag Force

FACS - Fluorescence activated cell sorting

GOD - Glucose oxidase

GUI - Graphical user interface

H - Height

HPLC - High performance liquid chromatography

HWCVD - Hot wire chemical vapor deposition

I - Identity tensor

i - Intrinsic

I_{ph} - Photocurrent

IgG - Immunoglobulin G

ITO - Indium tin oxide

JA - Jasmonic Acid

k - Stefan-Boltzman constant

K_M - Michaelis Menten constant

L - Length

L-DOPA - Levodopa

LDO - Low-dropout

LED - Light emitting diode

LOC - Lab-on-a-chip

LOD - Limit of detection

LOQ - Limit of quantification

m_p - Particle mass

MBTH - 3-Methyl-2-benzothiazolinone hydrazone

mCRC- Metastatic colorectal cancer

MCU - Micro controller unit

MEMS - Micro electromechanical systems

MOSFET - Metal oxide semiconductor field effect transistor

N - Flux

n^+ - n-type doping

OpAmp - Operational amplifier

P - Product concentration

p^+ - p-type doping

PA - Precision Agriculture

PBS - Phosphate buffer saline

PCB - Printed circuit board

PCR - Polymerase chain reaction

PDMS - Polydimethyl siloxane

Pe - Péclet number

PECVD - Plasma enhanced chemical vapor deposition

PEI - Polyetherimide

PLA - Polylactic acid

PMMA - Poly(methyl methacrylate)

POC - Point-of-care

PR - Photoresist

PS - Polystyrene

PVD - Physical vapor deposition

Q - Flow rate

R - Reaction rate

R$_h$ - Hydraulic radius

RC - Resistor-Capacitor

Re - Reynolds number

RF - Radio frequency

RGB - Red, Green, Blue

RNA - Ribonucleic acid

rp-HPLC - Reverse phase high performance liquid chromatography

SA - Salicylic acid

SAR - Systemic acquired resistance

Si:C - Silicon carbide

SMD - Surface mount devices

SUA - Sample under analysis

T - Temperature

t - Time

TFT - Thin film transistor

u - Velocity field

UAV - Unmanned aerial vehicle

USB - Universal serial bus

UV - Ultraviolet

V - Voltage, Volume

v - Velocity

V$_{max}$ - Maximum reaction velocity

W - Width

x - Position

Part I

Introduction and Motivation

Chapter 1

Thesis Outline

Typically, a dissertation will be comprised of an introduction of the topic followed by a succession of the contributions towards the scientific understanding of said topic. However that will not be exactly the case here in this doctoral dissertation. Due to my interest in a broad range of topics, which has been exasperated in these years due to the undying enthusiasm and interest of my advisors, this dissertation will be split into three different branches of work, with the common point amongst them being the use of microfluidic platforms to achieve a certain end-goal. These end-goals were the development of enzymatic synthesis platform, a portable device for plant health assessment and platforms to contribute towards the development of colon cancer treatments.

A large portion of the training I underwent to conduct my doctoral thesis was an extensive look into microfabrication technology. All devices, both microfluidic, optical and electronic were fabricated *in house* by myself (with help on the electronic part). With this in mind, before delving into the different work packages, there will be an introduction to core concepts necessary to develop fully integrated microfluidic platforms, such as microfabrication principles, photosensor characterization, computational fluid dynamics (CFD) modeling, amongst others.

Within each line of work there will be introductions to the topic in order to guide the reader of this thesis, followed by reports of what was achieved during this doctoral thesis. At the end of each part, there will be an assessment of the results achieved and input concerning what direction the project should follow. the dissertation ends with an assessment of the work performed and outlook towards the future.

Initially, my PhD thesis was supposed to revolve around the use of microfluidics technology for two branches of enzymatic applications. The first topic would concern the use of microfluidics as a vehicle for process development at larger scales, while the second topic would be the use of enzymes for biosensing in microfluidic devices. Both the objectives were achieved, however the thesis evolved into something more.

1.1 Microfluidic technology for biocatalysis applications

As seen in Part III of this doctoral thesis, I aimed to the development of a microfluidic platform capable of expediting bioprocess development, namely, enzymatic reactions. The main goal was to develop a system where the optimization of a continuous process was possible. This in itself presents an array of challenges even through conventional means. It is necessary to guarantee that the enzyme is not washed out of the system, not it is rendered inactive throughout the duration of the process. The microfluidic approach allowed for the optimization of three reactions, the conversion of L-tyrosine to levodopa, levodopa to dopamine and the combined reaction to generate dopamine from L-tyrosine.

In addition to the traditional challenges of enzymes stability, there is also the issue of monitoring product output. while this is also a challenge in conventional process development, when following a microfluidic based approach, conventional analytical techniques such as chromatography are no longer possible. Even something as trivial, at the bench-top scale, as oxygen content determination or pH monitoring, becomes a complex development issue for microfluidic systems. Sample volumes will be extremely as well as reduced and optical paths, for light based measurements. The initial challenge was being able to detect the product of reaction in order to monitor the microreactor output.

Another interesting challenge was designing the most appropriate geometry for the microreactors used and observe their impact on the final result. This is also relevant for the upscale process, as the generic shape between scales should be more or less similar. Designs that are two exotic may not be feasible to construct at a larger scale.

The most challenging portion of the work were the upscale experiments, as the characterization of the mass transport properties seen at the microscale needed to be very accurate for a successful transition to the bench-top scale.

1.2 Microfluidic based, biosensing in plant systems

Part IV of this doctoral project focused on the development of microfluidic biosensors for plant health. Through our collaboration with Professor Margarida Fortes from the Faculty of Sciences of the University of Lisbon, three metabolites of interest were determined. This enabled us to develop a quick, portable prototype capable of detecting fungal infections in two different type of vine trees at the point-of-need.

This portion of the doctoral thesis was the most complex in my opinion, this is due to the fact, that the metabolites of interest, azelaic acid (AzA), salicylic acid and jasmonic acid are not particularly unique in their composition, nor do they have interesting properties in comparison to the rest of the molecules present in grape juice, to build a detection device around them.

By far the most challenging of these molecules was AzA. The development of an inhibitory, enzymatic assay was very challenging, the choice of substrate was important, as AzA is capable of inhibiting the oxidation of tyrosine but doesn't inhibit the oxidation of catechol for example. Once the base of the assay was determined the it was very important to remove any interferents from the grape juice, as by simply mixing the enzyme with the grape juice and MBTH produced a very drastic pigment generation.

The development of the detection assays for the other two metabolites was more straightforward, as it was more a process of miniaturizing a known assay than developing one from scratch. In the end it was possible to develop a microfluidic device capable of a multiplexed detection of the 3 metabolites, which gives us an indication of the plant health.

The development of the electronic prototype would simply not be possible without the input and collaboration of Dr. Rui Pinto. Going into the development of the necessary electronics, I had no previous knowledge of electronic circuits or how to weld. The code development for the interactive menus was an interesting challenge to revisit some old coding capabilities.

1.3 Expediting cancer research through microfluidic technology

In addition to my initial work plan, I became heavily involved in a collaboration with the Faculty of Pharmacy of the University of Lisbon, which will be discussed in more detail in Part V of this doctoral thesis. Briefly, the aim of this project was to use microfluidic devices to expedite the development of potential therapeutic agents to help in the fight against colorectal cancer.

There were 3 components to this project, two of them which were developed in parallel. By collaborating with the groups of Professor Cecília Rodrigues and Professor João Gonçalves we worked on two microfluidic platforms. The first one was a cell chip to allow the culturing of HCT116 cells to perform a phage display assay to identify possible affinity ligands against the cancer cells. This project was extremely difficult as the know-how of growing mammalian cells was close to none from my side, while adapting to the idea of using unconventional equipment such as the microfluidic chips and pumps was also difficult for the team at FFUL.

Countless iterations of the device which took into consideration the material chosen for the fabrication, the sealing method, culture conditions, etc all seemed to have some typeof flaw or short coming Eventually, through persistence on both parts, we were able to create an effective protocol for the growth of these cells and optimized the conditions for the capture of the phages.

At a slower pace, but never forgotten I also accepted the challenge to develop a microfluidic module capable of detecting a specific biomarker that relates to the stability of the cell membrane, adenylate kinase I. Initially an enzymatic approach was attempted, to no real success so an immunoassay was developed which will be discussed in Chapter 19.

A third application was also developed through a collaboration with Dr. Ana Matos and Professor Helena Florindo, also from FFUL. Here the goal was to create a microfluidic *ex vivo* model to test combinatorial therapeutic strategies of the nanovaccine developed by Dr. Ana Matos with different inhibitors of the tumor microenvironment.

This portion of the doctoral thesis benefited greatly from the knowledge generated by the previous experiments and was much more quick and streamlined. Due to the facto that we were using primary cell lines, cooperation and coordination were key as these cells deteriorate fairly quickly once extracted from the animal. In the end we confirmed the efficiency of her proposed vaccine.

Chapter 2

Microfluidics

2.1 The Microscale

Microfluidics is a field of engineering where fluids are handled in sub-millimeter dimensions, which has showed promise in diverse applications within the fields of chemistry and biology in applications ranging from process optimization to synthesis. [1, 2] However before delving into these diverse applications it is important to understand the physical implications of working at this scale.

2.1.1 Surface to Volume Ratio

When working in microfluidics one has to first realize how certain geometrical aspects will change with the reduction of size. As an example, take the case of a stirred tank reactor and simplify its geometry to a cylinder. The surface to volume ratio is given by Equation 2.1, where r is the radius and h is the height.

$$\frac{Surface}{Volume} = \frac{2\pi\big(r \times h + r^2\big)}{\pi r^2 \times h} = 2\big(\frac{1}{r} + \frac{1}{h}\big) \tag{2.1}$$

By analyzing Equation 2.1 it is possible to conclude that as we go down in scale the surface to volume ratio will rapidly increase, this allows for surface phenomena such as **capillary flow** (which will be addressed further down in this text) and molecular adsorption to be much more efficient. This increased ratio also allows for surface chemistry processes to be much more controllable. [3]

2.1.2 The Reynolds Number

One of the most important aspect of fluid flow in any system is the existence of turbulence, which is translated by the **Reynolds Number** (Re). The Re is a dimensionless number which relates the inertial forces to the viscous forces in a fluid flow and is defined by Equation 2.2 . [4]

$$Re = \frac{Density \times Velocity \times Dimension}{Viscosity} \tag{2.2}$$

For fluids flowing through a pipe, when the Re assumes values higher then 2000, it is considered that there is a state of **Turbulent flow** and when the Re is lower than 1000 **Laminar flow** is assumed, the region between these boundaries is known as the transitional region. [5]

In microfluidics, we are always in a situation of laminar flow, with the exception of cases where turbulence is purposely induced,[6, 7]. This characteristic of the microfluidic systems allow for the parallel flow of different solutions without them mixing immediately, allowing for diffusion and hydrodynamic based events to take place, such as sample preparation/purification through the use of aqueous two-phase systems (ATPS) [8, 9] or passive cell sorting systems through hydrodynamic focusing and spreading events [10, 11]. The lack of turbulence also allows for applications regarding **digital microfluidics**, which are essentially systems that rely on droplet formation within the microchannel, these systems have recently seen an increase of applications since cell isolation and sorting [12, 13] to reaction optimization, where the droplet itself is used as a miniaturized vessel [14, 15].

2.1.3 The Péclet Number

The Péclet number (Pe) is another dimensionless number which represents the ratio between the advection rate of a physical quantity (such as mass or heat) caused by the flow of the fluid and the rate of diffusion based on the existence of a gradient of this physical quantity and can be determined by Equation 2.3. [16]

$$Pe = \frac{Dimension \times Velocity}{Diffusion} \tag{2.3}$$

In the case of mass transport, the diffusion parameter will be the mass diffusion coefficient while for heat transport this will be the thermal diffusivity.

By analyzing the Pe, it is possible to have a better understanding of the system at hand and thus increase the control over the system at hand. [17, 18].

2.1.4 Heat Transfer

Heat transfer within microfluidic devices tends to be more uniform and faster due to the increased surface to volume ratio discussed previously, however there is an issue with external heating of microfluidic devices. This is due to the fact that the bulk of the device is much larger than the fluidic section itself which leads to a slower diffusion of heat. [19]

2.2 Instrumentation

2.2.1 Pumping

From here on out I will focus more on microfluidic systems that uses liquids as these are the most common amongst those used for biological applications. In order to use liquids in the microchannels, there is a need for pumping, this can be divided into two categories, passive pumping and active pumping.

Passive Pumping Systems

Passive pumping systems are those which don't rely on an external driving force or actuation, but rely on the characteristics of the microchannel itself, capillary and gravity driven pumps are examples of these types of pumping systems.

Capillary pumps take advantage of the capillary force produced by the microchannel, this is achieved by patterning the channels with arrays of posts or ducts. Another important aspect for capillary pumps to work is the contact angle between the liquid and the surface of the channel, in some cases the microchannel may have to be functionalized in order to obtain the adequate hydrophobicity for the solutions to flow properly. The lack of of an external pump make these types of pumps very desirable for point-of-care (POC) applications, such as biosensing. However since the flow rate depends directly on the channel dimensions so the fabrication process has to be flawless, also there is an issue of air bubble formation which will interrupt the flow of the liquid and stop the flow all together. [20–23]

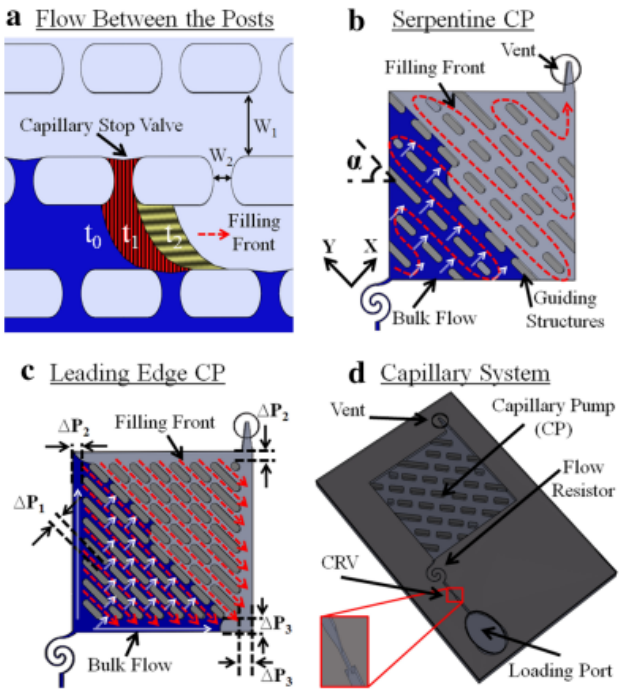

Figure 2.1: Illustration of the operation of a capillary pump, adapted from [20]

Gravity driven pumps have also been successfully used, mostly for cell culture and particle separation applications where very low flow rates and shear stresses are desirable. These pumps work by creating a pressure difference between the inlet and the outlet and the liquid will naturally flow from the point of highest pressure to the lowest, despite their success these pumps are very limited in terms of the flow rates produced. [24–26]

Active Pumping Systems

These systems refer to pumping induced by an external force, these can be divided into two categories, off-chip and on-chip pumping systems.

Off-chip pumps refer to external systems such as syringe, peristaltic pumps and electro-osmotic flow modules [27, 28], as of today these are the most commonly used pumps for microfluidic applications, while ideal for a laboratory setting they can be very cumbersome when the application intended is POC.

On-chip pumping refers to pumps that are built into the microfluidic devices but unlike the aforementioned capillary pumps, these require an external actuation, examples of this type of pumping are built in peristaltic pumps, and electro wetting-on-dielectric (EWOD) amongst others. [29, 30]

Centrifugal Force

Some microfluidic devices are built into circular modules which are then spun in an appropriate equipment, using the produced centrifugal force as the driving force to move the liquids, these devices are the so called labs-on-a-disk, these devices tend to be built in harder substrates and are usually discarded after one use. [31–33]

2.2.2 Valves

Microfluidic structures are usually built in a vertical fashion which can make the construction of three dimensional features such as valves somewhat complex, however complex does not mean impossible as seen in multiple reported cases in the literature despite the different ways to actuate and control these micro valves the working principal is the same, a thin layer of a flexible material, located above or bellow the channel of interest, is deformed in order to block the channel, as seen in Figure 2.2.

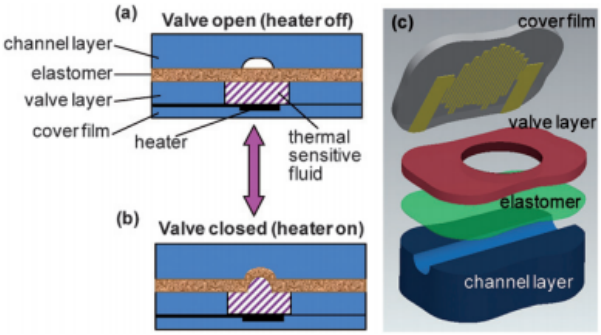

Figure 2.2: Example of a thermally actuated micro-valve, adapted from [34]

These micro-valves maybe classified according to their actuation method, dividing themselves into mechanical, which includes thermal [35], magnetic [36], piezoelectric [37] and electrically actuated valves [38]; non-mechanical which usually are induced by a chemical change of the environment or through light actuation [39–41]. These types of valves are the basis of the aforementioned peristaltic pumps.

2.2.3 Heaters and Coolers

Many biotechnological and chemical applications require a good control over the temperature of the system at hand otherwise cells or enzymes may not behave as intended. Due to this need, the development of micro-heaters is the object of focus of several research groups throughout the world. These usually are composed if a resistance coupled with a thermocouple in order to measure and control the temperature of the system. Coolers are a bit more tricky with limited capabilities to lower below room temperature without an external system, this is achieved by having a second channel in contact with the channel of interest, flowing a cooler liquid, essentially creating a heat exchanger. However the use of microfluidic structures as coolers for electronic systems has gained the interest of several groups in recent years.[42–44]

2.2.4 Sensors

Optical Sensors

Many biotechnological applications require optical monitoring to understand what is happening to the system or to quantify certain aspects, an example is measuring the fluorescence emitted by an ELISA experiment, the same is true for microfluidic systems. With that being said different types of optical sensors have been developed and integrated into microfluidic systems, I myself have fabricated amorphous silicon photodiodes for integration in my work in the same fashion as Novo *et. al* [45]. Other types of sensors may include photoconductors [46], optical fiber based sensors [47], lens free microscopy [48] and add ons for smart phone image acquisition [49].

Electrochemical Sensors

Sometimes optical sensors may not be capable of giving us the information needed in a specific type of experiment, this is especially true in cases where label free detection is preferred. With that in mind different type of electrical systems have been coupled to microfluidic platforms, with the most common being electrodes capable of detecting redox reactions in solution [50, 51] and also impedance sensors [52, 53] which allow to control parameters like cell growth through changes in the conductivity of the solutions running in the microfluidic system.

Magnetic Sensors

The recent use of magnetic particles in biological assays in microfluidic structures has caused a need to integrate ways to manipulate and transduce this magnetic signal. Fortunately due to the development of hard drives and other magnetically based electronics this technology already existed and just had to be adapted to the current needs. Mostly these sensors are comprised of spin-valves made of magnetoresistive material that is sensitive to changes in the magnetic field. This can be used for biomolecular recognition purposes. [54–56]

2.3 Bioreactors

2.3.1 Micro Bioreactors

Some microfluidic devices have a more industrial application and serve as bioreactors or fermenters, these types of devices typically have two types of applications. The first being used to produce a biomolecule of interest with much higher productivity then using typical macroscale equipment, as demonstrated in my previous work [57] and also by Garza-Garcia's group [58]. However despite the high productivity, there is still a logistical challenge due to the shear number of chips that would be required to achieve industrial levels of production. However there is still a very useful application for this type of system, which is for optimization of production conditions, however, these are not always accurate due to the fact that, as discussed before, aspects such like the Re are very different. [59]

2.4 Enzyme and other Protein Based Applications

In this section I will be addressing several applications where enzymes and other proteins play the major role, which is the main focus of my PhD thesis.

2.4.1 Biochemical Micro-reactors

The development of biochemical micro-reactors is somewhat similar to that of bioreactors, however instead of immobilizing cells inside the channel there is a need to immobilize enzymes or other catalysts. Several extensive reviews have been written on the subject recently. [60–62] As the case with enzymatic reactors at the macroscale, there are several strategies to do this at the microscale. [63]

As in the macroscale, the simplest method of immobilization is adsorption, this can be done on the surface of the microchannel itself, as is the case of PDMS or glass based chips, to glass micro-beads with functionalized surfaces containing specific chemical groups [63, 64] or certain polymer meshes such as the case of the methacrylate based denpol (dendronized polymer) reported by Küchler *et. al* [65]. Following the trend used at the macroscale immobilization in microfluidic channels have moved on to the use of hydrogels containing the enzymes [66] and also the use of porous micro-beads

Some novel methods to immobilize enzymes in microfluidic systems which aren't used at the macroscale have also emerged, one is the use of organic, inorganic or even hybrid **nanoflowers** and springs [67–69]; another is the use of **DNA origami** to produce scaffolds out of the nucleic acid in order to bind the enzymes, these can be useful in order to control the distance and placement when trying to perform reactions which require multiple different enzymes [70, 71].

These microreactors, which can be in the form of microfluidic chips or immobilized capillary tubes, have been used successfully in order to produce gluconic acid from cross-linked GOD (glucose oxidase) and catalase [72]; waxy esters from oleic acid [73], and also have been used in conjunction with chemical reactions to produce 2-Aminophenol [74]. However these types of chips often fail to include some type of downstream processing to eliminate any side products that may have formed or even substrate that

didn't react. Also these chips tend to lack the necessary instrumentation in order to have an online assessment of the reaction conditions.

One of the objectives of my PhD is the development of a microfluidic biochemical reactor capable of producing L-DOPA, which is a drug used in the treatment of Parkinson's disease.

2.4.2 BioFuel Cells

Fuel cells present them as an alternative to fossil fuels and nuclear fission as an energy source and are composed of an anode that oxidizes the fuel and a cathode which in turn reduces the oxidant, thus generating a current.[75] Over recent years people have tested the effectiveness of using enzymes in these types of cells, since enzymes have higher turn-over numbers, highly selective, renewable and also present the capability of working with biological fluids as a fuel source, which opens the door to self powered wearable electronics and biomedical devices.

The most studied enzymes used in these types of cells are very common and somewhat cheap and are summarized in Table 2.1.

Table 2.1: Typical enzymes used for microfluidic biofuel cells [75]

Anodes	**Cathodes**
Glucose Oxidase	Biliburin Oxidase
Glucose Dehydrogenase	Laccase
Alcohol Dehydrogenase	Ascorbate Oxidase

Usually these devices have a power output less then 1 V [76] which may be discouraging, however Desmaele *et. al* devised a strategy that led to an electric output that was enough to power a wireless temperature sensor, which sent measurement information every 2 min. This work shows that it maybe possible to use these devices to power small electronics in the future! [77]

2.5 Sample Preparation and Downstream Processing

We discussed previously that the modular nature of microfluidic structures allow for the integration of different operations within the same chip, this allows for the inclusion of purification steps which could be used as either sample preparation steps or even downstream processing units. [78]

2.5.1 Cell Sorting Chips

Due to the increase interest in developing cell chips for different applications their is a need to be able to separate different cells from a given experiment, whether this be to prepare the sample such as in the case of blood where we want to separate the blood cells from the rest [79]; or to isolate cells with a specific mutation, similar to how a fluorescence-activated cell sorter (FACS) would work, the separation can be done acoustically [80], mechanically [81] or even optically. [10]

2.5.2 Chromatography Based Chips

Chromatography is one of the most established purification methods used today with applications in both analytical science and in full blown industrial settings as the core of the purification process. Naturally researchers have tried to scale down thee systems in order to take advantage of them at the microscale. These devices generally take the form of a micro-column or channel packed with beads similar to those used to pack large scale columns, however there is also the possibility to build monoliths at this scale[82, 83].

These types of structures have been employed in several different strategies to isolate different types of molecules such as the use o **size exclusion** to isolate different nucleic acid strands[84]; **hydrophobic interaction** to isolate human genomic DNA [85]; **ion-exchange** for bovine serum albumin [86]. **Multi-modal** approaches have also been used by Pinto *et. al* to purify antibodies from a cellular supernatant.[87] More exotic techniques such as **affinity chromatography** [88] and **microchip electrophoresis** [89] have also been employed successfully.

2.5.3 Other Separation Methods

Due to the laminar nature of fluid flow in microfluidic systems it is possible to flow 2 or more liquids side by side without mixing or any dispersion in the opposite phase. This allows for liquid-liquid extraction techniques such as **aqueous two-phase systems** to shine. This technology has been employed multiple times successfully in recent years, which includes my own work, for the purification of antibodies using affinity tags, which is still under revision at the Journal of Chromatography A.[90–92]

Another technique is **continuous electrophoresis** on a chip. In this case a electrical field is applied to the sample, perpendicular to the flow of the liquid, this will move the molecules along the electrical filed according to some of their physical properties such as their isoelectric point.[93, 94]

2.6 Biosensing Chips

2.6.1 Proteomics Chips

Proteomics is the field that produces qualitative and quantitative information regarding the protein expression of a given sample, this is particularly useful to understand the physiology of certain organisms and also for biomedical research through the discovery of markers that allow for disease diagnosis and prognosis. [95] Standard protocols for proteome analysis are multi-step, long and tedious procedures, reasons that motivated researchers in recent years to look at microfluidics as a possible alternative. LOC devices allow for the integration of several steps of this analysis, as seen in Figure 2.3, and also the coupling to high resolution equipment for the final detection such as mass spectroscopy or HPLC.

In these microfluidic chips several types of reactors have been designed including capillary tubes and microchips (Open-Channel devices); filters and membranes (Membrane-based devices) and also hydrogel disks(Miscellany formed devices). [96] However one common feature between them is the

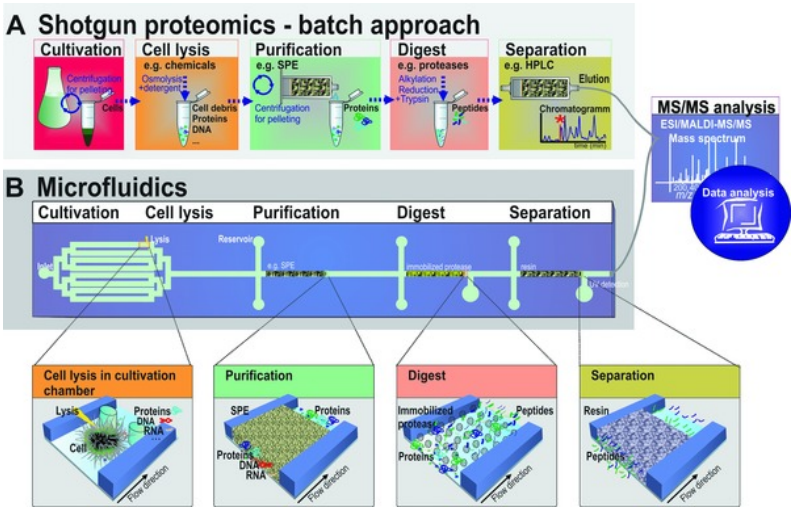

Figure 2.3: Comparison between proteome analysis performed in macro (A) and microscale (B), adapted from [95]

enzyme used for digestion, which for most cases, as with macroscale proteome analysis, trypsin is the enzyme of choice. [97–99]

2.6.2 Biosensors

A biosensor is defined as an analytical device capable of recognizing an analyte in a quantitative or qualitative fashion which uses a biological component as its recognition element and is coupled to a transducer. [100]

Due to the portability and possibility of instrumentation presented by microfluidic structures academic groups and companies around the world have been focusing their attention to the development of microfluidic biosensing devices, with the most successful applications being lateral flow pregnancy tests and blood glucose monitors. Other success stories include Abbott's i-STAT and FreeStyle precision monitors which provide a large selection of possible tests to be performed at the POC.

These biosensors can be broken into different categories according to their biorecognition element, we will separate the sensors into four different categories, **Cell** based; **Nucleic Acid** based; **Antibody** based and **Enzymatic** sensors.

2.6.3 Nucleic Acid Based Sensors

Nucleic acid sensors can be further divided into two groups those which rely on the complementary nature of these organic acids in order to detect specific strands of the molecule in a given sample or those who fold them to obtain **Aptamers** that allow for the detection of different types of molecules.

Nucleic Acid Hybridization Sensors

As mentioned before these sensors server the purpose of detecting specific strands of interest through the use of the complementary strand. Theses sensors can be used in order to detect the existence of

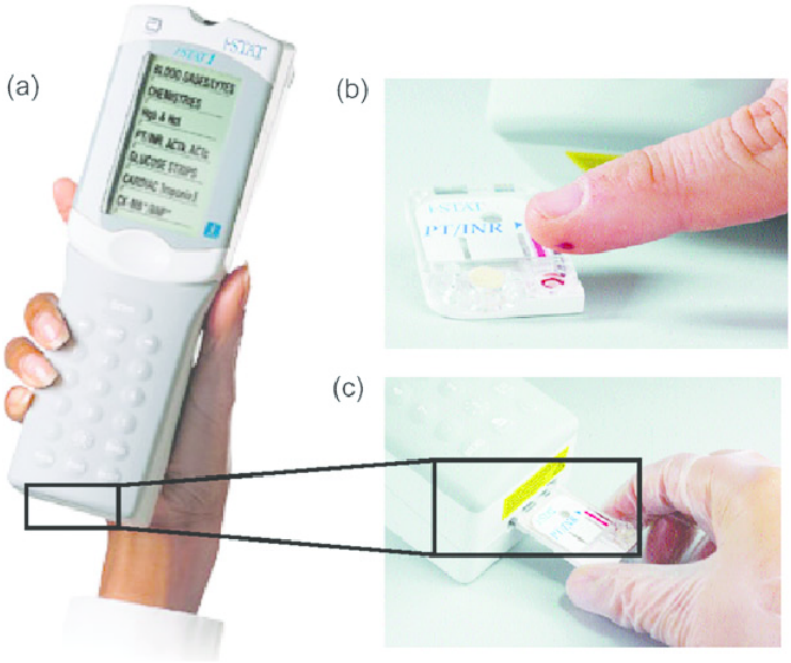

Figure 2.4: Abbot i-STAT hand-held analyzer, a drop of blood is retrieved from the patient, inserted into the microfluidic chip and then read on the device, adapted from [101]

pathogens in a sample (i.e. food borne pathogens)[102] or to detect biomarkers in circulation for patient diagnosis [103].

These hybridizations are often detected through the use of electrodes by electrochemical impedance spectroscopy [104, 105], however other methods have been employed such as the use of fluorophores and quantum dots by using a capture strand that shorter than the target strand and using a second strand labeled with one of these molecules that will hybridize with the other portion of the target molecule [106, 107]. These detection strategies are often complemented by on-chip amplification of the strand of interest through real time PCR techniques.[108, 109]

Apatamer Based Sensors

Aptamers are synthetic DNA oligomers which have a high affinity for non DNA targets such as proteins or other organic molecules. When an aptamer binds a analyte its configuration suffers a change which can be detected.[110]

Aptamer based detection has been successfully used in microfluidic systems for the detection of cardiac biomarkers [111, 112], allergens[113] and pathogens[114].

2.6.4 Antibody Based Sensors

Antibody based sensors rely on knowledge developed for standardized ELISA assays and can either work as a sandwich or a competitive assay.

Several applications have been developed such as the detection of toxins such as ochratoxin A [115, 116] in food products and cancer biomarkers such as prostate specific antigen [117]. Other disease

detection systems have been developed such as the one by Viswanathan *et al* for the detection of cholera toxins [118, 119]. Even sensors with potential military applications have been developed for example to detect the use of biochemical weapons such as anthrax [120] or ricin [121].

The transduction of these sensors are typically done by having a secondary antibody labeled with a light emitter such as a quantum dot or a fluorophore or even something that will generate light in a secondary reaction such as horse radish peroxidase.

These sensors suffer from the limitation of requiring an antibody capable of recognizing the required analyte without any cross contamination, this might be impossible all together or make the sensor very expensive depending on the molecule of interest.

2.6.5 Enzymatic Sensors

These sensors depend on the occurrence and kinetic nature of enzymatic reactions, they can be used by using the analyte as a substrate for the reaction or using the analyte as an inhibitor for the enzyme.

The most common use of these types of sensors is for the detection of glucose in a sample through the use of glucose oxidase or glucose dehydrogenase, which upon reaction generates hydrogen peroxide that is used during the transduction, either through reduction on an electrode or by using the peroxide in a second reaction.[122–124] The most successful case is personal glucose meters, they function, by possessing a capillary that sucks a small amount of blood into a chamber. This chamber contains glucose oxidase which then allows for electrochemical quantification of the amount of glucose in the patients blood stream by measuring the amount of oxygen consumed during the reaction. [125]

Other cases of microfluidic enzyme sensors include the detection of Adenosine- 5-triphosphate to assess fish freshness [126] through the use of glycerol kinase; phenol by using immobilized tyrosinase [127]; Epstein-Barr Virus[128] and many more [129–133]. The case of phenol detection, in my case, is very relevant because part of my PhD thesis is to develop a microfluidic biosensor for the detection of azelaic acid, which happens to be an inhibitor of the same reaction between tyrosinase and phenol compounds such as catechol. The idea will be to have tyrosinase immobilized in a microfluidic channel where a colorimetric reaction will take place, then if azelaic acid is present in my sample, the color generated will be less intense, thus enabling detection.

2.7 Cell Chips

Microfluidic chips have seen a great increase of cell based applications, mainly due to the high degree of control over culture conditions; the possibility of using bio-friendly substrates such as PDMS and the high degree of parallelization that comes with the reduced sizes of the devices.[1, 134]

2.7.1 Cell Culture Chips

Despite all the devices approached throughout this section allow for cell culture, I will first focus on those more dedicated to fundamental research concerning cellular behavior. With that being said, the first

types of structures to discuss are the simplest ones such as the chips presented by Tazawa *et. al* [135] which allows for the culture of adherent cells in a mono-layer fashion, while allowing to see differences caused by changes in culture temperature; or for example the device presented by Giulitti *et. al* [136] which allows for the culture of cells for 6 days, but still consists in a simple straight channel, which is only adequate for the culture of adherent cells that grow in mono-layers

An advancement from these types of devices are the ones presented by Fernandes *et. al* which allow for the parallel culture of cells under different culture conditions or even to screen the effect of a drug at different concentrations;[137] or the work presented by Junkin *et. al* which allows for single cell capture and culture in order to understand the immune response at the cellular level;[138]; and also devices similar to the work Fischer *et. al* which allow for the growth and viral infection of cells in a droplet culture system.[139]

2.7.2 3D Cell Culture Chips

As the aforementioned types of structures became limited for their needs, researchers moved on to more complex structures often comprised of multiple layers which allow for the cell culture to obtain a 3D conformation. This paved the way for one of the most exciting research topics in microfluidic cell chips to date, which is the development of **organs-on-a-chip**. As the name indicates these types of device are intended to mimic the conditions in which a organ grows and functions. The success of these devices will allow for an easier way to model diseases and for drug screening. The ultimate goal of this technology is a platform with several organ-on-a-chips assembled in a way to make a human-on-a-chip, this will be extremely useful in further pharmaceutical development to understand how drugs impact different body parts and also aid in the development of personalized medicine where one's cells could be grown and differentiated on chip to find what is the most suitable treatment.[140–142] Currently there are still issues with the devices in order to accurately mimic the whole micro-environment of a organ, however there have been quite the number of success such as a heart on the chip [143]; liver on a chip [144] and also kidneys on a chip [145].

In the next chapter, I will discuss in depth the concepts of microfabrication necessary to produce the microfluidic devices as well as the photosensors used throughout this work.

Part II

Microfabrication - Theory and Application

Chapter 3

Microfabrication Techniques

3.1 General Concepts

Microfabrication can be split into two different categories: **bulk micromachining** and **surface micromachining**.

Bulk micromachining consists on the selective removal (**etching**) of material within a substrate (i.e. a silicon wafer) in order to produce features such as cantilever that can then be used for diverse applications such as mass sensors or accelerometers. Since this was not a technique used throughout my work I will be focusing on the more versatile surface micromachining. [146]

An extremely simple manner of describing surface micromachining processes is the deposition of a thin layer of the desired material, pattern said material and remove the unwanted sections. This however is easier said then done, as one has to be mindful of the different interactions between the materials being used and the processes used for the removal of the excess material. This procedure is depicted in Figure 3.1.

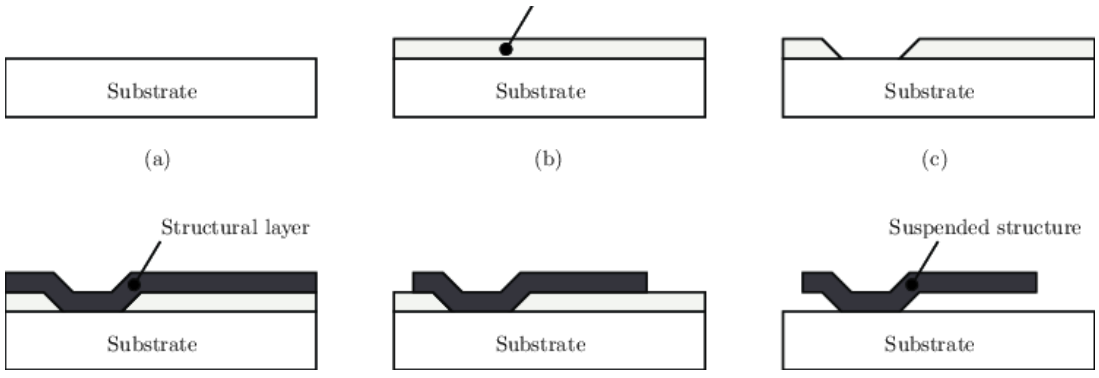

Figure 3.1: Example of a surface micromachining process for the fabrication of a cantilever. Adapted from [147]

First I will go through common techniques for material deposition, followed by the different etching options and finally discussing the patterning methods.

3.2 Spin Coating

Spin coating is the simplest and oldest method for material deposition, with the only requirement being the material has to be soluble in a solvent compatible with the rest of the process.

When spin coating, the material solution will distribute itself from the rotation center of the substrate to the edges. The final thickness of the film is dependent on multiple parameters such as the rotation speed, fluid viscosity and the time of rotation. Once the solution has been spread on the substrate, the solvent is then evaporated, allowing for the deposition of a thin layer of the dissolved material. Spin coating plays a crucial role in all the fabrication steps used throughout this work as it is the deposition method used for the photoresists used for patterning. A depiction of this process is presented in Figure 3.2.

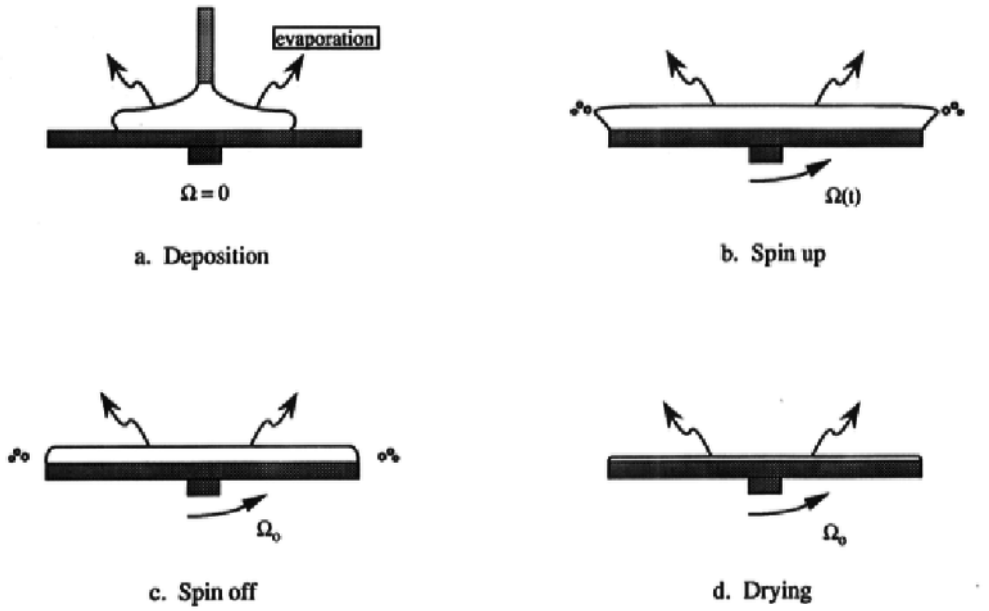

Figure 3.2: Schematic representation of the spin coating process. The first step is the placement of the desired material, which is then rotated, forcing the liquid to spread. Once the substrate has been covered, the solvent is then evaporated and the solid material is deposited. Adapted from [148]

.

Despite not being typically used for very thin films, there are reports for spin coating being able to achieve film thicknesses bellow 200nm. [149]

3.3 Physical Vapor Deposition - PVD

Physical Vapor deposition is the collective name that refers to a group of deposition processes for the creation of thin-films in the range of a few nm up to micrometer range. Despite the different natures within this process group, 3 steps can be identified throughout all of them: **i)** vaporization of the material from a solid target or a gaseous source (forming a plasm); **ii)** transportation of the vaporized material

in a vacuum (or partial vacuum) to the substrate surface; **iii)** condensation and film generation on the substrate surface. [150]

Throughout the rest of this section I will touch upon the different forms of PVD with a focus on sputtering since it was the only form of PVD used in this work.

3.3.1 Vacuum Evaporation

In vacuum evaporation the target material is evaporated through thermal evaporation in complete vacuum. The produced vapor will be rich in single atoms of the desired material as well as some clustered atoms which will have a very large free path due to the low pressure inside the chamber. This will allow the atoms to travel directly to the substrate and prevents the deposition of the material around the corners of the substrate. Typically the substrate will be grounded and can be heated or cooled down according to the properties of the desired material.

The main application of vacuum evaporation is the deposition of single metals such as Al, Ag and Cr which can be used for example in the fabrication of mirrors and reflectors or even in anti-reflection coatings in the case of MgF_2. [151] [152]

3.3.2 Ion Plating

In ion plating, instead of having a high vacuum as a sputtering environment, an inert gas such as argon is ionized. This ionized gas will bombard the surface of both the substrate and the target material. In the case of the substrate, this will act as a cleaning procedure, while the evaporated atoms of the target material will gain kinetic energy by colliding with the ionized gas. The resulting films from this technique tend to be very dense and well adhered to the substrate surface.

Typical applications for this method include the deposition of similar metals as mentioned in vacuum evaporation used in aerospace engineering.[153] [154]

3.3.3 Ion Implantation

Instead of creating a coating layer, ion implantation will insert atoms of the desired material into the bulk of the material. This is achieved by creating very energetic ionic beam capable of penetrating the material.

This technique is particularly useful in the creation of nitrites which can increase the mechanical resistance of the substrate material. [155]

3.3.4 Gas Sputtering

Sputtering differs from the aforementioned PVD techniques in the fact that the ejection of the atoms from the target material is not achieved through evaporation, but instead is due to the bombardment of the target with ionized atoms of an inert gas. This bombardment induces the release of material from the target, which is then accelerated in the direction of the substrate. Sputtering systems are contained

between two electrodes, where the target material is located on the cathode and the substrate is located on the anode. Figure 3.3 represents a schematic illustration of the sputtering process.

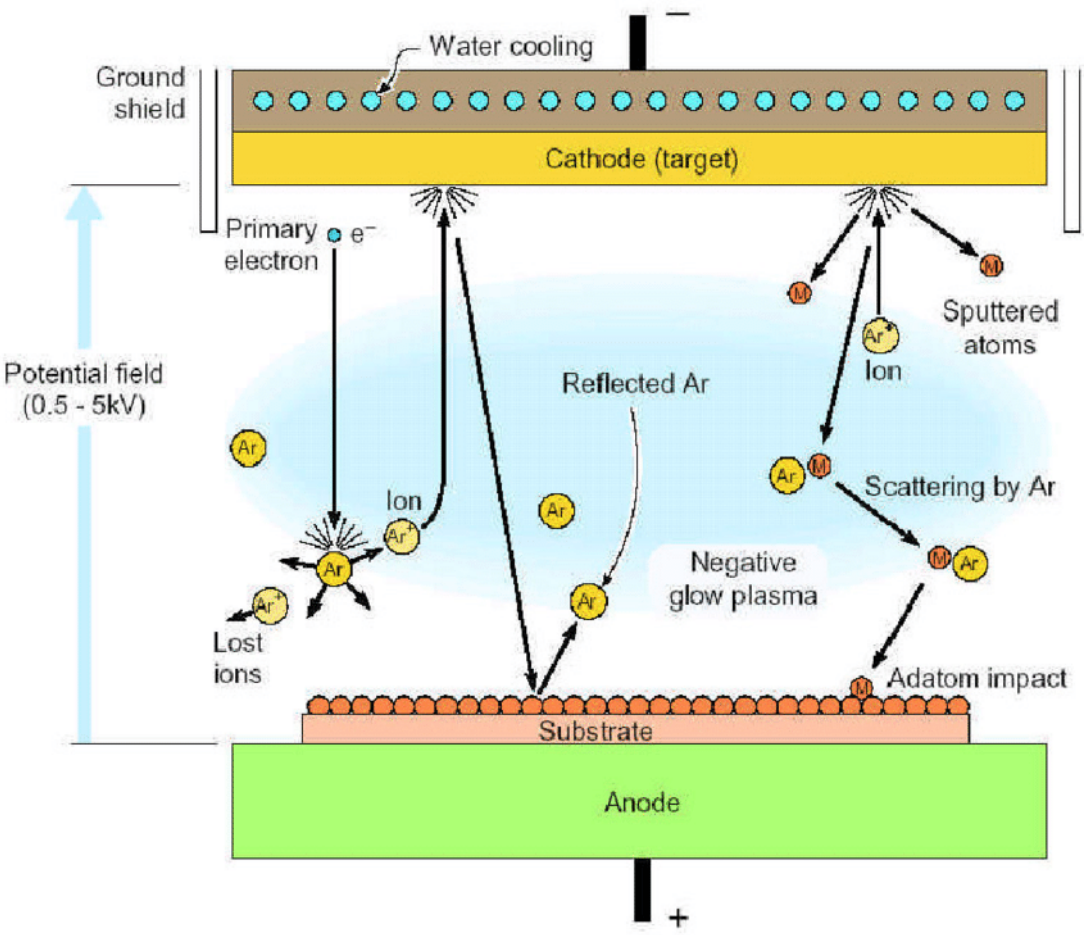

Figure 3.3: Schematic representation of the PVD sputtering process. The inert gas is ionized and accelerated towards the cathode, where the target material is located, forcing the injection of the target material upon collision. The ejected material is then directed to the anode where the substrate is resting, causing the deposition of the film. Adapted from: [156]

There are several types of sputtering, such as ion beam, reactive sputtering and ion-assisted sputtering, however here I will only discuss magnetron sputtering as it was the method used in this project. Here the plasma is contained and directed using a powerful magnetron. A typical work flow for a magnetron sputtering device is the heating up of the vacuum chamber, cathode cleaning by bombarding the surface of the target with ionized atoms of an inert gas, the actual film coating and cool down. [157]

Throughout these years I used two different magnetron sputtering machines, the Nordiko 7000 (Figure 3.4-A) for aluminum deposition and the Alcatel (Figure 3.4-B) for films of indium tin oxide (ITO), chromium and silicon dioxide.

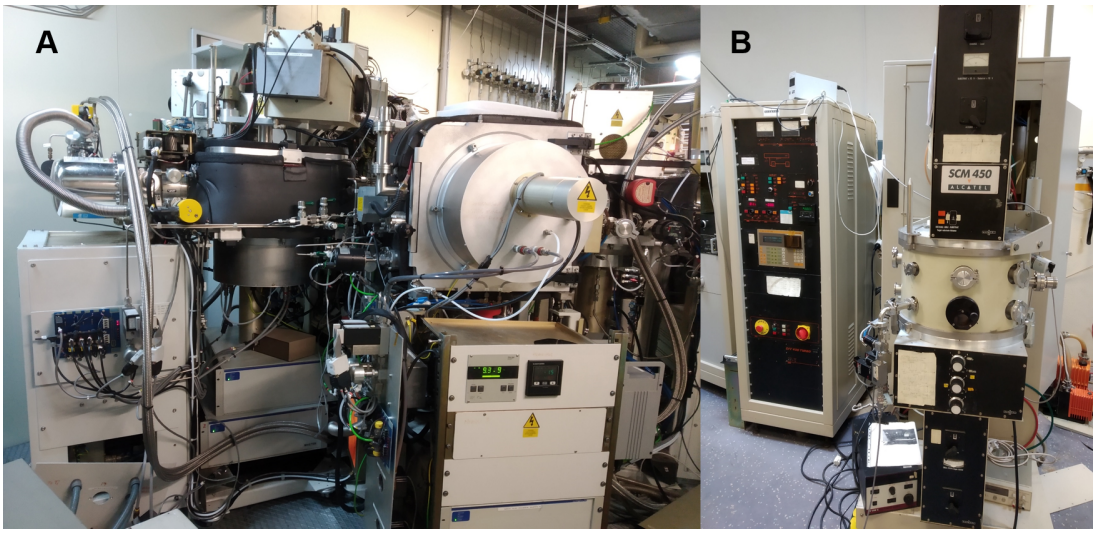

Figure 3.4: PVD machines used during my time at INESC-MN, Nordiko 7000 (A) and Alcatel SCM 450 (B).

3.4 Chemical Vapor Deposition - CVD

Chemical vapor deposition is a thin-film fabrication process that relies on the deposition of material originating from a precursor gas mixture that breaks down through chemical reactions close to the surface of a heated substrate. [158]

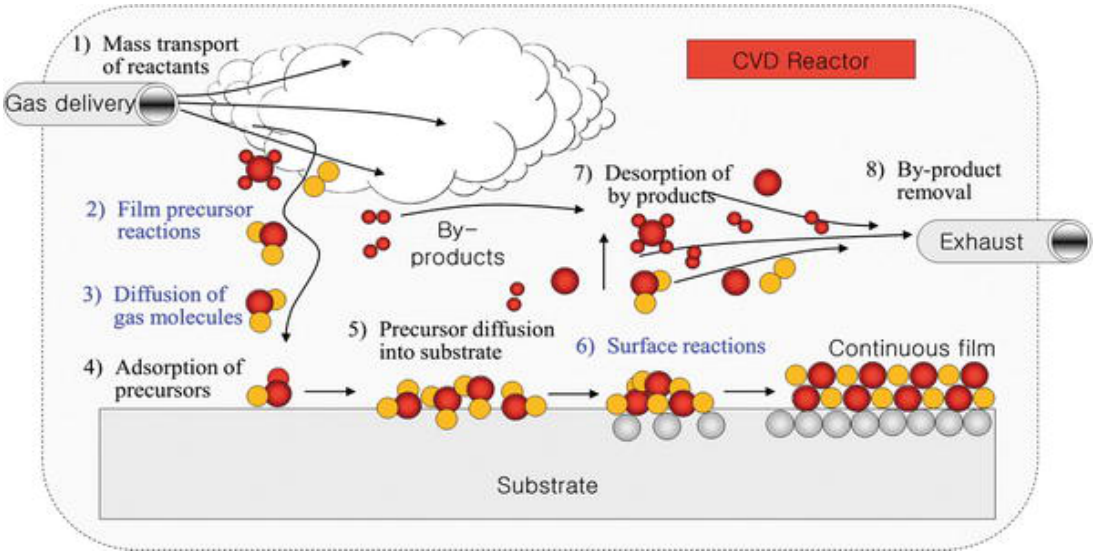

Figure 3.5: Schematic representation of the CVD process. The mixture of precursor gases are injected into the reaction chamber, where the chemical breakdown occurs. The reaction product diffuses in the direction of the heated substrate, where surface adsorption and diffusion occurs. At the surface of the substrate, additional reactions may occur and a cohesive, continuous film is created. Adapted from [159].

CVD processes can be performed at different pressure ranges depending on type of material, ranging from atmospheric pressure to ultra low vacuum (10^{-8}Pa). One other defining trait of CVD processes is how the precursor gases are broken down as in the case of plasma enhanced (PECVD) vs hot wire (HWCVD). Throughout this work the CVD process used was radio-frequency PECVD. [160]

A CVD system will be comprised by 3 essential elements: i) a gas dispensing system, ii) a reactor where the deposition takes place and iii) an exhaust system. [160]

The gas dispenser will be comprised of the gas sources and mass flow controllers in order to create the desired mixture for the process at hand. The reactor is the most complex part in the system and will house several components. In the case of our rf-PECVD system, we have 2 reaction chambers, one for the deposition of doped films of silicon and a separate chamber for intrinsic depositions. Each deposition chamber houses a heater where the substrate is placed and two electrodes for plasma generation.

The exhaust system is comprised of the vacuum pumps which maintain the pressure as well as the respective valves for pressure control. The reactive gases are pumped out of the system and typically go through a scrubber before being released to the atmosphere.

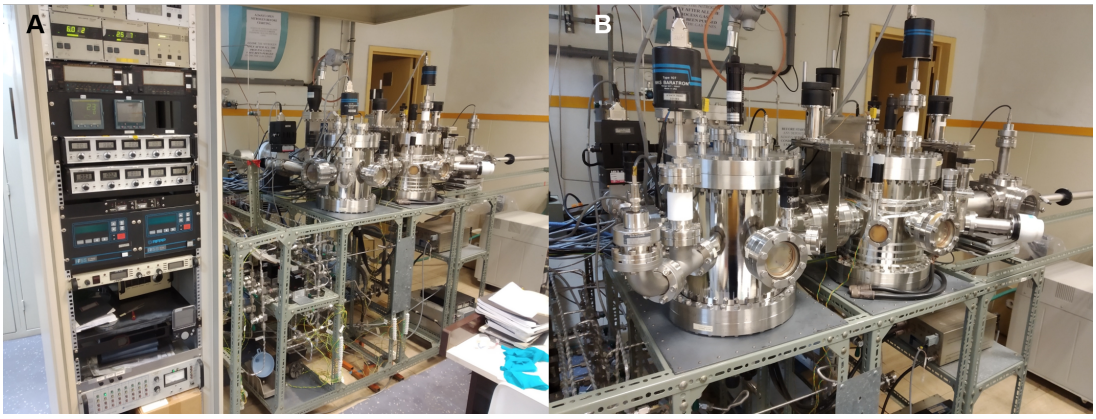

Figure 3.6: rf-PECVD machine, custom built by Professor João Pedro Conde and Dr. Virginia Chu, used for the deposition of silicon based films. The mass flow, temperature and pressure controllers are located on a electronic rack for easy access (A). The system has 2 deposition reactors (B), one for doped films (on the left) and the other for intrinsic films (on the right).

Throughout this work, CVD was used for all the silicon based films, which include both doped and intrinsic films of hydrogenated amorphous silicon which act as the functional layers in the photosensors, the silicon nitride, which acts as a passivation layer for the sensors and the silicon carbide layers used as fluorescence filters.

3.5 Wet Etching

Up until now the techniques discussed were for the addition of material, however microfabrication process also require the selective removal of the unnecessary materials, the first technique to be discussed is wet etching.

Etching in general, is an engraving process, in the case of wet etching this typically consists in dipping the sample into a solution of a selective etchant. This process is widely used in the patterning of the metallic layers of microfabrication procedures, but can also be applied to other materials. Common etchants typically are a mixture of strong acids or bases that are selective to a material or groups of materials in its etch rate.[161]

There are two different types of etching, anisotropic etching and isotropic etching, these are depicted in Figure 3.7. The first (anisotropic) will etch the material at the same rate in all directions, increasing

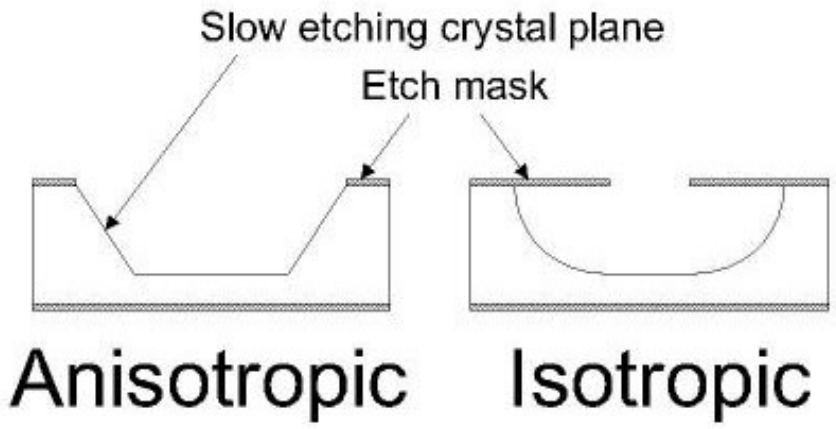

Figure 3.7: Depiction of the profile difference obtained when using anisotropic etching (left) and isotropic etching (right).

the difficulty in obtaining well defined walls when the thickness to be etched is very large. The second (isotropic) etch type is preferential to a specific direction, for example a specific crystal plane in the case of crystalline silicon.

The application of wet etching was necessary throughout this work for the fabrication of all the hard masks used for the microfluidic fabrication as well as certain steps in the photosensor fabrication.

3.6 Dry Etching

Dry etching processes rely on the use of gases or reactive plasmas as opposed to reactive liquids in order to remove the excess materials. Dry etching can be divided into physical etching, chemical etching and physical-chemical etching.[161]

In physical dry etching, focused ion or electron beams in order to eject material from the substrate surface using the kinetic energy of the beam. In theory any material can be etched using this type of process, however the material selectivity is low and the etch rates achieved are extremely low for most materials.[161]

Chemical dry etching uses reactive gases that will selectively attack the substrate material. This process is mainly isotropic and is typically plasma enhanced using, for example a RF field.[161]

There are different categories of physical-chemical etching such as anodic plasma etching, triode reactive ion etching and magnetically enhanced reactive ion etching. However here we will focus on deep reactive ion etching (DRIE) as this was the technique used throughout this work. In DRIE, the substrate is cooled which allows for the reactive gas to condense at the top of the etched cavity decreasing the exposure to the reactive plasma, minimizing the trench effects typically seen in reactive ion etching. These trench effects lead to poor definition of the etched region as the top section will be wider than the bottom section due to a longer exposure to the reactive plasma.[161]

In this work a DRIE machine from LAM technologies was used to selectively etch the silicon mesas used for the photosensors.

3.7 Lift-off

When fabricating devices comprised of multiple materials it may be hard to find a suitable etchant that will be selective enough and not destroy the layers of materials bellow the current active layer. Due to this, a secondary method was developed in order to successfully remove more layers of materials increasing the complexity and diversity of possible fabrication processes, this process is called lift-off.

When using lift-off, a sacrificial layer of material, often this material will be photoresist, is deposited and patterned in order to protect certain regions of the device. The active material is then deposited and will contact the surface of the substrate only in regions lacking the sacrificial layer as shown in Figure 3.8 . By then dissolving the sacrificial layer, the excess material that was located on top is lifted-off and removed from the device.

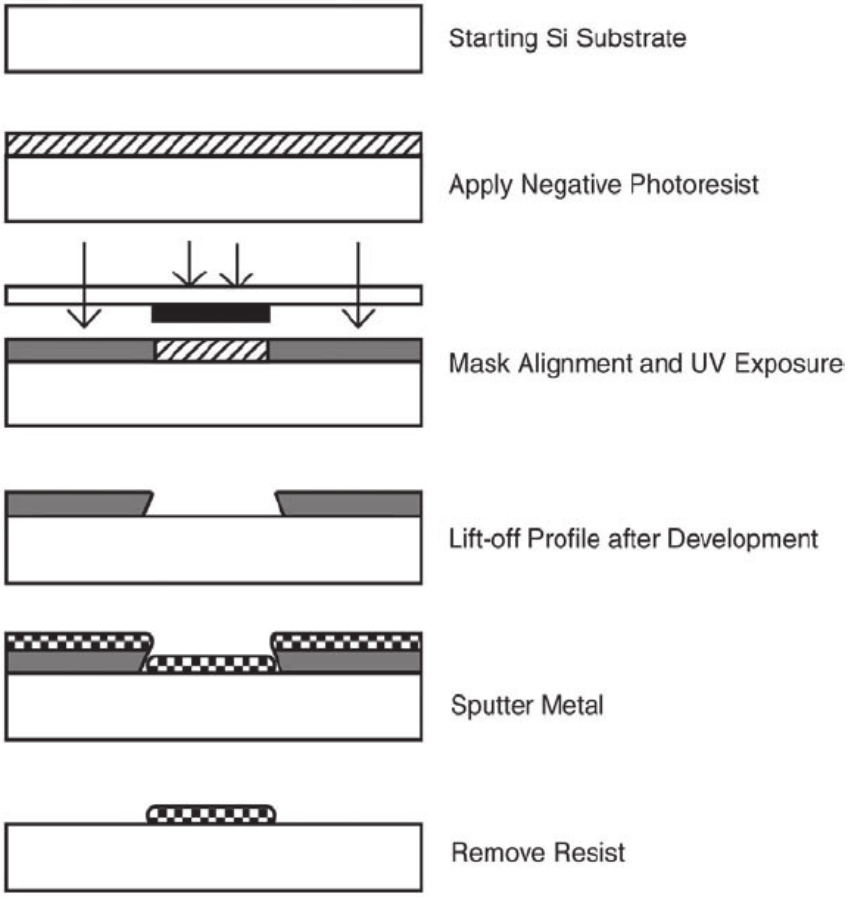

Figure 3.8: Step by step of a lift-off process. The substrate is coated with a photoresist, which is then patterned and a metallic layer is deposited through PVD. Then the photoresist is dissolved away leaving behind the remaining metal patch. Adapted from: [162]

Despite its use, lift-off has several drawbacks when compared to etching, such as the difficulty in achieving well defined lateral walls as well as having much longer process times.

3.8 Lithography

Up until now, I have discussed the techniques used to deposit the thin layers of materials and how to selectively remove them, however I have yet to discuss how one actually patterns the layer of material in order to obtain the desired features. This is done through what is called lithography.

3.8.1 Optical Lithography

Optical lithography, also known as photolithography, requires 3 elements to be performed: i) photoresist, ii) photomask and iii) light source.

Photoresists are photo-activated materials that will experience a change in physical properties when exposed to a light source, photoresists can be either positive or negative. A negative photoresist such as the SU-8 used for the microfluidic mold fabrication in this work, will become resistant to the developer solution when exposed to light. In contrast, a positive photoresist, such as the PFR7790G used for the photosensor fabrication will become soluble in the developer solution in the regions that were exposed by the light. An example of this is presented in Figure 3.9. The photoresist is typically spin-coated on to the substrate material and may have different thicknesses depending on if it will be used as a sacrificial layer or a structural layer for the final device (such as in the case of the microfluidic molds).[163]

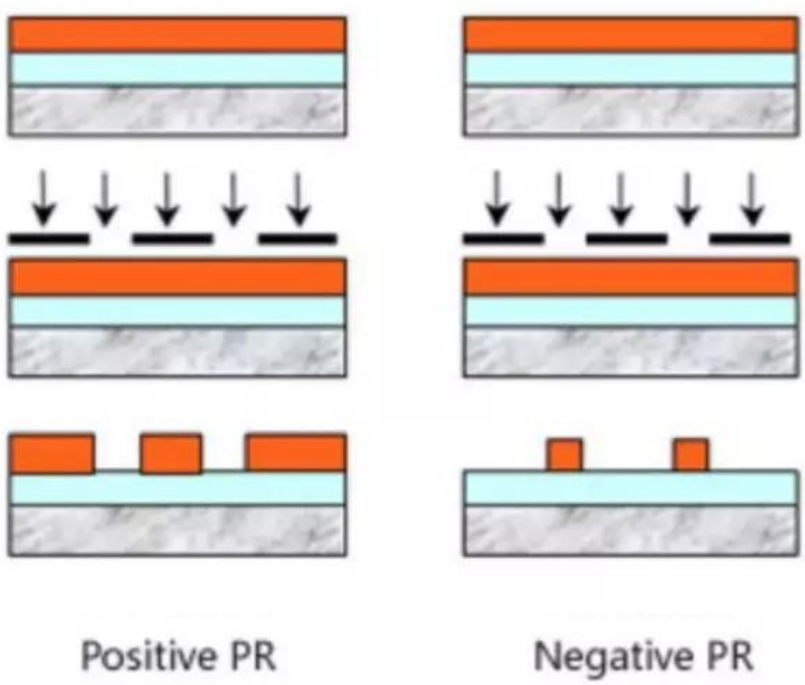

Figure 3.9: Results obtained using the same photolithography pattern using a positive photoresist (Left) and a negative photoresist (Right). Adapted from [164]

In order to create a pattern, one needs a photomask, represented by the black lines in Figure 3.9. These photomasks are typically composed by a film of an opaque material (Al i.e.) deposited and patterned on top of a transparent substrate such as glass or quartz. When using a photomask, the entirety of the substrate is exposed at once and new designs will require the fabrication of new masks. An alternative to these photomasks is direct write lithography (DWL). By using DWL one has free control on the design options (within in the limitations of the equipment), as the user will create a computer assisted design file (CAD) which will then be used by the machine to create the final design.[163]

The light source will depend on the type of mask used. In the case of a hard mask based lithography, it is possible to use a lamp with a wide exposure area to pattern large surfaces at once, however in the case of DWL, the light source will be some form of a computer guided laser which allows for higher precision and more design space but is a more time consuming process. In order to reveal the desired pattern, after the exposure step, the photoresist has to be baked, in order to accelerate the structural change of the photoresist and developed. The developing solution is specific for the type of photoresist that is being used.[163]

3.8.2 Soft Lithography

Soft lithography is based on the use of elastomer materials to achieve the desired pattern transfer, the most common use of this technique is the casting of PDMS on molds for microfluidic fabrication. Besides this application other have emerged such as solvent assisted micro-molding of polymers and micro-contact printing as depicted in Figure 3.10. [165]

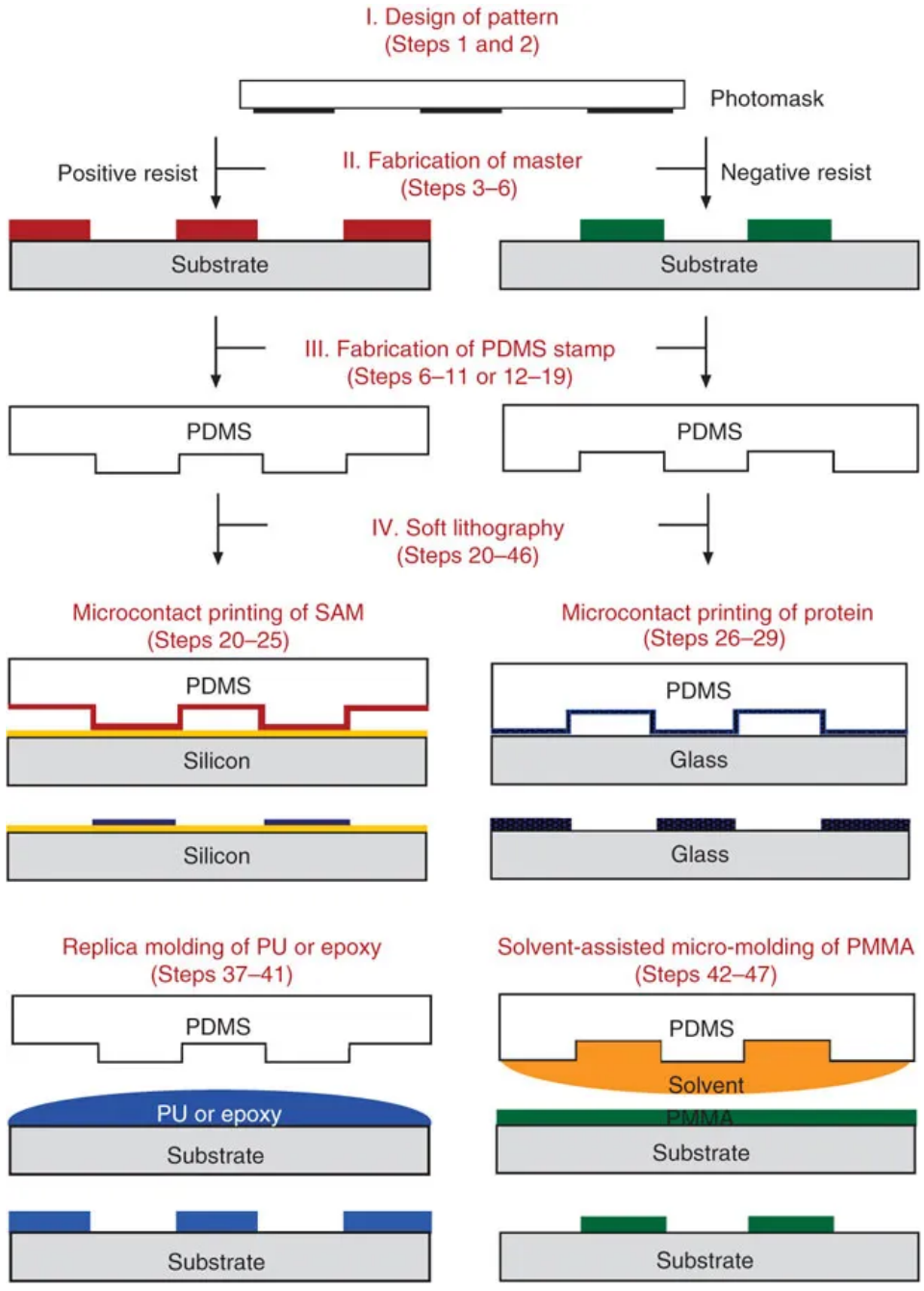

Figure 3.10: Different applications within soft-lithography techniques. Adapted from: [165].

3.9 CNC milling

Computer numerical control milling or CNC milling for short, is the use of a computer controlled milling machine in order to follow a certain pattern which is programmed by the end-user. Milling in general is a method for material removal using a sharp cutting tool, in the context of this work, I will be referring to the use of milling using plastics as a substrate.

The use of CNC milling is particularly useful for the production of structures (microfluidic or not) out of biocompatible polymers such as polystyrene (PS) and Poly(methyl methacrylate) (PMMA) or to use these devices as molds or auxiliary structures for microfluidic fabrication.

The working parameters of higher interest is the spindle speed, feed rate and overlap. The spindle speed is the revolutions per time unit at which the tool will rotate, the feed rate is the speed at which the material is pushed into the milling tool. The overlap, as the name suggests is the % of overlapping between consecutive passes in the same region. [166]

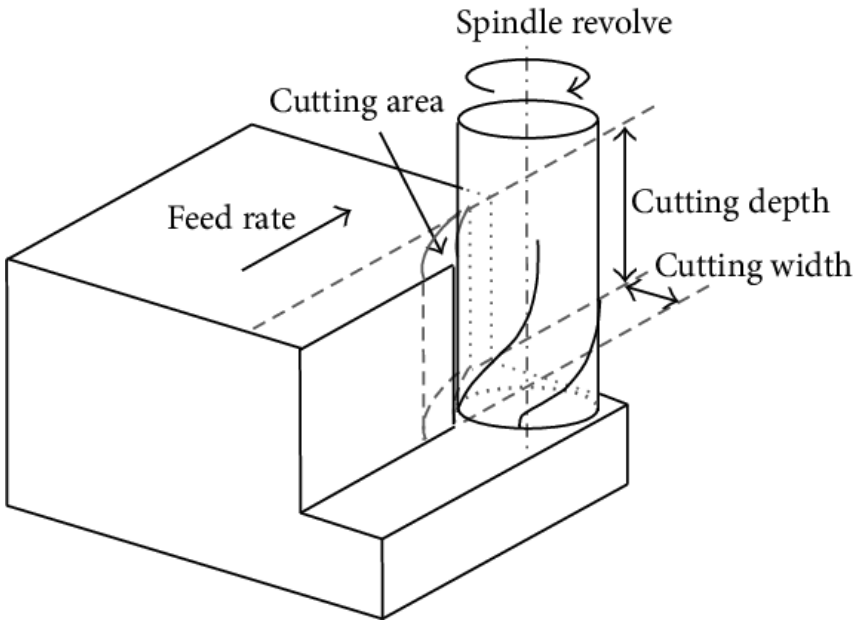

Figure 3.11: Process parameters relevant for machine milling. Adapted from: [167]

To successfully machine plastics there are some considerations to be taken into account. Most of the commonly used plastic will have relatively low glass transition temperatures, hence cooling the milling tool is extremely important, not only due to the possibility of melting, but also due to material expansion which will compromise the required tolerances. [166]

Another important consideration is to use tools with a low number of cutting edges as this will increase the final smoothness of the substrate as well as minimizing the vibrations along the milling process. [166]

In this work, CNC milling was used to fabricate a plethora of support structures within the context of microfluidic chip fabrication as well as some attempts at fabricating some microfluidic devices made of PS.

Chapter 4

Thin-film Hydrogenated Amorphous Silicon Photosensors

Throughout the work presented in this doctoral dissertation, thin-film hydrogenated amorphous silicon (a-Si:H) photosensors were used for different types of light based assays. These sensors were heavily deployed by previous PhD students from our groups such as Dr. Pedro Novo and Dr. Denis Santos, thus a well established fabrication method was given to me to start from.

In this chapter I will briefly go over the working principle behind these sensors, typical characterization scheme as well as some of the structural differences attempted in order to facilitate their fabrication process as well as improve their efficiency, namely in the detection of UV light.

4.1 Energy Bands Theory

Before delving into the details concerning the properties of a-Si:H as an active material for photosensors, one has to understand a bit about how semiconductors in general work. One important aspect is the notion of energy bands.

If one reads into the Paulli exclusion principle, it states that electrons cannot occupy the same energy level, however it is possible to group together electrons with similar energy levels to form what is called an energy band. The **valence band** of a material is the energy band that corresponds to the outermost electron orbital occupied by electrons in a material, where the valence states are also called as bonding states. [168]

Electrons in the valence band can be excited to what is called the **conduction band**. Electrons in this state possess the necessary energy to move free within the material, the energy difference between the latest, occupied valence band and the first unoccupied conduction band is called the **band gap**. Conductive materials, such as metals will have overlapping bands while insulators will have very large band gaps as seen in Figure 4.1. [168]

The distribution of electrons amongst energy bands is given by Fermi-Dirac distribution, presented in Equation 4.1.[168]

$$f(E) = \frac{1}{1 + e^{\frac{E - E_F}{kT}}} \tag{4.1}$$

In Equation 4.1, E represents the energy of a given particle state, k is the Boltzmann constant, T is the absolute temperature and E_F is the **Fermi level**. [168]

The Fermi level represents a theoretical energy level, where all energy states bellow it are occupied and all of the above states are empty as demonstrated in Figure 4.1. In a semiconductor material, the Fermi level will typically be placed in the middle of the gap except in the case of **doped** materials, which will be explored in further sections.[168]

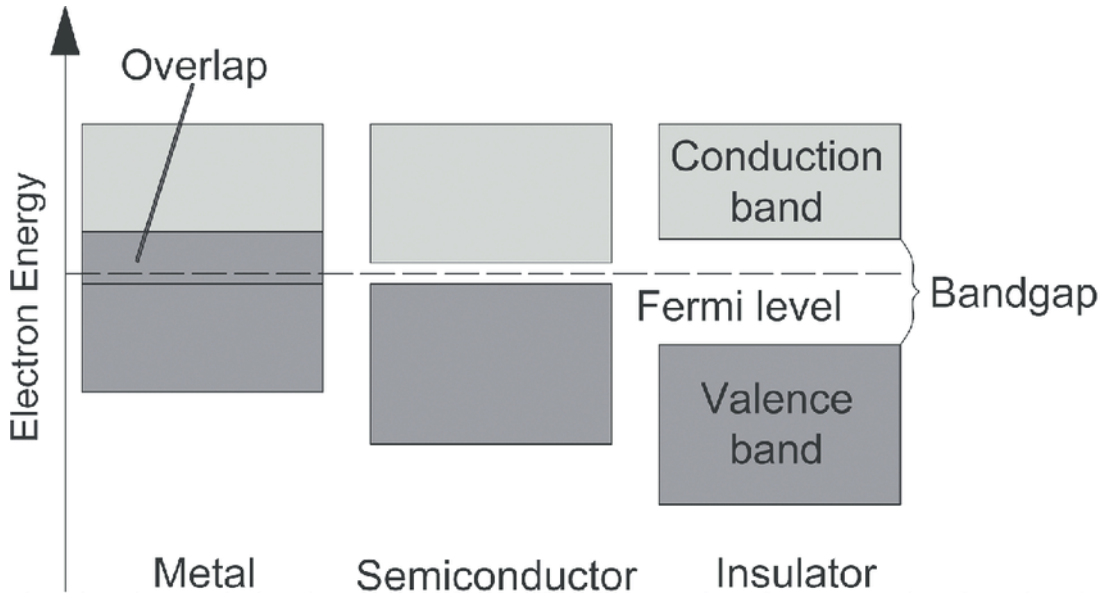

Figure 4.1: Band gap representation of different types of materials: i) metals, ii) semiconductors and iii) insulators. The location of the Fermi level of a semiconductor material will be located in the center of the gap. Adapted from: [169]

In the following sections I will address the specific properties of amorphous silicon and its doped versions as these are used in the fabrication of the photosensors used in this work.

4.2 Hydrogenated Amorphous Silicon and Other Material Properties

4.2.1 Intrinsic Amorphous Silicon

In the previous section, the notion of band gap was briefly explored, in crystalline materials, there are no energy states within the band gap. However, in amorphous materials there is a continuum of energy states called localized states as seen in Figure 4.2.

This continuum of energy states are due to the existence of **dangling bonds** within the disorganized material. These dangling bonds, in the case of amorphous silicon, are the result of the Si atom not creating the 4 bonds it is capable with the adjacent atoms, leaving a defect in the material. When

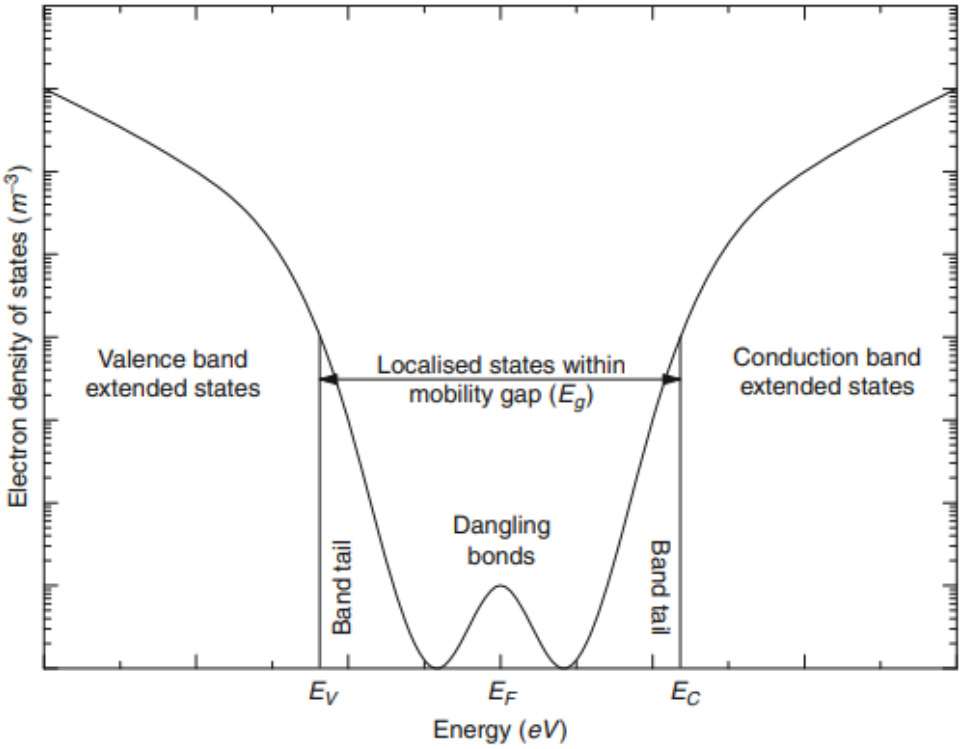

Figure 4.2: Distribution of energy states within the band gap for hydrogenated amorphous silicon. Adapted from: [170]

hydrogen is included into the material these dangling bonds are passivated, reducing the number of localized states and increasing the band gap, which for a-Si:H is 1.7 eV.

Due to it's high absorptivity in the visible region, a-Si:H is widely used in the fabrication of photosensors and solar cells for energy production. In the context of this work **intrinsic** a-Si:H is the main active layer of the photosensors produced.

4.2.2 Doped Amorphous Silicon

p^+ and n^+ Doping

One may want to alter the amount of charge carriers within a material, this is done by adding a foreign atom to the material through a process called **doping**. When the desired change is to increase the amount of available electrons, the material is doped with a Group V element such as phosphorous in what is called n^+ doping. When an excess of holes is wanted, an element from group III such as Boron is included, this process is called p^+ doping.

The inclusion of these atoms into the materials will induce changes in the Fermi level and also, in the case of an amorphous material, in the amount of localized states within the gap. This is due to the dangling bonds recombining with the included atoms. The changes in the band gap induced *via* doping are presented in Figure 4.3.

Doped films are more conductive than their intrinsic counter parts due to a higher concentration of

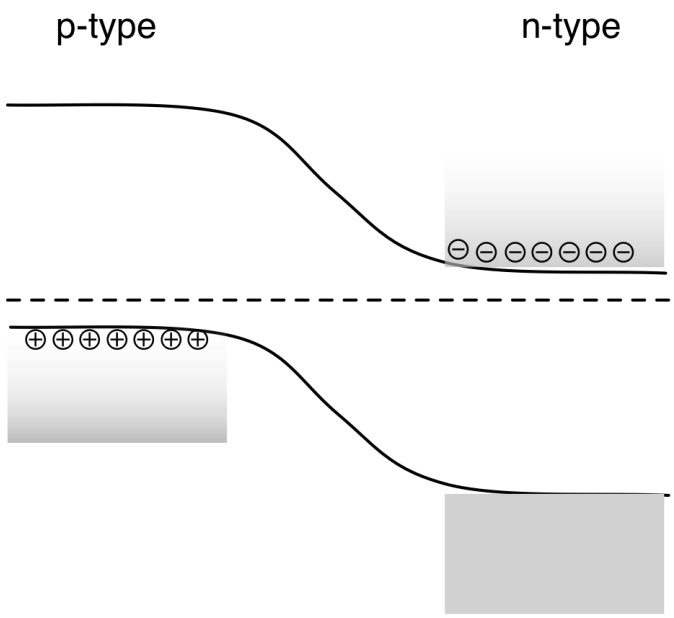

Figure 4.3: Difference registered in the band diagram for p-type (left), intrinsic (center) and n-type materials.

charge carriers (either electrons or holes) in the bulk material.

When a p-type and a n-type semiconductor are placed together, a **PN junction** is created. When in contact, the charge carriers at the junction will travel to the opposite material, in a process called **diffusion**. Once the an equilibrium is reached, there will be a region within the p-type material that is rich in negative charges and another within the n-type material which is rich in positive charges. when considered as a whole these regions are called the **depletion layer** of the junction.[171]

The differences in charge create a potential difference across the thickness of the depletion layer, as seen in Figure 4.4. This effect is one of the corner stones of modern electronics and is the basis of the PN diode.[171] The use of diodes will be further explored in the section referring to the fabrication of photodiodes.

Carbon Doping

Besides inducing changes in material conductivity, doping can be used in order to induce a change in the optical properties of the materials. Previously it was mentioned that the band gap of a-Si:H is 1.7 eV, if one converts this energy to the wavelength of a photon, the result obtained is approximately λ= 730 nm. This means that the film will be capable of absorbing light starting at this wavelength and moving into shorter wavelengths.

Through doping, it is possible to change the band gap of the material, thus changing the wavelengths where the film transitions from opaque to transparent. This is the case of carbon doping to form silicon carbide films. These films are extremely useful for the fabrication of high pass filters. In Figure 4.5 the change of the film transmission can be seen as a function of the carbon content. By tuning the carbon content of the film it is possible to use the fabricated photosensors for fluorescence based assays,

by making the film opaque at the excitation wavelength and transparent at the emission wavelength. However these filters demand the use of fluorophores with a Stokes shift of at least 50-100 nm.

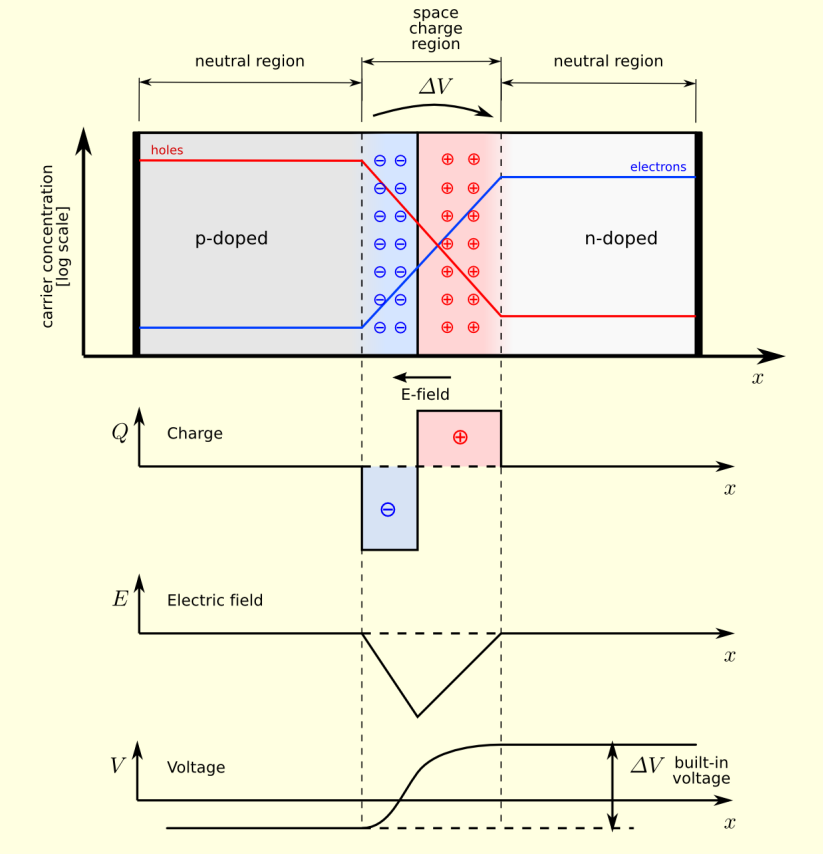

Figure 4.4: Depiction of the depletion region in a PN junction due to the different charges. This creates a built in electric field and voltage within the junction. Adapted from: [171]

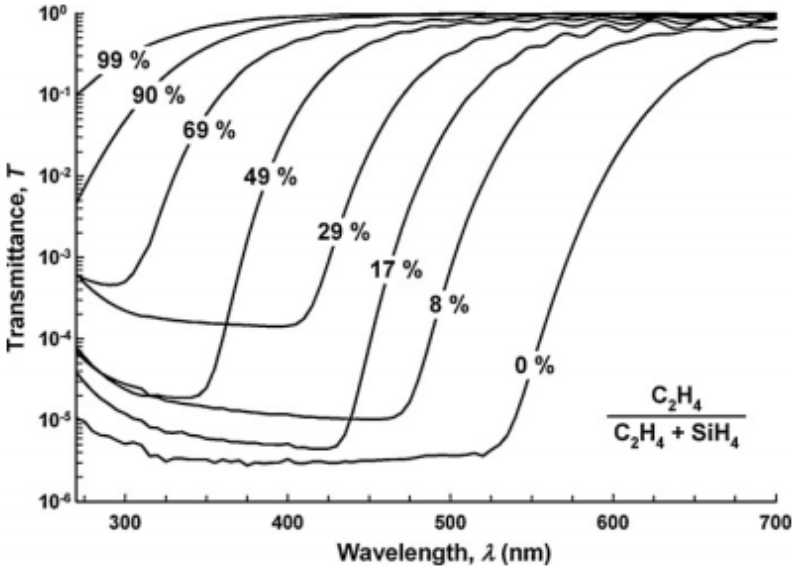

Figure 4.5: Silicon carbide high pass filters transmission curves as a function of the carbon content of the film, deposited in the in-house built PECVD machine at INESC-MN. [172]

4.3 Photosensors

In this section I will discuss the two types of photosensors used in this work, the simpler **photoconductor** and the more complex **photodiode**.

4.3.1 Parallel Contact Sensors - Photoconductors

Working Principle

The photoconductor, also called a photoresistor, is the simplest type of photosensor, composed of a slab of the photoresponsive material, in this case i-a-Si:H, capped on two opposite ends with an ohmic contact. An example of this device is presented in Figure 4.6.

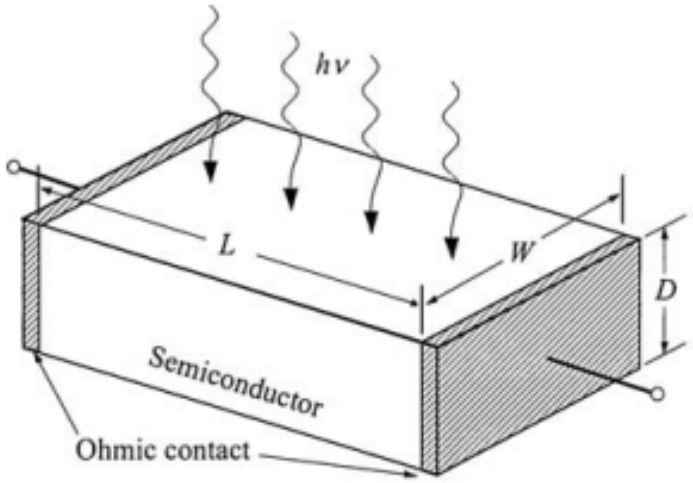

Figure 4.6: Representation of a photoconductor. Adapted from: [168]

When light with enough energy to excite electrons from the valence band to the conduction band hits the sensor, there will be a change of the resistance of the material and electron-hole pairs will be generated, producing a **photocurrent** (I_{ph}).

The photocurrent produced will not only be dependent on the incident photon flux (ϕ), but will also be a function of the external voltage (V_{Bias}) applied to the sensor.

The **dark current** is the basal current produced by the film in the absence of light. The dark current is an indication of the quality of the active layer film and will dictate the limit of detection of the sensor and will also depend on the applied voltage.

Fabrication Process

The fabrication process is summarized in work presented by Santos *et al* [173] and is depicted in Figure 4.7, while a more detailed run sheet is presented in the Supplementary Information. To fabricate a photoconductor, an insulating substrate such as glass is washed and a 200 nm thick layer of aluminum is deposited through PVD. This layer is then patterned via DWL to produce the geometry of the contacts,

which will need to have some degree of overlap with the sensor region and be large enough to allow for wire bonding on the other end for electronic addressing.

The aluminum layer is then wet etched using a commercial aluminum etchant and a 500 nm thick layer of i-a-Si:H is deposited through CVD. The a-Si:H layer is then patterned via DWL and undergoes a deep reactive ion etching step to produce the desired sensor geometry.

The whole sensor is then passivated with a 100 nm thick layer of SiN_x in order to passivate the whole device.

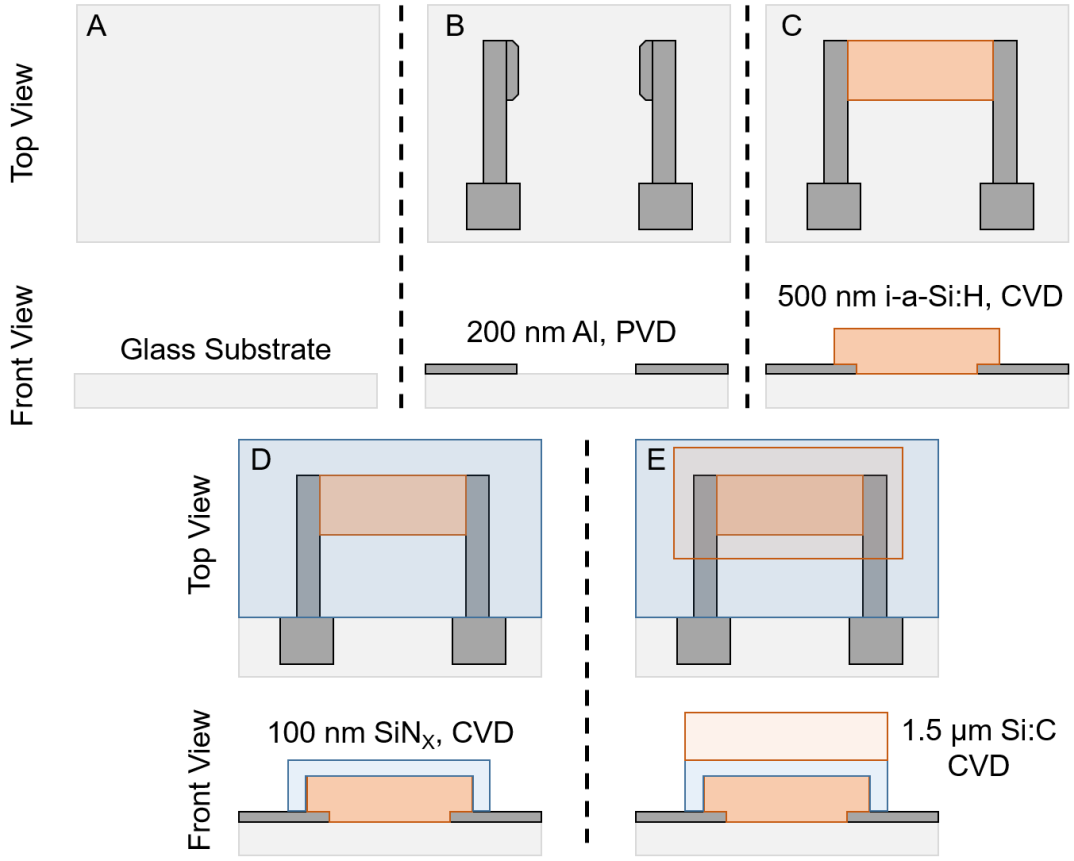

Figure 4.7: Representative diagram of the fabrication process for the thin film photoconductors. (A) The glass substrate is washed, (B) followed by the deposition of a 200 nm thick layer of aluminum. (C) After patterning, the 500 nm thick a-Si:H mesa is deposited and defined through etching. (D) The whole sensor is passivated with a 100 nm thick layer of SiN_x. (E) In the case of the sensors used for fluorescence measurements, a 1.5 μm thick layer of Si:C is deposited through CVD. Dimensions are not to scale.

Characterization

There are several figures of merit to evaluate the efficiency of the photosensors. As mentioned before, the dark current is an indication of the limit of detection of the photosensor when something like a chemiluminescence or fluorescent measurement is considered, where the control level will be darkness. In the case of an absorbance measurement, the limit of detection of the sensor is given by the noise of the measurement with incident light. To acquire the dark current, a Keithly 237 electrometer set to

measure current and apply a known voltage is used.

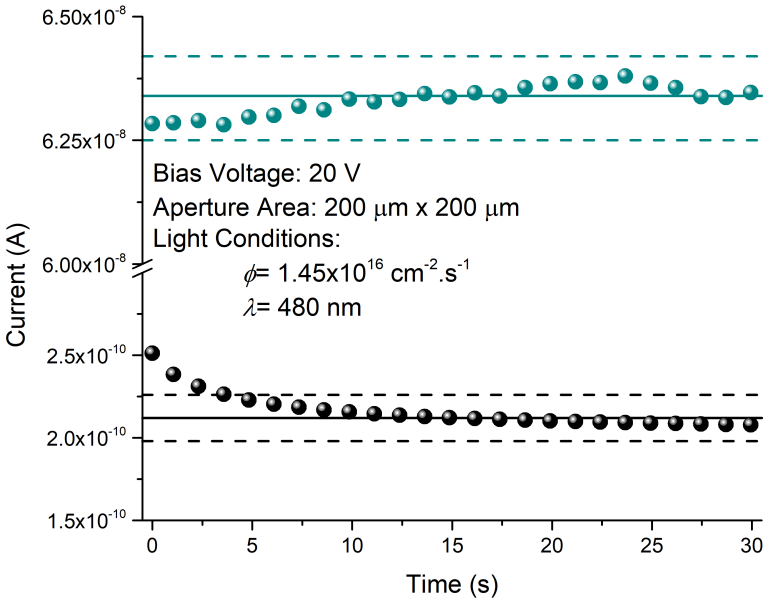

Figure 4.8: Comparison of the limits of detection in conditions of darkness (black) and with incident light (cyan). The sensors used here were 200 μm x 200 μm in area and operated at a 20 V bias. The dotted lines represent the LOD, calculated as the mean +/-3.29 the standard deviation of the measurement.

As seen in Figure 4.8, the photoconductors have different stabilities when used for low light or high light applications. As an example. for the sensor presented in Figure 4.8, the LOD for a transmission measurement would be around 98.7%, this value is obtained by determining the average of the curve presented and subtracting to it the value of 3.29x the standard deviation *(σ)*. For the low level measurements, we should be able to detect a photon flux that causes a shift in current *(I)* higher than 1.4x10^{-11} A.

The current obtained both in the dark as well as, in a state of incident light will depend on the V_{Bias} applied to the photoconductor. Being essentially a variable resistor, which is affected by the incident light, one can expect that the relation between the current generated and the V_{Bias} will be linear.

By measuring the dark current for different applied voltages, as well as with a strong incident light, *I-V* curves can be obtained, as seen in Figure 4.9.

The shape of the *I-V* curve shows that within this range there is a linear response of the dark current with the applied voltage.

Another important aspect is the **photoresponse** of the sensor. The photoresponse is the change of current registered for a given change of the incident photon flux. The photoresponse of the sensor will also depend on the applied voltage, as a rule of thumb, it is recommended an applied voltage of 1 V for every 10 μm of sensor width.

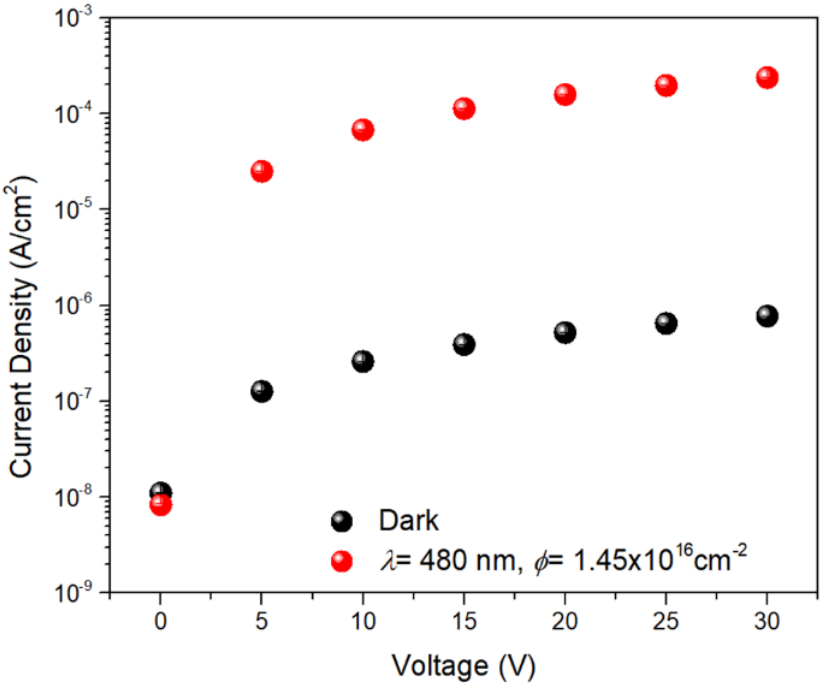

Figure 4.9: Current vs voltage (*I-V*) in the dark and with an incident light (λ= 480 nm) for a 200 μm x 200 μm photoconductor.

The setup used to acquire the photoresponse curve is depicted in and consists of an optical table, where a light source (Oriel) is connected to a monochromator (Oriel) and is aligned with neutral density filters. Once the light source is focused and the desired wavelength is chosen, the photon flux of the setup is determined using a commercially calibrated crystalline silicon photodiode (Hammamatsu, S1226-5BQ). By changing the neutral density filter place in front of the beam it is possible to have a controlled variation of the photon flux, thus obtaining the photoresponse curve. An example of the curve obtained for these photoconductors is presented in Figure 4.11.

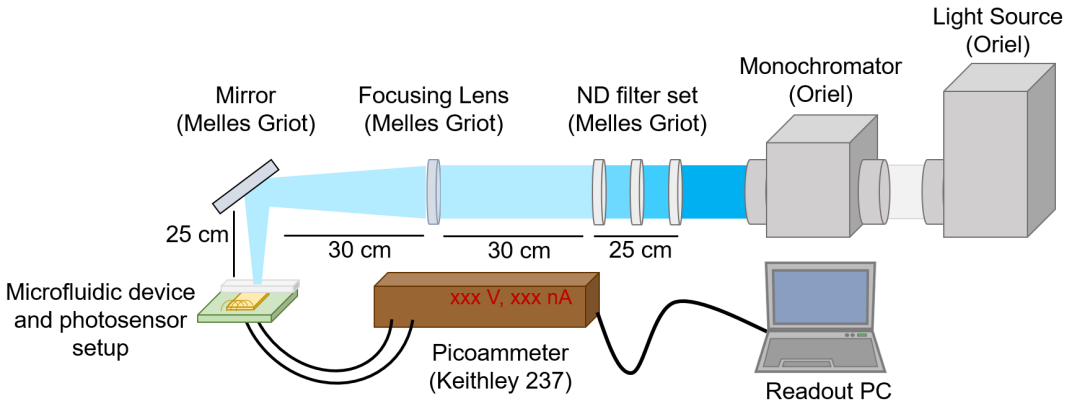

Figure 4.10: Optical setup used for the photosensor characterization. The setup is comprised of a halogen lamp light source (Oriel), which is fed to a monochromator (Oriel). Light intensity is adjusted using Neutral Density (ND) filters (Melles Griot) and focused to a final spot size of 1 mm on the photosensor plane. The sensor output is read by a Keithley 237 picoammeter and a personal computer. The PDMS slab is 3 mm thick.

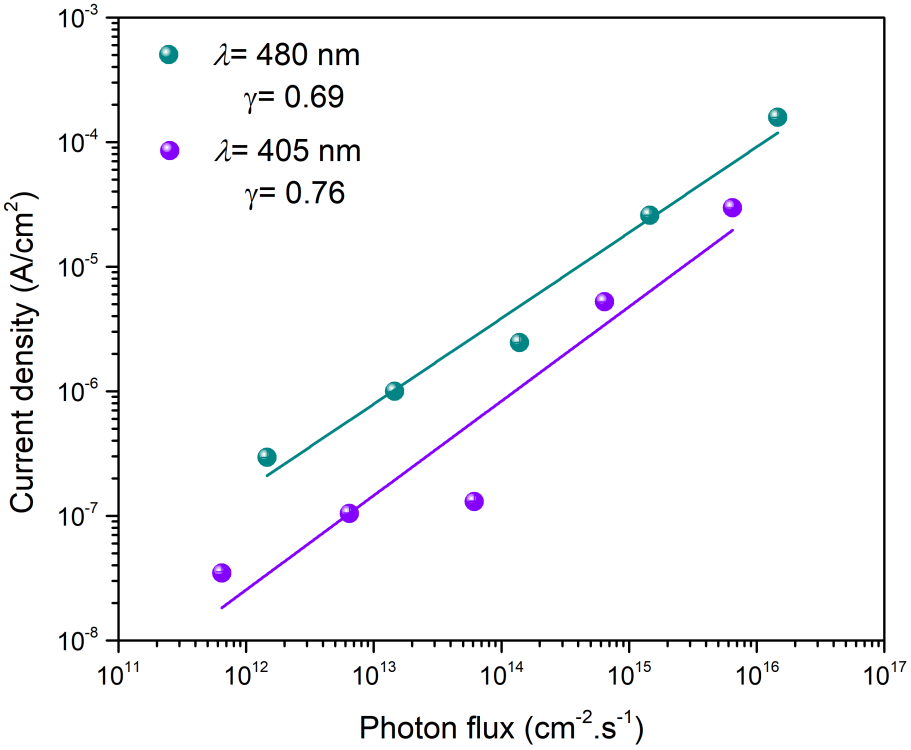

Figure 4.11: Photoresponses obtained for a 200 μm x 200 μm photoconductor at two different wavelengths of interest, λ= 480 nm and λ= 405 nm at a V_{Bias}= 20 V. The slope of the curves, γ is proportional to the carrier generation rate.

Figure 4.11 demonstrates that the sensors used in this work have a linear response towards light, in multiple wavelengths. The slope of the curves obtained, γ, is closely related to the **generation rate** of the sensors. The generation rate is the amount of charge carriers that are generated by the sensor per absorbed photon. An ideal sensor will have a γ= 1. By using the value of the minimal current detectable obtained from Figure 4.8, one can calculate that the minimum ϕ detectable for λ= 405 nm would be around 6x10^{11} cm^{-2}.s^{-1} and 10^{11} cm^{-2}.s^{-1} for λ= 480 nm.

Si:C Filters for Fluorescence Measurements

In this work, there was only one instance where a filter was needed due to the fluorescent nature of the measurement. This will be discussed in more detail in Chapter 13.

As demonstrated in Figure 4.5, the ”cut-off” region of the silicon carbide filters is dependent on the carbon content of the film. In order to determine how much carbon one needs to introduce into the filter composition, first it is necessary to observe the fluorophore spectra. Both the emission and excitation spectra for the commercial fluorescent label Alexa 430 are presented in Figure 4.12.

For this experiment it was decided that a laser at λ= 405 nm was going to be used as the excitation source, so the filter used could be very generous in terms of the sharpness of the cut-off region, as long as, most of the light above λ = 500 nm went through the filter.

The Si:C filter composition was tuned based off the previous work of Santos *et al.*. [173] The filter characterization is presented in Figure 4.13.

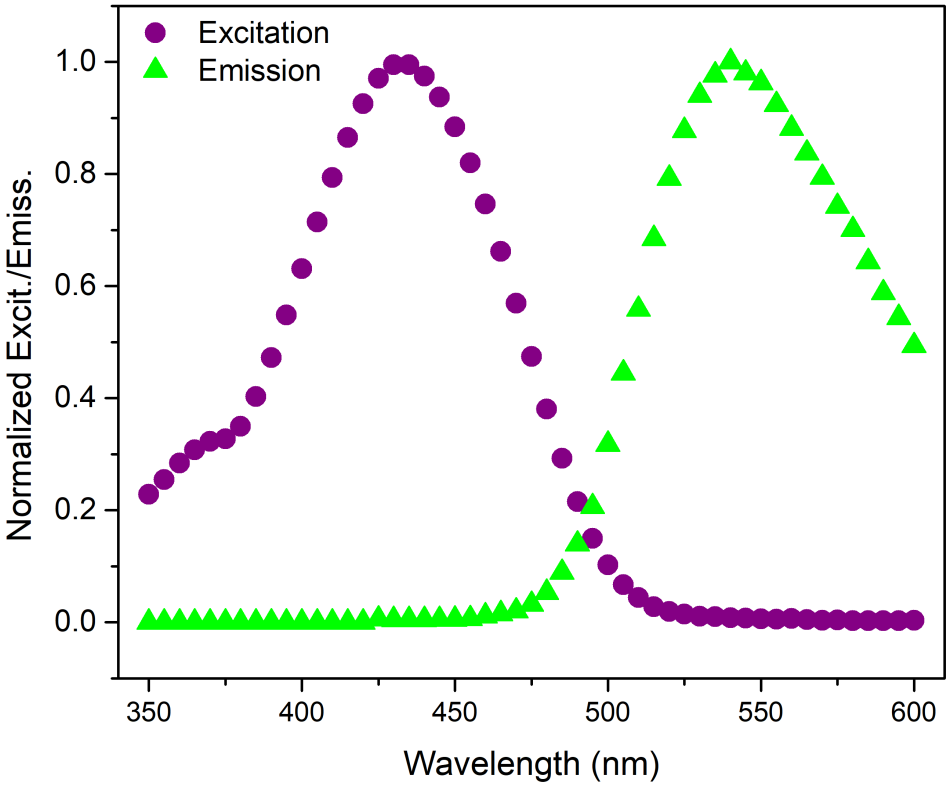

Figure 4.12: Excitation and emission spectra for the commercial fluorescent tag Alexa 430.

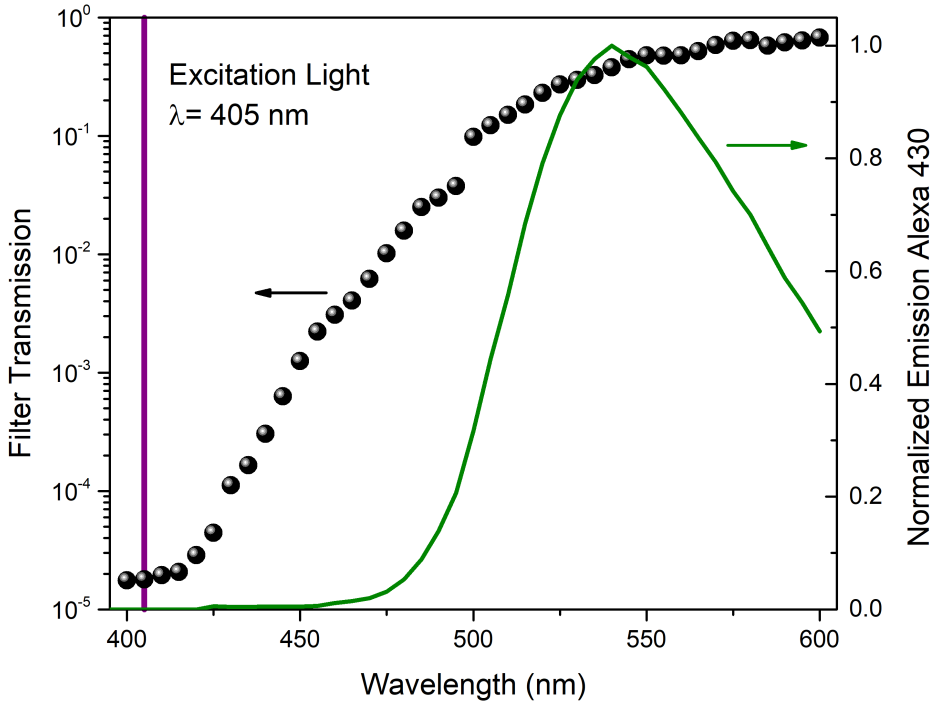

Figure 4.13: Transmission curve obtained for the Si:C filter deposited on 0.7 mm thick Eagle glass, Corning (Black) and the emission spectrum of the Alexa 430 fluorescent tag (Green).

The film presented in Figure 4.13, was then deposited on top of the 200 μm x 200 μm photoconductors and the photoresponse at both λ= 540 nm and λ= 405 nm was determined, with the later being non-detectable.

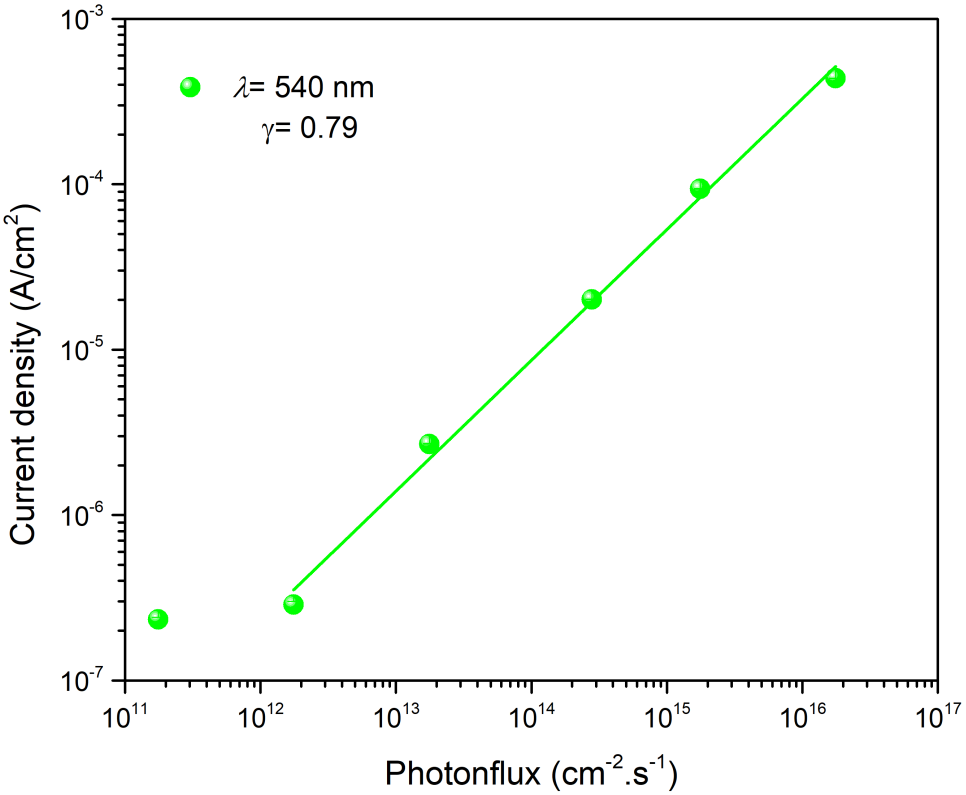

Figure 4.14: Photoresponse for the Si:C filter covered photoconductor at a V_{Bias} = 20 V at the peak emission of the Alexa 430 fluorescent tag λ= 540 nm.

By comparing Figure 4.14 to Figure 4.11 it is possible to observe that the generation rate of the photosensor, nor it's sensitivity are significantly impacted by the presence of the Si:C filter at the wavelength of interest, making it suitable to use as an optical transducer for the fluorescence based assays.

4.3.2 p-i-n Junctions - Photodiodes

Working Principle

A more complicated approach to building a photosensor is to fabricate a ***p-i-n* junction**. As mentioned before, when a p^+ layer and a n^- layer are placed together, a *PN* junction is created which possesses an intrinsic potential difference called the **built-in voltage**. The built-in voltage will affect the movement of the charge carriers without the need of an external power supply, thus creating a self sustained photosensor.

When the desired active material is a-Si:H, just using a *PN* junction does not produce an effective photosensor, as the doped materials tend to be extremely defective, promoting the recombination of the charge carriers within the material. In order to by-pass this issue, an intrinsic layer of a-Si:H is placed between the doped layers. It is in the intrinsic layer that the photons will be absorbed leading

to the creation of the electron-holes pairs which will then travel to the doped layers, generating the photocurrent.

Previously it was mentioned that these photodiodes are capable of functioning without the use of an external power supply, due to the presence of the built-in voltage. However there are some advantages in applying an external voltage to the diode. When the voltage applied is in the same direction of the built-in voltage, we are working in what is called **forward bias**, here the energy barrier between the doped layers is decreased, facilitating electron movement throughout the material. If the voltage applied is in the opposite direction, it is considered to be a **reverse bias**, which leads to a larger potential difference between the doped layers. A visual representation of this effect can be seen in Figure 4.15.

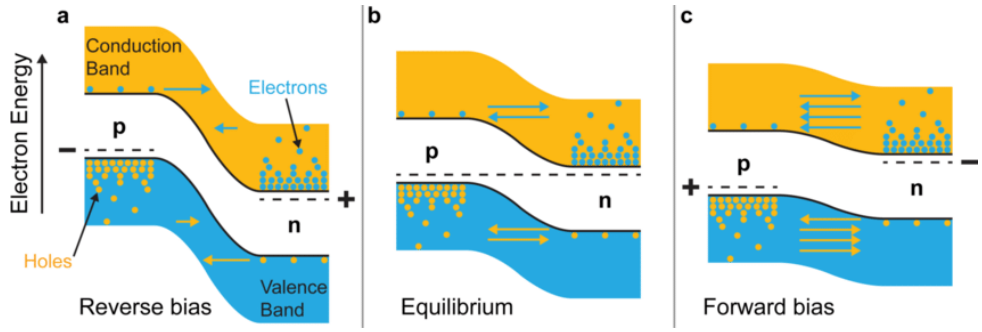

Figure 4.15: Effect on the application of a voltage bias on the band diagram of a PN junction. [174]

By applying a negative bias, theres is a slight increase in the dark current (as will be seen in the characterization section), however it may be beneficial for larger bandwidth applications. In the context of this work, there was a need to minimize the dark current in the case of fluorescence measurements, while not being relevant in the case of transmission based measurements (which comprised the majority of the work presented) thus the diodes were always used in an unbiased working mode.

Fabrication Process

In Figure 4.16 a schematic representation of the fabrication method is demonstrated and a detailed run sheet for the fabrication process can be found in the Supplementary Information. Briefly, in order to fabricate the photodiodes the initial step for the bottom contact definition is the same as for the photoconductors. Then the a-Si:H stack is deposited through rf-PECVD in the following order: n^+ (10 nm); i (500 nm); p^+ (10 nm). The *p-i-n* mesa is then etched *via* DRIE. The subsequent layers of material are all removed through lift-off in order to avoid damaging the *p-i-n* stack.

After the mesa definition it is necessary to immediately passivate the side walls of the stack as these tend to be very defective and can lead to shorting of the device. This passivation is achieved by depositing 100 nm of SiNx through rf-PECVD.

The next step is to define the top contact of the device, which will require a transparent material or some type of a mesh. The typical material of choice is a 50 nm thick layer of indium tin oxide (ITO) deposited through PVD. ITO is a conductive oxide with a band gap of 4 eV, meaning it is transparent in the full visible spectrum. There was an attempt to swap this material for an aluminum mesh, which will

be discussed in the next section.

To finish the device, the ITO top contact is partially covered with aluminum through PVD (200 nm thick) in order to facilitate the wire bonding of the device and the whole device is then covered with another layer of 100 nm thick SiNx through PVD for a final passivation.

In the case of being used for fluorescent measurements, a 1.7 μm thick layer of the desired Si:C filter was deposited through rf-PECVD.

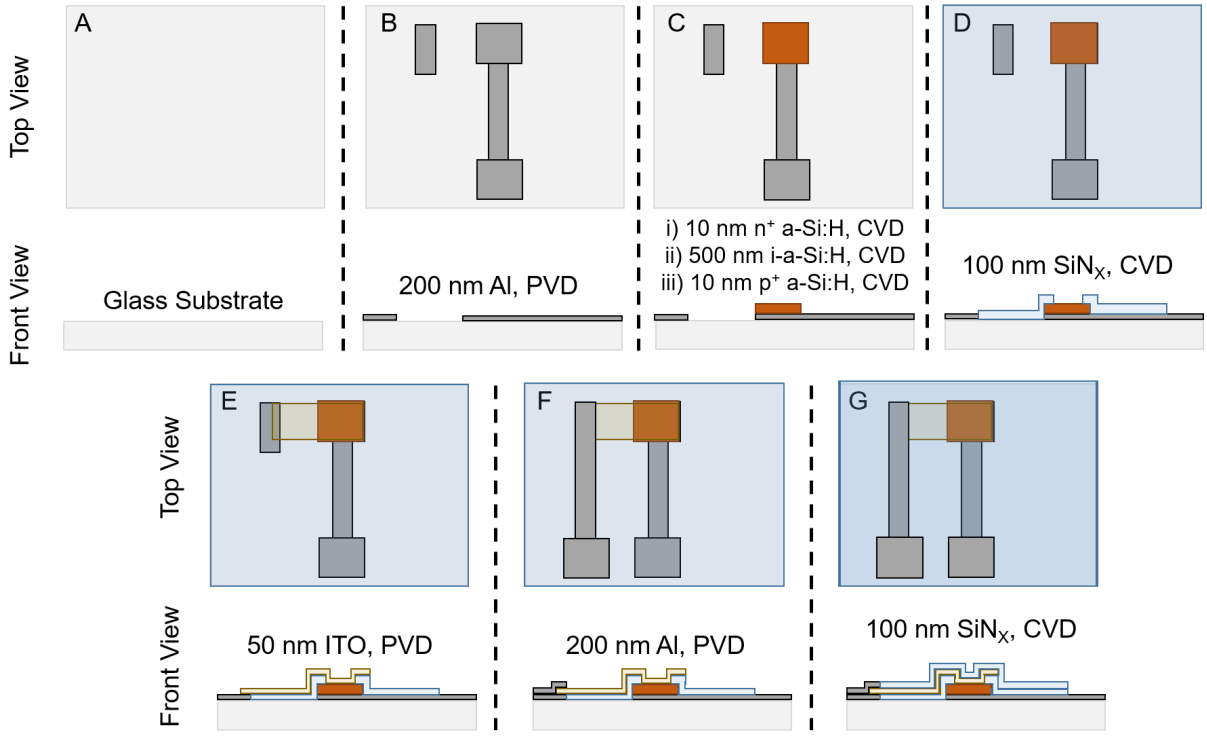

Figure 4.16: Visual diagram of the photodiode fabrication process. (A) Similar to the photoconductors, a glass substrate is washed, (B) followed by the bottom aluminum contact deposition. (C) The *p-i-n* stack of a-Si:H is deposited in the order of n^+, i, p^+. (D) After etching the active sensor area, the side walls are passivated with a layer of SiN_x to avoid possible short-circuiting through the side wall defects. (E) The ITO window portion of the top contact is deposited, (F) followed by an aluminum deposition for the actual contact pad due to the difficulty in wired bonding to ITO directly and to decrease the resistivity of the overall contact. (E) The whole structure is once more passivated with SiN_x for physical protection of the sensor due to handling. Dimensions are not to scale.

Characterization

Similar to what was done for the photoconductors, the photodiodes used in this work were characterized in terms of dark current stability, *I-V* behavior and photoresponse.

In Figure 4.17 the stability of the sensors in dark conditions as well as in a high light scenario is demonstrated.

On feature that is evident when comparing the results presented here compared to Figure 4.8, is the difference in currents produced by both of the sensors, with the photodiodes producing much lower currents, however it is important to remember that the photoconductors were operated by applying 20 V

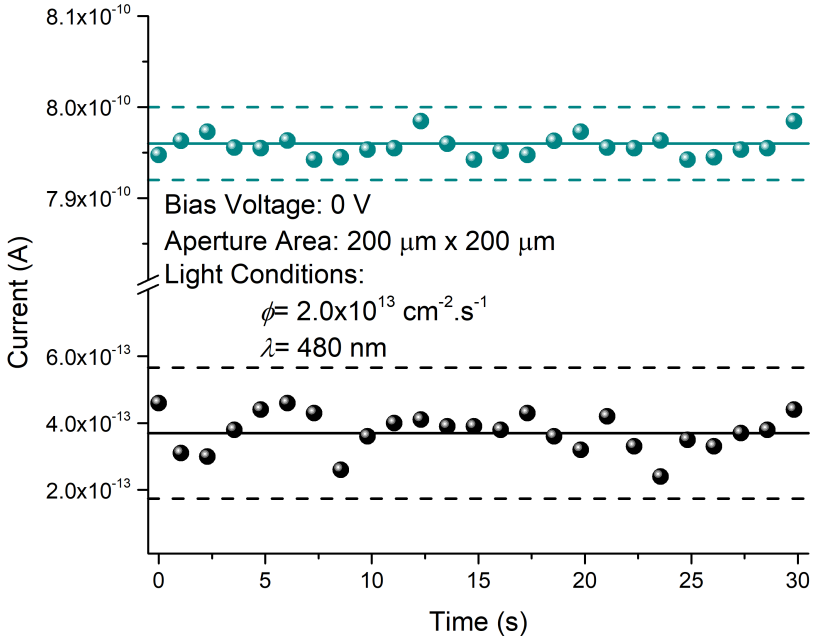

Figure 4.17: Comparison of the limits of detection in conditions of darkness (black) and with incident light (cyan). The sensors used here were 200 μm x 200 μm in area and operated at a 0 V bias. The dotted lines represent the LOD, calculated as the mean +/-3.29 the standard deviation of the measurement.

of external bias, while the diodes presented here have no external voltage being applied.

The diodes are also much more stable, producing much lower oscillations in the measured current. I mentioned that using the photoconductors, the minimum transmission shift that would be possible to observe is 1.3%, in the case of the photodiode presented in Figure 4.17, this minimum shift is 0.5%. This may seem like a small difference, however if one considers a absorbance measurement to determine the concentration of a molecule in solution this corresponds to an increase of sensitivity of 2.6 fold.

The dark current produced by the photodiode is also more stable than the aforementioned photoconductor, here the minimal shift in current that can be considered is 1.96x10^{-13} A.

Similar to the characterization of the photoconductors, the *I-V* curve for the diode was determined in the dark. However in this case, the behavior is very different from before as shown in Figure 4.18.

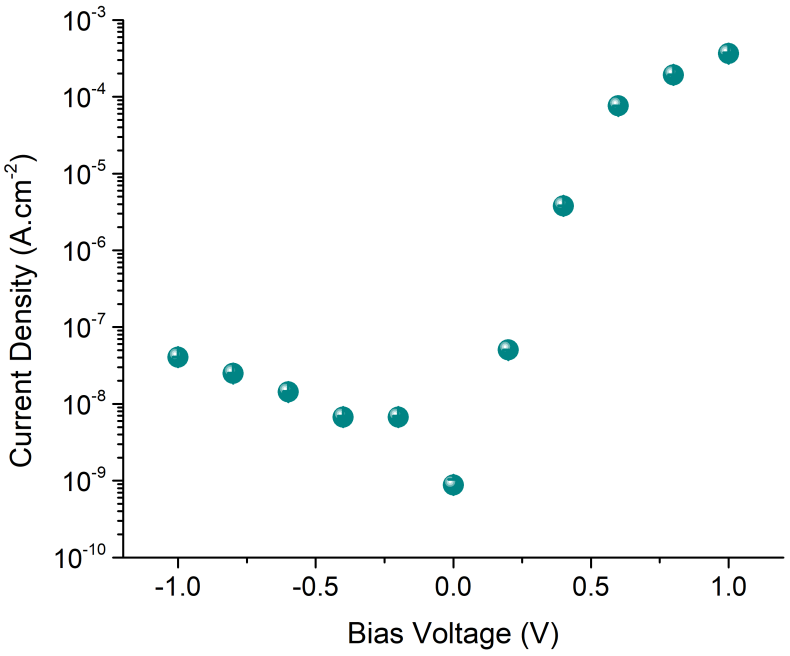

Figure 4.18: *I-V* curve determined for the thin-film photodiode. The rectifying behavior of the diode is visible in the different shapes of the curve when reverse and forward bias are applied.

In Figure 4.18, it is possible to visualize the different response the diode has when forward or reverse bias, which reveals the rectifying nature of the diode. However, it is possible to notice that when a reverse bias is applied, the current output changes slightly, this is an indication that the photodiode has some current leakage. This leakage can be due to several factors such as imperfections or defects which appear during the fabrication process, or to the poor quality of the films produced, for example, if the lateral wall passivation is not done properly, this could have a negative effect on the diode performance.

The photoresponse of the diode was determined for λ= 480 nm and is presented in Figure 4.19.

The γ obtained for this type of photosensor is significantly higher than the previously shown photoconductors, which implicates a better response of the sensors to light. In fact, using the same calculation as before, by taking the lowest current detectable with a reasonable significance and calculate the resulting photon flux, a sensitivity of approximately ϕ= 10^{-9} $cm^{-2}.s^{-1}$. This is two orders of magnitude lower then the photoconductor sensors presented previously.

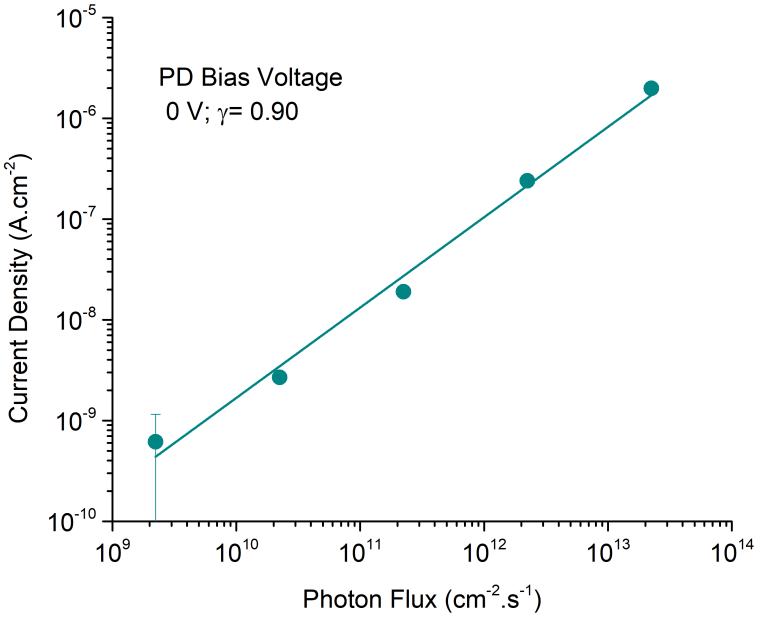

Figure 4.19: Photoresponse curve for λ= 480 nm obtained for the photodiode functioning at V_{Bias}= 0 V. The γ of the photodiode is 0.9

4.3.3 Final Remarks

Having demonstrated the superior performance in several aspects of the photodiode sensor over the photoconductor, there is still the question of why was part of the work developed using photoconductors over photodiodes?

It is true that the photodiodes are faster and more sensitive then the photoconductor, however they have their own disadvantages. The first is the time required to fabricate them. Assuming that I had a cleanroom all to myself (which is not remotely true), the fabrication process for the photodiodes would be between 2-3 weeks, while the photoconductor would be 2-3 days of processing. Factoring in the availability of the equipments and scheduling issues the process time for the photodiodes could be pushed to a month. The second issue is the life time of the devices. Due to be constantly exposed to their own built-in voltage, the photodiodes tend to have shorter life-times than the photoconductors. They also tend to be more sensible to poor handling such as static electricity discharges and excessive light exposure.

It is important to state that the fabrication methods for the sensors discussed here were developed by previous PhD candidates working at INESC-MN and not developed by myself. However they are some of the more complicated devices to microfabricate and were a key factor in a large portion of the work developed by myself. The fabrication of these sensors, tailored made to my work, allowed me to learn several aspects of microfabrication and optoelectronics, as well as to operate most of the equipments available in the cleanroom at INESC-MN, which can be translated into the fabrication of different types of structures, since the unit operations are similar.

Chapter 5

Microfluidic Device Fabrication

In this chapter, I will go over the simulation and fabrication processes employed for the creation of the devices used throughout this work in the following chapters. Some examples of the final output will be given and detailed run sheets will be provided as Supplementary Information.

When designing a microfluidic device, one has to think about the experiment at hand. Will there be multiple reaction steps? What is the height of the channel needed? Do I need mixing steps? Do I need to accommodate sensors or pumps? Once the necessary elements have been established, one can proceed to the initial designs of the device and the subsequent fabrication process.

5.1 Computational Fluid Dynamics Simulations

5.1.1 Understanding How to Employ CFD

In order to properly design a microfluidic chip, I always relied on the use of computational fluid dynamics (CFD). These types of software allow for the analysis of fluid flow properties within the device such as liquid speed and shear stress, as well as, mass transport properties such as diffusion of molecules or transport and distribution of cells within a device.

There are several softwares available, capable of running CFD simulations such as OpenFoam and Ansys, however my preferred tool was the use of COMSOL Multiphysics, combined with the use of AutoCAD for the actual design of the structures. Independently of the software chosen, the approach to the problem is the same, the correct equations that govern fluid flow have to be used, as well as the appropriate boundary conditions for the given model.

Navier-Stokes Equations

One can't start to describe the movement of a viscous liquid without using the **Navier-Stokes equations**. These equations are used throughout several fields of engineering, including aerodynamics calculations in aeronautical engineering,[175] as well as the dispersion of fluids in video games [176]. Even from a purely mathematical stand-point, there is a great interest in these equations, as there is no certainty

as to there are always solutions in 3D systems, or weather theses are smooth or not. Determining this is one of the seven millennium problems, for which the Clay institute will reward the solver with a one million dollar prize.[177]

The Navier-Stokes equations are the direct result of the application of Newton's second law to the movement of a viscous liquid, while assuming that the stress felt by the liquid is due to an viscous term and a pressure term. I could spend a good deal of time deriving and discussing the Navier-Stokes equations for the remainder of this thesis, however that would be beyond the point of the presented work. Below I present the simplified form of the equations, starting with the conservation of momentum in Equation 5.1, followed by the continuity equation in Equation 5.2.

$$\rho(\frac{\partial v}{\partial t} + v.\nabla v) = -\nabla p + \nabla.[\mu(\nabla v + (\nabla v)^T) - \frac{2}{3}\mu(\nabla.v)I] + F \tag{5.1}$$

$$\frac{\partial \rho}{\partial t} + \nabla.(\rho v) = 0 \tag{5.2}$$

In Equation 5.1, the first term is related to the inertial forces felt by the fluid, where ρ is the fluid density, and v is the fluid velocity. The inertial forces are equal to the sum of the pressure forces (∇p), externally applied forces (F) and the viscous forces, where T is the temperature of the fluid and μ represents the fluid viscosity, while I is an identity tensor. By using Equation 5.2, it is determined that there is conservation of mass during the movement of the fluid.

When applying these equations in the context of a microfluidic system there are some simplifications that can be applied. The first is that the external forces term is neglectable, gravity plays a very small low on the impact of fluid flow in a microfluidic system and the forces caused by pumping will appear in the pressure term of the equation, so it is reasonable to assume F= 0. Going back to Equation 2.2, we can determine the regime of fluid flow in microfluidic systems, which will, in most scenarios, fall under laminar or even creeping flow ($Re < 1$). Due to this, the inertial forces are minimized and can be considered to be null. these assumptions give way to a simplified version of Equation 5.1, presented below.

$$0 = -\nabla p + \nabla.[\mu(\nabla v + (\nabla v)^T) - \frac{2}{3}\mu(\nabla.v)I] \tag{5.3}$$

Now that we understand the equations that are going to be applied by the model to determined the movement of the fluid in the microfluidic system, it is possible to determine the boundary conditions. One important aspect is how the liquid will move in relation to the wall of the channel. This movement is called "*slip*", in a scenario of "*no slip*", the velocity of the fluid in contact with the wall is considered to be 0, while in a "slip" condition it will hold a different value as depicted in Figure 5.1.

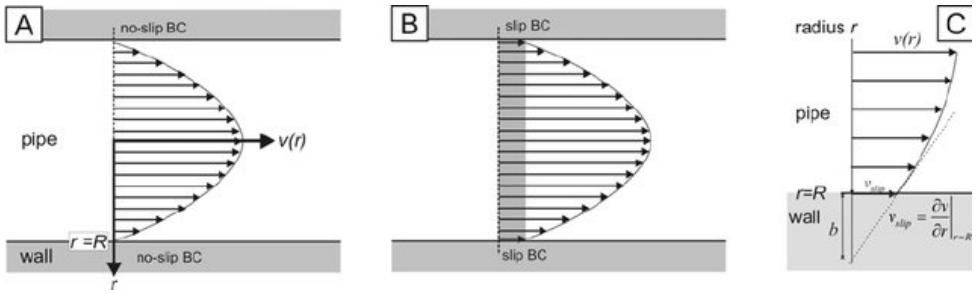

Figure 5.1: Visual representation of the existence of ”no slip” (A) and ”slip” (B) in a fluid movement. In a ”slip” scenario, the velocity can be determined as shown in (C). Adapted from [178].

In these simulation, it is assumed that the fluid is in a ”*no slip*” scenario.[179] This is because, in most cases, the adhesion forces between the first layer of the fluid molecules will have a higher adhesion force to the material of the wall than the cohesion forces between them and the remainder bulk of the fluid, leading to a monolayer of static fluid molecules coating the channel walls. One example for the existence of ”*slip*” is in high altitude aerodynamics, where the molecules tend to bounce off the surface. [180] Other assumptions used in order to determine the movement pattern of the fluid in the channel will be case dependent, and are related to how the fluid driving will be performed.

As for the equations that govern mass transport, these will be specific to the application at hand, and will be discussed in the next sections. In the following sections I will provide examples of two devices with very different end goals as an example of the work flow using this type of software. The first will be a biosensing device that was used in Chapter 14, but was eventually dropped to reasons that are related to the dynamic range of the assays. The second device is a cell culture platform that is then used in Chapter 19.

5.1.2 Design of a Multiplexed Biosensing Device

Problem Statement

The first step as mentioned before is to understand what is the requirements of the device that we want to develop. I will omit the biochemical details of the device as these will be discussed in a further chapter. Here we needed one inlet for the insertion of the grape juice sample *via* pipette tip, 3 parallel chambers to accommodate microbeads, one for each assay and each assay has a liquid reservoir on chip that would hold a given substrate for the needed reaction. For the first assay dedicated to the detection of azelaic acid, a second chamber is needed for sample pre-treatment. The sample and the assay substrate should reach the entry of a passive mixer before entering the detection chamber. All these liquids are driven using a single pump at the outlet, by applying a negative pressure.

Passive Mixer

To simplify the problem, first I proceeded to design and simulate the appropriate geometry for a passive mixer. For this element of the chip, a simple T-shaped channel with two inlets and one outlet was used. This channel is presented in Figure 5.2, as well as the result obtained from the absence of a mixer.

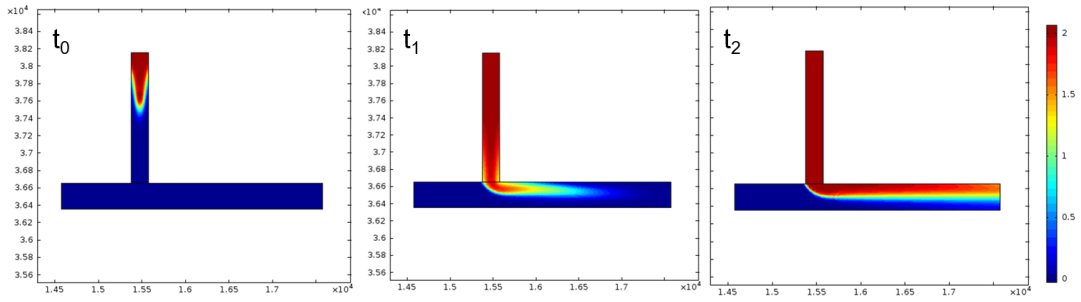

Figure 5.2: Simulation results for a T-junction channel where a solution of molecule, A, is injected at a concentration of 2 mM in the top inlet, while just water is injected in the side inlet. The color gradient represents the concentration gradient between 2mM (Red) and 0 mM (Blue), while the x and y axis are the coordinates of the system in the x-y plane in μm. The channel height is determined as 20 μm and the flow rate is defined as 1 μL/min for each inlet.

To obtain the results presented in Figure 5.2, one has to first solve the Navier-Stokes equations as described in the previous section, which will give us the movement of the liquid. However, in order to study the mixing of the solutions, one has to add information considering mass transport to the system. To do this, we will introduce the equations related to mass transport, with the first being a a mass balance over time as presented in Equation 5.4.

$$\frac{\partial C}{\partial t} + \nabla.\mathbf{N} - \mathbf{R} = 0 \tag{5.4}$$

Since we are only looking at mixing and mass transport, the amount of the analyte consumed through reactions (**R**) is equal to 0. This leads to the change in concentration (C) over time equal to the mass flux of the analyte under analysis (**N**). The mass flux is a function of both the diffusion of the molecules as well as movement induced by convection as demonstrated in Equation 5.5.

$$\mathbf{N} = -D\nabla C + uC \tag{5.5}$$

Equation 5.5 shows us that the movement of the molecules in the liquid will be dependent on their intrinsic properties such as the diffusion coefficient (D) and on the movement of the bulk of the liquid represented as the velocity field (u) calculated previously. Replacing Equation 5.5 in Equation 5.4 we can obtain the simplified version of the equation presented below.

$$\frac{\partial C}{\partial t} + \nabla.[-D\nabla C + uC] = 0 \tag{5.6}$$

Typical diffusion coefficients for small molecules will be of the order o 10^{13}cm^2.s^{-1} [181], while for proteins and cells it can easily be estimated using the Einstein-Stokes equation, which depends on the temperature (T) and viscosity (μ) of the solvent and the hydraulic radius of the protein/cell (R_h) and are related through the Stefan-Boltzmann constant (k) as presented below.

$$D = \frac{kT}{6\pi\mu R_h} \tag{5.7}$$

Now we can proceed to test different geometries, in the interest of time, I will give and example of an

inefficient mixer presented in Figure 5.3 and the final design that was chosen, presented in Figure 5.4.

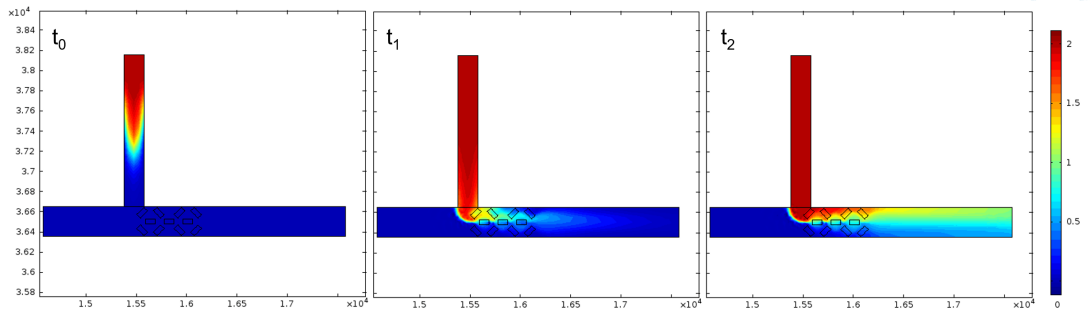

Figure 5.3: Simulation results for a T-junction channel with an inefficient passive mixer, where a solution of molecule, A, is injected at a concentration of 2 mM in the top inlet, while just water is injected in the side inlet. The color gradient represents the concentration gradient between 2mM (Red) and 0 mM (Blue), while the x and y axis are the coordinates of the system in the x-y plane in μm. The channel height is determined as 20 μm and the flow rate is defined as 1 μL/min for each inlet.

Despite being an improvement over Figure 5.2, by looking at the concentration distribution in Figure 5.3, it is possible to observe that at the outlet, the concentration of A is still not evenly distributed. This lack of uniformity may impact the results obtained by the assay due to the liquid entering the detection chamber as a gradient instead of a homogeneous liquid.

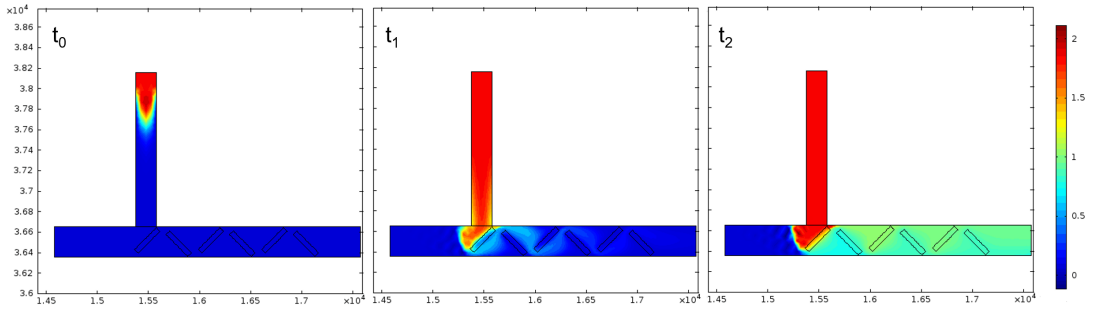

Figure 5.4: Simulation results for a T-junction channel with an efficient passive mixer, where a solution of molecule, A, is injected at a concentration of 2 mM in the top inlet, while just water is injected in the side inlet. The color gradient represents the concentration gradient between 2mM (Red) and 0 mM (Blue), while the x and y axis are the coordinates of the system in the x-y plane in μm. The channel height is determined as 20 μm and the flow rate is defined as 1 μL/min for each inlet.

In Figure 5.4 it is possible to observe that the output solution of the channel is much more homogeneous than in Figure 5.3. This is due to the geometry presented in Figure 5.4 forcing the liquid to change its free path to a higher degree and colliding head front with itself by going around the obstructions. This increases the convection term presented in Equation 5.6, thus increasing the overall mass transport of the system. This design was then employed as the mixer for the three sections of the multiplexed device.

Simulating the Multiplexed Device

Now that we have our passive mixer geometry we can proceed to simulate the actual device itself. As stated before th device requires the use of chambers to accommodate microbeads. Through microscope

photography, we determined that the average voidage (ϵ) of a chamber with a height of 100 μm packed with beads with an average diameter of 50 μm is around 0.4. With this in mind and in order to reduce the computational time, the chambers were changed to channel constraints as demonstrated in Figure 5.5. Another simplification at the moment was the inlet and outlet geometry used as our goal is to get the liquids stored in the reservoirs to reach the mixers at the same time as the sample by applying a negative pressure at the outlet.

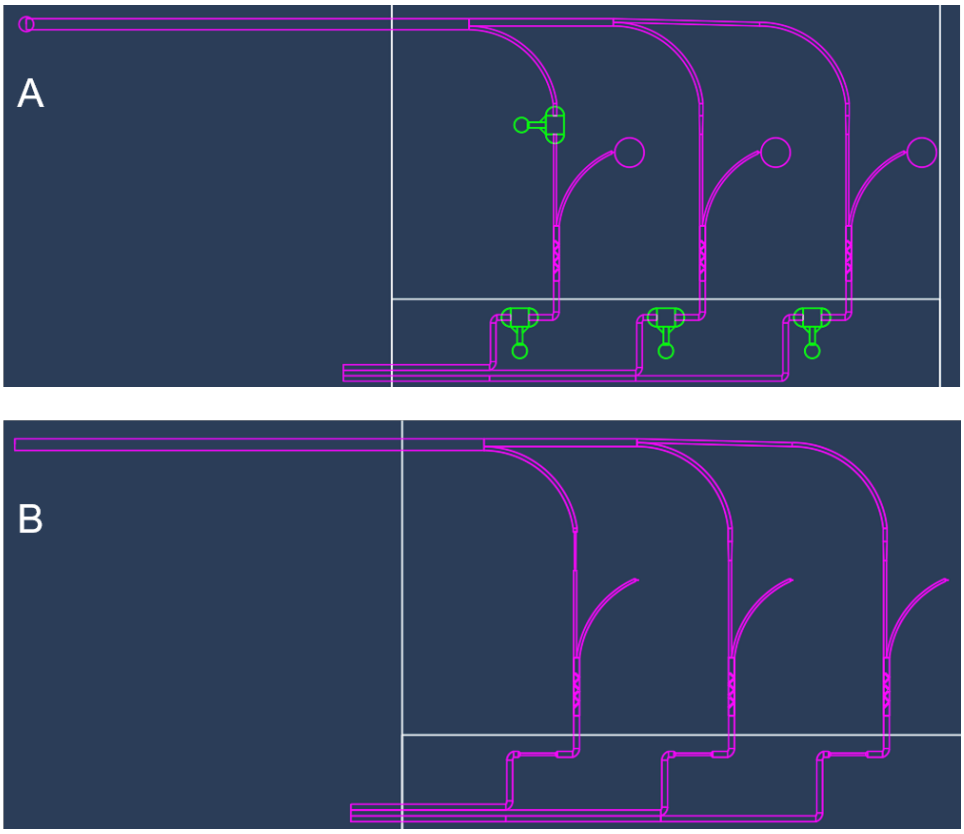

Figure 5.5: Initial design used for the simulation of the multiplexed detection chip. (A) In green we have the 4 chambers needed to accommodate the necessary microbeads for the assays as well as the large circle reservoirs for the substrate inclusion on chip. The sections in green are 100 μm in height while the purple interconnecting channels are 20 μm tall. (B) These features were replaced to reduce the computational time.

The initial result produced with this geometry is presented in Figure 5.6 and it is possible to see that the sample is reaching the detection chambers before the assays substrates.

The initial geometry was then worked upon by adding liquid constraints to slow the sample entrance and facilitating the substrate entrance by diminishing the hydraulic resistance. Once a final geometry was obtained (15 iterations later), the simplifications initially used were substituted for the real case scenario and a final simulation was performed, with the device being fabricated and tested as seen in Figure 5.7.

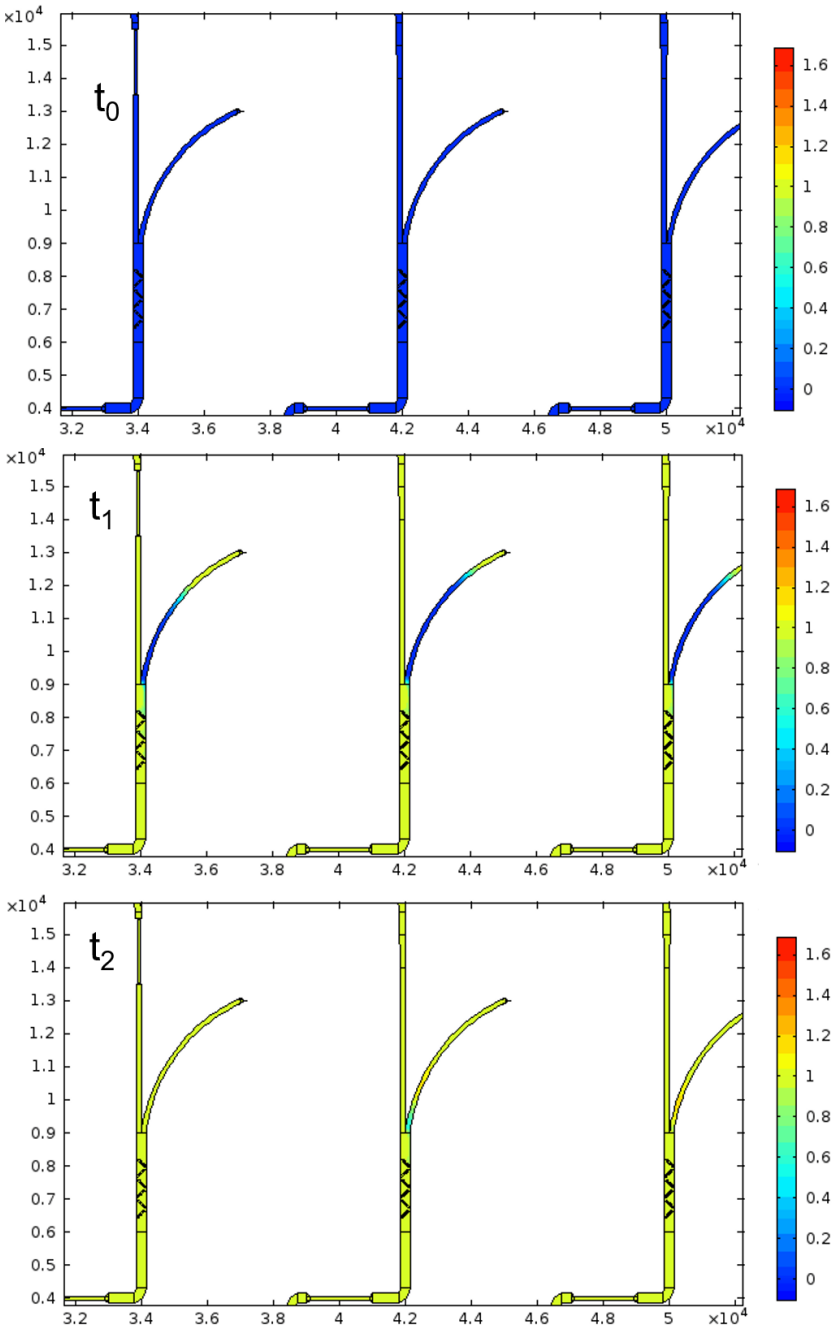

Figure 5.6: Results obtained for the simulation of the initial chip geometry for the multiplexed detection of grape health indicators.

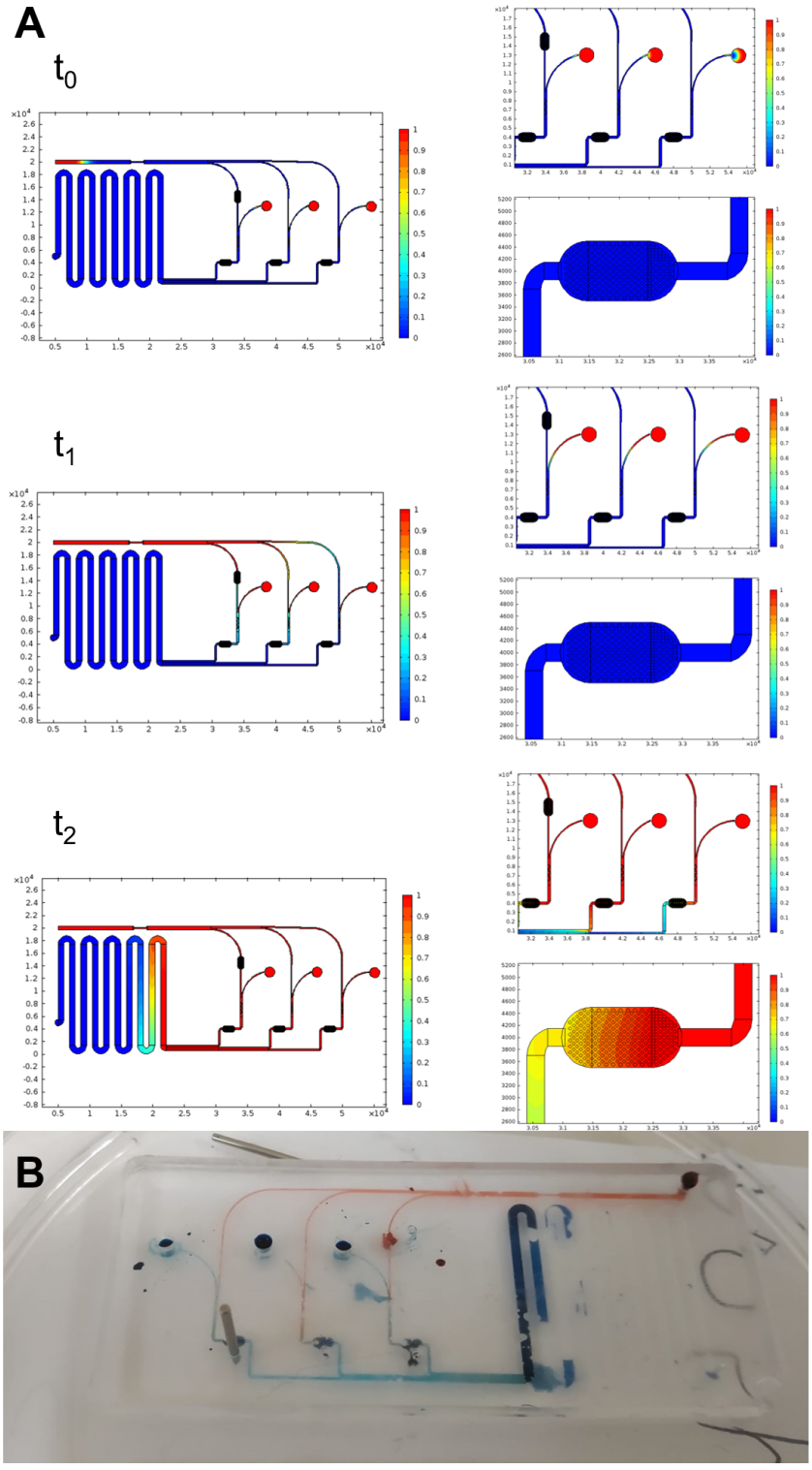

Figure 5.7: (A) Results obtained for the simulation of the final chip geometry for the multiplexed detection of grape health biomarkers. (B) Testing the actual microfluidic chip using food coloring, important to notice the red a blue liquids meeting at the same time in the chambers.

As seen in Figure 5.7-B the fabricated microfluidic chip has the predicted behavior, validating the previous simulations

5.1.3 Designing and Simulation of a Cell Culture Chip

Problem Statement

In this case study, the challenge was different, here the objective was to design a microfluidic cell chip that would allow for the culture of Human HCT 116 cells in order to perform a phage display assay. More details on this project will be discussed in Chapter 19.

The microfluidic chip needed to allow for an even cell distribution within the chip followed by an even medium distribution to maintain the cell culture.

Cell Insertion Simulation

In this case we are not interested in the diffusion of small molecules within the chip. In this scenario the cells have an average diameter between 7 and 10 μm making them very comparable to some of the dimensions of the chip itself (chip height was determined to be 20 μm to force the cells to grow as a monolayer).

Due to the dimension of the cells, their diffusion within the channel will be neglectable during the injection step. So instead of using the mass transfer equations shown before, we will treat the cells as particles moving in a liquid bed.

The information regarding the fluid velocity field will be determined in the same fashion as before through the use of the Navier-Stokes equations, which will yield us the velocity field of the liquid (u). Now we need to understand the forces affecting the cells, the first factors to consider are Equation 5.8 and Equation 5.9.

$$\frac{dx}{dt} = v \tag{5.8}$$

$$\frac{d(m_p v)}{dt} = \sum F \tag{5.9}$$

Equation 5.8 tells us that the change in the cell position (x) is equal to the velocity of the cell, while Equation 5.9 tells us that the sum of all forces exerted on the cell are equal to the mass (m_p) times the acceleration of the cell ($\frac{dv}{dt}$), nothing more than Newton's second law of motion.

In addition to these equations we have to consider the drag force imposed by the movement of the liquid on the particle, which is a bit more complicated. The drag force (F_D) can be calculated using Equation 5.10, where τ_p represents the particle velocity response time and is given by Equation 5.11.

$$F_D = \frac{m_p}{\tau_p}(u - v) \tag{5.10}$$

$$\tau_p = \frac{4\rho_p d_p^2}{3\mu C_D Re_r} \tag{5.11}$$

In the calculation of τ_p, C_D represents the drag coefficient, ρ_p is the cell density (assumed as 1200 kg/m^3), while d_p is the cell diameter(assumed as 10 μm). The drag coefficient can be simplified to $C_D = \frac{24}{Re_r}$, where Re_r represents the relative Reynolds number between the cell and the bulk of the fluid. The simplification of the drag coefficient number stems from the low Reynolds number of the system ($Re < 1$). this leads us to the simplified equation for the drag force presented in Equation 5.12

$$F_D = \frac{18 m_p \mu}{\rho_p d_p^2}(u - v) \tag{5.12}$$

With these equations I can proceed to determine the cell position upon injection, as in the case of the mixer, I will demonstrate the results obtained for a inefficient system and for an improved one.

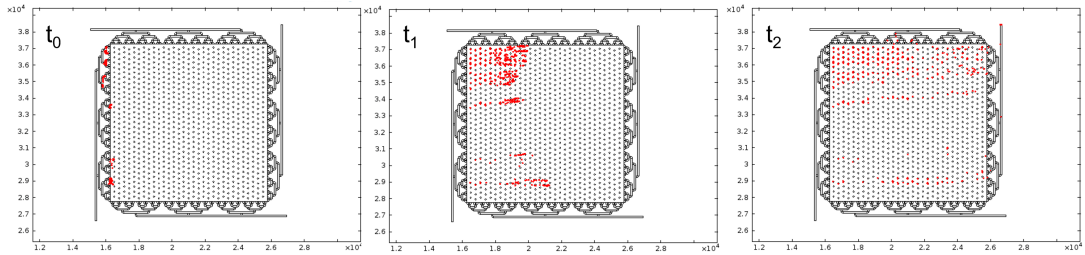

Figure 5.8: Results obtained for the initial geometry simulation. The channel height is defined as 20 μm and the cell injection was defined as 1000 cells/min using a liquid flow rate of 0.5 μL/min. The red dots represent the cells in suspension and are enlarged for visualization purposes.

Figure 5.8 shows the 1 cm x 1 cm microfluidic cell chip simulations. The existence of 2 inlets and 2 outlets located perpendicular to each other was to insert the cells in one direction and the phages in the other as cells could become trapped in the small inlets causing clogging of the device. It is possible to observe that the cells don't distribute themselves in an uniform fashion throughout the length of the microfluidic chip. This poor distribution is related to how they distribute themselves in the initial inlet due to the profile of the liquid velocity following the typical parabolic shape.

Knowing this a new version was designed and is presented in Figure 5.9. The inlets of this device were optimized to accommodate the cell distribution in the inlet section of the device. As seen in Fig-

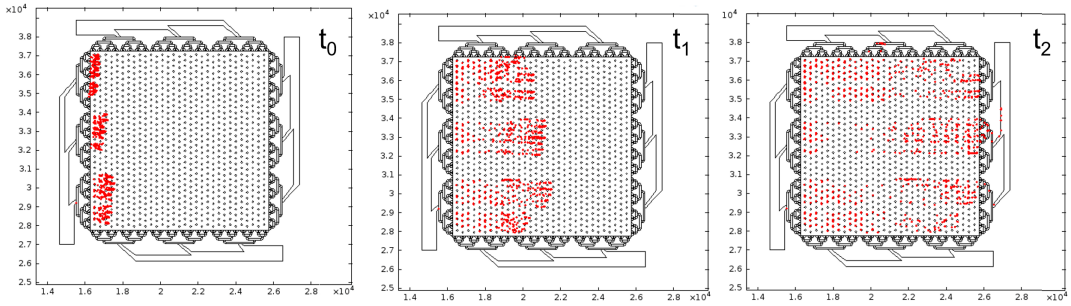

Figure 5.9: Results obtained for the hydrofocusing geometry simulation. The channel height is defined as 20 μm and the cell injection was defined as 1000 cells/min using a liquid flow rate of 0.5 μL/min. The red dots represent the cells in suspension and are enlarged for visualization purposes.

ure 5.9 the change in the inlet geometry significantly improved the cell distribution inside the cell culture area. This design was then tested and the cell distribution obtained is presented in Figure 5.10.

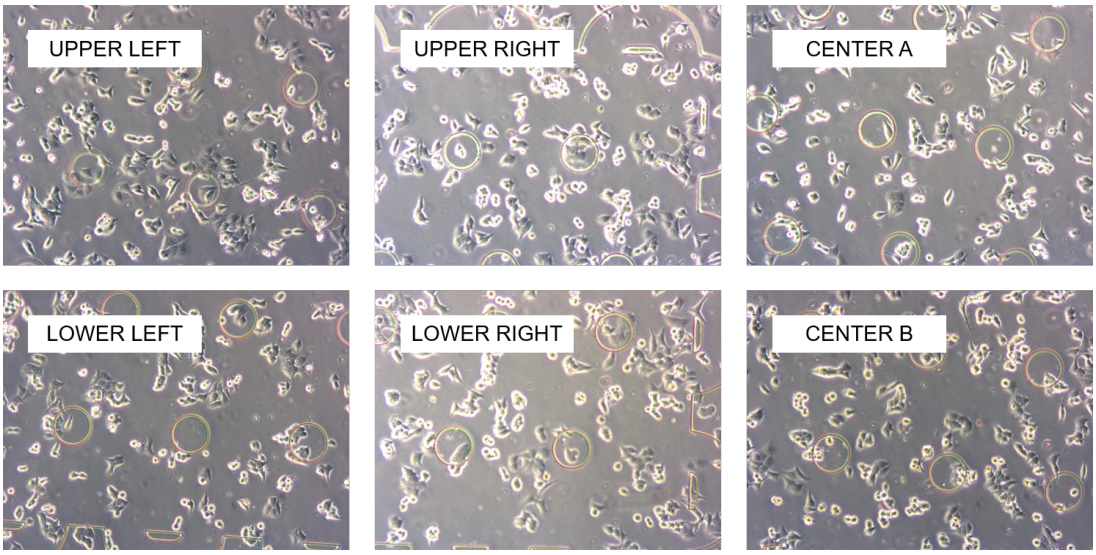

Figure 5.10: Cell distribution in the microfluidic chip obtained using the HCT116 cells.

As can be seen in Figure 5.10 the cells were evenly distributed within the channel, however the insertion of the cells was very user and cell culture dependent and not robust enough, for example if the culture used was more aggregated than usual, caused the clogging of the device in the inlet section. This lead to a change in the cell insertion protocol that will be discussed in Chapter 19.

5.2 Fabrication Methods

Once the simulations have been performed and the CAD file with the design prepared we can commence the fabrication of the microfluidic structures. The strategy used to fabricate these structures in this work was through soft-lithography.

5.2.1 Hard Mask Fabrication

The fabrication of microfluidic structures is partially done inside the clean room, due to the possibility that we have in fabricating our own hard masks. The hard mask will later be used as a stencil to define the dimensions in the $x - y$ plane of our device, with a minimum feature size of 2 μm. A schematic of the process is presented in Figure 5.11. As will be discussed in a future section, the microfluidic mold used to cast the microfluidic devices is fabricated layer wise, so if more than one height is needed in the device, for example, in the case of a chamber to trap microbeads, more than one mask will be necessary. Here we will consider the process for a one layer structure, detailed run sheets will be presented in the Supplementary Information.

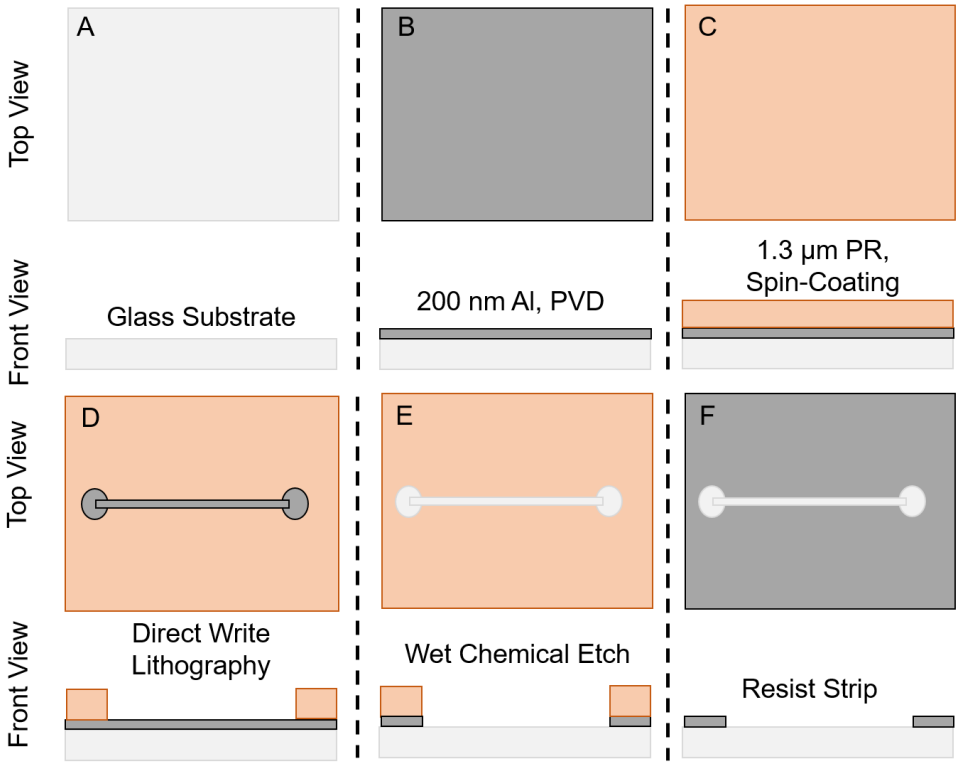

Figure 5.11: Schematic representation of the hard mask fabrication process. (A) A clean glass substrate is used as the base of the hard mask. (B) A 200 nm thick layer of aluminum is deposited through sputtering. (C) The sample is then coated with a 1.3 μm though spin coating. Once the sample is patterned though direct write lithography (D), the exposed aluminum is chemically etched (E). After visual inspection under the microscope, the remaining photoresist is removed.

The photoresist used in this process is a positive one (PFR7790G), meaning that all exposed areas will be removed after the development step, exposing the aluminum layer below.

The etching process used for this process is a wet, chemical isotropic etch. This will also etch away at the side walls of the exposed metal, however it is not a issue as the typical feature size will be above 10 μm and the thickness of the metal layer is just 200 nm.

5.2.2 Mold Fabrication

Having the necessary hard masks, one can now proceed to fabricate the actual mold. Depicted here will be an example for a single layer structure, however to add on layers one needs to repeat the process, being certain of the alignment between levels using alignment marks in the masks. A schematic of the fabrication process is presented below.

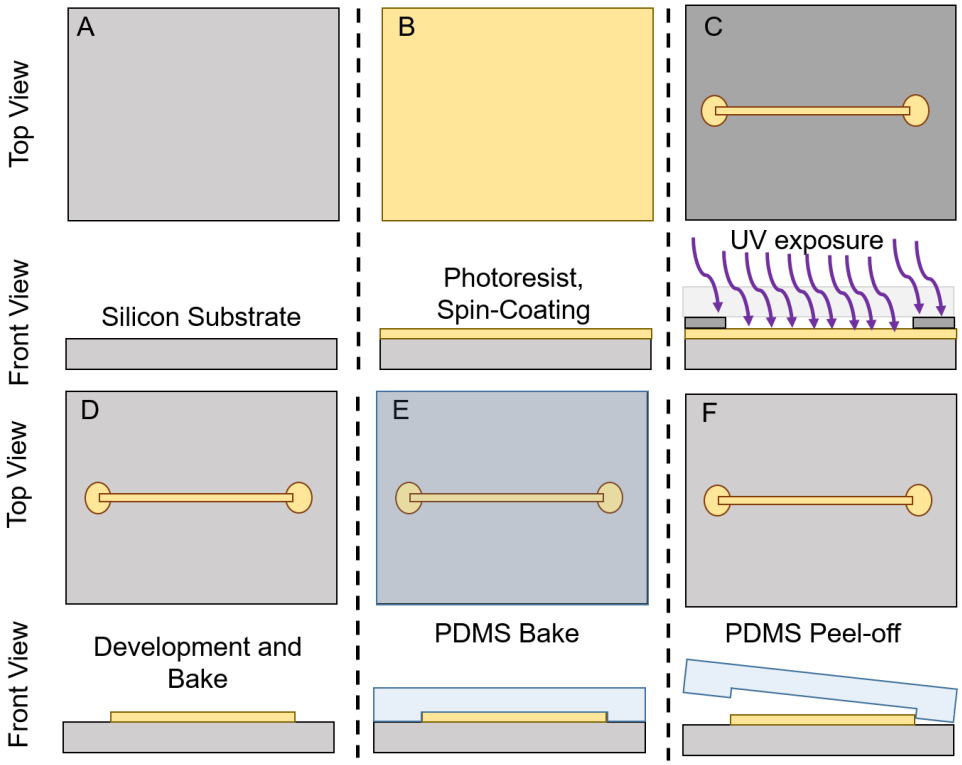

Figure 5.12: Schematic description of the mold fabrication process. (A) The first step is to clean a silicon substrate, followed by (B) a layer of photoresist through spin coating. (C) The photoresist is then exposed to a UV light source through the previously fabricated hard mask, paying attention to place the glass layer in contact with the photoresist. (D) After baking and development, the features are revealed and are ready for a longer hard bake. (E) PDMS is prepared an poured on the mold and (F) is peeled off after baking.

In this fabrication process a negative process is used, this means that the exposed regions will reticulate during the exposure step, making the photoresist insoluble in the developer solution. To fabricate the different heights needed, several formulations of the negative photoresist SU-8 (Microchem) have been used throughout this work, with the different process run sheets being presented in the Supplementary Information.

For the PDMS casting, the monomer form is mixed with the corresponding reticulating agent and degassed to remove bubbles introduced by the mixing step. The degassed mixture can than be poured on top of the mold in a container such as a Petri dish.

Despite this being the simplest approach, often I would fabricate a plastic enclosure through CNC milling to allow for the consistent replication of the structures in both area and PDMS thickness. These enclosures also had perforated lids, where metallic rods could be placed in the inlet and outlet regions of the device to allow for consistent inlets which impact the tube fittings as opposed to the typical, manual punching of the inlets.

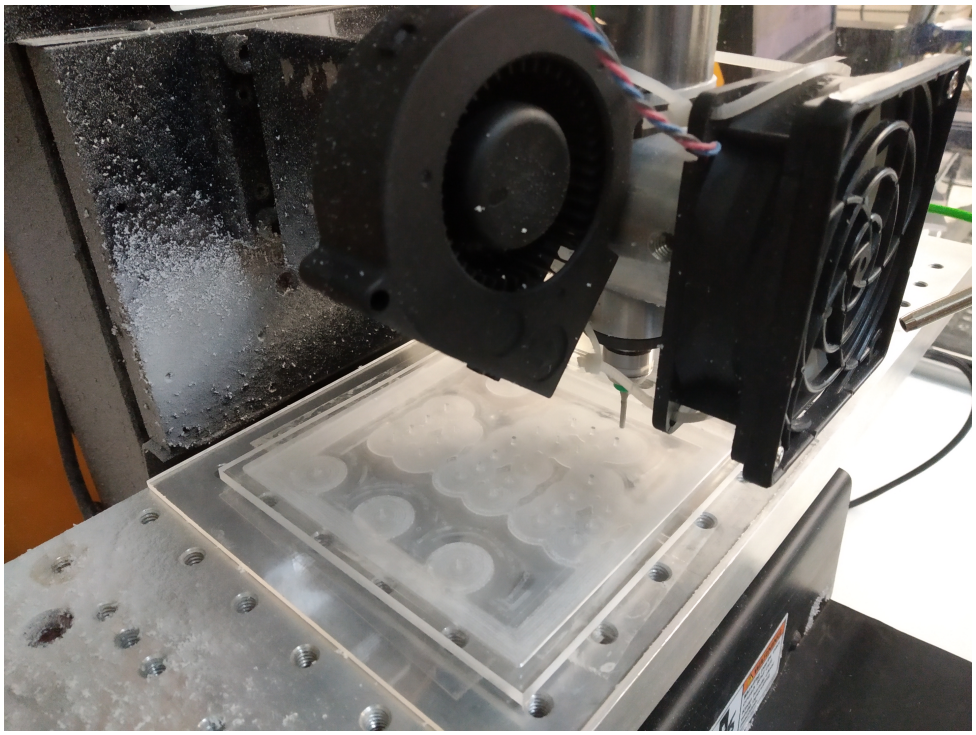

Figure 5.13: Fabrication of a molde enclosure.

5.2.3 Chip Sealing

At this point in the fabrication process we have 3/4 of a functional structure, now the final step is to seal the structure off. This will depend on the material used for the sealing.

In most cases, the sealing will be PDMS-PDMS or PDMS-glass, which can be done through oxygen plasma activation of the surfaces, which has been described extensively in the literature. [182, 183]

Briefly, by exposing both the materials to an oxygen rich plasma, one can oxidize the surface of the material producing reactive hydroxyl (OH) groups. When both materials are brought into contact with one another and by applying a very light pressure, covalent bonds are formed, with the release of a water molecule, permanently bonding the two materials together.

In the case of the work discussed in Part V, the cells preferred to adhere and grow on polystyrene (PS) as opposed to both glass and PDMS. In this case, a silanization process using (3-Aminopropyl)triethoxysilane (APTES) was used to create the reactive hydroxyl groups on the surface of the PS. [184]

In Figure 5.14 we can see several types of microfluidic structures developed by me and some *alumni* from INESC-MN.

Figure 5.14: Examples of structures used throughout the years at INESC-MN. i) Fermenter [57], ii) Adherent cell chip, iii) mycotoxin detection device [46] iv) L-L extraction devices [185]

The techniques described here were the basis of all the microfluidic chips developed throughout this dissertation and are extremely versatile to produce a wide array of different devices, as I hope to demonstrate throughout this work.

Part III

Bioprocess Development at the Microscale - Biocatalysis for Pharmaceutical Compound Production

Highlights

- A microfluidic packed-bed reactor for enzymatic synthesis of L-DOPA and dopamine is presented;
- Single step production schemes for both L-DOPA and dopamine are presented, in addition to the cascade reaction from L-Tyrosine to dopamine;
- A scale-up strategy to bench-top scale is demonstrated, with matching results between both the micro and macroscale approaches;
- This type of system can be used to expedite process development in the future.

Roles and Colaborations

- In this part of the work, I planned out the experiment sequence, designed and fabricated the microfluidic structures used and defined the initial detection method as well as the image processing method for L-DOPA. I performed all scale-up procedures and bench-top scale experiments as well as enzyme stability studies presented in this part of the work.
- **Cristiana Domingues, MSc.** performed her Master's thesis within the context of this portion of my dissertation. She performed all the microscale experiments as well as the miniaturization of the detection protocol from a 96-well plate to a microfluidic based assay.

Scientific Outputs

MSc. Thesis Supervised

- Cristiana Domingues, *Enzyme Immobilization in porous micro beads in microfluidics for continuous production of L-DOPA and dopamine*, 2019

Publications

- Brás, Eduardo J.S., *et al.* "*Microfluidic Bioreactors for Enzymatic Synthesis in Packed-Bed Reactors - Multi-Step Reactions and Upscaling*" Under Peer Revision, Journal of Biotechnology.

Chapter 6

Biocatalysis and Bioreactors

A biocatalytic process is one that uses biological systems to accelerate, or **catalyze** a given chemical reaction or sequence of reactions. [186] The most common form of biocatalysis relies on molecules called enzymes, these maybe isolated and used in their pure form or as part of cell metabolism. [187]

6.1 What are enzymes?

Enzymes are biological catalysts that accelerate chemical reactions. The majority of enzymes are from the protein family, however there are some from the nucleic acid family, namely certain RNA molecules [188]. Enzymes are the building blocks of the metabolic pathways presented by the cells and allow for these to occur at the speed necessary to sustain life. [189]

Enzymes function in the same way that inorganic catalysts do by lowering the activation energy needed for the reaction to occur, thus increasing the speed of the reaction. In Figure 6.1 the comparison of the energy balance for a typical reaction with and without the addition of an enzyme is depicted.

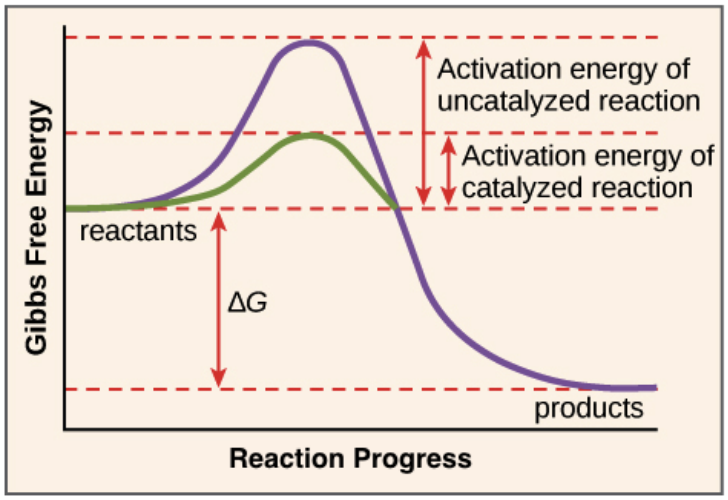

Figure 6.1: Depiction of the effect of enzymes on activation energy necessary for a typical chemical reaction. Adapted from [190]

Typically enzymes possess active centers which may or may not require cofactors in order to function

properly. As an example let us look at the molecular structure of tyrosinase as presented in Figure 6.2 Tyrosinase plays an important role in the metabolic pathway responsible for melanin synthesis in humans, to do this it catalyzes the oxidation of phenols such as tyrosine or dopamine, taking one of these organic molecules and molecular oxygen as substrates for the reaction.

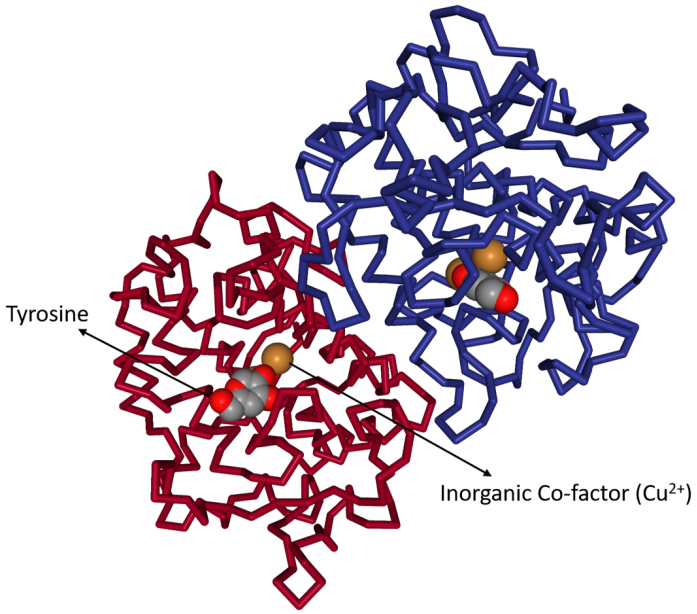

Figure 6.2: Tyrosinase 3D structure obtained from the RCSB Protein Data-Bank as of July 2017. The molecular weight of tyrosinase distributed by Sigma-Aldrich is approx. 130 kDa.

Tyrosinase is an example of an enzyme that requires the presence of a cofactor to function properly, in this case it uses copper ions (Cu^{2+}) as an inorganic cofactor. Cofactors may be of organic or inorganic nature, the first are typically smaller non-protein molecules that help carryout reactions that are impossible for the enzyme to carry out by itself and are referred to as co-enzymes Prominent examples of these molecules are nicotinamide adenine dinucleotide (NADH), flavin adenine dinucleotide (FADH) and quinone. The second type of cofactors are typically metallic ions, most common metallic cofactors include iron, copper, manganese and zinc.

As most biomolecules, enzymes also posses optimal pH and temperature values with their activity dropping dramatically if the working conditions are out of their optimal range. The reason behind this loss in activity is due to denaturation of the protein which changes the conformation of the active site that limits the capability of the enzyme to bind its substrate. These specific requirements make it difficult to have sequential enzymatic reactions with very different optimal working conditions. [189]

Modeling and quantifying enzymatic reactions

As I referred before, enzyme activity consists on lowering the activation energy required for the reaction to take place, however to plan out and model complex reaction sequences its important to understand how to quantify this enzymatic activities.

The main unit of measure are **enzymatic units** (U), a U is defined as the amount of enzyme that

catalyzes the conversion of 1 μmole of substrate per minute. Another unit that can be used is the **katal** which is the amount of enzyme that converts 1 mole of substrate per second. [189]

To be able to model a enzymatic process it is important to understand the kinetics behind the enzymes that are being used. For reactions that possess a single substrate the reaction kinetics fall under the Michaelis-Menten model (however there are exception such as catalase activity). Under this kinetic model there are two steps, a binding step between substrate and enzyme which give origin to a substrate-enzyme complex, followed by a reaction step where the product is formed. Since the reaction speed depends on the amount of binding sites available the reaction rate does not scale in a linear fashion with the concentration of available substrate. The reaction rate can be predicted according to the Michaelis-Menten equation as seen bellow and has a typical profile as the one presented in Figure 6.3. [189]

$$v = \frac{dP}{dt} = -\frac{dS}{dt} = \frac{V_{max} \times [S]}{K_M \times [S]} \tag{6.1}$$

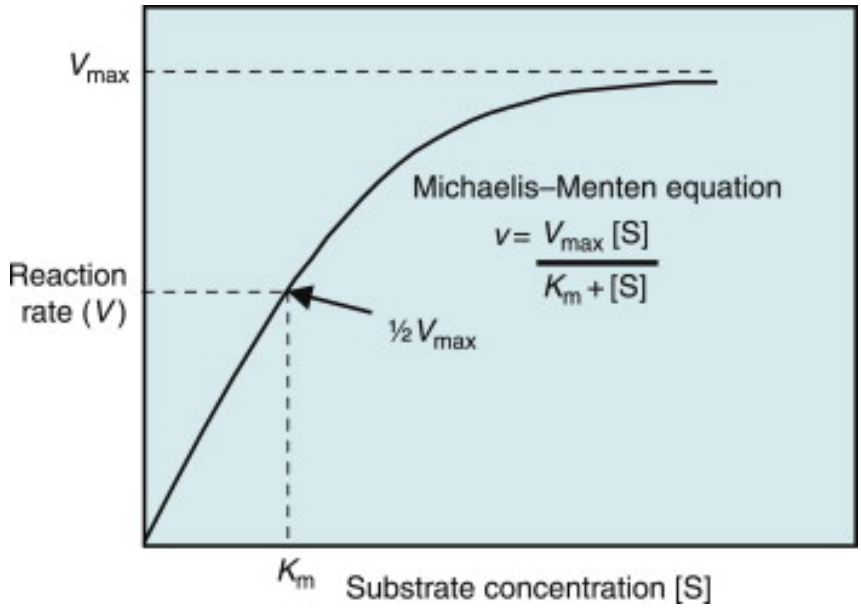

Figure 6.3: Reaction rate vs substrate concentration under Michaelis-Menten kinetics, adapted from [191]

In Equation 6.1 v represents the reaction rate, V_{max} is the maximum rate achieved when the system is saturated and K_M is the concentration at which half of the maximum reaction rate is achieved. As seen in Figure 6.3 reactions that follow this kinetic model saturate at high concentrations, this is due to the existence of more substrate molecules than actual binding sites for said molecules.

In some cases enzymes may need two substrates to function, when this happens the kinetic behavior will not always fall under the Michaelis-Menten model. Depending on how the substrates bind to the enzyme the reaction can follow a **ternary-complex mechanism** or a **ping-pong mechanism**. [189]

In the first case, both substrates bind to the enzyme simultaneously in order to form a enzymatic complex, the order at which the substrates bind to the enzyme can be random or sequential. After binding, the reaction occurs and two products are released from the enzymatic complex. A prominent

example of a ternary-complex mechanism is the reaction carried out by DNA polymerase. In the case of the ping-pong mechanism, the enzyme will change its conformation after the first substrate is bound to it. After the reaction takes place and the product is released, the enzyme will maintain its altered conformation and now be able to bind the second substrate. When the second reaction is concluded, the enzyme will be restored to its initial conformation.

Besides the aforementioned kinetic models there are others that will not be discussed here such as Pre-steady-state kinetics and Non-Michaelis-Menten kinetics, however these are also relevant for enzymatic analysis and modeling. [189]

Enzyme inhibition

Besides enzyme denaturation that was briefly reported before, enzymes may also be reversibly inhibited which also leads to a decrease in enzyme activity. This inhibition can be divided into 4 groups, **competitive inhibition**, **non-competitive inhibition**, **anti-competitive inhibition** and **substrate induced inhibition**. [189]

Competitive inhibition is the reversal bonding of a substrate to the active center of the enzyme, this connection blocks the connection between the true substrate and the enzyme. When both substrate and inhibitor are present in the medium with the enzyme, they will both compete for the active center of the enzyme, effectively decreasing the activity of the enzyme solution. In contrast, in uncompetitive enzymatic inhibition, the inhibitor does not bind to the enzyme active center, however it will bind to another region of the enzyme, compromising its function. In these cases the inhibitor will bind to both the free enzyme and the enzyme-substrate complex. When the inhibitor binds solely to the enzyme-substrate complex the inhibition is classified as anti-competitive. The last inhibition mechanism is of a different nature then the previously described. Typically when the substrate concentration is increased, enzyme activity is increased due to the shift of the reaction in the direction of the products, however when the substrate concentration is increased above a certain threshold, a threshold that depends on the enzyme that is being studied; this activity will decrease instead. This decrease of speed is due to the formation of enzyme-substrate-substrate complexes which become inactive and thus, decreasing the overall activity of the solution. [189, 192]

Enzyme immobilization

When considering the production of a biological commodity the first equipment that comes to mind are bioreactors, these can have different configurations and modes of operations. However the use of enzymes in bioreactors present a problem, not only when these equipments are operated in a continuous regime due to the permanent output of the reaction medium, but also due to their instability when removed from their natural environment. [193]

Enzyme immobilization, as the name indicates, is the binding of the enzyme to a surface. This binding to a support serves different purposes, such as, preventing wash-out of the enzyme, protection from denaturation processes, increase of surface area and therefore enzyme concentration in the reaction

medium, to name a few. Immobilized enzymes can be used in different modes of operation and tend to be simpler to implement in continuous processes than their free counter parts.

Enzyme immobilization can be achieved through different means with the simplest being the physical **adsorption** to a solid substrate such as glass or ceramic, this immobilization is maintained through weak interactions such as van der Waals or electrostatic forces. This type of immobilization can be improved by functionalizing the surface with different chemical groups, such as hydrophobic or ionic species, to the surface of the support and thus increasing the adhesion of the enzymes to the substrate, due to the creation of **covalent and/or ionic bonds**. [194]

Aside from this, other methods have emerged which allow for the complete protection of the enzyme, such as **entrapment**. As the name suggests, the enzyme is completely trapped in a mesh which is dense enough to prevent the enzyme from escaping, however is porous enough to allow for the movement of both the substrate and products of reaction.

Besides theses techniques, there are less used methods such as **metal binding** where transition metals such as zirconium and titanium are used to improve the adhesion of the enzymes to the support; and the formation of **disulfide bonds** through the very established thiol chemistry which create covalent bonds which are easily disrupted using a suitable agent such as dithiothreitol (DTT). [195]

6.2 Whole Cell Catalysts

It is well known the ability of exploiting microorganisms such as bacteria and yeast in order to produce a desired chemical commodity, which has only been expanded upon with the advent of DNA recombination technology. [196, 197]

Whole cells can be used in fermentation processes such as the production of dopamine using glycerol as a carbon source [198] or insulin production from glucose [199]. In a fermentation process, the cells will produce the desired product as a consequence of their metabolism using the growth substrates as the base of the process. [200] A similar approach is whole cell catalysis, where the cell growth and product synthesis are distinct phases in the process. The cells will be grown in order to produce the necessary enzymes to then catalyze a precursor to the desired product. [201]

Whole cell catalysis presents several advantages over the use of isolated enzymes, such as the cost basis of the catalyst. Biomass in general is easy and cheap to obtain when compared to the hassle behind enzyme production, where the same biomass production step is present in addition to a series of downstream processing operations. Previous estimates place enzyme production at a 10x higher price point for the catalyst, then whole cell catalysis. [202] Due to the enzymes being in their natural environment (inside the cell), longevity tends to be higher in the case of whole cell catalysis, this is due to the cell providing an environment which prevents protein unfolding and denaturation. [203] The use of whole cells also allows for unconventional medium to be used as opposed to pure enzymes, such as organic solvents and ionic liquids. [204, 205]

No process can go without some disadvantages, in the case of whole cell catalysis, I believe that the two major disadvantages are mass transport restrictions imposed by the presence of the cellular

membrane and the increased difficulty of the DSP steps,not only due to the presence of cell debris but also the presence of secondary metabolites that are a result of the cell metabolism. [206–208]

6.3 Optimization of a Biocatalytic Process

Most (bio)chemical commodities today are produced using a biological approach, either by fermentation or by enzymatic synthesis. These goods range from pharmaceutical compounds to everyday commodities such as cosmetics, cleaning products and alcoholic beverages. [209–211] Enzymatic synthesis or biocatalysis is widely used for the production of relevant molecules such as steroids [212] and other pharmaceutical compounds. [209, 213, 214] This leads to a need to reduce the cost of the production of these compounds as well as the development of efficient screening systems for process optimization.

Optimization of a biocatalytic process can be split into three main steps **catalyst selection**, **process conditions optimization** and correct **scale-up**/**scale-out** of the process. In the following sections I will discuss the different approaches to these steps and how microfluidic based systems can play a role in each one of them.

6.3.1 Catalyst Selection

Catalyst selection is the first step to design a novel biocatalytic production scheme. The three main methods of performing this selection are i) **brute force screening**, often using samples of sea water or soil to identify novel enzymes appropriate for a given reaction [215–217]; ii) **directed-evolution** where cells are given random mutations to produce variants of a given target which is then selected through some form of screening; iii) ***in silico* design**, to produce tailored made enzymes with specific features.

Brute Force Screening

The oldest and more commonly used method for catalyst isolation is to truly brute force screen a soil or sea water sample to attempt to identify useful catalysts.

The work flow of this approach is to initially take a given sample and retrieve the microorganisms present there such as bacteria and microalgae. These are then placed typically on a solid culture plate with a general medium. The issue with this approach is the amount of different media that have to be used to culture all types of organisms presented in the sample, as they will require different carbon sources, inhibit each other or have different temperature necessities. [218, 219]

Colonies are then separated according to morphology and their ability of performing the desired transformation of the substrate is tested. This is usually confirmed with some form of chromatography analysis or by using a colorimetric reaction as the base of the transformation. [220, 221]

At this point the best candidates are chosen and their genome is sequenced and proteomics studies are performed. This will allow to identify the the organisms species and strain, as well as to identify the composition of the desired enzyme, making way to an initial isolation process from, for example, the cell

lysate. During this entire process extreme care has to be given to not denature or inactivate the target enzyme. [222, 223]

An alternative to this method is the use of metagenomic analysis of the sample as a whole in order to determine what protein sequences are presented, however these types of analysis tend to be time consuming. [224]

Microfluidic systems, more specifically droplet microfluidics can and have been used in the context of this approach towards enzyme identification. By allowing the separation of single cells, placing each cell in its individual vessel (droplet), one can perform high throughput testing of the catalytic activity of a given cell, if the reaction is colorimetric in nature for example, followed by the retrieval of said cell, or performing single-cell sequencing on chip. [225–227]

In Silico Design

A completely opposite approach to the brute force method described previously is the use of computational power to design new enzymes. These can be completely new or consists of minor tweaks to improve the stability of a known enzyme. [228, 229]

These methods rely on a very extensive knowledge of protein functional groups as well as 3D folding patterns and require extremely high computational power to employ. In present times although there is a substantial amount of work done this way, I believe we are still to see this approach to dominate over more traditional approaches. Nevertheless, within this strategy, microfluidic systems can still play a role as an aid of the process. Once the ideal candidate proteins have been designed and produced, one can use a microfluidic platform to perform the screening for the ideal protein structure as well as the screening of potential substrates and inhibitors. [230]

Directed Evolution of Enzymes

One of the upcoming methods for protein identification and isolation is directed evolution. This method can be viewed as a middle ground between the aforementioned methods.

In directed evolution one will generate a random genomic library, translate the library to an enzyme bank and check the efficiency for each generated enzyme. By using random mutations of DNA, through error prone PCR or random mutagenesis, one does not need the degree of information concerning the enzyme structure that is needed for *in silico* design, nor the ability to culture unknown organisms required for brute force screening, relying on the best of both worlds. [231–233]

For this approach, the role of microfluidics is very similar to that in the case of screening from environmental samples. Taking advantage of the high throughput capabilities provided by droplet microfluidic systems, and the ability to create nL sized ”reactors” each containing one version of the enzyme, the screening of the randomly generated enzymes can be done very quickly. [234, 235]

6.3.2 Process Optimization

Once the ideal enzyme has been obtained, one now has to optimize the working conditions for said enzyme. At a glance, parameters such as temperature and pH are obvious as they impact directly the conformation of the enzyme, thus having an effect on the enzymatic activity. Other less intuitive parameters include the ratio between enzyme and substrate to avoid inhibitory effects, while maintaining high enzymatic yield; product removal is an important consideration for the same motives. If the enzyme requires a co-factor to function properly the process may need co-factor regeneration. The speed of the enzymatic conversion is also particularly important, in order to feed the system with an appropriate contact time between enzyme and substrate, this is particularly important in cascade systems where enzymes have very different kinetic properties. [236, 237]

To properly evaluate and enzymatic process, there are some figures of merit that can be used. The substrate yield, which is the percentage of substrate consumed is the more obvious one, however this has to be brought into context taking into consideration the amount of enzyme used. By using the biocatalyst yield, which is the amount of product per amount of enzyme used, one can take into account the loading of the system. Another important metric is the space time yield, which corresponds to the amount of product output per time and volume output. By taking all these numbers into consideration, one can better evaluate the optimization process for a given reaction.

Microfluidic devices present themselves as prime candidates for high throughput screening of enzymatic process conditions due to the high degree of control over the physical state of the reaction mix as well as, the ease of sensor integration. [194, 238]

Other miniaturized systems such as 96-well plates and capillary tubes are also used in biocatalysis development and have both advantages (ease of use) and disadvantages (lack of control) over microfabricated chips, however they will not be discussed here, as they are not the focal point of this thesis. [239, 240]

To Immobilize or Not to Immobilize?

There are extensive reports on the use of microfluidic devices for enzymatic process optimization. Some of these refer to the use of free enzymes in solution such as the case of soybean oil hydrolysis using *Thermomyces lanuginosus* lipase. [241] Another example if the modular system presented by O'Sullivan *et al.*, where they assess the kinetic parameters of the enzyme in the first module and separate the catalyst from the product in the second module. [242]

This type of approach suffers from the same drawbacks of its macroscale counter-part, which is the use of high quantities of the enzymatic catalyst and low enzyme stability, thus the approaches are less prevalent than the use of immobilized enzyme systems.

As discussed previously, there are several strategies for enzymatic immobilization this holds true and is expanded upon in the case of microfluidic systems, as the microreactor itself is now a viable target for an immobilization surface. Examples of this type of work include the integration of glucose-oxidase functionalized SU-8 micropillars; [243] the inclusion of pL pores in a silicon structure for horse radish

peroxidase (HRP) based fluorescence generation; [244] or the 3D printed devices presented by Peris *et al.*. [245] These approaches are limited to using the surface of the microreactors as an active surface, this not only reduces the potential volumetric activity of the device, but as well as increasing the average distance traveled by the substrate to reach the enzyme. The increased distance in addition to the lack of turbulence presented in microfluidic devices limit the mass transport of theses systems and their overall output.

One solution to increase the enzyme content within a microbioreactor is the use of solid carriers in a similar fashion to packed-bed reactors used at the microscale. These are by far the most common type of microfluidic bioreactors found in the literature, where the solid support is some form of nanoporous bead. These can be silica [98], polyethylenimine (PEI) [246] or even gold based [247] and are used to place the enzyme at the surface of the carrier (which includes the pore walls) either through adsorption or through covalent bonds. When using these types of system, stability of the enzyme is increased however, in the case of adsorption washout is still a possibility. Care also has to be given to the possibility of the reaction product being adsorbed to the carrier, which results in misleading results for enzyme productivity.

An alternative method to these types of carriers, as mentioned before is the use of polymers to encapsulate the enzymes. While increasing mass transport limitations, the stability of the enzyme tends to be severely increased, leading to longer production runs. Examples of works performed at the microfluidic scale are the the use of silicon based materials [248] and alginate [249] for the encapsulation.

Other examples of immobilization strategies are similar to their macroscale counterparts and include for instance, polymer based monoliths [250], magnetic particles [251] and membrane reactors [252].

6.3.3 Process Upscale

Once the catalyst has been chosen and the process parameters defined, one can now proceed to increase the scale of the process to fit the production needs necessary. This poses an issue, as a large number of pilot scale and industrial scale reactors function differently to bench-top systems both in terms of mass and heat transport.

Typically the upscale of a bench-top process will revolve on trying to maintain basic parameters constant between the bench-top scale reactor and the pilot-scale. This is insufficient for a successful process upscale, where a finer understanding of mass and heat transfer of the system is required, as will be discussed later in the results section.

Due to their capability of high throughput screening of process conditions and catalysts, in addition to the excellent control over local conditions within the device, microfluidics have, in my opinion, a huge opportunity to become staples in bioprocess development.

Although most reports in the literature mention the usefulness of the microfluidic systems for process screening in enzymatic reactors, very few actually proceed to increase the scale in order to benchmark the results obtained. [253] Some previous reports exist on the upscale of chemical reactions [254] as well as some fermentation processes,[57], [255] however there are very few reports on the upscale from microfluidics to bench-top scales or higher for enzymatic reactions. This lack of demonstrations of

successful upscaling of microfluidic systems is part of the motivation of the presented work, where we aim to demonstrate the upscale of packed-bed systems for enzymatic synthesis.

Chapter 7

Cascade Synthesis of L-DOPA and Dopamine

Dopamine and its precursor levodopa (L-DOPA) are two important signaling molecules in the human organism, playing roles as neurotransmitters and, in the case of dopamine, a major signaling molecule in the brain reward system. An imbalance of these molecules can cause several types of neurological disorders such as Parkinson's disease. L-DOPA is used as a drug in order to increase dopamine production in Parkinson's disease. Dopamine is not used in the treatment of these types of diseases due to its inability to cross the brain-blood barrier, however it is used in the treatment of low blood pressure and cardiac arrest. Both molecules can be produced enzymatically using tyrosine as a substrate and were chosen as a model for this work due to their clinical relevance.

Throughout this chapter we will show that is possible to produce not only L-DOPA and dopamine individually using a microfluidic system, but that it is possible to perform the cascade reaction necessary to convert tyrosine into dopamine.

7.1 Reagents

Stock solutions of Tyrosine (2 mM), Ascorbic Acid (1 mM), Levodopa (L-DOPA) (1 mM) and Dopamine (1 mM) were prepared in phosphate buffered saline (PBS), while a stock solution of sodium hydroxide (1 M) was prepared using Milli-Q water. All these reagents were acquired from Sigma-Aldrich. To produce L-DOPA, Tyrosinase from mushroom was purchased from Sigma-Aldrich, and a stock solution of 2 g/L was prepared, while the DOPA Decarboxylase used for the Dopamine synthesis was purchased from Antibodies-Online and kept at a concentration of 1 mg/mL in PBS. Substrate solutions were prepared fresh for each experiment from the aforementioned stocks, where oxygen content of the solutions was determined to be 160.5 μM using an oxygen probe (ElectroLab).

7.2 Reaction Pathway

The use of tyrosinase as a catalyst to produce L-DOPA and as an initial step towards the production of dopamine poses a challenge. On the one hand, the enzyme is cheap enough to be a viable industrial catalyst [256], but on the other, the lack of specificity towards phenolic compounds other than tyrosine limits its own efficiency as can be seen in Figure 7.1.

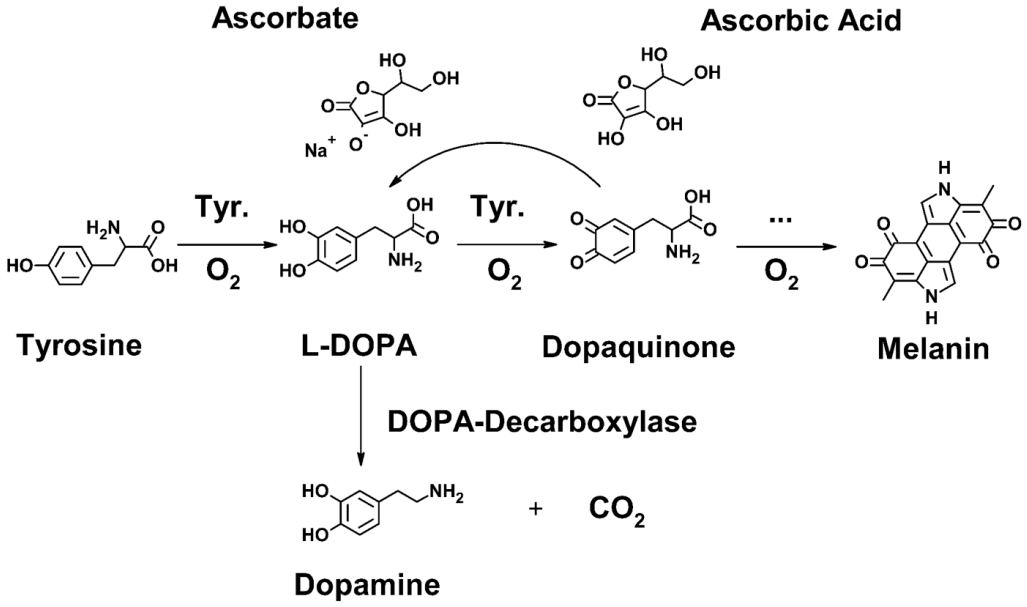

Figure 7.1: L-DOPA and dopamine reaction pathway using tyrosine as a substrate. Tyrosinase plays a part in several of the reactions that take place, which eventually culminate with the production of melanin. Ascorbic acid is added to the reaction as the reducing agent of choice. DOPA-decarboxylase is than used to convert the produced L-DOPA into dopamine, with the release of CO_2.

Tyrosinase participates in several oxidation reactions up until the production of melanin, hence there is a need to add a reducing agent to the reaction medium to avoid further oxidation of L-DOPA.[257] Ascorbic acid was chosen as the reducing agent as it does not produce a toxic by-product and does not appear to interfere with the enzymatic activity of the DOPA-decarboxylase needed for the second step of the reaction.

The second step of the reaction is the decarboxylation of L-DOPA into dopamine using DOPA-decarboxylase. Working conditions for these enzymes (pH and temperature) are very similar, thus there is no need for complex buffer exchanges or heating strategies to keep both reactions functioning in sequence. [258]

7.3 Product Detection

Detection Protocol

Before proceeding to attempt to produce these molecules, it is necessary to have a robust detection method for both products of reaction. Hormozi-Nezhad *et. al* developed a facile method for L-DOPA

detection based on the synthesis of polylevodopa nanoparticle production. [259]

Under alkaline conditions, L-DOPA is oxidized to quinone and eventually to dopachrome (similar to Figure 7.1). Dopachrome then has the ability to polymerize with itself forming nanoscale structures through covalent attachment and aggregation. [260] These nanoparticles display fluorescent properties as demonstrated in Figure 7.2.

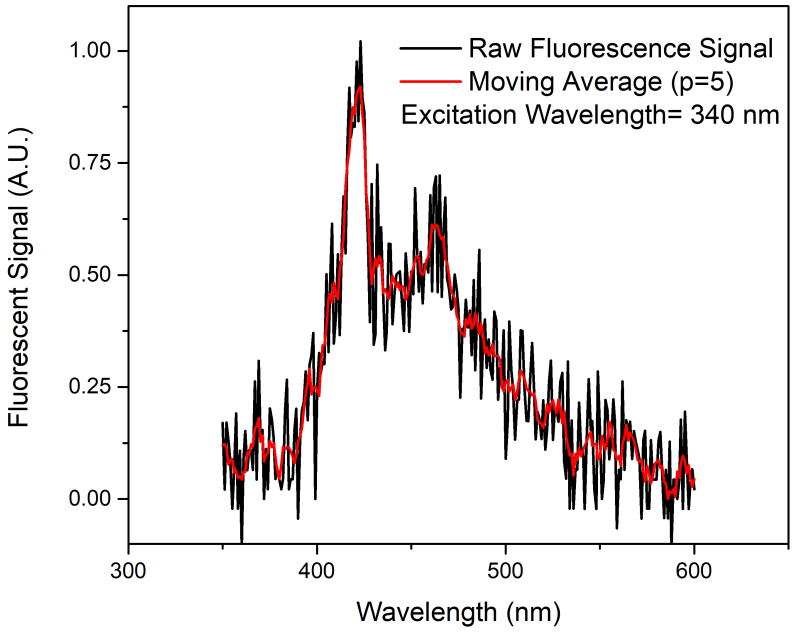

Figure 7.2: Normalized fluorescence spectrum obtained for a mixture of 100 μM of L-DOPA and 1M of NaOH prepared as a 1:5 mixture (V:V) and a reaction time of 10 min. The excitation light used was at λ= 340 nm.

The next step was to check the sensitivity of the detection method as described by Hormozi-Nezhad *et. al.* [259] To do this, several known concentrations of L-DOPA were prepared in PBS and mixed with a 1 M solution of NaOH. The fluorescence emission of the solution was then measured at $\lambda_{Emission}$ = 419 nm while exciting the solution using $\lambda_{Excitation}$ = 340 nm. These measurements were performed in a 96-well plate using a Cary Eclipse Fluorescence Spectrophotometer, and the subsequent concentration curve is presented below.

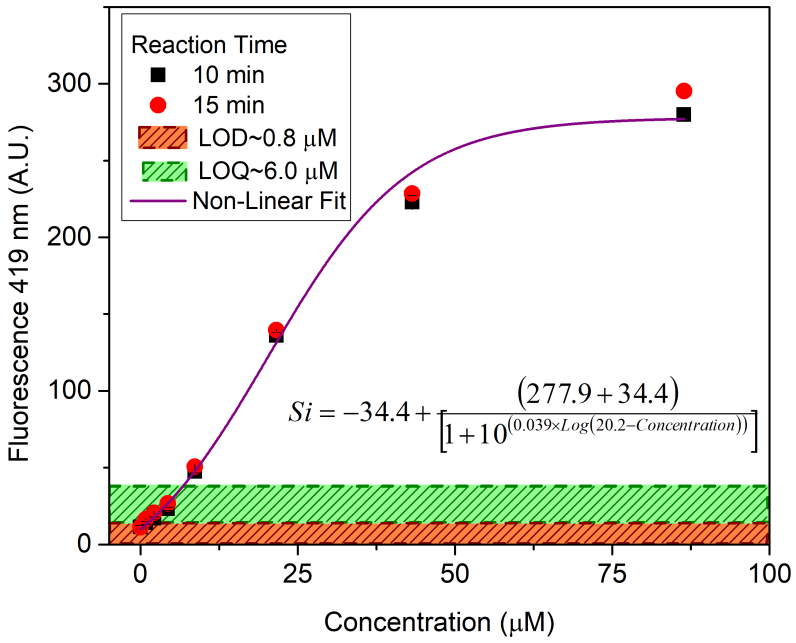

Figure 7.3: Fluorescent signal obtained using the described detection protocol as a function of the concentration of L-DOPA in solution. LOD was defined as 3.29xσ of the blank measurement while the limit of quantification (LOQ) was defined as 10xσ of the blank measurement.

The measurement was performed after 10 and 15 minutes to check if the reaction was completed in this time frame, as well as to check the stability of the particles within a time frame suitable for a detection protocol.

With these initial detection experiments the MSc. student I mentored, Cristiana Domingues, was capable of starting to miniaturize the assay. This miniaturization would allow us to perform the detection experiments at the INESC-MN facilities as quick as the samples were retrieved, avoiding the degradation of the product due to contact with oxygen. Although not having concrete data for the oxidation speed, we know that L-DOPA solutions (C= 100 μM) were completely oxidized when kept overnight in the fridge (going from transparent to black in color). Besides this, the miniaturization of the assay would make it an easier transition if we decided to include on-chip detection of L-DOPA.

For the microfluidic assay, we decided to use microbeads typically used in chromatography procedures due to the low signal exhibited by the nanoparticles in solution. By capturing the nanoparticles we effectively concentrating them in a smaller volume, thus increasing the fluorescent signal per concentration of injected nanoparticles. These microbeads were packed into a microchamber with a length of 1500 μm, width of 1000μm and a height of 100 μm.

In order to choose the appropriate microbeads, the zeta potential of the nanoparticles were measured, which indicated that the were more likely to be negatively charged. However we had no concrete information about the hydrophobicity of the nanoparticles. With this in mind, an assortment of microbeads were used in an initial screening assay, consisting in flowing a solution of 100 μM of L-DOPA with NaOH as described previously and measure the fluorescence signal after 10 min. These

initial screeing results are presented in Figure 7.4.

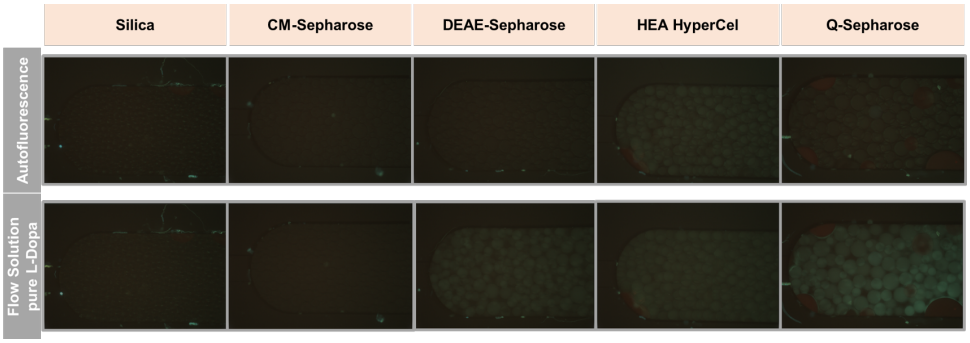

Figure 7.4: Results obtained for the initial microbead screening for different viable microbead options. The micrographs labeled autofluorescence are the initial fluorescent signal of the beads prior to any nanoparticle solution, while the bottom micrographs are the results of 10 min of flowing a solution of pure L-DOPA which was polymerized using NaOH at a flow rate of 1 μL/min. The micrographs presented here were acquired using a Leica microscope with a DAPI filter.

From Figure 7.4, the most viable candidates appear to be the Q-Sepharose, which are agarose beads functionalized with a quaternary amine; HEA HyperCel, which is a cellulose bead functionalized with a secondary amine and an aliphatic chain for multimodal interaction; and the DEAE Sepharose beads, which are agarose beads functionalized with diethylaminoethyl (a weak anionic exchange group). These three microbeads were re-tested, however instead of an end-point measurement, micrographs were acquired over time, in order to better understand the kinetics of the adsorption. These results are presented in Figure 7.5. It is important to note that at this point, due to logistical reasons, we had to move from working with the Leica (DMLM, Leica) to the Olympus microscope (CKX41, Olympus) , which not only has a weaker fluorescent lamp (50 W vs 100 W) but also has different fluorescent filters.

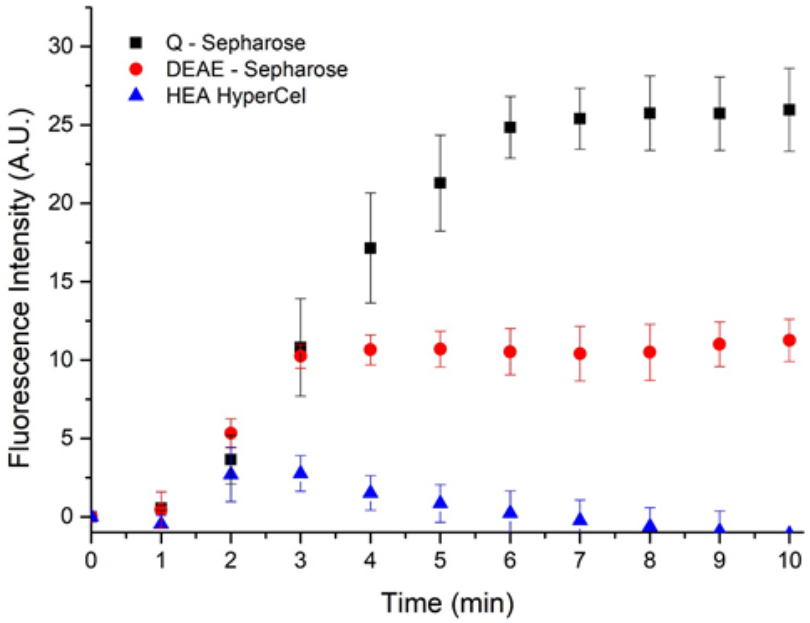

Figure 7.5: Comparison of fluorescence signal increase between Q-Sepharose, DEAE-Sepharose and HEA HyperCel beads, using 100 μM of L-DOPA, n=3.

In Figure 7.5, it is possible to observe that the fluorescent signal is the highest for the Q-Sepharose

microbeads, as well as that the signal plateau is reached after 6 minutes of flowing the nanoparticle solution. This led us to fix the detection time for the assay to be 6 minutes.

Going back to Figure 7.1, we can recall that ascorbic acid was chosen as the reducing agent for the production of L-DOPA. Screening assays were performed to check for any interference of the ascorbic acid on the detection method. This was done by fixing the concentration of L-DOPA at 100 μM and the concentration of NaOH at 1M while increasing the concentration of ascorbic acid present in the solution. These results are presented in Figure 7.6.

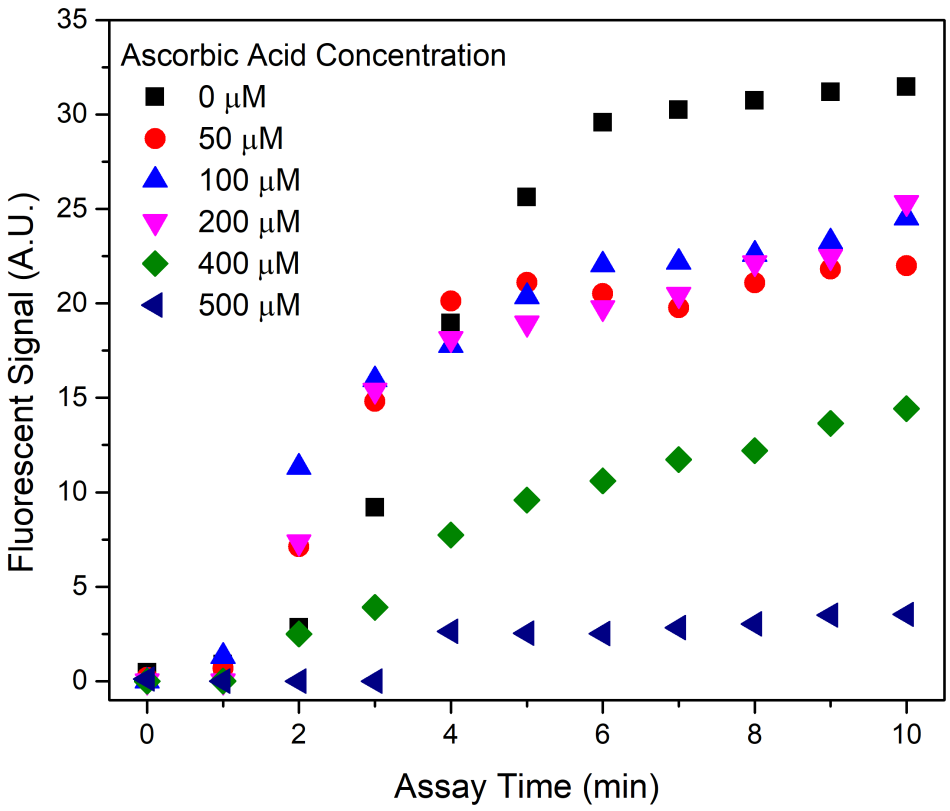

Figure 7.6: Results obtained for the study of the interference of ascorbic acid on the detection method for L-DOPA. n=1.

In Figure 7.6, it is possible to see that when ascorbic acid is added to the reaction, the fluorescent signal for the same concentration of L-DOPA drops immediately. When a concentration above 200 μM is used, that signal drops close to 0. It is not clear what is happening to the reaction, the initial thought is that the ascorbic acid is reacting with the NaOH, forming an ascorbate salt, however there is not enough ascorbic acid to fully consume the NaOH molecules present in the mix. There can be some inhibition effect by the aforementioned ascorbate, however we decided to proceed to work at a maximum of 200 μM of ascorbic acid in our system.

With these results in mind, calibration curves for known amounts of L-DOPA with 0, 100 and 200 μM of ascorbic acid were determined. These three curves were used to take into account the consumption of ascorbic acid in the reaction process, with the results presented in the detection section being an average of the result obtained with the most reasonable curve. For example in a system where 100 μM of ascorbic acid was used, the results obtained are the average of the 0 muM and 100 μM curves.

These calibration curves as well as the general detection schematic are presented in Figure 7.7.

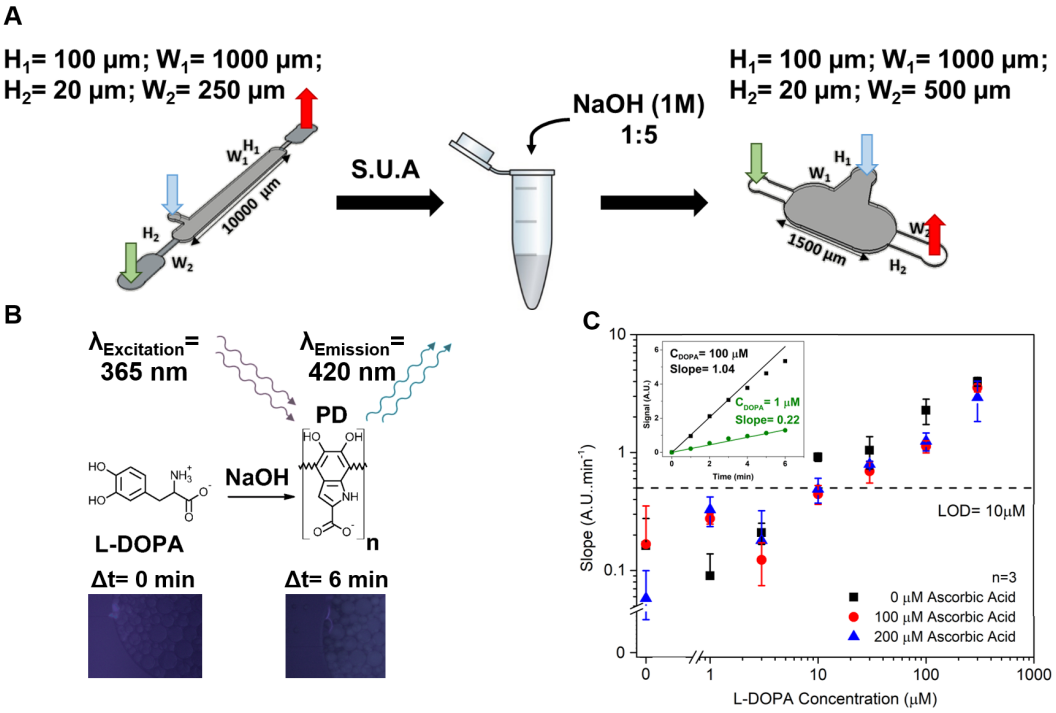

Figure 7.7: Schematic representation of the experimental method for L-DOPA quantification (A). The sample under analysis (S.U.A) is collected in intervals of 10 min and is mixed with NaOH at a 1:5 ratio. In the microreactors (left on (A)) the functionalized microbeads are packed through the side inlet (Blue arrow), which is then sealed off. The reaction medium is then injected in the primary inlet (Green arrow) and retrieved at the outlet (Red Arrow). The resulting solution is then injected into a microfluidic column packed with Q-Sepharose beads (detection chamber, right on (A)) for nanoparticle capture and florescence monitoring. Here the beads are packed into the chamber through the lateral inlet (Blue arrow), while the sample is injected at the primary inlet (Green arrow) and collected at the outlet (Red arrow). Once the polymerization reaction is complete and the nanoparticles captured, L-DOPA is detected using an excitation in the UV (λ= 365 nm) and detection using a blue filter (λ= 420 nm) (B). The resulting calibration curve for the detection of L-DOPA is presented, n=3. (C) The contrast of the presented micrographs have been enhanced for visualization purposes.

Figure 7.7-A, presents the work flow of the production experiments, where the sample is retrieved from the reactor outlet, mixed with the NaOH solution and injected in a new chamber packed with the appropriate microbeads for product detection. The fluorescent signal (Figure 7.7-B) in monitored for 6 min. The slope of the increase in signal is the metric used for the detection protocol as seen in Figure 7.7-C.

For the detection of Dopamine, the same polymerization assay was tested, initially with just pure Dopamine in solution and also using a mixture of 100 μM of Dopamine and 100 μM of L-DOPA. The results obtained (data not shown) were very low fluorescent values, which were consistently overshadowed by the presence of L-DOPA (for the same concentration of both molecules, Dopamine presented less than 10% of the signal of L-DOPA). Due to these results, the detection method chosen for Dopamine was to determine the reduction of L-DOPA.

Image Analysis

The fluorescent micrographs obtained were than processed using the open software Image J. Figure 7.8 depicts the image treatment method, despite obtaining a very high blue background, by splitting the color channels of the micrograph and monitoring the Green channel, it is possible to obtain a better signal to noise ratio then when the full image is considered. This is due to the fact that despite the peak emission (λ_{max}= 420 nm) corresponding to a RGB code of (106,0,255), which is in its majority blue, the emission spectrum presented in Figure 7.2 shows us that the nanoparticles formed have a high emission up until λ= 500 nm, which is a transition from the previous RGB code to (0,255,146). This means that most of the wavelengths captured by the microscope will have a high G-channel component as demonstrated by Figure 7.8.

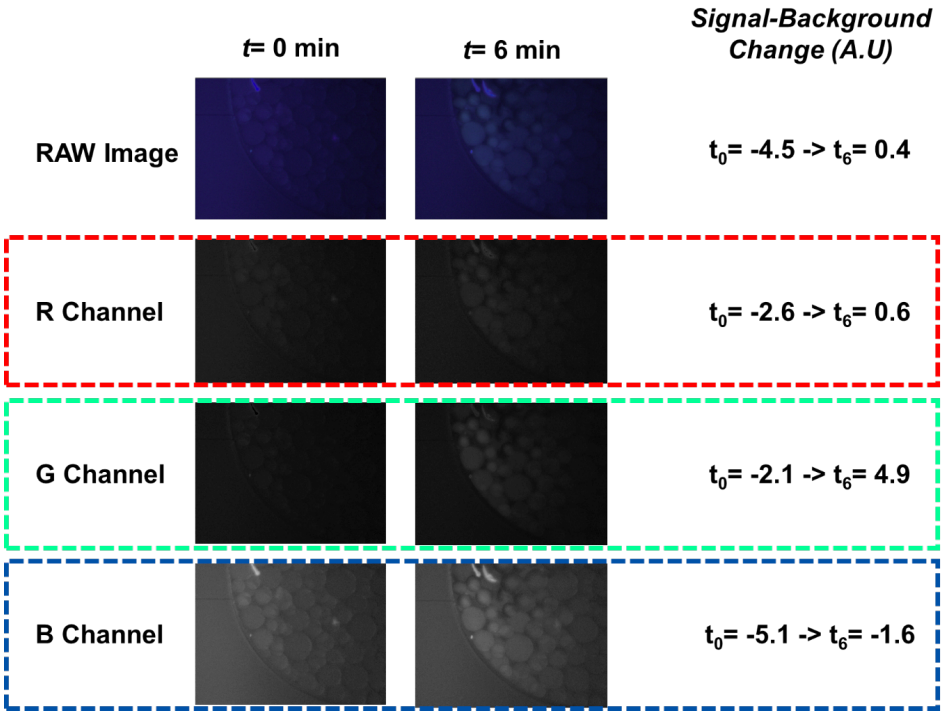

Figure 7.8: Experimental Image analysis method. By splitting the RGB color channels a better signal to ratio is obtained, especially for low concentrations of L-DOPA. Image contrast was improved for visualization purposes.

7.4 L-DOPA and Dopamine Production Optimization at the Microscale

Enzyme Immobilization and Stability

Silica beads, with an average diameter of 50 μm (97728-U Supelco Analytical (Bellefonte, PA)), functionalized in-house with a primary amine by silanization, were used to electrostatically bind both the tyrosinase and the DOPA-decarboxylase. Enzyme stock solutions were left overnight at room temperature with equal parts (v/v) of a suspension of the functionalized beads. The silica beads were functionalized by exposing them to an oxygen plasma and incubating them in a solution of 2% (v/v) of

(3-aminopropyl)triethoxysilane (Sigma-Aldrich) in HPLC grade acetone, under constant mixing for 3h. The beads were than washed and stored in MilliQ-water. [261]

The enzyme immobilization was always performed on the day before the start of the experiment. Given the immobilization protocol, the enzyme will adsorb to the surface of the microbeads as well as to the pore walls.

Immobilization of total protein was measured using the Bradford method, producing a yield of 53% (m/m) in the case of tyrosinase and 100% (m/m) in the case of DOPA-decarboxylase (calibration curves for both proteins are presented in the Supplementary Information). Immobilization yield based on activity measurements (Equation 7.1) resulted in an immobilization yield of 69% (U/U) for tyrosinase and 100% (U/U) for DOPA-decarboxylase. Efficiency of the immobilization (observed activity/immobilized activity, Equation 7.2) was determined to be 170% for tyrosinase and 33% for DOPA-decarboxylase. Although uncommon, it is possible to obtain efficiencies of immobilization above 100%, this typically being attributed to the support stabilizing the active center of the enzyme or preventing aggregation which could impede the enzyme activity in solution. [262, 263]

$$Immobilization\ Yield(\%) = 100 - \frac{Activity_{Supernatant}}{Activity_{Enzyme\ Stock}} \tag{7.1}$$

$$Immobilization\ Efficiency(\%) = \frac{Activity_{Immobilized\ Enzyme}}{Immobilization\ Yield \times Activity_{Enzyme\ Stock}} \tag{7.2}$$

In the case of tyrosine, longer time frames for the experiments were used as will be discussed in further sections of this thesis. Due to this, the thermal stability of both the free and immobilized enzyme were monitored for 48 h. This was done by maintaining both the free and the immobilized enzyme in a hot bath (32.5 °C), with periodic samples being retrieved. The results obtained are presented in Table 7.1.

Table 7.1: Data for thermal stability of immobilized and free tyrosinase.

Time (h)	Immobilized Enzyme Activity (U/μL)	Free Enzyme Activity (U/μL)
0	0.175 $\pm$ 0.078	0.133$\pm$0.010
1.5	0.222$\pm$0.065	0.131$\pm$0.014
3	0.173$\pm$0.029	0.118$\pm$0.011
4.5	0.180$\pm$0.015	0.143$\pm$0.014
6	0.175$\pm$0.009	0.137$\pm$0.012
24	0.191$\pm$0.049	0.136$\pm$0.015
36	0.121$\pm$0.001	0.111$\pm$0.013
48	0.076$\pm$0.00	0.168$\pm$0.012

For the thermal stability of tyrosinase, no activity loss was seen in the initial 24 h, however there was a drop in activity of 35% in the time frame between 24 and 36 h and an additional drop in activity of 37.5% between 36 and 48 h. In the case of DOPA-decarboxylase this was not attempted as there is no loss of activity to be registered within the time frame of the microfluidic experiments.

L-DOPA Process Conditions Optimization

For the optimization of the reaction conditions, the main parameters of interest include temperature, pH, flowrate, residence time and substrate concentration. For tyrosinase and DOPA-decarboxylase activity, reported optimal values of temperature is approximately 30°C and pH between 6 and 8. [264] With this in mind, temperature and pH were maintained at 32.5°C and 7, respectively. For the production of L-DOPA, oxygen is necessary as an oxidant, the oxygen content was determined to be 160.5 μM, which prevents reaction limitation on this end. Optimization experiments focused on the variables flow rate, substrate ratio in the reaction medium and reactor geometry. The metric used for the optimization of the microreactor was the yield (%) defined as the concentration of L-DOPA/dopamine divided by the concentration of the respective substrate being injected into the system. The results are summarized in Figure 7.9.

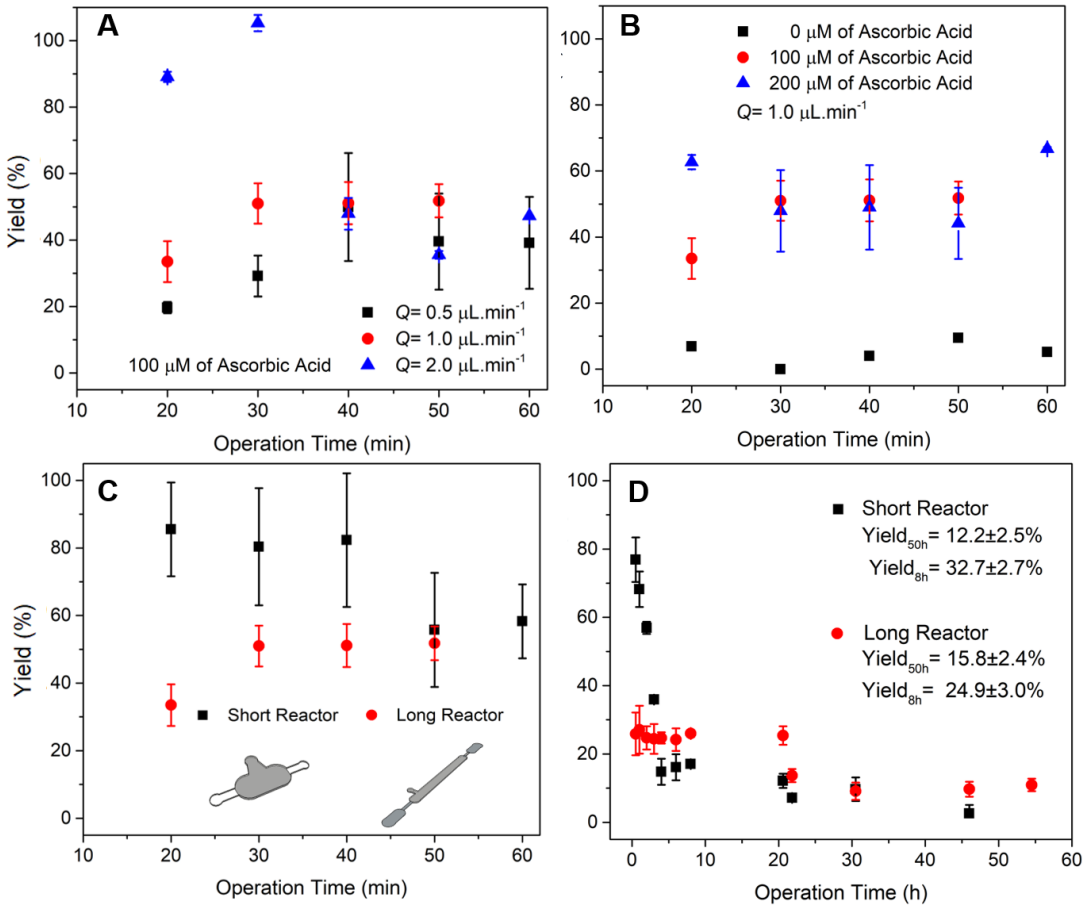

Figure 7.9: Optimization experiments to produce L-DOPA using 100 μM of tyrosine as a substrate. Flowrate (A, n=3), reducing agent concentration (B, n=3) and reactor geometry (C, n=3) were studied. For the flowrate studies the concentration of ascorbic acid was kept at 200 μM, while the flowrate (Q) was kept at 1 μL/min for the reducing agent studies. Using the optimal conditions of 1 μL/min 100 μM of ascorbic acid, both reactor geometries were checked for long term viability (D, n=4)

For these optimization experiments, two reactor geometries were considered, the "*Long Reactor*", which has $L_{Bead\ Chamber}$= 1 cm, H = 100 μm and W= 1 mm, while the "*Short Reactor*" differs only by having a $L_{Bead\ Chamber}$= 1.5 mm, obtaining volumes of 978.5 nL and 128.5 nL respectively. The average

voidage of the reactors was determined to be 0.45, resulting in a dry weight of the microbeads of 187 μg and 1426 μg for the *Short* and the *Long* reactors, respectively. The amount of tyrosinase per bead was determined to be 6.03 $\mu g_{Tyrosinase}$/mg_{Bead}, resulting in a volumetric activity of 0.186 U/μL and an amount of tyrosinase of 1.1 μg in the *Short Reactor* and 8.6 μg in the *Long Reactor*.

Figure 7.9-A shows that the working flowrate has a significant impact on the initial moments of the reaction, but after 30 min the yield reaches a steady state which is independent of the flow rate. This was not expected, as the lower flowrates increase the residence time inside the reactor, which should increase the probability of the reaction reaching a post-L-DOPA stage due to the catecholase activity of the enzyme. [257] However, it is possible that the changes in residence time are not sufficient to cause a significant difference in the output of the reactor, or that enough of the reaction by-products have accumulated on the bead surface that introduce some mass transfer limitations to the system. Based on these results, a flowrate of 1 μL/min was chosen for the subsequent experiments. The impact of the reducing agent, ascorbic acid, in the medium was studied next (Figure 7.9-B).

Figure 7.9-B shows that in the absence of ascorbic acid, there is nearly no production of L-DOPA. However, increasing the amount of ascorbic acid from 100 μM to 200 μM did not further improve the yield. Intrigued by the lack of impact of the residence time on the yield of the microreactor, which was attributed to there being multiple chances of the substrate encountering the enzyme throughout the reactor length, we proceeded to test a shorter microreactor.

The yield of the shorter microreactor was compared to that of the longer version, and the results are shown in Figure 7.9-C. It is possible to observe that the Short Reactor largely outperforms the *Long Reactor*. This is attributed to the low residence time inside the *Short Reactor* and to the fact that each substrate molecule will encounter less enzymes in the Short Reactor compared to its longer counterpart, decreasing the possibility of side reactions and further product degradation.

The operational stability over longer periods of time is presented in Figure 7.9-D. It can be seen in both types of microreactors that there is an initial loss of enzymatic activity in the system which wasn't registered in previous experiments which had a shorter time frame. As mentioned before, the thermal stability was tested by keeping the immobilized and also free tyrosinase incubated at 32.5 °C for 48 h, with no loss of activity registered in the initial 24 h, however with drops of activity after 36 and 48 h. This loss in activity is most likely the reason for the drop in activity registered after the initial 24 h for both reactors, however does not explain the loss registered in the initial 24 h time frame. This initial loss of activity can be due to multiple reasons such as fouling of the reactor, preventing newer substrate to reach the enzyme, as can be seen in Figure 7.10; the suicide nature of tyrosine as a substrate for tyrosinase activity; [265, 266] or enzyme wash-out of the system due to poor interaction between the beads and the enzyme. This last scenario was tested using the Bradford method, and no enzyme was detected in the reactor outflow, as shown in the Supplementary Information, however there could had been washout at concentrations not detectable using the Bradford assay.

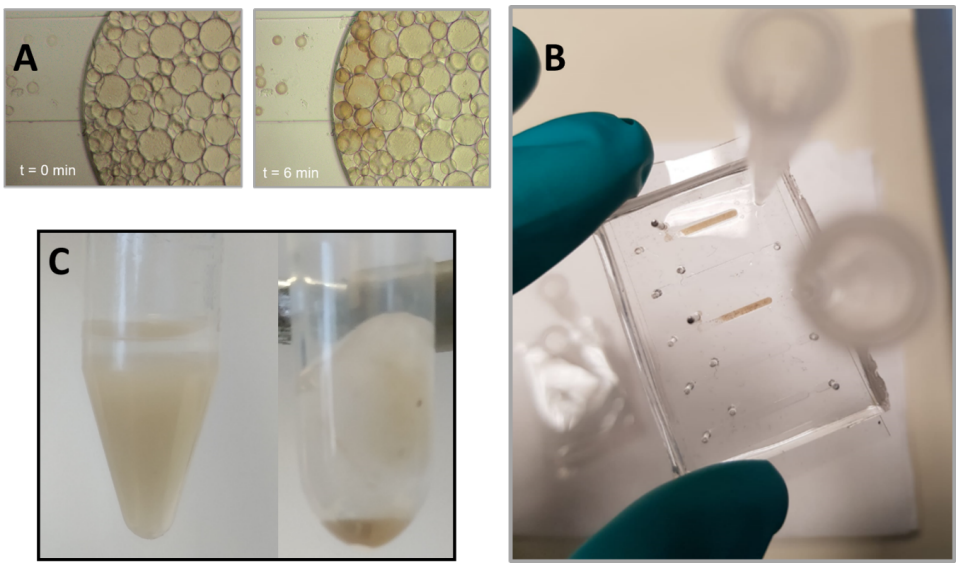

Figure 7.10: Byproduct accumulation at different scales. Initial moments when monitoring the experiment using a microscope (A); overall look of the device after a long assay (B); comparison between the original bead stock and the beads used for 8 h at the macroscale (C). The white substance above the beads in C is the cotton used to prevent bead washout from the column.

Dopamine Process Conditions Optimization

To facilitate the integration of the dopamine production step with the L-DOPA step, similar conditions to the ones used for L-DOPA production, namely the flow rate and reactor operation time, were tested. For these experiments, pure L-DOPA was used as a substrate and the results are presented in Figure 7.11.

Due to the inability of direct detection of dopamine at this scale, the yield of the conversion of L-DOPA to dopamine was indirectly determined through the consumption of L-DOPA in the system. With that in mind, a control assay without DOPA-decarboxylase present was performed in order to consider any L-DOPA loss due to adsorption to the beads or spontaneous oxidation, which was determined to be between 5 and 10% of the initial amount of L-DOPA, as seen in Figure 7.11 in the "*no Enzyme*" condition.

Overall the productivity of this system shows an average yield of 22%. Like in the case of L-DOPA production in this range, the flowrate doesn't have a significant impact on the system output. A flow rate of 1 μL/min was chosen for subsequent experiments.

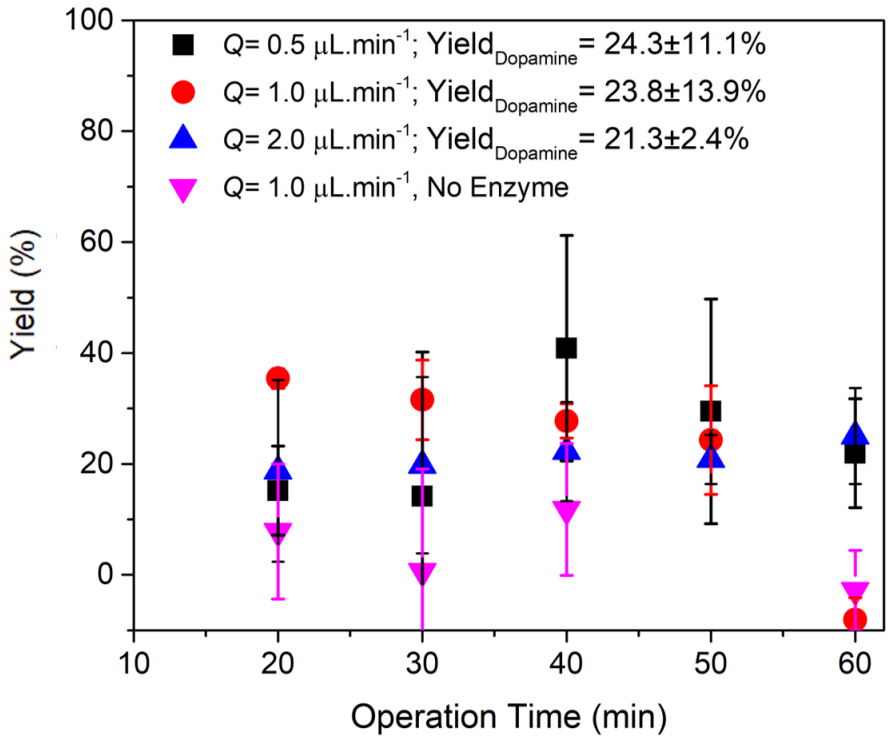

Figure 7.11: Flow rate (Q) screening of the dopamine production using SiO_2 microbeads functionalized with DOPA-decarboxylase. A pure L-DOPA solution was used as a substrate and its consumption was monitored using the described method.

Cascade Production

Once the optimization of the production of L-DOPA and dopamine were performed, the cascade reaction was tested. The system comprising two sequential chambers is schematically shown in Figure 7.12-A. The first chamber is packed with tyrosinase-functionalized beads, and the second chamber is packed with DOPA-decarboxylase- functionalized beads. A small outlet between the two chambers allows retrieving samples for L-DOPA production assessment. A total of 4 systems were used simultaneously for these experiments, where samples from the first column were retrieved from 2 of them, for L-DOPA assessment (Figure 7.12-A), while the remaining structures, had this outlet sealed and were used for dopamine determination at the outlet Figure 7.12-B).

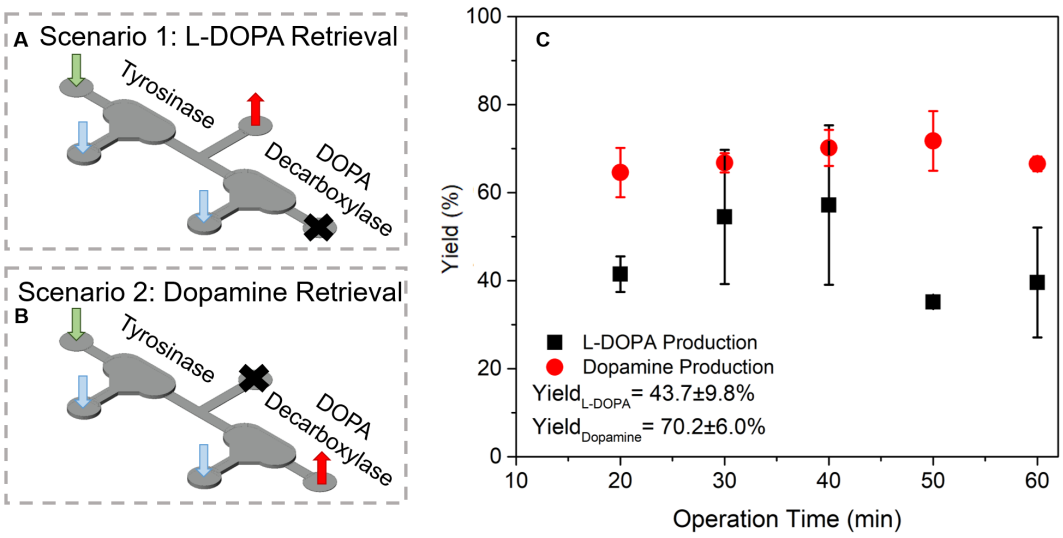

Figure 7.12: Sequential production of both L-DOPA and dopamine in a single integrated microfluidic system. The reaction medium is injected at 1 μL/min and is composed of 100 μM of tyrosine and 100 μM of ascorbic acid. For the monitoring of L-DOPA production, the outlet is sealed off and the middle outlet is used for sample retrieval (A). For the detection of dopamine, the middle outlet is sealed off and the sample is collected at the outlet (B). Productivity for both reaction steps (C). n=2.

Figure 7.12-C shows that the dopamine yield is 70% in relation to the amount of L-DOPA that is produced by the first stage, which is approximately 45 μM. This productivity is much higher than what was registered when pure L-DOPA at 100 μM was used (Figure 7.11). This leads the authors to believe that in the case of the experiments depicted in Figure 4, the DOPA-decarboxylase chamber is being injected with higher concentrations of L-DOPA than it can convert. One hypothesis to improve the yield would be to increase the protein content per bead by improving the immobilization protocol. The overall yield of the combined system is approximately 30%.

The results demonstrate the feasibility of microfluidic packed-bed reactors, not only for single step reactions but also for multistep reaction sequences. One could argue for the use of these types of microreactors for large scale production using complex scaling-out methods. However, the authors believe that the best current use of these microreactors is for the screening of process conditions/enzymes. However, even for screening applications, it is necessary to perform an adequate upscale of the system. This topic is further discussed in the next chapter.

Chapter 8

Scale-up of a Microfluidic Packed-Bed Reactor

In order to correctly upscale a system, there are certain physical characteristics that should be maintained such as the aspect ratio of the system and flow and mass transport behavior. In order to maintain mass/heat transport consistent in both systems, we first need to characterize the microfluidic system by calculating the Reynolds number ($Re_{Packed\ Bed}$) and the Péclet number (Pe). In the case of the Pe, two variants can be calculated, one that is dependent on the particles that make up the packed bed (Pe_P), the other relates to the axial dispersion throughout the length of the reactor (Pe_L). The method of calculating these dimensionless numbers is presented below, where v is the liquid velocity and R_P is the particle radius. [16]

$$Re_{Packed\ Bed} = \frac{2R_p \times v \times \rho}{\mu(1-\epsilon)} \tag{8.1}$$

$$\frac{1}{Pe_P} = \frac{0.7D}{2R_p \times v} + \frac{\epsilon}{0.18 + Re_{Packed\ Bed}^{0.59}} \tag{8.2}$$

$$Pe_L = Pe_P \frac{L}{2R_p} \tag{8.3}$$

As a proof of concept, only the synthesis of L-DOPA was up scaled. Using Equation 8.1 through Equation 8.3, the properties of the microfluidic system were calculated and the necessary working conditions for the bench-scale system were determined.

Before reaching a viable bench-top system, two failed approaches were tested. The initial attempt was a direct increase in all dimensions from the microfluidic structure. These devices were fabricated using CNC milling and PMMA as a substrate and are presented in Figure 8.1.

The structure presented in showed some degree of success, however it wasn't possible to flow the liquid across the entirety of the channel due to the huge pressure drop throughout the length of the packed-bed. This led to leakages both through the inlet and the side of the packed-bed.

The next attempt was to used a previously designed system described elsewhere and is presented in Figure 8.2. [267] In this system, despite being able to flow liquids through it, it was not possible to

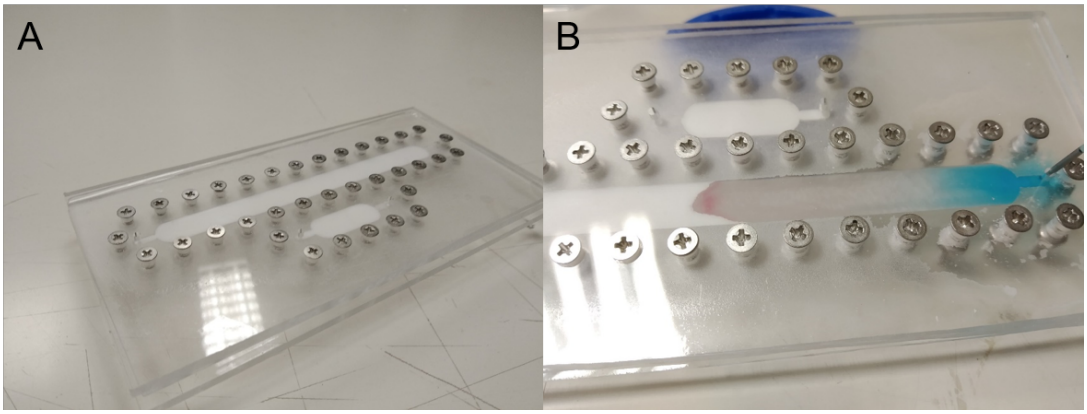

Figure 8.1: First attempt at an upscale of the original devices. (A) The channel cavity is milled into a PMMA substrate and screwed tightly to another PMMA substrate, with a 500 μm thick PDMS layer in between acting as an "o-ring" to avoid leakage. (B) Initial experiment to test the system by using silica beads similar to the ones used in the enzymatic experiment to separate two colored components from a commercial food coloring.

reach the necessary flowrates to replicate the mass transport conditions registered at the microscale due to leakages at the tube level.

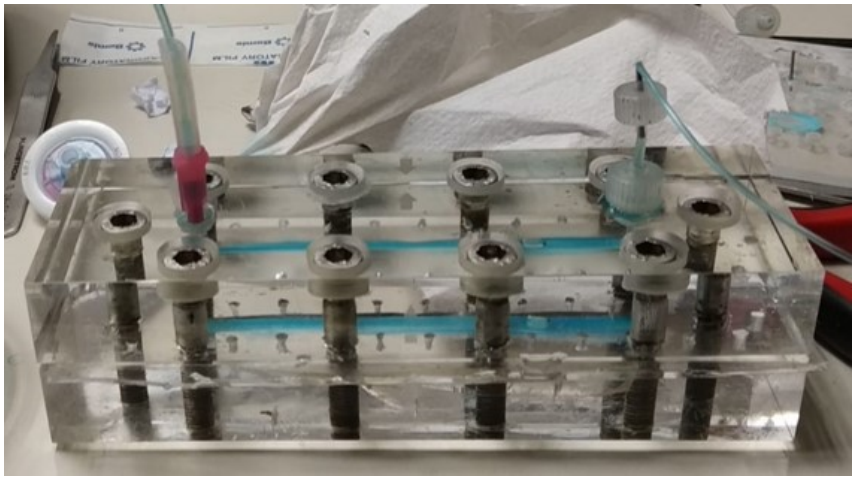

Figure 8.2: Device used for the second attempt at the up-scale of the enzymatic production of L-DOPA.

This led us to the final version of the upscaled device, the working conditions are summarized in Table 8.1.

Table 8.1: Flow properties and resulting working flow rates for both micro and milliliter scale.

System	Hydraulic Diameter (m)	Voidage (ϵ)	Flow rate (μL/min)	$Re_{Packed\ Bed}$	Pe_P	Pe_L
Short (micro)	1.8x10^{-4}	0.43	1	1.74x10^{-3}	1.8x10^{-5}	5.4x10^{-3}
Long (micro)						3.6x10^{-2}
Short (milliliter)	10^{-2}	0.44 [268]	780			5.4x10^{-3}
Long (milliliter)						3.6x10^{-2}

As can be seen, it is possible to upscale packed-bed reactors while still maintaining the same flow characteristics as the microfluidic system in terms of Pe and Re numbers due to the fact that the flow behavior will be dominated by the bead packing instead of the reactor geometry, as would be the case for plug flow reactors and tank reactors.

The milliliter scale version of the bioreactor consists of a chromatography pre-column packed with the functionalized beads. In order to prevent the washout of the beads through the reactor outlet, a small piece of cotton was placed at the bottom of the bed, the height of the bed was fixed by using an appropriate volume of beads. Production experiments were carried out for 8 h and compared to their microscale counterparts, as shown in Figure 8.3. The yield of the *Short* reactor (Figure 8.3-C)

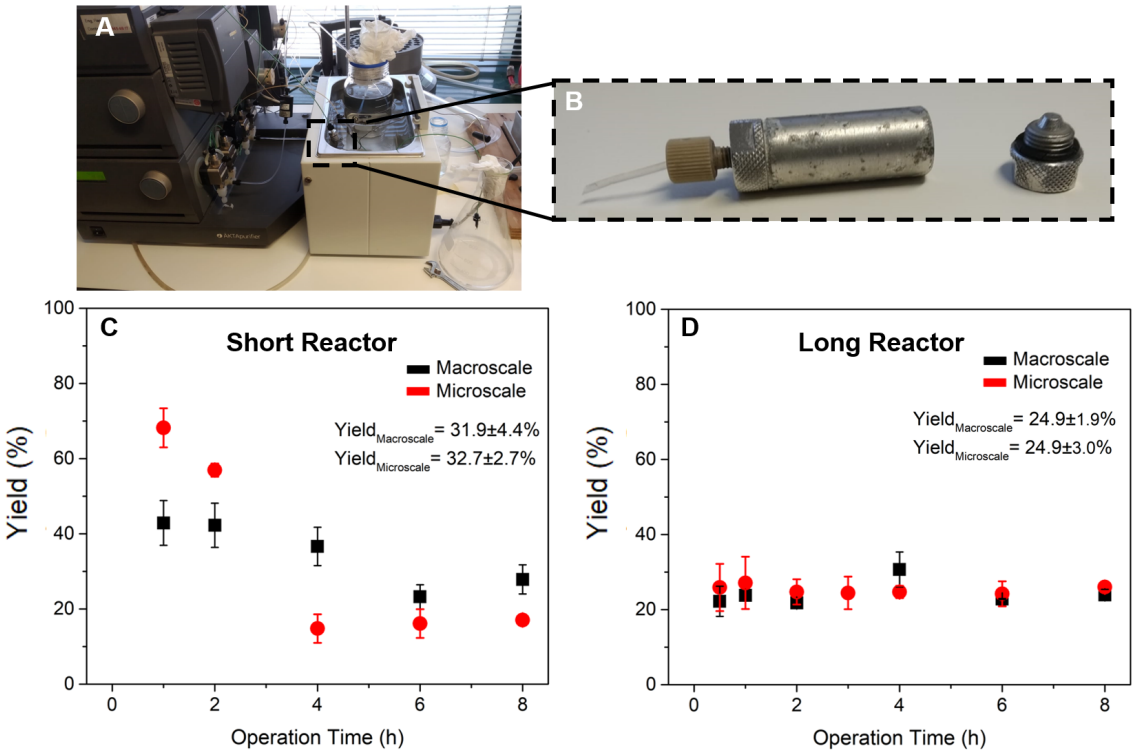

Figure 8.3: Milliliter scale production setup, consisting of an AKTA system for pumping, a hot bath, substrate reservoir which is also in the bath and a collection flask (A). The beads are packed into a stainless-steel pre-column (B). The experiment lasted for 8 h for both the Short reactor (C) and the Long Reactor (D). For the milliliter scale experiments, n=2.

shows a good correlation at both scales, with similar losses of enzymatic activity being registered. This activity loss is probably due to the accumulation of reaction by-products as mentioned previously. As for the *Long* version of the reactor (Figure 8.3-D), the results obtained at the microscale match the results obtained at the larger scale for the entire duration of the experiment. By looking at these results, it is safe to say that by using a microfluidic system and maintaining similar mass transport conditions, it is possible to accurately predict process outcome at the milliliter scale for packed-bed reactors.

The microreactor, as well as the milliliter reactor, were then compared in Table 8.2 to other enzymatic reactors reported in the literature, using the yield, as well as the space-time yield and biocatalyst yield as figures of merit. While the system presented in this work has similar yield as other reports in the literature, it has inferior performance when the space-time yield is accounted for, especially when compared to a batch system. However, the system presented in this work shows comparable output or even largely outperforms other continuous systems in terms of biocatalyst yield. It can also be seen in Table 8.2 that the space-time yield and biocatalyst yield are very similar between the microscale and milliliter approach within this work, further validating the microfluidic system as a useful screening tool

for enzymatic reactions.

Table 8.2: Yield for the production of L-DOPA comparison to literature reports. yields marked with "*" refer to the initial 8 h working period. The systems presented by other authors are all macroscale systems.

System	Yield (%)	Space-Time Yield (mg_{L-DOPA}/(L.h))	Biocatalyst Yield (mg_{L-DOPA}/($mg_{Tyr.}$.h))	Total L-DOPA produced (mg)	Mode of Operation
Microscale (Short)	12.2 (32.7*)	$4.46x10^{-2}$ (0.806*)	131.2 (351.7*)	$7.80x10^{-3}$ ($3.10x10^{-3}$*)	Packed Bed 54 h (8 h)
Milliliter scale (Short)	31.9	0.786	340.9	2.36	Packed Bed 8 h
Microscale (Long)	15.7 (24.9*)	$5.73x10^{-2}$ (0.606*)	21.6 (33.9*)	$1.00x10^{-2}$ ($2.33x10^{-3}$*)	Packed Bed 54 h (8 h)
Milliliter scale (Long)	24.9	0.614	34.0	1.84	Packed Bed 8 h
Yang et al. [269]	53.0	209	1045	104.5	Batch Reactor 2 h
Yang et al. [269]	28.5	103	515	3.30	CSTR - Continuous 8 h
Yang et al. [269]	13.5	48.9	0.88	7.60	Packed Bed 36 h
Choi et al. [209]	44.1	5.54	0.55	1.99	Batch Reactor 36 h

Chapter 9

Final Remarks - Bioprocess Development at the Microscale

With this, we've reached the end of the bioprocess portion of my doctoral thesis. In this part of the dissertation, I demonstrated the use of microfluidic structures to optimize not only production conditions for enzymatic based processes, but also, if one thinks about it, an initial screening for chromatography processes, by screening the most adequate microbeads to capture our reaction product.

Throughout this work a microfluidic approach to the optimization of biochemical enzymatic production was demonstrated. We successfully demonstrated the use of microfluidic bioreactors for 2 single step reactions, the generation of L-DOPA using tyrosine as a substrate and the production of dopamine using L-DOPA. In addition, feasibility of using this type of system for a multi-step production scheme was demonstrated by converting tyrosine into dopamine in a continuous mode in a two-chamber microfluidic reactor. In all these reactions, the yields obtained were like those obtained by other macroscale works reported in the literature.

This work also demonstrated the successful upscale of the system, obtaining similar results at both the microscale and at milliliter scale to produce L-DOPA. Hopefully this demonstrates, once more, the importance of understanding the process in terms of transport phenomena in order to successfully up-scale a given process.

In terms of complexity, I believe that the most challenging aspect of this type of work is the correct assessment of the reaction output, which will be entirely dependent on the detection method chosen, which will depend on the product of reaction, which brings me to the topic of future work.

If time was infinite, the next step for this work was to develop a more universal detection method, such as a miniaturized chromatography column coupled to UV detectors (which could be the thin-film silicon photosensors discussed before). This would allow us to possibly detect not only L-DOPA and dopamine, but in this case, possible also tyrosine and dopachrome to havea better assessment of the reaction output.

Another aspect which is relevant is actual process control. In this work, for example, temperature was maintained using a hotplate, however if integrated sensors were used we would have better knowl-

edge regarding the state of the reactor, this addition of sensors and controlling units is not limited to temperature and should be extended to, at least, pH and oxygen content.

Another interesting aspect of these microbioreactors which wasn't studied is the possibility of using them for production. As a thought experiment, let us assume that connecting the necessary tubing to feed all these systems is a trivial matter. One could possibly have an array of several hundreds of structures which would take up a very small footprint, and use them for instance, to produce necessary compounds in remote regions.

To conclude, I believe that, even though microbioreactors are not the sole tool to be used in process optimization, I think that they are a very powerful tool for initial assessment of process conditions such as temperature and pH, but also aspects such as reactor geometry.

Part IV

A Truly Portable Microfluidic System for the Multiplexed Detection of Plant Health

Highlights

- This work presents a microfluidic device capable of a multiplexed detection of salicylic, azelaic and jasmonic acids
- The device is coupled to thin-film photosensors for real time detection under 7 minutes
- The device was used to detect fungal infections caused by two different pathogens, *B. cinerea* and *E. necator*, in two different grape cultivars, *Trincadeira* and *Carignan*
- Metabolite expression patterns per disease were identified and confirmed using gold standard techniques

Roles and Colaborations

- In this portion of the work, I designed all assay geometries and necessary microfluidic chips, as well as, the photosensors used. I also performed all the experimental procedures related to the detection assays, as well as, the sample preparation assays. I also developed the electronics for the initial version of the portable prototype as well as the controller programing for the necessary operations to run the assays.
- **Dr. Ana Margarida Fortes** was responsible for providing the biological samples used and maintaining the grape cultivars, both infected and healthy.
- **Dr. Rui Pinto** helped in developing the electronics of the final version of the portable prototype, as well as, the initial programming of the GUI used.
- **Dr. Teresa Esteves** mentored my use of the HPLC equipment in order to benchmark the biosensing assays developed here, as well as providing solutions to overcome challenges in this field.

Scientific Output

Publications

- Brás, Eduardo JS, et al. *"Microfluidic device for multiplexed detection of fungal infection biomarkers in grape cultivars"* Under Peer Revision at Biosensors and Bioelectronics Journal.
- Brás, Eduardo JS, et al. *"A Versatile and Fully Integrated Hand-held Device for Microfluidic Based Biosensing: A Case Study of Plant Health Biomarkers"* Under Peer Revision at IEEE Sensors Journal.
- Brás, Eduardo JS, et al. *"A Portable Microfluidic System for the Detection of Health Biomarkers in Grapes at the Point of Need."* 2019 20th International Conference on Solid-State Sensors, Actuators and Microsystems & Eurosensors XXXIII. IEEE, 2019.
- Brás, Eduardo JS, et al. *"Microfluidic Device for the Point of Need Detection of a Pathogen Infection Biomarker in Grapes."* Analyst 144.16 (2019): 4871-4879.

- Brás, Eduardo, et al. *"Development of a Point-of-Care Platform for Plant Health Assessment: A Microfluidic Approach."* Multidisciplinary Digital Publishing Institute Proceedings. Vol. 2. No. 13. 2018.

Conference Presentations - Oral

- *"Development of a Point-of-Care Platform for Plant Health Assessment: A Microfluidic Approach."*, Eurosensors XXXII, Graz, Austria, 2018.

Conference Presentations - Poster

- *"Multiplexed Detection of Plant Health Biomarkers"*, 23rd International Conference on Miniaturized Systems for Chemistry and Life Sciences (MicroTAS), Basel, Switzerland, 2019.
- *"A Portable Microfluidic System for the Detection of Health Biomarkers in Grapes at the Point of Need"*, 20th International Conference on Solid-State Sensors, Actuators and Microsystems & Eurosensors XXXIII, Berlin, Germany, 2019.

Chapter 10

Microfluidic Biosensing for Precision Agriculture Applications

In this section of the dissertation I will be discussing what was the main focus of my PhD, which was the development of a portable system for the detection of three different plant metabolites which play roles in plant immune responses. With a growing world population there is a need to provide quality crops in order to feed the masses, however, even with the increased level of technology employed in the Agricultural sector, there are still challenges that need to be addressed.

10.1 Climate Change and Fungal Infections

At the time of writing of this thesis, it is no secret that the planet faces a climate change crisis. Some of the direct impacts, which include the melting of the polar caps, which raise sea water levels [270] as well as, a diminished biodiversity in the animal kingdom [271] are very visible in social media and are used as discussion focal points. Other cases is how the rising temperature will lead to increased propagation of diseases such as Malaria and Ebola. [272] However, what is not as commonly discussed, is how our entire food supply will be directly impacted with the change in weather patterns worldwide, indeed, the pandemic which is called climate change does not only mean a reduced amount of beef in an attempt to reduce carbon emissions, [273] but also that entire crop fields can be wiped out at a moments' notice. [274, 275]

Most reports will relate the effects of rising temperature and erratic precipitation patterns to crop yield, however these two parameters do not show the whole picture. Parameters such as air humidity and wind velocity are equally important has these impact plant growth and pollination. [276]

Not only will plant growth be affected due to the plant itself, but also there will be different growth patterns for the microorganisms that live in proximity to the plants, some that are beneficial, such as nitrogen fixating bacteria, [277] others are pathogenic to the plant such as the fungus *Botrytis cinerea*. [278]

There is already an increased number of reports on the rise of atypical fungal infections amongst

crops, these include higher infection rates caused by typical pathogens, as well as, the appearance of uncommon fungal species. [279–281] Another cause for worry is the increased resistance to anti-fungal treatment that these species present. [282]

It is estimated that currently around 30% of the crops worldwide are lost due to fungal infections of the plants themselves or to post-crop spoilage due to poor storage strategies. [283] One approach to tackle the issue is to develop quick and easy detection methods to diagnose fungal infections early in the plant developmental cycle in order to avoid widespread propagation of the infections and allowing farmers to take appropriate countermeasures. Early detection of the signs of infection are important in order to allow farmers to act in order to avoid widespread propagation.

10.2 Precision Agriculture

What is Precision Agriculture?

Technological developments had always found their way into the agricultural industry such as the introduction of mechanization and synthetic fertilizers brought by the industrial age and the use og genetic engineering in the technology age. Now we are in the information age, so what capabilities can we now introduce into the agricultural industry? The answer is **precision agriculture** (PA). [284]

A brief description of PA would be the local measurement and tailored action on the state of the plants. This means the acquisition of information regarding soil nutrients, insect damage and also pathogen presence. [285]

Ideally every single plant should be assessed, however that is not feasible from a pratical stand-point, so reasonable sampling strategies have to be employed. [286]

In the following sections I will be discussing the different approaches to PA both for nutrient management and pest/pathogen monitoring.

Satellite Based Technologies

The first technology that I will be discussing is the use of satellite imagery in crop evaluation. There are several ways to implement this resource, with the first bing the monitoring of vegetation density and color, which allow for the remote sensing of plant growth. [287, 288]

Another interesting application is the use of satellite imagery to determine water needs. [289] This can be achieved by assessing the soil moisture level [290] or be measuring the water evaporation by the plants themselves. [291]

Even though this approach is very useful for large area applications it comes at a cost. Satellite imagery often suffers from a loss in space-time resolution, often having to sacrifice one for the other. [292] One solution is the use, in tandem, with unmanned aerial vehicles (UAVs).

Unmanned Aerial Vehicles

With the advent of commercial drones, it has been possible to introduce the use of these small UAVs into the agricultural sector to different ends. These can be used in similar contexts as the satellite imagery discussed before for crop growth control and water necessity assessment. [293] Besides this, it is also possible to determine nitrogen concentrations, [294] as well as other nutrient needs similar to the satellite technology. [295]

In addition to this, the use of UAVs have been used to determine not only the needs for pesticide/herbicide administration, but also the application of said pesticide, proving to be a truly remote controlling tool and not only useful for monitoring. [296, 297]

Another curious use of drone technology was the use of high resolution imagery for the rapid phenotyping in a research farm. [298]

Ground Units

Despite the development of areal systems, most forms of monitoring crops are land based systems. These range from infra-red sensors to monitor crop growth to soil quality sensors. [299, 300] Other reports mention the use of unmanned terrestrial robots for soil measurement [301] and building complex infrastructures based of the Internet of things paradigm. [302]

In this category I would also like to include sensors that require human action to employ at the point-of-need, more specifically those used in pathogen detection.

For early detection of fungal infections in agricultural crops one must rely on biosensing assays and efficient sampling strategies. Some groups have attempted to perform this detection based on the release of organic volatile compounds from plants, however this approach can lack specificity concerning the type of infection. [303, 304] Other approaches rely on the detection of pathogenic DNA through PCR or other molecular amplification technologies [305] or using immunoassay based approaches. [306] These molecular technologies are extremely specific, however they can often fail to recognize a pathogen that does not have the very precise molecular signature investigated. [307] It is within this realm of applications where microfluidics may bring several advantages to the table.

Microfluidics Technology in Agriculture

Microfluidic technology holds great potential for point of need applications where there is a limited amount of equipment available and where a short time of analysis is necessary. Microfluidic platforms for health and food safety have been presented in the past as well as for some agricultural applications. [308–310] These agricultural applications range from electronic based sensors to assess soil quality, [311, 312] to devices that enable more fundamental studies such as phenotyping of agents that are pathogenic towards plants [313] or the growth of the plant species in early stages of development [314]. Of particular interest in the application of microfluidics technology in precision agriculture is the use of portable biosensing devices that can be employed at the point of need for the detection of plant infections. Reports demonstrate the use of microfluidic based systems for the detection of pathogenic

DNA [315, 316], however there are very few reports on systems that look at the plant's metabolites as biomarkers of infection. [317]

Chapter 11

Detection of Azelaic Acid

11.1 Introduction

Bacterial and fungal infections can lead to the widespread destruction of crops. [318, 319] Routine retrieval of samples that are sent for testing tends to be costly, labor-intensive and involve a significant delay between retrieval and result which could allow the infection to spread, as they often depend on a variant of an ELISA assay, extraction of the pathogenic DNA/RNA, or on a light-based measurement at a specific wavelength. [320–322] Another issue with these infections is that, similar to what is happening in farmed animals, pathogens are continuously gaining resistance to antibiotic and antifungal treatments, which prompts farmers to increase the dosage of these products thus creating a selective evolution of drug-resistant microorganisms. [323, 324] These two problems, in addition to the ability that these pathogens have to be passed on to livestock and humans, provide the motivation for the development of a quick point-of-use device to detect plant infections at early stages. [325]

Once the plant is infected, there is an immune response called systemic acquired resistance (SAR) which will culminate with the production of salicylic acid. [326] Salicylic acid is then used by the plant to fight off the infection. Azelaic acid (AzA) primes plants to accumulate this hormone with the involvement of AZELAIC ACID INDUCED 1 (AZI1) gene. This makes AzA a prime candidate target molecule for an early detection of infection in plants. [326, 327] The increased concentration of AzA in infected plants has been demonstrated in the past, not only for grapes,[328] but also in other plants such as thale cress [329] and tobacco. [330] In grapes, an induction of AzA synthesis was noticed upon infection with Botrytis cinerea, a fungal pathogen that affects several fruits such tomato, strawberry and orange11. Moreover, when mutants lacking the ability to produce AzA are sprayed with the acid, a decrease in infection progression has been reported. [331] Currently there is a lack of a miniaturizable method for AzA detection, often relying on different methods of chromatography. [332, 333]

Microfluidics is often applied to Point-of-Need systems due to its portable nature and due to the possibility of inclusion of sample treatment/concentration on chip, which is not possible using standard Eppendorf tubes without creating an excess of waste. A frequently used microfluidic biosensing method is the miniaturization of an ELISA assay, with systems for the detection of food mycotoxins,[334] and

the Avian Influenza Virus [335], for example, reported in the literature. However, to the best of the authors' knowledge, there is no known antibody against unconjugated AzA, making the development of an ELISA assay for AzA unfeasible. As an alternative to ELISA assays, enzymatic biosensing in microfluidics has been reported in the literature, [336] taking advantage of the common redox nature of enzymatic reactions to perform electrochemical assays. [337] The most common applications of microfluidic-based enzymatic assays are for glucose detection in different biological fluids [338, 339] however other uses have been reported such as the detection of pesticides [340] and cholesterol.[339] Other examples of microfluidic biosensing methods include the detection of nucleic acids (both DNA and RNA) for pathogen detection. [341, 342] This approach however, requires the collection of the pathogen itself during sampling which may prove difficult for early detection, as the pathogen may present itself in different parts of the plant.

AzA has been widely used in dermatology for many years as a component in topical ointments to fight a variety of skin ailments. This is due to its antibacterial properties and for its inhibitory effect on the enzyme tyrosinase. [343] Tyrosinase is an oxidase which converts phenols into quinones at the expense of oxygen consumption and is a central part of melanin synthesis in humans. [344] Through oxidative coupling, it is possible to convert quinones in colored precipitates which can be quantified through absorbance measurements. [345]

In this portion of the work, a microfluidic device for the detection of infections in grapes through the quantification of AzA via an enzymatic colorimetric assay based on the inhibitory effect of AzA on tyrosinase is proposed. The optical detection module is integrated with a sample preparation module and can produce an answer in less than 10 min.

11.2 Materials and Methods

11.2.1 Reagents

For all assays, stock solutions of Azelaic Acid (AzA, 1 mM), Tyrosine (2 mM) and 3-Methyl-2-benzothiazolinone hydrazone (MBTH, 100 mM) were prepared in phosphate buffer saline (PBS) and diluted to the required concentration. Tyrosinase from mushroom was also prepared in PBS at a concentration of 2 g/L. All reagents were acquired from Sigma-Aldrich. Healthy table *Ophelia* grapes were acquired from a local supermarket, while wine producing *Trincadeira* grapes were infected and collected according to Agudelo-Romero *et al.* 2015. [328]

11.2.2 Microbead Functionalization

Throughout this work silica microbeads, with an average diameter of 50 μm (97728-U Supelco Analytical (Bellefonte, PA)) were functionalized with different chemical groups in order to provide different types of molecular interactions. For the functionalization of primary amines on the microbead surface, the silica beads were oxidized using an oxygen plasma (Harrick Plasma PDC-002-CE) and then immersed in a 2% (v/v) solution of (3-aminopropyl)triethoxysilane (APTES, Acros Organics) in acetone for 3h at room

temperature. The beads were then washed and stored in Mili-Q water. Alternatively, to functionalize the beads with carboxyl groups, the first steps of the protocol were the same as the functionalization using APTES. In this case, the beads were then incubated in a 0.1 M solution of succinic anhydride (Merck) in dimethylformamide (DMF) overnight and washed and stored in DMF until use. Silica beads functionalized with a long aliphatic chain (C_{18}) were also purchased from Supelco Analytical (Bellefonte, PA). Microbeads immobilized with tyrosinase were prepared by incubating a tyrosinase solution at 2 g/L with an APTES-functionalized bead suspension at a 1:3 volume ratio for 12 h at room temperature.

11.2.3 Phenolic Content Determination

The total phenol content of the samples was determined using an adapted version of the Folin-Ciocalteu method. In an Eppendorf tube, 10 μL of the desired sample was added to 720 μL of Mili-Q water and 120 μL of the Folin-Ciocalteau reagent (Fluka Biochemika) and incubated at room temperature for 5 min. Then, 136 μL of Na_2CO_3, 7.5% (m/m), was added and incubated at room temperature for 90 min. Sample absorbance was then measured at λ= 750 nm. Standard solutions of gallic acid (Acros Organics) were prepared in Mili-Q water and used as calibration to determine the total phenolic content in gallic acid equivalents (GAE). The calibration curve of the gallic acid standards obtained for this method can be found in Figure 11.1.

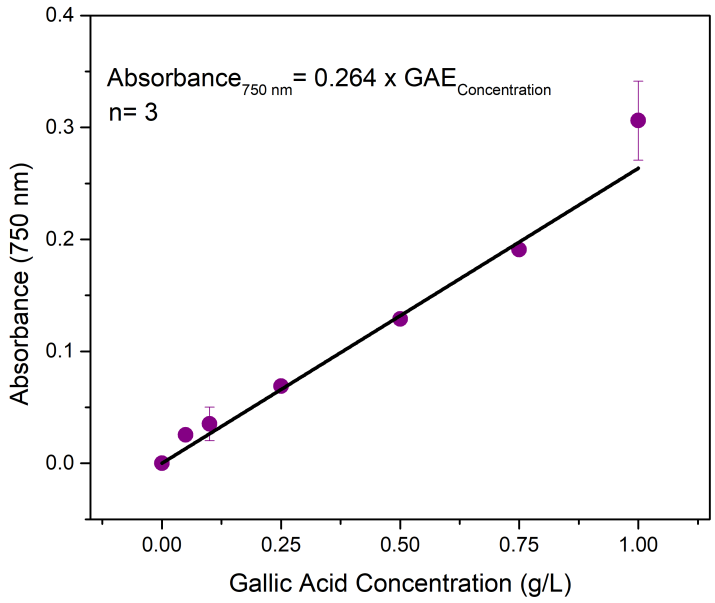

Figure 11.1: Gallic acid standard calibration curve for phenol quantification via the Folin-Ciocalteau method.

11.2.4 Grape Juice Sample Preparation

The grape juice used for each sample was obtained by first crushing whole grapes without the seeds, using a mortar and pestle and centrifuging the pulp for 5 min at 2000 G to separate the fibers from the juice. When necessary, the supernatant juice was diluted using PBS. The grape samples obtained at different stages of maturation in the field were frozen at the harvest point in liquid nitrogen, mashed and then kept at -80 $^{\circ}$C until needed. To prepare for testing, the grape samples were thawed and centrifuged for 5 min at 2000 G and the supernatant retrieved.

11.2.5 Microfluidic Assays

The microfluidic structures were packed with the appropriate microbeads by inserting 20 μL of the bead suspension into the microfluidic channel using a micropipette and then applying a negative pressure at the outlet using a syringe pump working in the fluid pulling mode (New Era Pump Systems, NE-1002X). Once the beads were packed, the inlet for bead insertion was sealed using a metal tube (INSTECH). Samples were then injected by using the pushing mode of the syringe pump. In the case of the experiments involving AzA, the change in transmittance was monitored for 400 s. Transmittance at λ= 480 nm was measured in real time by focusing light from a Tungsten-Halogen lamp which has passed through a monochromator (Oriel) onto the microfluidic device, with the detection zone aligned with the a-Si:H photodiodes. The signal from the a-Si:H photodiode at zero voltage bias, which is proportional to the transmittance through the microfluidic device, was measured using a picoammeter (Keithley 237).

11.3 Results and Discussion

11.3.1 Biochemical Assay Development and Miniaturization

The proposed reaction mechanism is initialized by the oxidation of tyrosine by tyrosinase in order to generate a quinone, which will then react, through oxidative coupling with MBTH, to generate a colored pigment. This type of reaction sequence is well documented at the macroscale for different types of phenolic compounds and is depicted schematically in Figure 11.2.

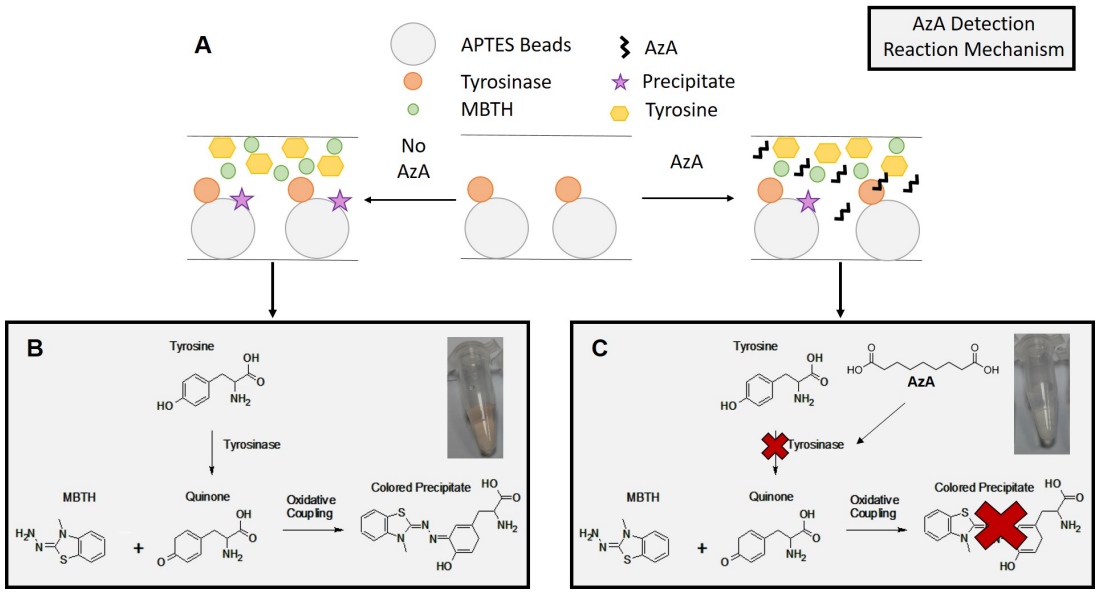

Figure 11.2: (A) Overall reaction schematic for AzA detection. (B) Reaction mechanism in the absence of AzA, which allowed for the production of a colored precipitate. (C) Reaction mechanism in the presence of AzA, where, due to its inhibitory effect, the pigment generation rate will be significantly lower as seen in the color difference between the Eppendorf tubes.

In the absence of AzA, oxidation of tyrosine will occur, leading to the oxidative coupling of the reaction product with MBTH (Figure 11.2-B), and the solution will change to a pink color over time. However, in the presence of AzA, this color change is extremely slow or non-existent, depending on the concentration of the acid, due to AzA's ability of inhibiting tyrosine activity (Figure 11.2-C). Kinetic studies of the tyrosine and tyrosinase system were performed at the macroscale. The kinetic model used is presented in Figure 11.3.

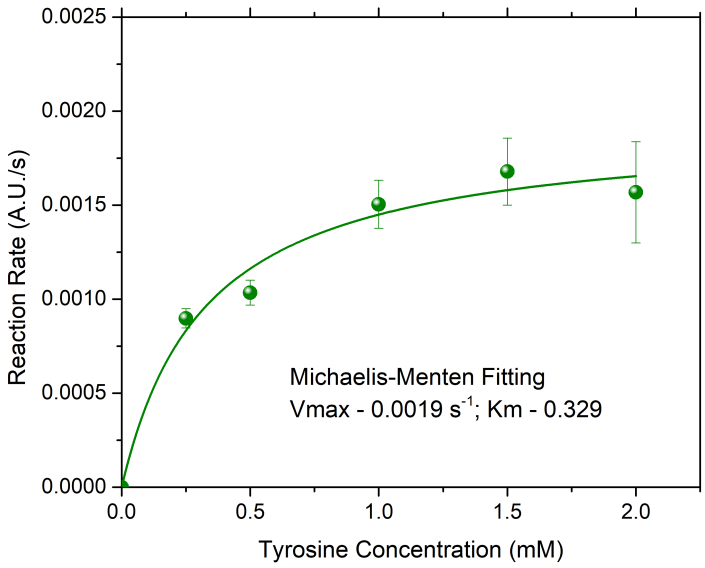

Figure 11.3: Tyrosinase kinetic modeling using the Michaelis-Menten model.

To miniaturize the assay to the microfluidic scale, microbeads were used in the microfluidic channel as they allowed for an increased immobilization density of tyrosinase molecules and as well as enhanced capture of the generated pigment due to the increased surface area. [346] The colored pigment produced during the enzymatic reaction was captured and accumulated at the surface of the microbeads. A schematic representation of the microfluidic device can be found in Figure 11.4.

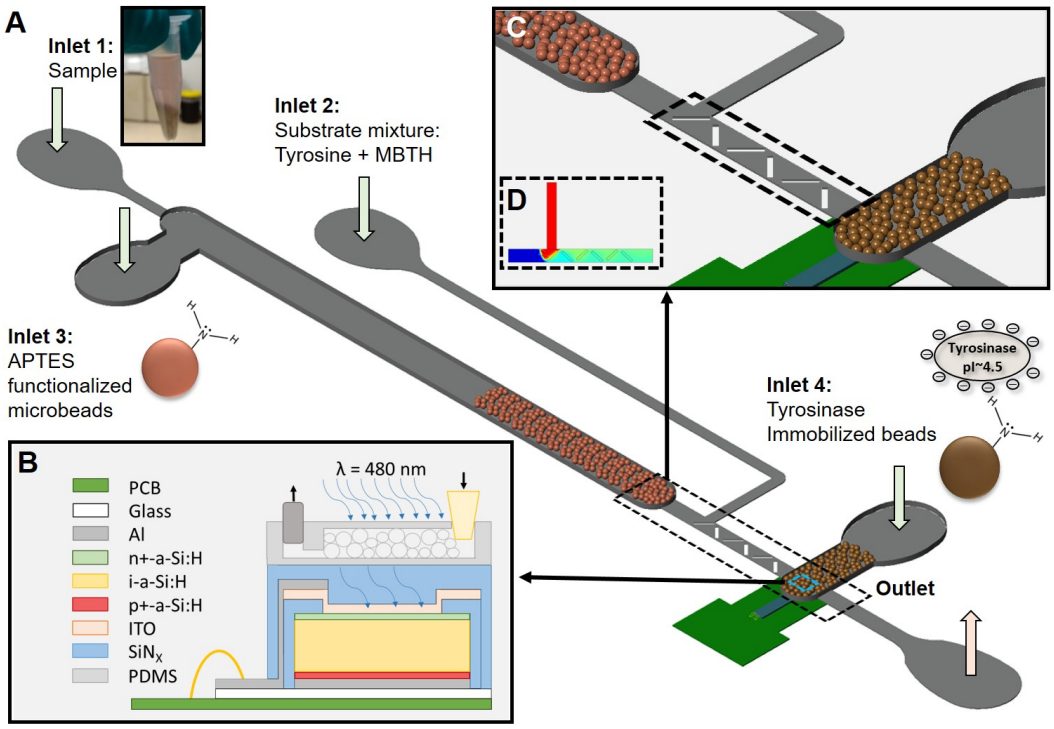

Figure 11.4: (A) Overall schematic description of the microfluidic device, composed by a sample pre-treatment column where chromatography beads were packed and the sample was injected. The treated sample was then mixed with the enzyme substrate solution which was injected into Inlet 2. This mixture than reached the detection chamber (B) which was packed with chromatography beads functionalized with tyrosinase and was aligned with thin-film silicon photosensor for optical signal transduction. (C) Between the sample pre-treatment column and the detection column there was a need for the integration of a mixer to ensure that treated sample and substrate are thoroughly mixed by the time they reach the detection chamber. (D) Mixer geometry was optimized *via* CFD simulations .

The microfluidic device was comprised of three sections, one for sample preparation, one for mixing and one for detection.

The sample preparation section (Figure 11.4-A) consisted of a long microcolumn with dimensions of 1 cm x 700 μm x 100 μm. This column was packed with microbeads that could clean the sample matrix by removing possible interferents, namely phenolic compounds that are abundant in grape juice, prior to detection.

The mixing zone (Figure 11.4–C) was necessary in order to create a homogeneous mixture before the cleaned sample and the enzyme substrates reached the detection zone. The design of this mixing zone was optimized using Computational Fluid Dynamics (CFD) software (Figure 11.4-D). The enzyme substrate was not injected together with the sample to avoid its retention by the beads at the sample preparation step.

The detection module (Figure 11.4-B) is comprised of a shorter version of the channel used for

sample preparation (1 mm x 700 μm x 100 μm) and was aligned with the 200 μm x 200 μm thin-film a-Si:H photodiodes. The detection column was packed with microbeads functionalized with tyrosinase to allow for the enzymatic reaction to take place as well as for the capture of the resultant colored reaction product.

The microfluidic platform was operated by injecting both sample and substrate mixture at 0.5 μL/min while measuring the signal produced by the photodiode in real time for 400 s.

11.3.2 Sample Treatment and Detection in Spiked Grape Juice

Due to the richness of the grape juice in phenolic compounds such as flavonoids, anthocyanines and gallic acid, [347] it was necessary to reduce the concentration of these compounds from the sample before measurement, as they interfere with the kinetics of the enzyme. This is due to tyrosinase's capability of oxidizing phenolic compounds, resulting in the production of colored products similar to those resulting from the oxidation of tyrosine.

To assess which microbeads should be used for phenol removal from the sample, silica micro beads with an average diameter of 50 μm were functionalized with 4 different chemical groups covering different types of molecular interactions. Each type of micro beads was packed into 8 microcolumns, with a working volume of 1 cm x 700 μm x 100 μm. The grape juice sample was injected at a flowrate of 0.5 μL/min for 20 min. The output of each set of microcolumns was then pooled together (so that the total volume collected was enough for the analysis) and the phenolic content was determined. Bare silica beads provided a hydrophilic interaction while beads functionalized with the long aliphatic chain, C_{18}, provided a hydrophobic interaction. Electrostatic interactions were also tested by using positively charged beads in the form of NH_2 groups while negatively charged beads were obtained by functionalizing with carboxyl groups. Screening results for phenol removal are presented in Figure 11.5.

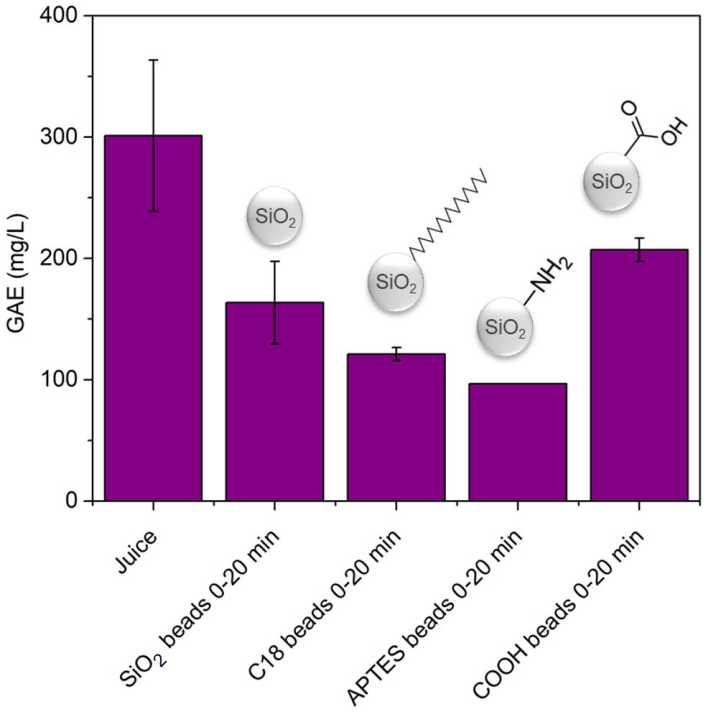

Figure 11.5: Quantification of sample phenolic content using different types of microbeads for phenol extraction. Electrostatic interaction and hydrophobicity were tested as driving forces for phenol retention. APTES and COOH-functionalized beads provided for positive and negatively charged beads, respectively. Bare SiO_2 and C18 beads provided different hydrophobicity character, with the C_18 being more hydrophobic. Phenolic compound concentration was determined by the Folin-Ciocalteu method, where each sample was measured 3 times.

Figure 11.5 shows that, overall the largest decrease in phenolic content was obtained with the APTES and C_{18} beads which is likely due to the presence of aromatic rings in the phenolic compounds that confer hydrophobicity and also due to the available negative charges presented in the aforementioned aromatic rings. Based on these results, the remainder of experiments were performed using APTES-functionalized beads in the sample preparation module.

As seen in Figure 11.5, it was not possible to completely remove phenolic compounds from the grape juice sample. In order to further decrease the sample matrix interference in the detection reaction, sample dilution was used as a complementary step in the sample treatment. To assess the impact of the dilution rate on the dynamic range of the assay, grape juice samples were spiked with different concentrations of AzA and diluted at the appropriate rates for a final constant AzA concentration of 100 nM. The signal obtained for the spiked samples was then compared to a non-spiked sample with the same dilution rate which acted as the control in this experiment. These results are presented in Figure 11.6-A.

In Figure 11.6-A, one observes that as the dilution rate of the sample is increased, there is a gain in the dynamic range of the assay, since the difference in response between the spiked and unspiked (control) sample increases. However, this gain in dynamic range ceases when the sample is diluted more than 100x. It is also important to note that even at these high dilution rates, the dynamic range obtained in buffer could not be reached. This observed difference between grape juice and buffer can be due to the presence of basal levels of AzA or due to other substances present in the grape matrix

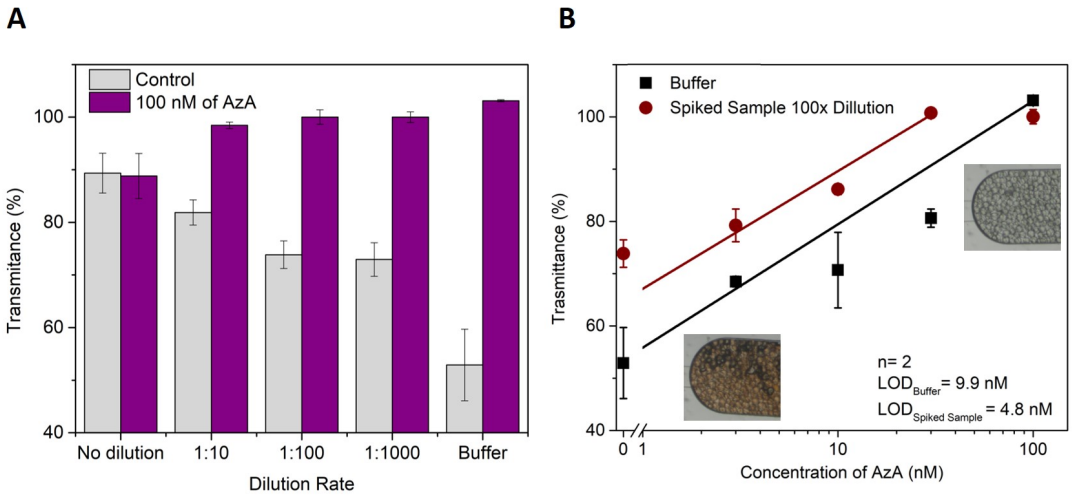

Figure 11.6: (A) Assessment of the effect of dilution of the grape juice sample on the assay dynamic range. Different dilution rates were tested while maintaining a constant concentration of 100 nM AzA (post-dilution) and the signal obtained was compared to the control assays. Each data point corresponds to the average of two repetitions. The control sample has no AzA. (B) Using a 100x dilution rate, known amounts of AzA were added to the grape juice and the detection assay was performed and compared to results obtained in buffer (B). Limit of detection (LOD) was calculated as 3.29x$\sigma_{Control}$.

that may inhibit the enzyme activity or interfere with the oxidative coupling. Figure 11.6-B it is possible to observe that in the presence of the grape juice matrix, the assay saturates (meaning that a transmittance of approximately 100% is reached) at a lower concentration of AzA then in buffer, despite maintaining a similar LOD between 5 and 10 nM. However, it is possible that the grapes used, despite being store-bought and grown in a greenhouse, possess a basal level of AzA which can be responsible for shifting the calibration curve obtained in the spiked samples upwards towards smaller changes in transmittance with respect to the values obtained in buffer. This is true for different types of grapes and has to be elaborated further in future work.

11.3.3 HPLC Method Development for AzA Detection

Once we started the HPLC detections, I knew that the range of concentrations in the grape samples were around 3-10 μM for healthy grapes and above 30 μM for infected samples (as will be demonstrated in Chapter 14), according to the microfluidic results, so this was the target concentration range. However, the initial experiments concerning the detection of AzA were somewhat lackluster.

As a starting point, I followed the protocol presented by Malik *et al.* [332], using a composition of the mobile phase of 75% phosphate buffer (pH 3.5, 50mM) and 25% acetonitrile. The injection volume was 10 μL and the detection wavelength, λ= 209 nm. It was possible to detect the AzA with an average retention time of 9.5 min by using a flow rate of 1.2 μL/min. The chromatograms obtained are visible in Figure 11.7.

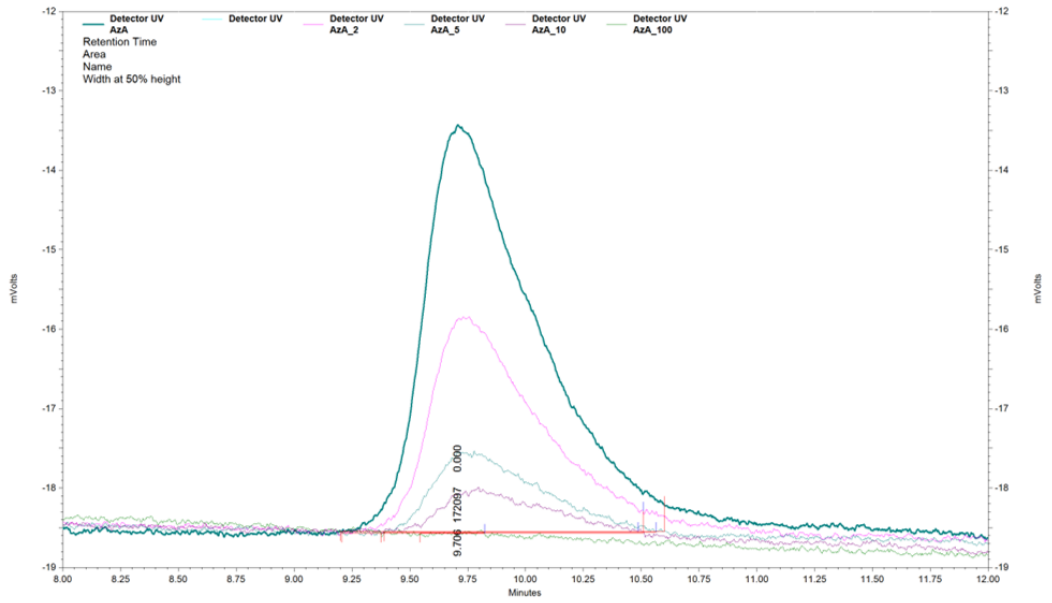

Figure 11.7: Example of the chromatograms obtained for the detection of AzA standard in the range of 20mM and 0.2mM.

By plotting the peak area as a function of the concentration, the standard curve is obtained. This curve can be seen in Figure 11.8.

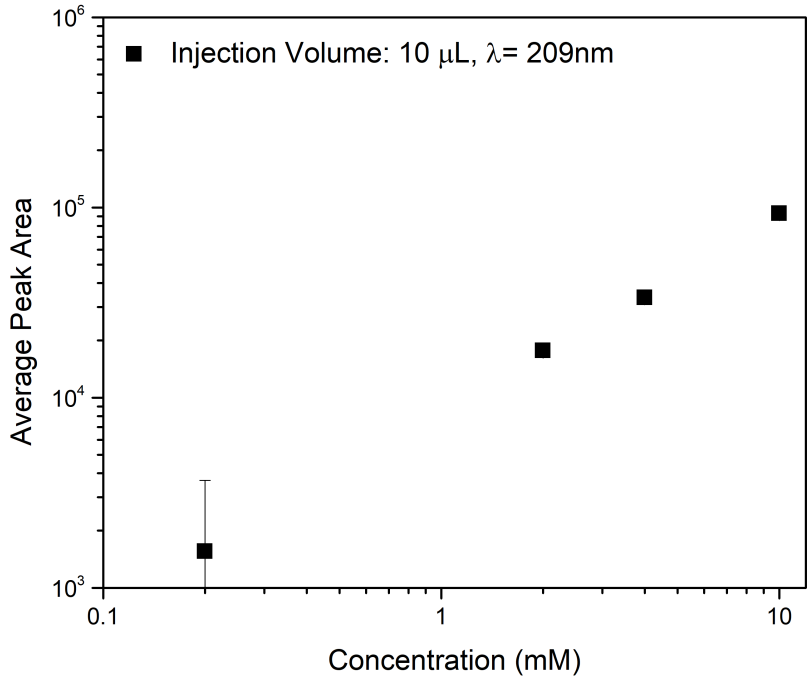

Figure 11.8: Standard curve obtained for the initial process conditions for the detection of AzA. Each point is the average of two measurements.

This level of detection is not sensible enough, thus the method had to be optimized. The variables

changed were the mobile phase composition, which worsened the sensitivity, the sample injection volume was changed from 10 to 25 μL and the detection wavelength was changed to λ= 206 nm, due producing a absorbance spectrum of the compound. This improved dramatically the sensitivity of the method, with the results being presented in Figure 11.9, where a comparison to the microfluidic method is presented.

This method was sufficient to obtain information in regards to the infected and healthy samples as will be discussed in Chapter 14.

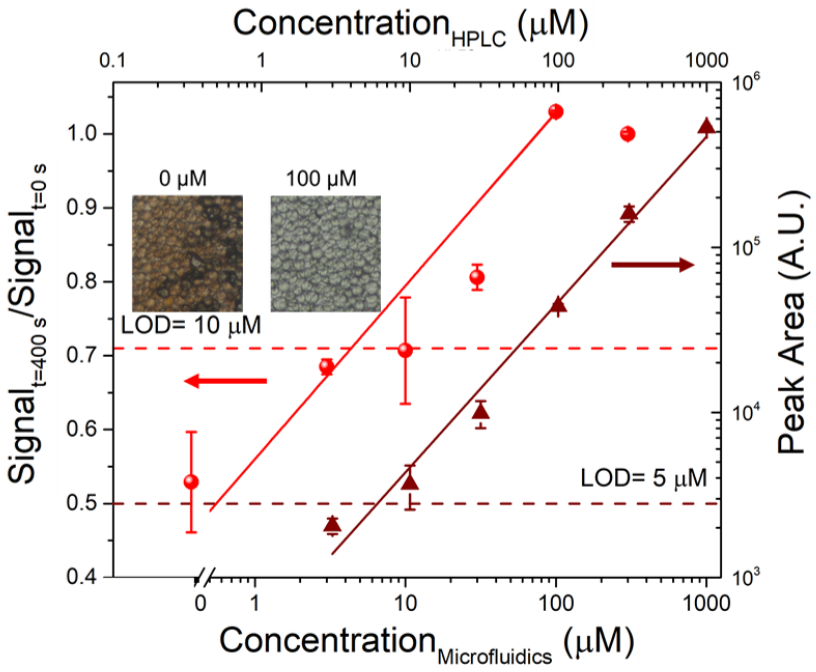

Figure 11.9: Calibration curve obtained in buffer for the AzA detection using the microfluidic chip (red spheres, r^2= 0.96) and the standard curve for the HPLC measurements (dark red triangles, r^2=0.98).

11.3.4 Initial Grape Samples Testing

Highly infection-susceptible *Trincadeira* berries were inoculated with *B. cinerea* conidial suspension at the peppercorn-sized fruits stage corresponding to developmental stage EL29 according to the Coombe (1995) classification. [348] The ripening stages investigated in this study were identified as EL32 characterized by hard green berries, EL35 corresponding to *veraison* when anthocyanin accumulation initiates and EL38 corresponding to fully ripe berries (harvest stage). *Trincadeira* clusters presented, at the EL32 stage a high infection level with *B. cinerea* which further increased throughout ripening. Evaluation of sample infection was performed by visual inspection and additionally by qPCR using primers specific to the fungal genomic DNA (data presented in the Supplementary Information).

These samples were then analyzed using the enzymatic assay, the results obtained are presented in Figure 11.10.

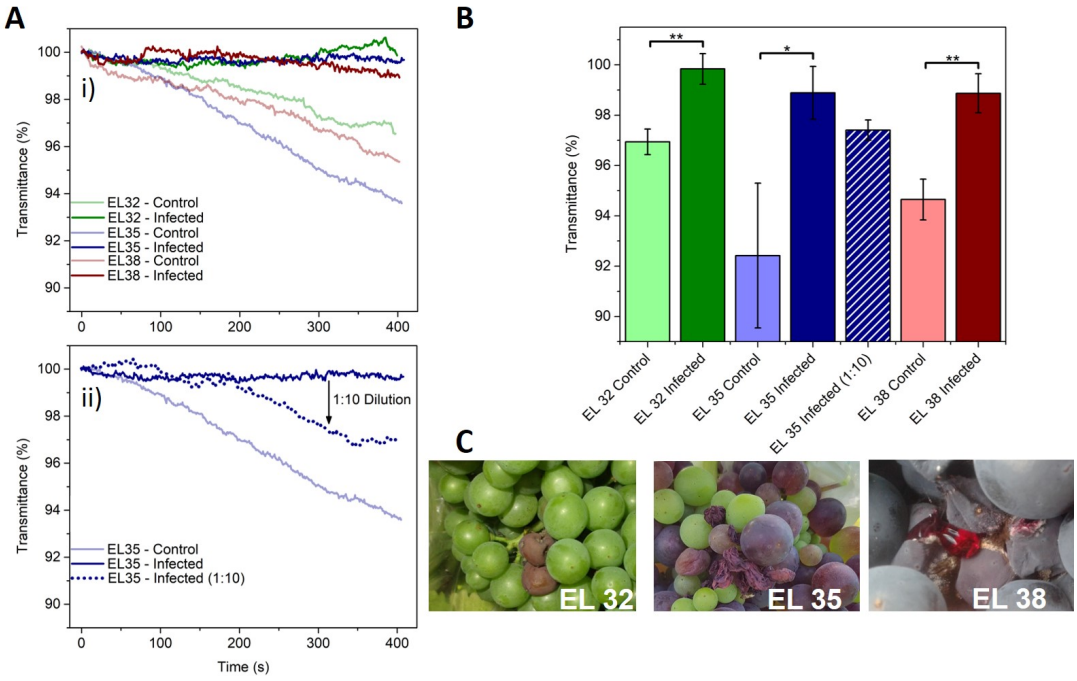

Figure 11.10: Photosensor acquired transmittance values obtained by applying the enzymatic assay to samples of "*Trincadeira*" grapes at different developmental stages. The control group were healthy grapes. The "EL" prefix is a standard reference to the grapes' developmental stage. The reaction rate is shown as the variation of transmittance as a function of time (A-i)). For the EL35 sample a further dilution was measured (A-ii)). An alternative method of analysis can be an end point measurement such as averaging the signal of the last 10 s of measurement, this was done three times for each sample (B). The concentrations of AzA in the grape samples were confirmed by rp-HPLC (C). The Limit of detection (LOD) is defined as 3.29x the standard deviation of the lower points added to the average value of those points, while the limit of quantification (LOQ) is defined as 10x the standard deviation added to the average. EL 38 was not tested using this method due to a lack of sufficient sample. Photographs of the infected grapes tested at different ripening stages. At EL38, sporulation of the fungus on the grapes is quite visible (C). Significance levels used for ANOVA analysis: α=0.05*, α=0.01**. r^2 (HPLC standard) = 0.999

By acquiring the transmission continuously in real time, it is possible to obtain a quick assessment of the presence of AzA by comparing the reaction rate, i.e. the slope of the transmission versus time, between the sample and a control. An alternative method of analysis would be to fix a time and average the difference in transmission values. In this set of samples, it was possible to successfully distinguish the infected samples from the non-infected samples either by measuring and comparing the slopes of the transmission-time plots obtained in both samples (Figure 11.10-A) or by doing an endpoint measurement (Figure 11.10-B). By taking the values obtained in Figure 11.10-B and calculating the estimated AzA concentration using the calibration curve obtained in Figure 11.6-B, it is possible to determine that the healthy samples have an AzA concentration of 2.1 μM (EL32), 1.3 μM (EL35) and 1.7 μM (EL38). In the case of the contaminated samples it is not possible to determine the concentration as the values are too close to the saturation point of the assay. In order to estimate the quantitative difference in AzA levels between the infected and healthy sample, the infected sample at EL35 was diluted an extra 10x (resulting in a 1000x dilution in total) which allows for the transmission-time signal to be within the dynamic range of the assay. Using the calibration curves presented previously, the infected sample is estimated to have

between 20-40 μM (20-30x the amount of AzA of the healthy sample). These results are supported by the results obtained using HPLC, as the healthy grape samples are all close to the LOD of 16.5 μM, while the EL 35 infected samples have a concentration of approx. 56 μM and the EL32 infected samples present an AzA concentration of approx. 144 μM. Once again, despite the clear differences shown in Figure 11.10 between the responses of infected and healthy samples, it is still necessary to determine a standard value for what is considered a healthy and an infected plant in order to obtain a more robust infection evaluation system. Another aspect to take into consideration is that different grapes will have different chemical compositions, which may lead to the presence of different contaminants that may interfere with the assay which may need to be removed in the sample preparation step with alternative cleaning strategies.

Chapter 12

Detection of Salicylic Acid

12.1 Introduction

Plants, in general, have different response pathways available to them to fight off infections, however most will rely upon systemic acquired resistance (SAR) as their immune response. In SAR, once the pathogen has come into contact with the plant, there will be an increase of the production of organic acids such as Azelaic and Salicylic acids (SA) in order to fight off the infection. In this response pathway, fatty acids are cleaved and converted into azelaic acid, which has some anti-microbial properties, however its major role is to promote the transduction of the AZI gene, which will induce the production of salicylic acid, which will coat the exterior of the plant and inhibit the pathogen propagation. [328, 331] With this in mind the second metabolite added for an eventual multiplexed detection was SA.

12.2 Materials and Methods

12.2.1 Reagents

Stock solutions of titania (TiO_2) nanoparticles (10 g/L) and Salicylic Acid (SA, 2 mM), were prepared in Milli-Q water, as opposed to the typical preparation in buffer due to interferences of commonly used buffers in the SA detection protocol. The microbeads used fort his portion of the work were functionalized in the same fashion as before using silanization through APTES.

12.3 Results and Discussion

12.3.1 Assay Development

The protocol for the detection of SA was adapted from the work reported by Tseng et al. [349] In this work, the use of TiO_2 nanoparticles are reported as an simple method for the detection of salicylic acid due to the shift in absorbance behavior, from absorbing light with $\lambda < 350$ nm to having significant

absorbance (A>0.75) using 350 nm $< \lambda <$ 425 nm, as seen in Figure 12.1, when the particles complex with the SA.

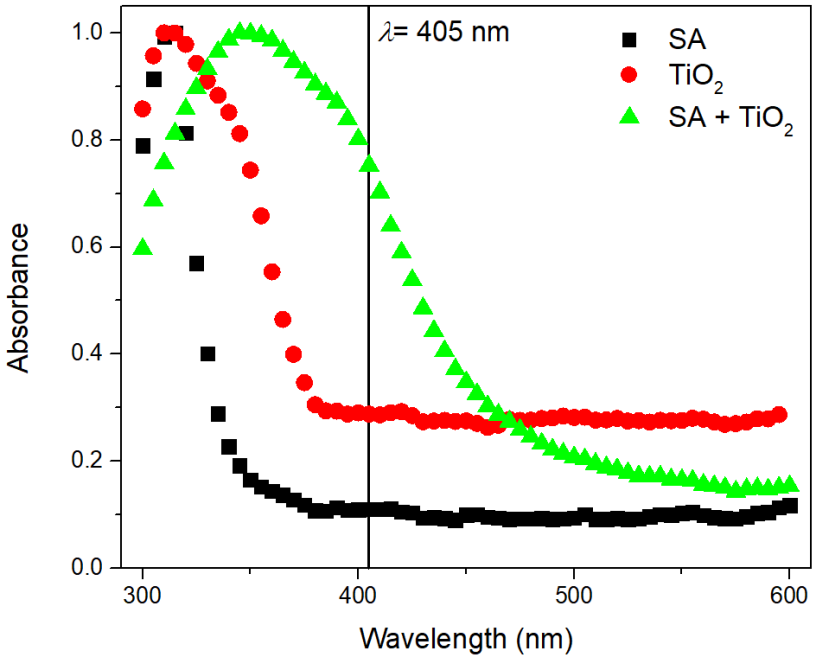

Figure 12.1: Absorbance spectra of free SA (black), free TiO_2 nanoparticles (red) and the product of the reaction (green). The shift in absorbance from the UV range into the visible due to the reaction is visible here. The vertical line at λ= 405 nm represents the chosen wavelength for the assay.

This shift in optical properties can be seen depicted in Figure 12.2. In this work, we aim to capture the complexes formed by the reaction between the TiO_2 nanoparticles and the SA using the amine-functionalized microbeads packed into the channel, while monitoring the transmittance at λ= 405 nm, as depicted in Figure 12.2. The use of silica beads with a positive amine group to capture the TiO_2-SA complexes was motivated by the report of Tseng et al, where they determine that the complexes lose their positive charge in comparison to the "free" TiO_2 nanoparticles, thus possibly being susceptible to an ionic interaction with the primary amine of the microbeads. [349]

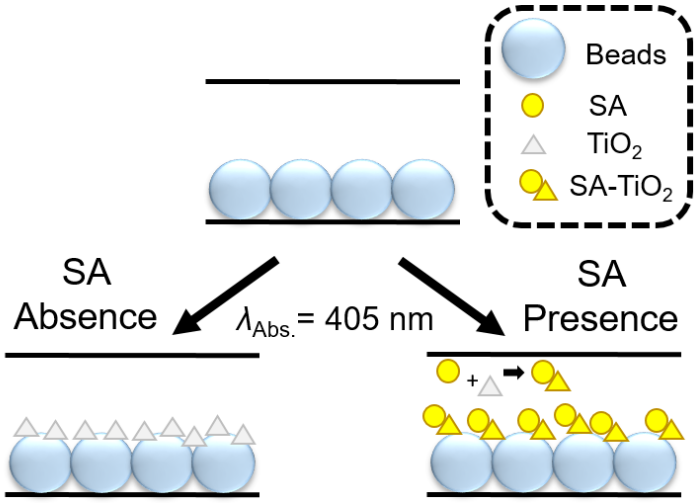

Figure 12.2: Schematic description of the detection assay for SA, where the free SA in solution will complex to the TiO_2 nanoparticles causing a shift in color from transparent to yellow

The assays for the detection of SA were performed using DI water instead of a typical buffer due to the interference caused by inorganic salts as demonstrated in Figure 12.3

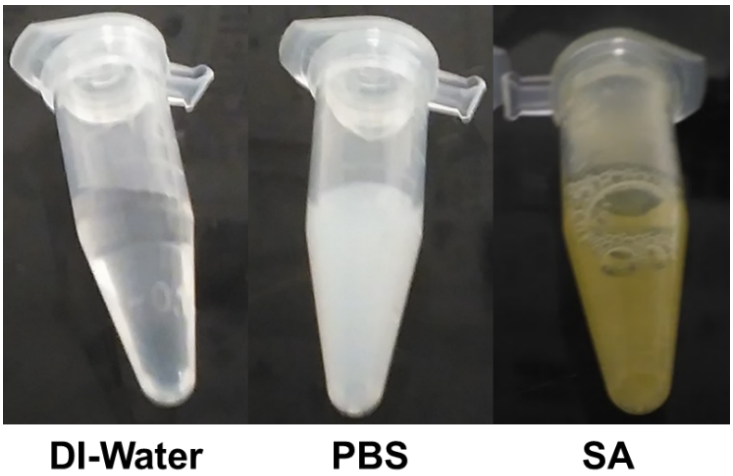

Figure 12.3: Result of mixing the TiO_2 nanoparticles with DI-water, PBS and SA. It is important to notice the turbidity caused by the presence of PBS.

In order to have both the SA and AzA detection on sequential chambers, it was necessary to confirm that the TiO_2 nanoparticles didn't interfere with the enzymatic assay. For this, know amounts of AzA and TiO_2 were mixed in solution and the AzA detection assay was performed. These results are presented in Figure 12.4.

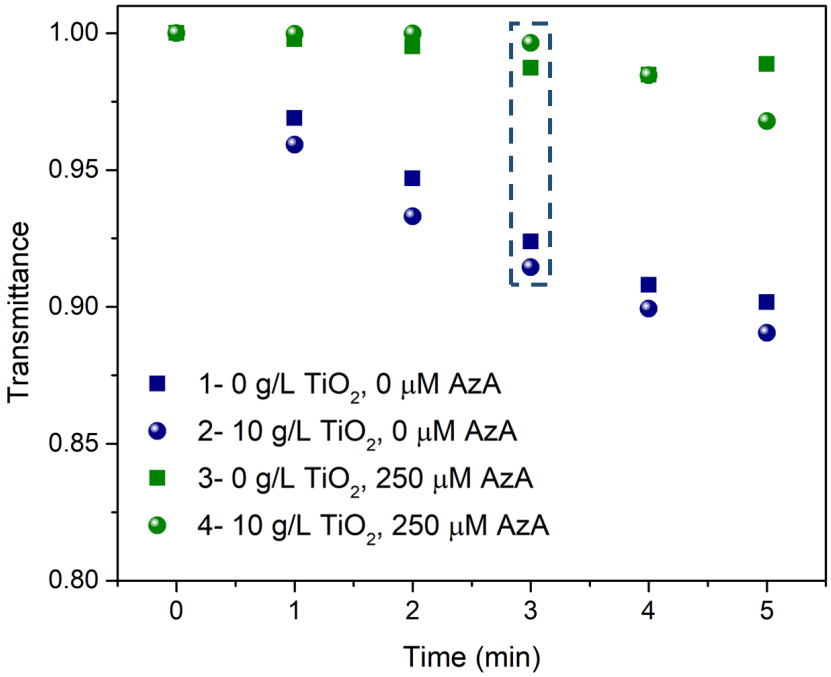

Figure 12.4: Assays performed to determine the existence of interference from the TiO_2 nanoparticles on the enzymatic activity of tyrosinase.

12.3.2 HPLC Method for SA Detection

For the detection of SA, the optimization procedure was more laborious. Here it was more dubious the range of interest, due to the microfluidic work being more delayed and the uncertainty of the specificity of the assay.

As in the previous section, the starting point was a method described in the literature by Arimboor *et al.*.[350] Here they suggested a mobile phase of phosphate buffer(pH 3.0, 50mM) and methanol, usign a gradiant elution, and a detection wavelength of λ= 220nm. When these conditions were used, independant on the mobile phase composition (75:25; 50:50 and 25:75 were tested) no peak was detected except for the initial liquid front as seen in Figure 12.5.

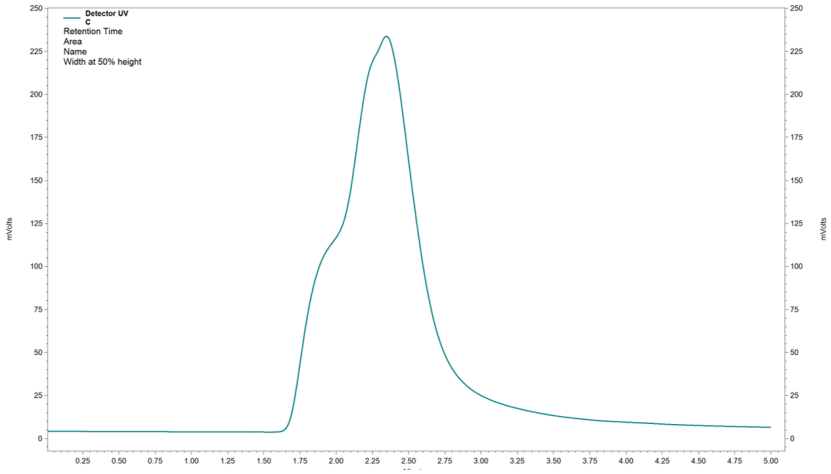

Figure 12.5: Demonstration of failed SA detection method.

Initially as an easy to perform attempt, the experiment was repeated with the mobile phase used for the detection of AzA, composed of phosphate buffer and acetonitrile. Initially a composition of 70:30 was tested, which produced a postive result as seen in Figure 12.6. Despite this minor success the SA peak was still too close to the liquid front, which is a problem due to the large peak of non-interacting compounds present in the grape juice. The optimization procedure focused on delaying the SA peak by changing the mobile phase composition as seen in Figure 12.6. The ideal composition is 80:20, despite the peak broadening produced by this composition.

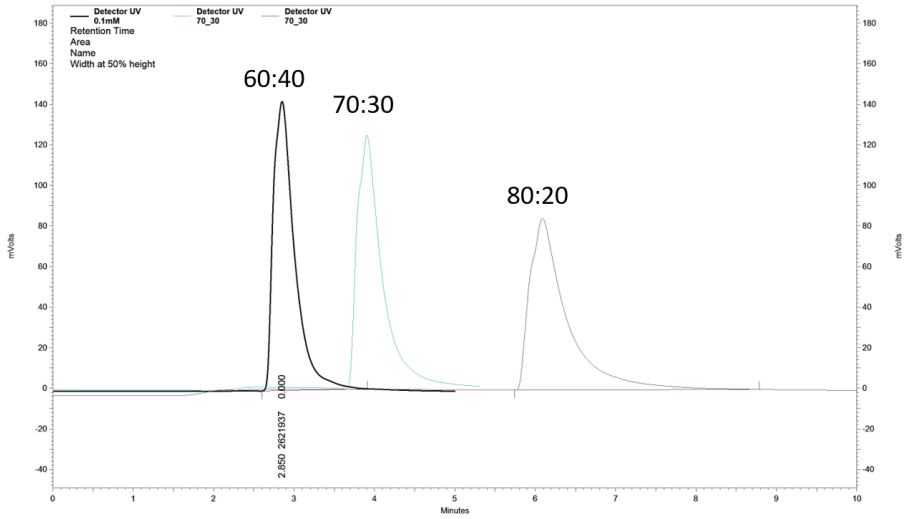

Figure 12.6: Optimization of the mobile phase composition in order to delay the SA peak in relation to the liquid front. The ideal composition was determined to be 80:20, phosphate/acetonitrile.

Using this method, a standard curve was produced for SA and is presented in Figure 12.7 as well as the standard curve for the microfluidic assay.

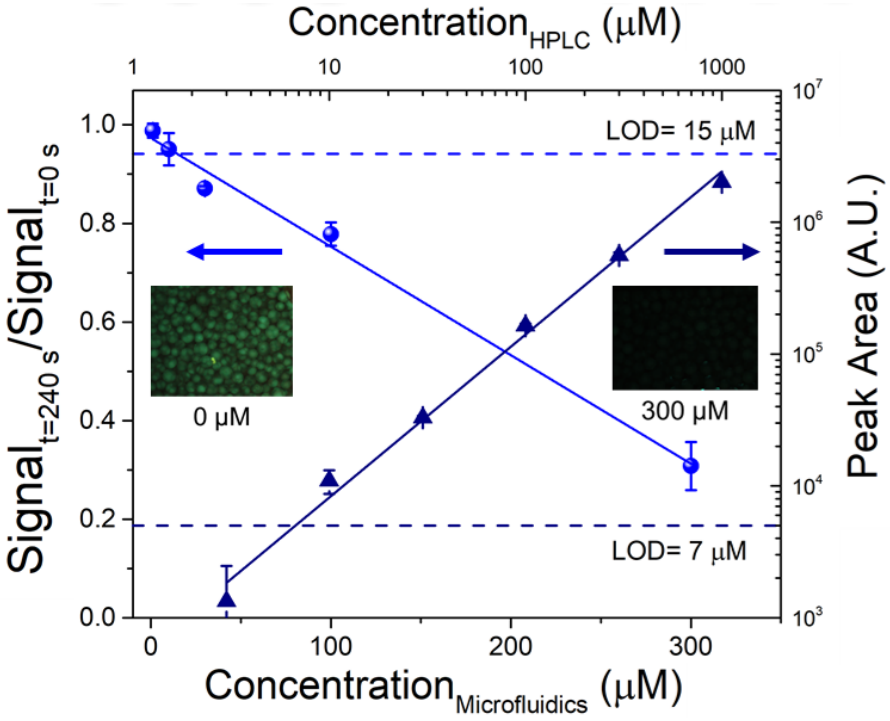

Figure 12.7: Calibration curve obtained in buffer for the SA detection using the microfluidic device (blue spheres, r^2=0.99) and standard curve obtained for HPLC benchmarking of the microfluidic results (dark blue triangles, r^2=0.99); the micrographs demonstrate the increased absorbance at λ=405 nm of the SA-TiO_2 complex by blocking the excitation light that would otherwise cause the beads to fluoresce.

Having successfully determined the necessary standard curves it was possible to proceed to the detection of both acids in the real grape samples.

Chapter 13

Detection of Jasmonic Acid

13.1 Introduction

As mentioned in the previous chapters, SA and AzA are prime metabolites to identify plant infections. A third metabolite that was identified as a potential target was Jasmonic acid (JA), due to its role in Effector-Triggered Immunity (ETI) and as an indicator of physical trauma to the plant, which may prove relevant in some cases. [351, 352] JA is upregulated in the presence of pathogenic agents, as well as of some herbivores, and, besides promoting the expression of secondary metabolites with established roles in plant defense, JA is toxic to several species including fungusfungi, caterpillars and beetles.

13.2 Materials and Methods

For the detection of JA, two different conjugation reactions had to be performed beforehand: (i) the conjugation required for the labeling of the α-JA antibody with an appropriate fluorophore (Alexa 430® succinimidyl ester amine-reactive dye, Thermo Fisher); and (ii) the conjugation of JA to bovine serum albumin (BSA) through carbonyldiimidazole (CDI) chemistry. The labelling protocol for the Alexa 430® was performed according to the manufacturer instructions. The BSA conjugation protocol consisted of mixing 5 mg of CDI to 1 mg of JA in 100 μL of HPLC grade acetone, incubating in the dark for 30 min under continuous agitation. Then, 1 mL of a BSA solution (10 g/L) prepared in 0.1 M of sodium bicarbonate was added and continued to incubate at room temperature for 2 h. The sample was then washed several times by centrifuging Amicon® tubes with a 10 kDa cut-off for 5 rounds, 5 min each, at 14000 g as a diafiltration step. The conjugation success was confirmed through fluorescent microscopy using the labeled antibody as demonstrated in Figure 13.1.

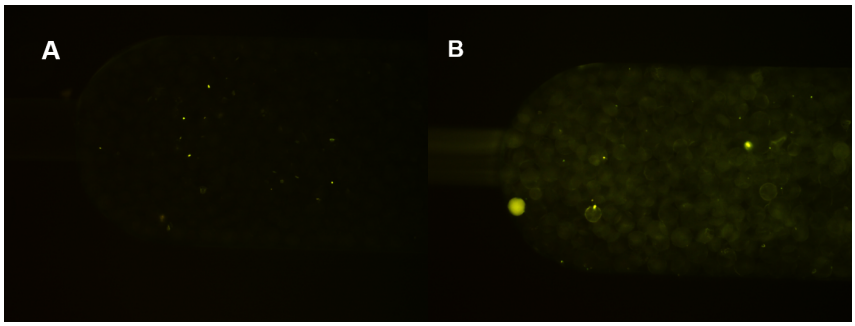

Figure 13.1: Results obtained concerning the interaction between the α-JA antibody with microbeads functionalized with BSA (A) and JA-BSA (B). Pictures were enhanced for visualization purposes.

13.3 Results and Discussion

The assay developed for the JA detection is a competitive immunoassay, where microbeads functionalized with a BSA-JA conjugate are packed into the microfluidic channel. The sample is then spiked with a labeled α-JA IgG that will compete between the free JA in the sample and the BSA-JA immobilized on the microbeads in a similar fashion to reports in the literature for microfluidic, immunoassay-based biosensing devices. [46] A schematic representation of the assay is presented in Figure 5-A.

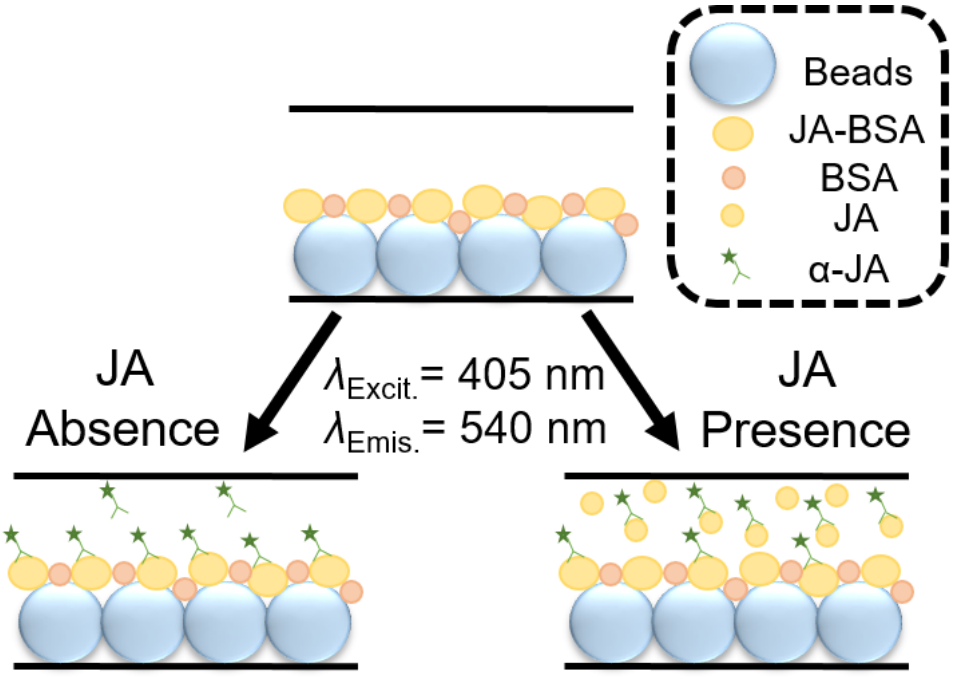

Figure 13.2: Schematic description of the competitive immunoassay for the on-chip detection of JA.

At the start of the assay a pipette tip is placed in the inlet containing the SUA mixed (1:1) with the α-JA antibody solution (100 g/L) The liquids are simultaneously driven into the device by applying a negative pressure at the chip outlet using a syringe pump.

13.3.1 ELISA Benchmarking

As opposed to the previous metabolites, I was not possible to develop a HPLC method for the detection of JA. Due to this, a commercial ELISA kit was acquired and used to test the samples. A comparison between the ELISA kit and the microfluidic assay is presented in Figure 13.3.

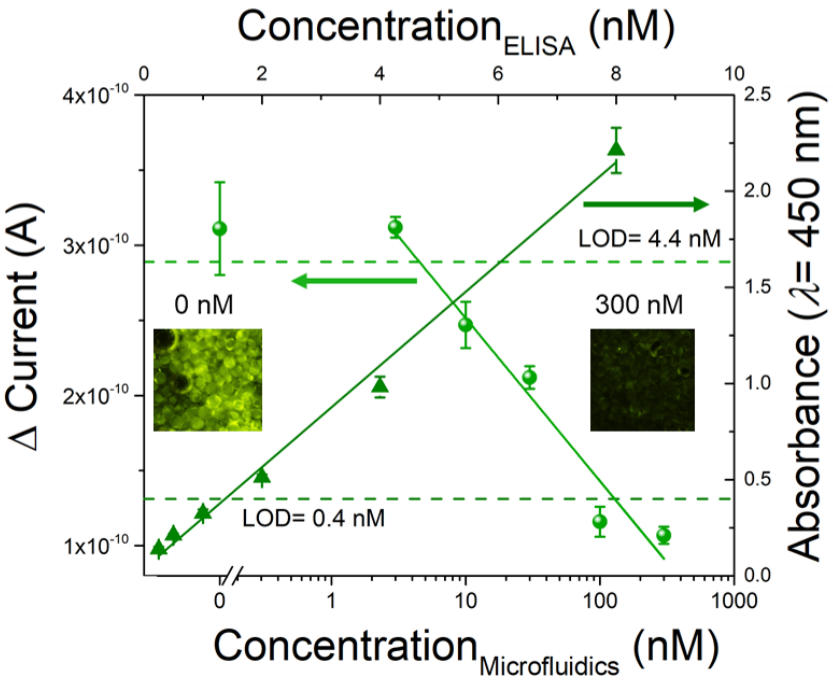

Figure 13.3: Calibration curve obtained in buffer for the JA detection using the microfluidic chip (green spheres,r^2= 0.95), the micrographs demonstrate the competitive nature of the assay. In order to benchmark the results obtained at the microscale, a standard curve was determined using a commercial ELISA kit (dark green triangles, r^2= 0.99.

Chapter 14

Multiplexed Detection

By developing the individual assays presented in the previous sections, I was now in a position to perform the multiplexed detection of the three hormones in actual grape samples.

14.1 Results and Discussion

14.1.1 Grape Cultivars

Grape cultivars of two distinct wine producing varieties, *Trincadeira* and *Carignan*, were cultivated, where half of the samples were inoculated with a fungal spore suspension directly on the fruit, where a plastic container was placed over the grape bunch and the other half were maintained in a healthy state. In the case of the *Trincadeira* samples, infections were performed in separate years, with the initial batch being performed in 2016 when the cultivars were infected with *Botrytis cinerea*, while the second batch was infected with *Erysiphe necator* in 2019. For the *Carignan* cultivars, the plants were infected with *E. necator* in 2017.

Figure 14.1 presents a visual summary of the samples tested. It is interesting to note the visual difference in symptoms produced by the different fungal infections, with B. cinerea producing shriveled fruits, while E. necator creating a powdery mildew around the plant. Table 14.1 presents all the samples tested in the present work.

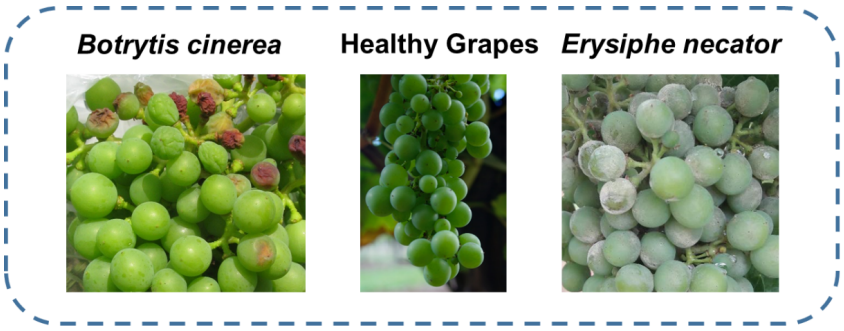

Figure 14.1: Photographs with examples of the symptoms presented in cases of advanced infection from *B. cinerea* and *E. necator*.

Table 14.1: Summary of the different grape samples

Cultivar Species	Maturation	Infection
Carignan	EL 32	-
Carignan	EL 32	*E. necator*
Carignan	EL 35	-
Carignan	EL 35	*E. necator*
Trincadeira 2019	EL 33	-
Trincadeira 2019	EL 33	*E. necator*
Trincadeira 2016	EL 32	-
Trincadeira 2016	EL 33	*B. cinerea*
Trincadeira 2016	EL 35	-
Trincadeira 2016	EL 35	*B. cinerea*

14.1.2 Microfluidic Device

In this work, a microfluidic platform comprised of three 100 μm-high chambers connected by 20 μm high-channels is demonstrated. A schematic representation of the device is presented in Figure 14.2-A.

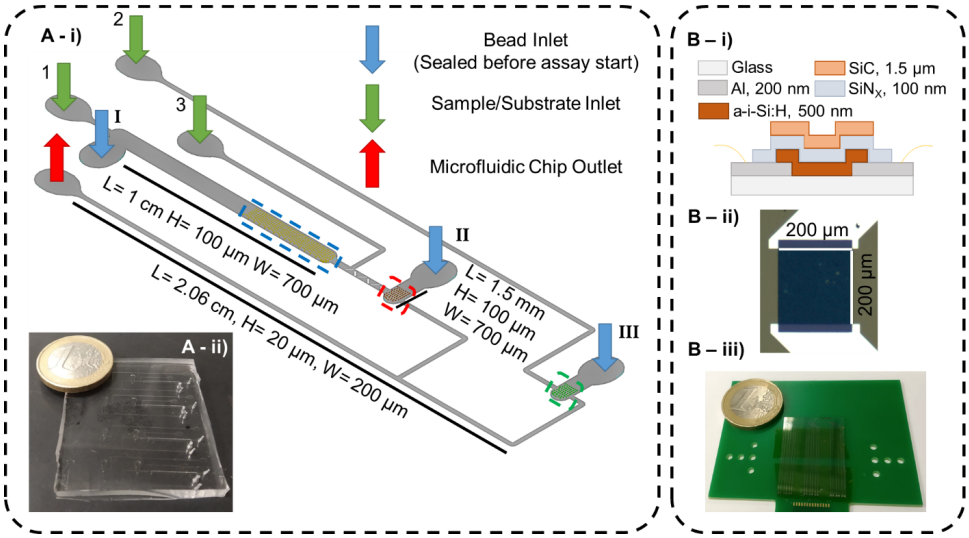

Figure 14.2: (A) Microfluidic device developed for the multiplexed detection of the plant hormones. (A-i) In a first fluidic network, the first chamber (indicated by a blue outline) is used for the detection of SA, followed by the chamber for AzA detection (indicated by a red outline). In a second fluidic network a third chamber is used for the detection of JA (indicated by a green outline). (A-ii) These devices are fabricated in sets of 4 in 4 cm x 4 cm pieces of PDMS. (B-i) Each of the 3 chambers is coupled to a thin-film a-i-Si:H photoconductor, comprised of the parallel aluminum contacts, a-Si:H mesa and passivated, for physical protection, with a layer of SiN_x. In the case of the sensor for the detection of JA, the mesa is topped with a a-Si:C:H filter layer. All sensors have an aperture area of 200 μm x 200 μm (B-ii) and are taped and wire bonded to a custom-built printed circuit board (PCB) for electronic addressing (B-iii).

Before the start of the assay, each of the three detection chambers is pre-packed with the appropriate chromatography microbeads using the inlets marked with blue arrows in Figure 14.2-A, which are then sealed using a metal plug during the execution of the experiment. In inlet I, silica beads functionalized with a primary amine are packed for the detection of SA and removal of phenolic content from the grape sample, while in inlet II, the silica beads that are placed inside the chamber are functionalized with immobilized tyrosinase for AzA detection. Inlet III is used to pack beads functionalized with a BSA-

JA complex for the detection of JA. All these detection methods have been described in the previous sections.

At the start of the assay pipette tips are placed in the inlets marked with green arrows. In inlet 1, the sample under analysis (SUA), diluted 1:50 in a solution of TiO_2 (10 g/L), is introduced while in inlet 2, the SUA mixed (1:1) with the α-JA antibody solution is introduced. In inlet 3, the substrate mixture necessary for the AzA detection is introduced. The liquids are simultaneously driven into the device by applying a negative pressure at the chip outlet using a syringe pump (red arrow).

Due to the optical nature of the different assays, thin-film a-Si:H photoconductors are used to acquire the light in the different detection chambers (Figure 14.2-B). The individual sensors have an aperture area of 200 μm x 200 μm and are powered by a 20 V bias (Figure 14.2-B-ii). These photosensors are fabricated as an array of 9 sensors, with each set of 3 sensors being aligned with the respective microbead chamber of the microfluidic chip and wire bonded to a custom PCB for electronic addressing (Figure 14.2-B-iii). In the case of the third set of photoconductors, used for JA detection, an extra layer of a-SiC:H is used since the fluorescent assay requires cutting-off of the excitation light used (λ= 405 nm). The use of 3 sensors per chamber is for redundancy reasons. The whole assay has a duration of 400 s.

14.1.3 Salicylic Acid Detection

Once the calibration curves were determined, the grape samples were tested in both the microfluidic platform and using rp-HPLC and the results are presented in Figure 14.3-A.

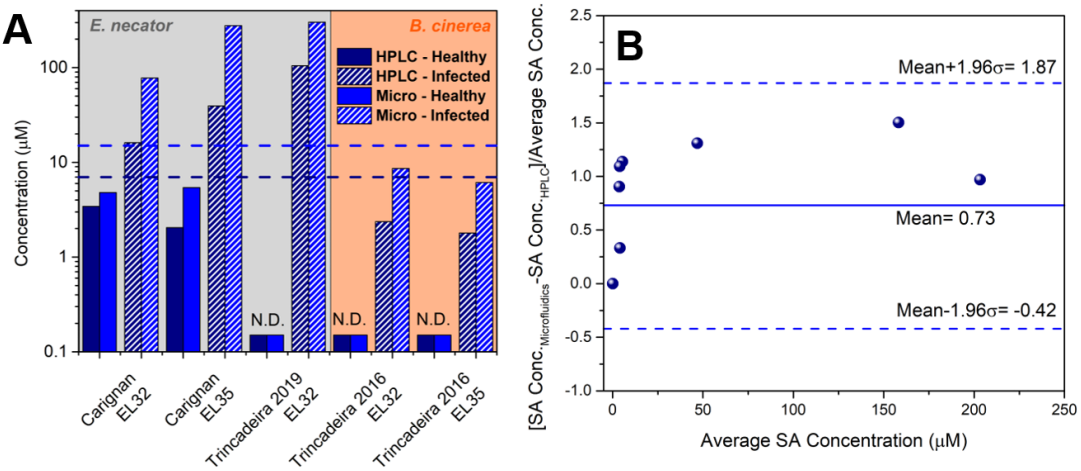

Figure 14.3: (A) Comparison of the results obtained for the cultivar samples with the microfluidic device and by HPLC. Samples within the grey region were infected with *E. necator*, while the orange region correspond to samples infected with *B. cinerea*. The solid bars correspond to healthy samples, while the striped bars are the infected samples. (B) Bland-Altman plot to assess the correlation between the measurements obtained with the microfluidic system and the HPLC. Differences of measurements followed a normal distribution according to the Shapiro-Wilk test at a significance level α= 0.05, p-value= 0.0925.

It is possible to observe that in the case of infections with *E. necator* the amount of SA appears to be always up-regulated, independent of the maturation stage of the grape and cultivar species. This is

in line with previous reports from the literature. [353, 354] In the samples infected with *B. cinerea*, there also seems to be an increase in the amount of SA in the infected samples, however the values obtained are always below the LOD of both the HPLC and the microfluidic methods, thus is not considered a real increase. This could be explained if the infection by *B. cinerea* interferes with the pathway responsible to produce SA, or, in contrast, does not trigger the overexpression of the SA-dependent pathways as seen in other plant species. In these cases, the plant sample possessed resistance to the infection caused by *B. cinerea* without increased expression of SA, meaning that SA does not play an active role in fighting *B. cinerea.* [355, 356]

It is also important to note that despite the trends for SA concentration measured being similar in the microfluidic device and the HPLC, the concentration detected by both techniques is different. To determine the correlation between the measurements obtained using the two systems, the Bland-Altman plot was determined and is presented in Figure 14.3-B. The Bland-Altman plot, allows to compare directly two measurement methods to determine the existence of a bias of one method in relation to another. [357] In order to successfully employ the Bland-Altman method of analysis, the differences of the values obtained for each method are plotted as a function of the average of the measurements obtained for both methods. If the range of values under assessment is large (as in the case of this study, with values $<$10 and $>$100 for the same population), it is recommended that the differences between measurements are presented as a percentage in relation to the average of the results obtained for both the methods under comparison. A necessary condition to employ this type of analysis, is that the differences registered between the measurement techniques under comparison follow a normal distribution, and this was confirmed using the Shapiro-Wilks test for a significance level of α= 0.05.[357] If both measurement methods are in complete agreement, the mean value would be 0. In the case of the results presented for SA detection in this work, the mean obtained is 0.73, which suggests that the microfluidic system overestimates the amount of SA in the sample in comparison to the HPLC system, which is also verified in Figure 14.3-A. With the 95% confidence interval (CI), represented in Figure 14.3-B as the mean +/- 1.96σ limits, being very close to 0 in the lower limit and fairly high in the upper limit also suggests that the microfluidic will consistently overestimate the amount of SA in the sample when compared to the HPLC system.

Based on other reports in the literature, it is possible that, besides the increase in SA upon vine infection, there is also an increase in the production of SA-Glucoside and other similar molecules such as methyl-salicylate. [358, 359] Due to the similarity of the chemical structure of these compounds to SA it can be assumed that these SA-analogues will also react with the TiO_2 nanoparticles. Besides this possible interference there is also a degree of interference from inorganic salts as shown in section S4 of the Supplementary Information, which is the reason why the assay is performed in DI water instead of a typical buffer.

Despite the interferences registered, the microfluidic device is capable of distinguishing healthy from infected grape samples for *E. necator* infections, however there is a lack of certainty in for infections of *B. cinerea*, indicating the need for the quantification of additional metabolites to obtain a more accurate diagnosis of the plant state.

14.1.4 AzA Detection

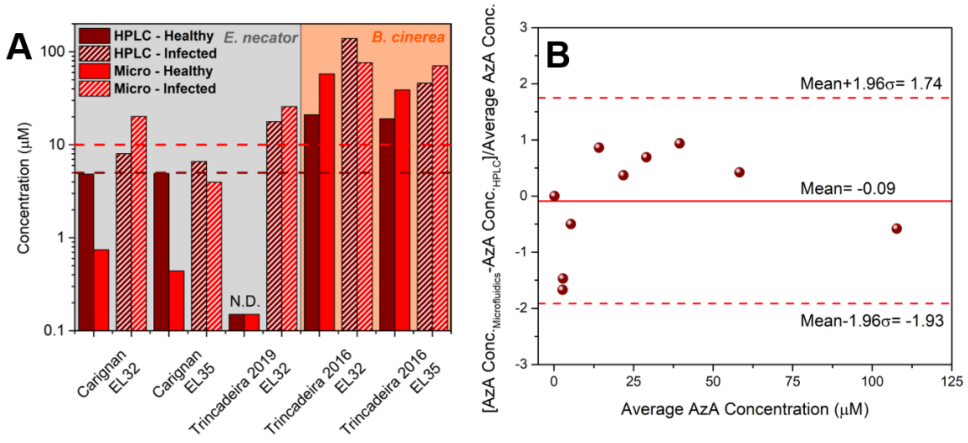

Figure 14.4: Comparison of the results obtained for the cultivar samples with the microfluidic device and by HPLC. Samples within the grey region were infected with E. necator, while the orange region correspond to samples infected with B. cinerea. The solid bars correspond to healthy samples, while the striped bars are the infected samples. Bland-Altman plot to assess the correlation between the measurements obtained with the microfluidic system and the HPLC. Differences of measurements followed a normal distribution according to the Shapiro-Wilk test at a significance level α= 0.05, p-value= 0.232.

Figure 14.4-A shows the comparison of the results obtained for the grape cultivars using both the microfluidic and HPLC approaches. Looking at the infections performed with *E. necator*, the infection produces an increase in the AzA levels presented for the early stage maturation samples while an increase is not observed in the case of the EL35 samples due to the values obtained for AzA being just at the level of the LOD of the techniques so they were not considered to consist of a true increase of AzA. For the infections performed with *B. cinerea*, an increase of AzA content occurs in all samples tested. Overall, AzA is overexpressed in all cases of infection with *B. cinerea*, however produced mixed expressions in the case of *E. necator* indicating that it may be used as a marker for *B. cinerea* infection. Other reports in the literature correlate the expression of AzA with defense against diseases induced by the *B. cinerea* fungus, [328, 331] while no reports could be found at this time that relate AzA expression to *E. necator* induced disease.

Figure 14.4-B enables us to assess the correlation between the microfluidic measurements and HPLC measurements for AzA. In this case, the mean of the differences is very close to 0, which is the ideal scenario in the Bland-Altman analysis. However, the limits of the CI are very distant from the mean and are similar in absolute value, and this is an indication that the discrepancies registered between the values obtained using microfluidic system and the HPLC values are not systematic. After a closer analysis it is possible to see that most of the measurements that are underestimated by the microfluidic system match samples that are below or close to the LOD for the method, which may be negatively impacting this analysis.

When we combine the information of the quantification of AzA with that of the quantification of SA, it is possible to observe that AzA appears to be a biomarker more directed towards infections caused by *B. cinerea*, despite having a slight expression in the samples infected with *E. necator*. While SA was

only upregulated in the case of plants infected with *E. necator*. These results seem to suggest that AzA may be a more generic response metabolite, however there are cases where it was not overexpressed, leading the authors to believe that more plant types as well as more pathogens would need to be tested to make the claim that AzA can be used as a generic biomarker for plant health. By combining the response between the SA and AzA, we are able tocan narrow the type of infection the plant is suffering, where a *E. necator* infection will induce upregulation of SA, while *B. cinerea* will only induce the production of AzA.

14.1.5 Jasmonic Acid Detection

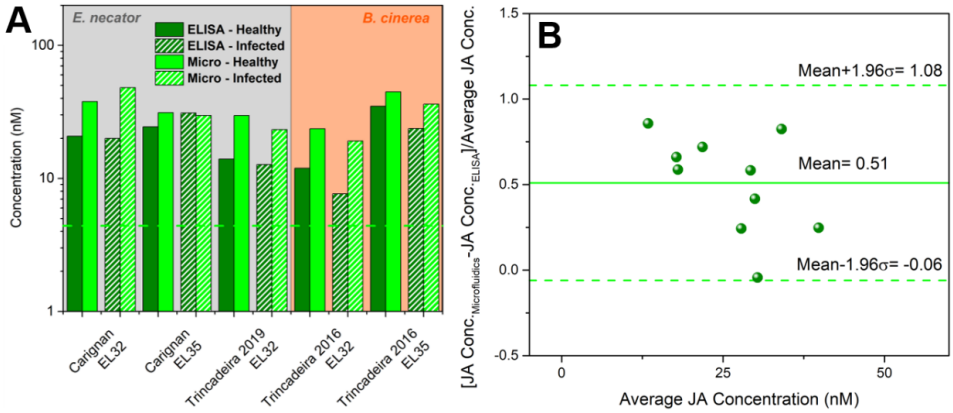

Figure 14.5: (A) Comparison of the results obtained for the cultivar samples with the microfluidic device and by ELISA. Samples within the grey region were infected with *E. necator*, while the orange region correspond to samples infected with *B. cinerea*. The solid bars correspond to healthy samples, while the striped bars are the infected samples. (B) Bland-Altman plot to assess the correlation between the measurements obtained with the microfluidic system and the HPLC. Differences of measurements followed a normal distribution according to the Shapiro-Wilk test at a significance level α= 0.05, p-value= 0.510.

Figure 14.5-A summarizes the results of JA concentration obtained for the real grape samples for both the microfluidic assay and the commercial microplate ELISA assay. In the case of the *Carignan* samples, there seems to be no change in JA content due to infection for the EL 32 samples, while there is a slight increase in the JA content for the EL 35 samples infected with *E. necator* according to the commercial ELISA, while the microfluidic results present the opposite response. For the *Trincadeira samples*, the ELISA measurements suggest that the infected samples present a lower content of JA in the different maturation stages independently of the infection type, which agrees with the results obtained with the microfluidic results.

Figure 14.5-B gives us the correlation between the microfluidic system and the commercial ELISA. It is possible to observe that the microfluidic assay presents consistently higher results than its commercial counterpart, with a mean value of 0.51 and all the samples having an overestimated concentration of JA. However, the overestimation in JA content provided by the microfluidic system seems to be very consistent across most of the samples tested. This may be due to the lower specificity of the antibody used in the microfluidic assay when compared to that of the commercial kit as well as some cross

reactivity with molecules such as Methyl-JA and JA-isoleucine, that are also commonly present in the plant samples. [360] Despite registering the same trend as the commercial ELISA assay in the case of the *Trincadeira* results, the differences between infected and healthy samples are very subtle which suggests that JA may not be an ideal biomarker for plant health assessment. However, JA can be used as a redundant source of information for the infection caused by *B. cinerea*, providing confirmation of the diagnosis.

14.2 Infection Patterns

In a first attempt to establish a pattern for infection assessment based on the three metabolites studied, scores were attributed to the different acids studied in relation to them being up- or down-regulated in comparison to their healthy counterpart. For this, a score of 1 was attributed to infected samples that were up-regulated, -1 to those that were down-regulated and 0 for those that did not present a change in the respective hormone content within the experimental uncertainty. These results are summarized in Figure 14.6-A.

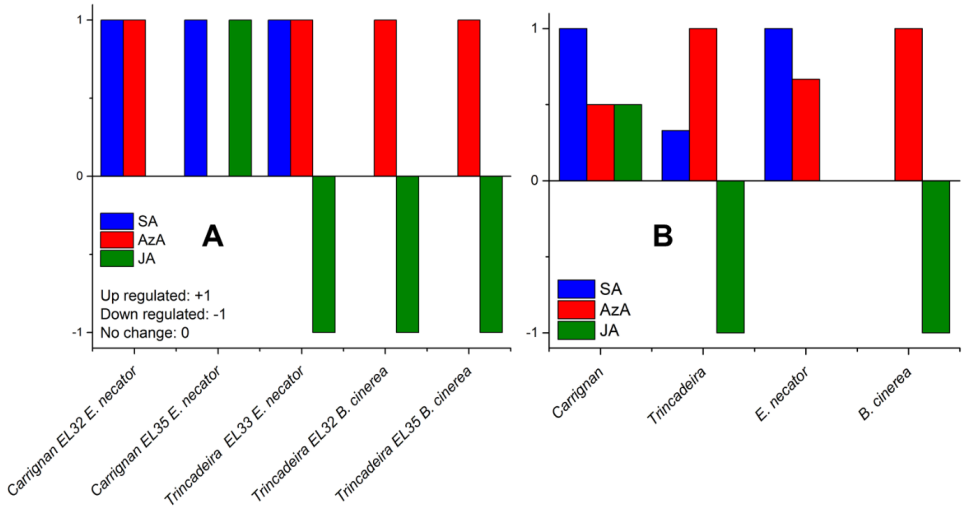

Figure 14.6: (A) Qualitative assessment of hormone variation between infected and healthy samples. (B) By grouping the results in the same cultivar group and the same fungal infection source it is possible to determine behavior patterns specific for each group. The grouping of the qualitative scores was done by performing the average of the scores attributed in A.

By grouping the results obtained in terms of cultivar species and fungal infection source, as presented in Figure 14.6-B, several conclusions can be extracted. When looking at the variation of SA, it is possible to observe that it is consistently up-regulated in the infections using *E. necator*, while not changing significantly in the infections with *B. cinerea*, (although this lack of change has mostly to do with the fact that the levels detected are below the LOD for the detection protocols employed in this work). AzA expression is consistently upregulated in *B. cinerea* infections as well as in both types of infection for the plant. In contrast, the variation registered for JA indicates that it is consistently down-regulated in the case of infections using *B. cinerea*, while presenting mixed results for infections with *E. necator*. Even though these results concerning JA point towards its specificity as an indicator for *B. cinerea* infections,

it is important to note that in this work we only had access to *Trincadeira* cultivar infected samples, which may mean that this response is due to the immune response of the plant itself and not due to the nature of the infection. Ideally, in future work, more different infection types and cultivar species should be tested in order to determine more robust hormone variation patterns.

14.3 Conclusions

In this work a microfluidic device coupled to thin film photosensors for the multiplexed optical detection of 3 plant hormones is demonstrated. The plant hormones chosen, SA, AzA and JA, are known indicators of plant health as they play active roles in different plant immune responses. The microfluidic device presented can detect all 3 hormones in under 7 minutes using a simple sample preparation method consisting of a simple dilution of the grape juice obtained from sample maceration.

Two different grape cultivars were tested, *Trincadeira* and *Carignan*, at different maturation stages, both these cultivars being relevant species for the wine industry. The cultivars were infected with two different types of fungal infections, *E. necator* and *B. cinerea* with samples being tested using both the microfluidic device as well as a gold standard technique (HPLC in the case of SA and AzA, ELISA in the case of JA). The metabolite expression was shown to be disease dependent, with SA being overexpressed in the case of infection caused by *E. necator*, while AzA (overexpressed) and JA (under-expressed) presented consistent behaviors when the cultivars were infected with *B. cinerea*.

Not only was the microfluidic device successful in distinguishing infected from healthy samples across both cultivar species, but by combining the information provided by the 3 hormones tested it was possible to distinguish between the different infection types, demonstrating the utility of the microfluidic device presented in this work as a method for the point-of-impact early detection of fungal infections is grapes.

Chapter 15

Portable Prototype Development

15.1 Introduction

In the past decade, microfluidics technology has evolved into a very complex field, allowing for a diverse range of applications including fundamental biology research through the study of single cell behavior [13, 361], as well as drug screening applications [362, 363] and disease modeling through the development of organ-on-a-chip models [321, 364]. One of the more powerful applications is the development of (bio)sensing platforms. [365–367] By using microfluidics, it is possible to integrate several unit operations into a single chip, allowing for a wide range of assay possibilities such as bacterial DNA detection for environmental studies [368], toxin detection in raw materials for the food and feeds industry [369] and biomarker detection for clinical applications [370].

A Point-of-Need device will have to perform a number of steps if it is to be able to allow a sample-to-answer type of operation. These steps include: sample insertion, sample treatment, the molecular recognition event, transduction and output to the end-user.

Most biological assays will require some degree of sample preparation ranging from a simple dilution of the sample or centrifugation to more complex cleaning or concentration steps. In the case of microfluidic based assays, the sample treatment may be performed on- or off-chip or a mix of both depending on the application. For a clinical setting it may be reasonable to have some steps of the sample preparation off-chip as many hospitals will have basic laboratory equipment. [371, 372] However if one considers a setting where equipment is lacking, sample preparation should be performed on chip or if not possible, be very easy to execute in the absence of laboratory equipment. [373, 374]

Sample insertion and liquid handling is critical in a portable system. Some microfluidic biosensing systems will rely on bulky bench-top pumping systems and sample/reagent insertion equipment which compromises the advantages gained by the miniaturization. In some cases, liquids are driven by capillarity by placing a drop of the sample under analysis in a specific region of the chip. Paper based microfluidic platforms (lateral flow assays) are a prime example of this approach, which avoids complex sample insertion equipment but is limited in terms of handling of complex liquid sequences and final assay sensitivity. [375, 376] Other approaches include the use of needles or pipette tips for liquid insertion

and small pumping systems, such as peristaltic pumps on chip for liquid driving. [377, 378]

There is a wide array of molecular recognition biosensing strategies based on enzymatic or immunochemical reactions or nucleic acid recognition events. [379] Across all types of biosensors there is a need to perform a transduction of the recognition event into an output to the end user.

One commonly used method is the use of photosensors that transduce an optical event (reflectance, absorbance, fluorescence, etc.) into an electrical signal. Our group has previously reported the integration of thin-film silicon photosensors with microfluidic platforms for optical transduction of biosensing assays for clinical applications [380] toxin detection in animal feeds [369] and plant biomarkers for precision agriculture [381]. Other transduction methods include the use of magnetoresistive sensors [382], impedance sensors [383] and electrochemical sensors [340]. However, most reports on these types of approaches in the literature still rely on bulky electronics or computers for the final read-out and data processing and are not demonstrations of fully integrated, portable devices capable of being used at the point of need.

Some of the more promising fully integrated devices include a wearable system for glucose monitoring and insulin administration [384] and a portable ricin detection system [385]. Some recent work includes the development of smartphone peripherals which can read out the result of the microchip [386, 387], or by exploiting the smartphone camera for colorimetric detection. [388] Other reports in the literature include the development of portable platforms for very specific, single-use applications, [389] while others, despite being portable, are too bulky for certain settings (e.g. a farm) [390]. Despite the widespread effort to develop point-of-need products, with possibly the best example being the i-STAT® developed by Abbot, there are still very few commercially available fully integrated Point-of-Need devices. [391]

In this paper, we demonstrate a portable system with multiple read-out and actuation possibilities that can be used at the point of need for performing optical based assays. This prototype has simple sample insertion in the form of a pipette tip as well as automated liquid driving.

As a model assay we will use the enzymatic detection of azelaic acid (AzA) in grapes reported previously. [381] AzA is a biomarker present in plants which is part of the systemic acquired resistance immune response. When the plant is faced with a pathogen, as in the case of the fungus B. cinerea, there is an increased production of this organic acid, which will induce the production of salicylic acid in order to fight off the infection.[331] Early detection of this increased production of AzA would allow a faster response to infection and earlier treatment to the vine tree, avoiding wide spread propagation to the rest of the crop.

15.2 Materials and Methods

15.2.1 Main Components and Prototype Enclosure

A polylactic acid (PLA) enclosure (dimensions 13.5 x 8.5 x 7 cm) box was 3D printed (BoxQ 3D printer) in order to house the electronic setup, peristaltic pump, light sources, microfluidic chip and TFT/touch

screen for user interface. The PCB shown in Figure 15.1 was custom made (Eurocircuits N.V.) and contains 4 amplification circuits, 4 driving circuits, a socket for a Teensy® 3.6 micro-controller (MCU) development board, an area for the placement of a sensor array, and voltage regulators and battery charge controllers.

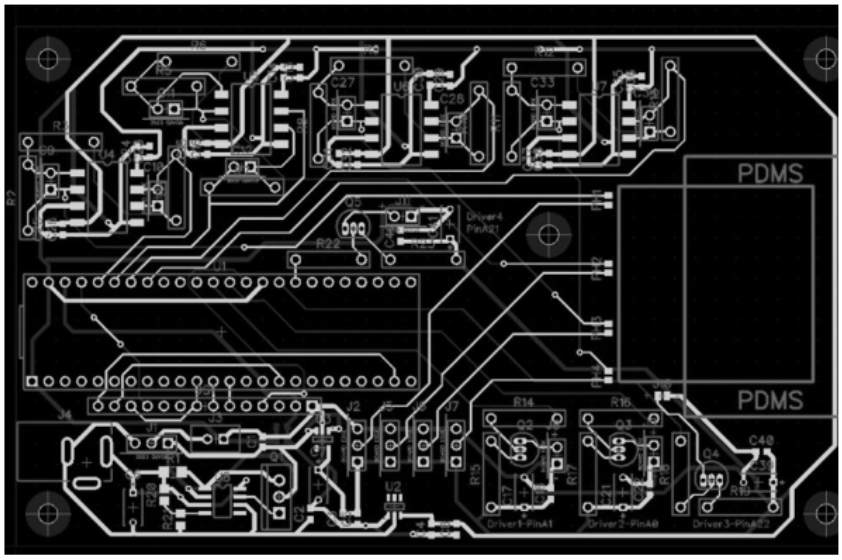

Figure 15.1: PCB layout custom designed to house 4 amplification circuits, Teensy 3.6 microcontroller board, power management and 4 driving circuits. The custom PCB was ordered from Eurocircuits.

The amplification circuit consists of a transimpedance amplifier in series with an inverting operational amplifier, both implemented with the same integrated circuit (LMC6842IN, Texas Instruments) with a total transimpedance gain between 200 dB and 260 dB(V/A) depending on the application. These amplifiers are supplied with a symmetric power supply of +/- 3.3V.

The power is supplied by two 3.7 V batteries (MIKROE-2759, Mikroe) and the voltage is regulated by two low drop-out (LDO) voltage regulators, one for +3.3V (755-BU33SD5WG-TR, Rohm Semiconductor) the other for -3.3 V (865-XC6902N331PR-G, Torex), as depicted in Figure 15.2.

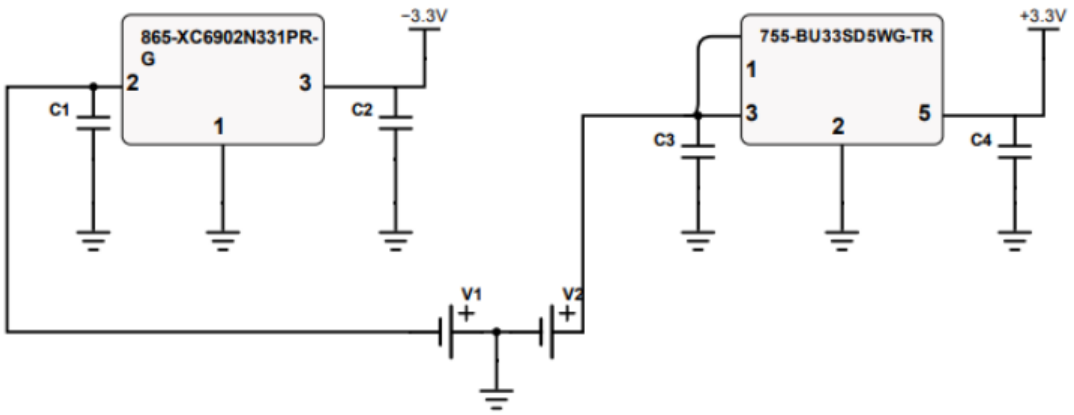

Figure 15.2: Voltage regulators used to provide symmetric voltage to the system. C1=C2=C3=C4= 1 μF in order to stabilize the system. The pinout of the negative voltage regulator (left) are: 1- ground, 2- Vin, 3- Vout, while on the positive voltage regulator the pinout is: 1- Vin, 2- Ground, 3- , 5- Vout . The ground of the system is considered to be the central point of the batteries connected in series.

The battery charging is controlled by a linear charge management controller (MCP73811/2, Microchip), shown in Figure 15.3.

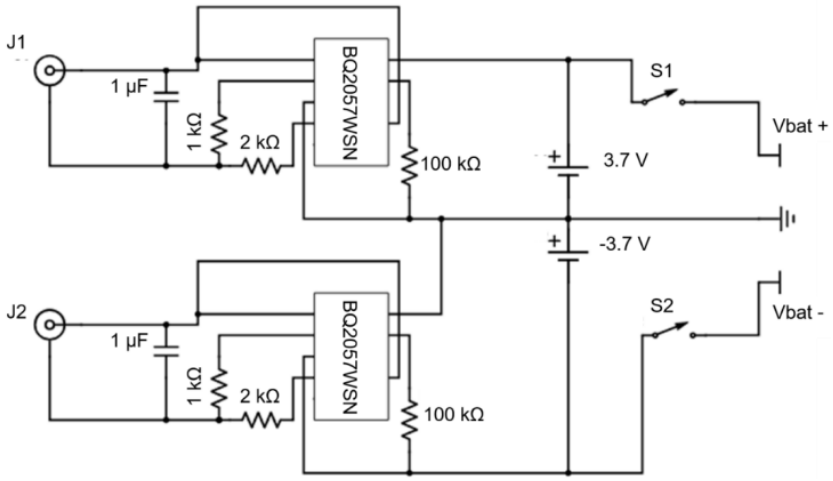

Figure 15.3: Battery charging circuit. Batteries are charged individually using a 9 V power supply using the individual jacks (J1 and J2). The normal charge current is 500 mA while the pre charge is 100 mA. The temperature sensing has been disabled by including the 100 kΩ resistors.

The high-side drivers which power the pumping system and LED for the light transmission measurements are composed of NPN transistors (512-2N5550TAR) in series with both the device to be actuated and a resistor for current limiting. The pumping system is comprised of a homemade peristaltic pump, actuated by a small DC motor. The LED used for the transmittance measurements is a blue LED (LTL17KTBS3KS-032A, LITEON). The emission spectrum of the LED is shown in Figure 15.4.

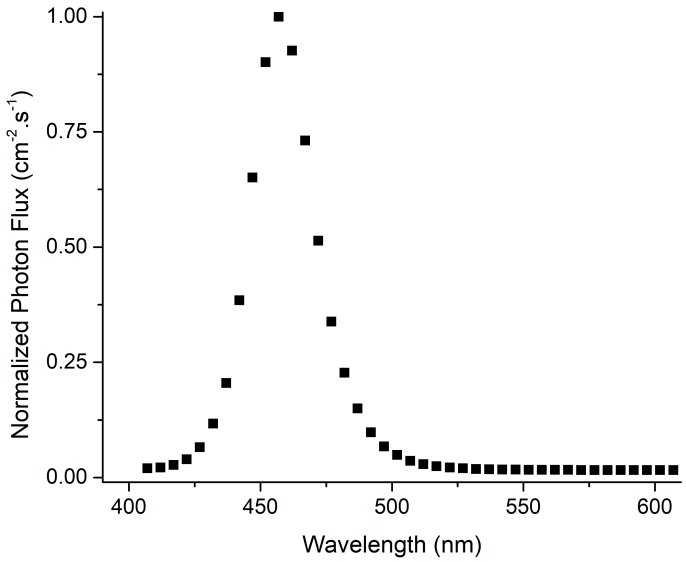

Figure 15.4: Normalized emission spectrum of the LED used in the portable setup.

15.2.2 Electronic Characterization

The transfer curves of the 2-stage transimpedance amplifiers was done by applying known currents (measured with a Keithley 237 picoammeter) while measuring the output voltage with a voltmeter (Agilent 34411A digital multimeter). This was performed within a grounded, metallic cage. The amplifier linearity and dynamic range were characterized for different gains, by changing the feedback resistors. The pumping system was also characterized by measuring the flow rate through a straight microfluidic channel with a height of 100 μm a width of 700 μm and length of 1 cm, packed with silica beads used in the bioassay.

15.2.3 AzA Detection Assay

Grape samples were centrifuged for 5 min at 10000 rpm and the supernatant was retrieved and diluted in Milli-Q water at a 1:100 dilution rate. A stock solution containing 2 mM of tyrosine and 100 mM of MBTH (3-Methyl-2-benzothiazolinone hydrazone hydrochloride) was prepared in DI water, acting as the substrate solution of the enzyme tyrosinase. All reagents were acquired from Sigma-Aldrich. The microfluidic chip was packed with the microbeads in each chamber as described in previous work. [381] The first chamber is packed with amine-functionalized beads, while the second one is packed with tyrosinase functionalized beads. Both the sample and the substrate solutions were injected at a flow rate of 1 μL/min for 10 min, while the transmission using the light from the Blue LED is acquired in real time.

15.3 Results and Discussion

15.3.1 Prototype Design

The design of the prototype presented in this portion of the work had to take into consideration the choice of various components including: amplification circuits for the photodiode signal, pumping system for fluidic handling, light source for transmission measurements, a microcontroller for data treatment and a screen for user interface, an internal storage for data acquisition and a portable power supply. Several iterations were produced until the final version.

Version 1

The initial version of the prototype consisted of an instrumented Ferrero Rocher box. This allowed for the inclusion of the LED used as a light source as well as the photosensors and access holes to connect the necessary tubing for the microfluidic assay. Figure 15.5 shows the initial version of the system.

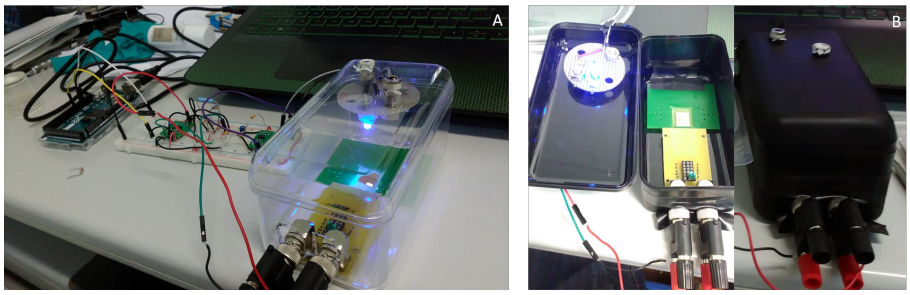

Figure 15.5: (A) Plastic box and circuit setup for the acquisition of the signals (B) which was then painted black to avoid stray light from the outside.

This prototype set the foundation for the amplification circuit needed as well as part of the programming for the microcontroller used. However all of the electronics were outside the box itself.

Version 2

The next version of the prototype allowed for the inclusion of the necessary electronics into the same enclosure as the sensor as seen in Figure 15.6.

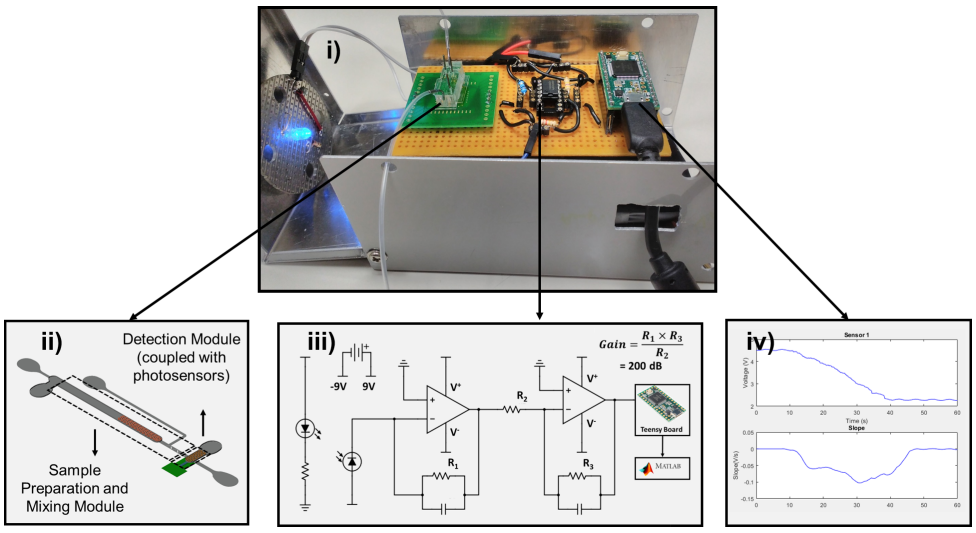

Figure 15.6: – Layout of the early version of the portable system (i), comprised of the microfluidic structure coupled with the a-Si:H photosensors (ii); amplification circuit (iii); and the Teensy board for signal acquisition and further processing (iv). The whole system is powered by a battery pack (not visible in the photograph). The complete prototype will include integrated pumping and a display for autonomous operation at the point-of-need.

This version of the prototype is close to being portable, with the electronics being powered by a battery pack, however data is still received through an USB cable connected to a computer for real time acquisition.

At this point I was fairly happy with the electronics and was ready to design the final version of the device.

Final Version

The prototype enclosure blocks out ambient light, as our applications are light-sensitive. The custom built PCB features four main sections: the sensor placement area, the signal amplification area, the pump and light source driver region and the power management section. One important aspect to note is that the whole system could have a smaller footprint at the cost of versatility. This could be achieved by using surface-mount devices (SMD) instead of through-hole components. The use of large, hand-replaceable resistors and capacitors (mounted on headers) allows to quickly adjust the gain (and time-constant) of the amplifiers and current in the drivers without re-soldering components, so that the circuit is quickly adapted for different applications.

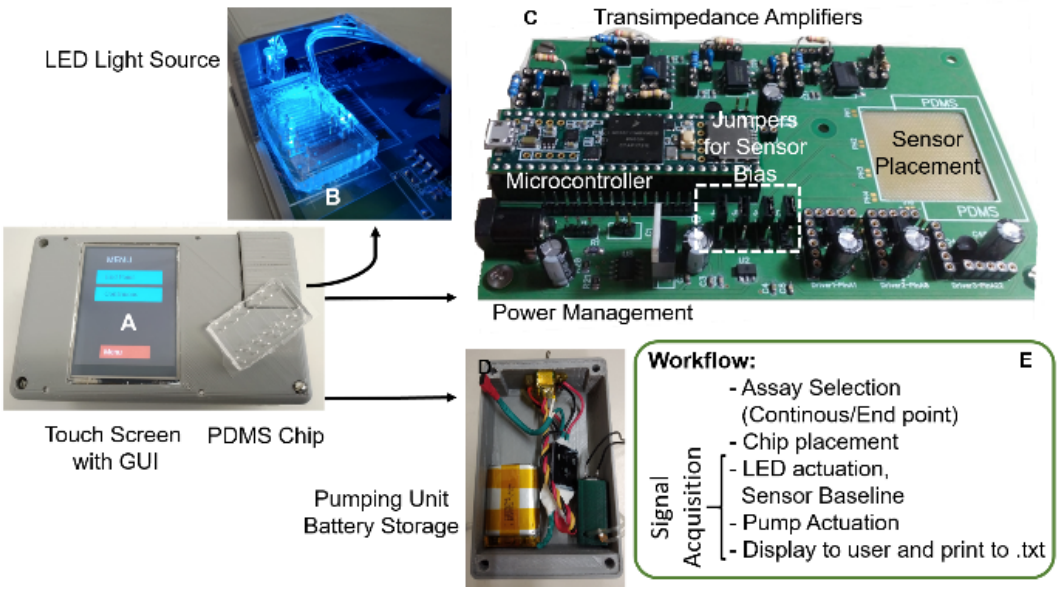

Figure 15.7: Prototype system composition. On the outside of the box a touch screen is available for user interaction (A), and on the upper right corner is a lid which allows for the placement of the microfluidic device in the sensing region ready for the transmission measurement (B). The prototype is comprised by a 14 x 8 cm, custom made, PCB which holds the necessary components for light and pump actuation, signal acquisition and amplification as well as data treatment (C). Underneath the PCB are located the batteries which power the entire circuit as well as the peristaltic pump for fluidic handling (D). The workflow of the prototype starts with the selection of the type of assay and placement of the microfluidic device. Then the system will acquire a baseline of light intensity for transmission calculation and initiate the assay (E).

The sensor area is comprised of a 3 cm x 3 cm pocket with a depth of 700 μm (the thickness of the photodiode substrate). The photosensors are fabricated with metal pads for wire bonding to the metallic pads of the PCB for addressing. Depending on the type of sensor being used, one might want it to be grounded, such as the thin-film photodiodes used in this work, or to apply a bias voltage (when using photoresistors, for example). With this in mind, one of the sensor pads is connected to a jumper which allows the easy interchange between these two modes of operation (3.3 V bias or 0 V bias). The other pad is connected to the amplification circuit. The prototype at present is designed to be able to address 4 sensors simultaneously.

The point-of-need device demonstrated in this work operates based on the measurement of a change

in transmission. Because of this, it is necessary to choose the appropriate light sources for assay quantification as well as drivers to power multiple light sources. This driver circuit can also be used to for pumping control for the liquid handling and, if needed, to power a heating element to maintain the temperature of the assay. In a typical measurement, the PDMS microfluidic chip is placed in the sensing region and connected to the pumping unit using a small tube. Then the sample to be measured and the substrate solution are coupled to the microfluidic chip through pipette tips. The assay is chosen and the system then initiates the pumping of the sample through the microfluidic chip. The results are displayed on the screen in real time in the case of a continuous assay or at the end of the experiment in the case of an end point measurement. The full code for the graphical user interface and operation setup will be provided in the Supplementary Information.

15.3.2 Photosensor Characterization

In this work, the sensors of choice are based on thin-film a-Si:H which will be used as the optical transducer, converting the incident light into an electrical current. The first step is to characterize the sensors to be used and subsequently the light source of the experiment. These results are presented in Figure 15.8.

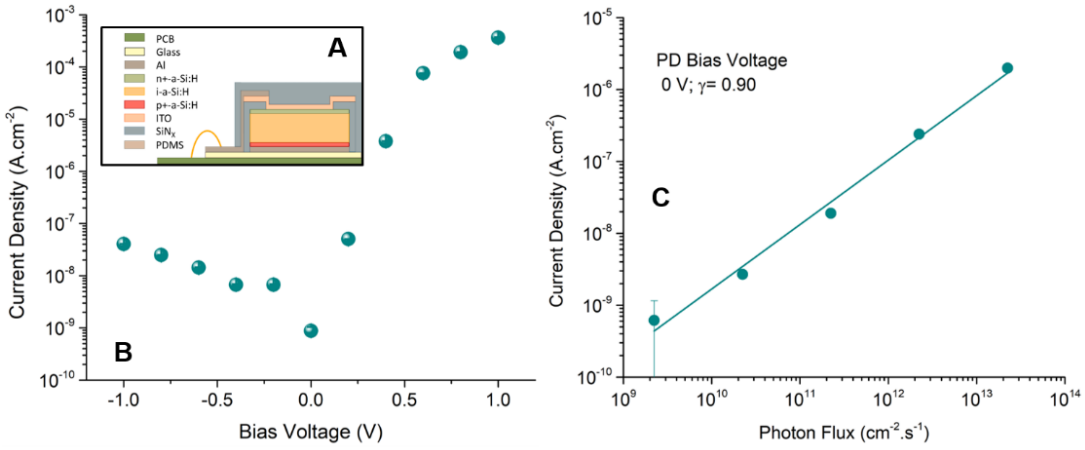

Figure 15.8: Device structure and characterization of the photodiodes used. A cross section of the material stacks that comprise the device is presented, although thicknesses are not to scale (A). The dark I-V curve (B) represents the rectifying nature of the photodiode, while the photoresponse curve at λ=480 nm (C) shows the dynamic range of detectable light as well as current output of these devices.

The photosensors used in this work have a 200 x 200 μm^2 aperture area and are used with a 0 V voltage bias (Photovoltaic mode). As can be seen in Figure 15.8-B, by using a null voltage bias the dark current is minimized, while also presenting a linear relation between the output current and the incident photon flux, given by the slope (γ) of the curve, as can be seen in Figure 15.8-C. Assays involving very low light levels, such as fluorescence or chemiluminescence, require minimal dark current to increase sensitivity. Our assay measures light transmission, which has relatively high light signal levels, but the linearity of the signal with light level is very important for sensitivity to small changes in transmission.

15.3.3 Signal Amplification

By taking the current density of the sensors and the aperture area, one can calculate the range of currents that will be produced in both low and high light level measurements and design an appropriate amplification circuit. For these sensors the output current will range between 10^{-13} and 10^{-9} A.

With such low-level signals, it is easy to suffer the effects of electrical noise induced by other equipment or by the power line (50 Hz or 60 Hz). The time constant of the RC filter created by placing a capacitor in parallel with the feedback resistance, should be long enough to average the powerline cycle or multiples of it. Because the photodiode signal is essentially DC and evolving slowly over time (over tens of seconds), the bandwidth of the system can be kept low.

The Texas Instruments LMC6482 OpAmps were chosen due to their low input current (20 fA). Because two inverting stages were mounted in series, a symmetric power supply was used. Both amplification stages of the LMC6482 were set up as inverting amplifiers as shown in Figure 15.9-A.

By powering the OpAmp with a symmetrical power supply of 3.3 V the output voltage will be capped at this value, as seen in Figure 15.9-B. The presence of the capacitors in parallel with both R1 and R3 will act as filter to reduce the noise of the system. Since the signal a DC current, it is possible to eliminate the other frequencies that would impact the measurement. The resulting time constant, τ, is calculated as 4.6x10^{-3} s (cut-off frequency of 35 Hz).

Figure 15.9-B shows that this setup can measure currents down to 10^{-13} A. This capability demonstrates the diversity of applications and ranges that can be used with this type of setup by simply changing a couple of resistors in the system.

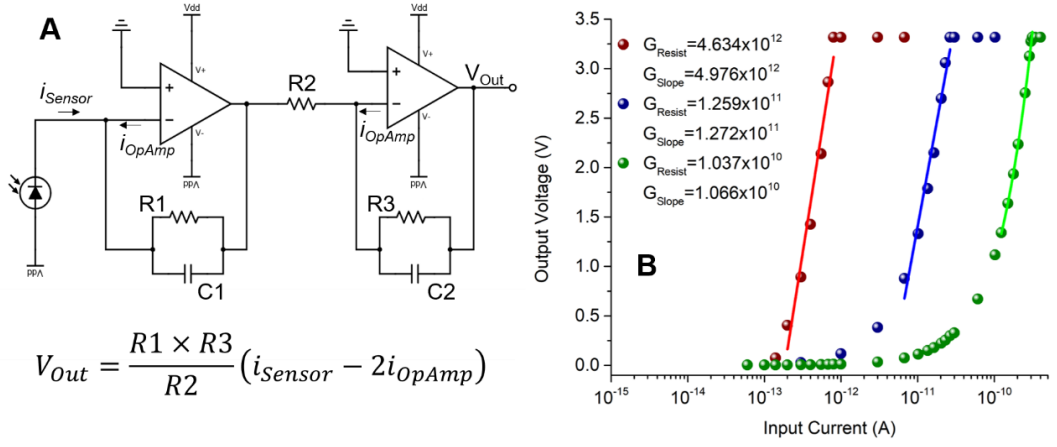

Figure 15.9: Double step amplification circuit used (A). The resulting transimpedance gains is dependent on the feedback resistances used (R1 and R3) as well as the connecting resistance (R2) between stages. Transfer curves obtained using 3 different gains: 4.6x10^{12} (253 dB), 1.3x10^{11} (222 dB) and 1.1x10^{10} (200 dB), the experimental gain obtained by measuring the slope of the linear response region of the transfer curve is identical to the expected gain based off the resistors chosen for the setup (B).

15.3.4 Light Source and Pump Characterization

To perform the bioassay, a light source for the transmission based measurement and a pumping system for fluidic handling are required. To control these components, drivers are necessary.

The photon flux of the LED and the flowrate of the pump were characterized as a function of the driving voltage and current as shown in Figure 15.10. For the assay, the necessary photon flux is approximately 10^{14} cm^{-2}.s^{-1} (corresponding to 2 V and 725 μA to actuate the LED), while the required flow rate is 2 μL.min^{-1} (corresponding to 0.3 V and 40 mA to actuate the pump).

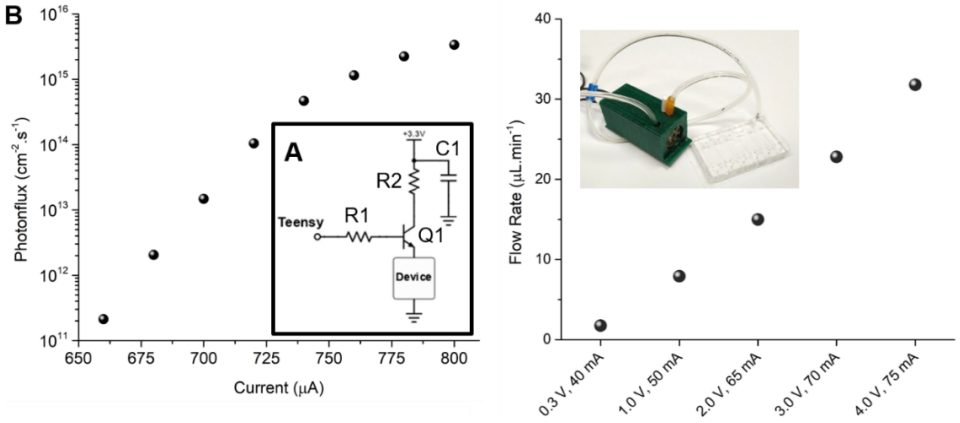

Figure 15.10: Electronic circuit used to control both the pump and the LED (A). Photon flux characterization of the chosen LED as a function of the applied current (left) and pump flow rate as a function of the applied power (right) (B). The green casing was 3D printed to house the peristaltic pump, which can then connect to the microfluidic chip as shown in the inset photograph.

The driver transistors were chosen according to the range of currents required to actuate the pumping system and light source necessary for the assay. The schematic for the driving system is presented in Figure 15.10-A. A simple high-side driver was implemented with a NPN transistor (Q1) and two current-limiting resistors (R1 and R2). The transistor chosen was the 2N5550 (Fairchild) given that the TO-92 package is easy to replace and it provides an adequate maximum collector current of 600 mA. In this application, the highest current drawn is 40 mA (by the pump). The control of the driver is provided by the Teensy MCU through a DAC output, which is fed to the transistor base. A decoupling capacitor (C1) is used to avoid sudden voltage drops in the positive rail (3.3 V) in case of high current demands (as in the case of the pump motor starting). An n-channel MOSFET can be used instead, with the advantage of a lower voltage drop across the transistor (especially if higher currents are required).

15.3.5 Biological Assay

To demonstrate its utility, we applied the prototype system to perform an enzymatic assay for the detection of Azelaic Acid (AzA), a biomarker for the early detection of fungal infection in Trincadeira grapes by the common pathogen B. cinerea. AzA is a signaling molecule which plays an active role in the plant immune response called systemic acquired resistance and will be upregulated in presence of a pathogen. The biological assay used for the detection of Azelaic acid (AzA) has been previously reported. [381] but in this section of the work, the full point-of-need detection is demonstrated.

The enzyme tyrosinase, which can convert molecules such as tyrosine into colored pigments through oxidative coupling, is used for the enzymatic assay. Since AzA is a competitive inhibitor for the enzyme, it is possible to determine the amount of AzA in the sample by measuring the transmission of λ= 480 nm light, the wavelength of absorption of the color pigments produced by the enzymatic reaction. In this competitive assay, the quantity of AzA in the sample is proportional to the level of measured transmission. In order to perform this assay, a microfluidic device as shown in Figure 15.11 is used.

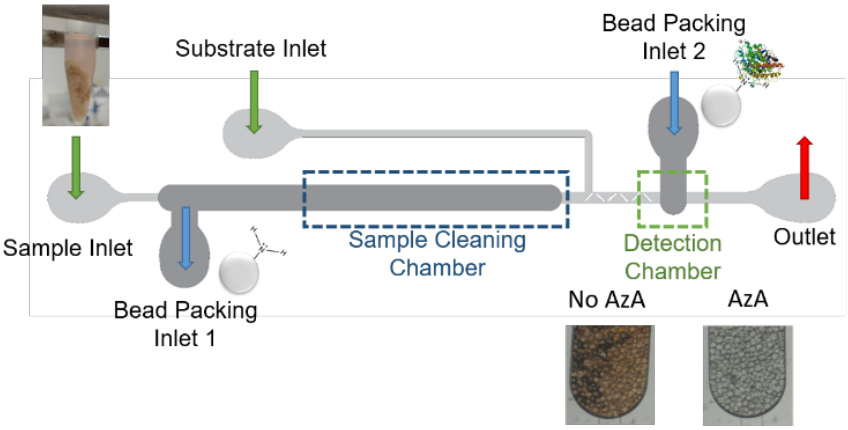

Figure 15.11: Representation of the microfluidic device used for the detection of AzA. The blue arrows depict the inlets used to pack the microchannels with the appropriate microbeads for both sample cleaning (1) and AzA detection (2). After packing, these inlets are sealed off. Then the grapes are macerated, centrifuged and the resulting supernatant is then diluted 1:50 and placed in the sample inlet with the help of a pipette, while a second pipette containing the necessary substrate is placed in the second inlet (green arrows). Both liquids are pulled by applying a negative pressure at the outlet using the pump (red arrow), with the sample going through the sample cleaning chamber to remove phenols, reaching a passive mixer at the same moment before entering the detection chamber. Here depending on the amount of AzA in the sample a colored pigment will be produced and captured by the beads, which can be quantified through transmittance measurements at λ= 480 nm. The dark areas have a height of 100 μm while the lighter areas have 20 μm in height.

To begin the assay, the PDMS chip is placed in the system and the Teensy MCU will perform a baseline check of the photosensor by actuating the LED and acquiring the initial signal. Then the pump is actuated in order to pull both the sample and substrate solutions into the microfluidic chip. Once the sample enters the system, it will encounter silica microbeads functionalized with a primary amine which will help remove the phenolic content of the grape juice which would otherwise interfere with the detection of AzA. Then, the clarified sample is mixed with a substrate solution consisting of a mixture of tyrosine and MBTH, and proceeds to flow to the detection chamber where the transmission is measured. The LED will be actuated during the entirety of the assay, while the photosensor signal measuring the light transmission is displayed on the screen to the user.

As a proof of concept we performed the detection of AzA in both healthy and infected grapes at the EL 35 maturation point, with the results presented in Figure 15.12.

By analyzing the results presented in Figure 15.12 it is possible to distinguish between both healthy and infected samples using both the laboratory benchtop setup as well as the portable prototype. Due to the presence of the pathogen, the infected samples will have produced higher levels of AzA to try to combat the infection, which is reflected here in higher levels of transmittance. This is due to the AzA

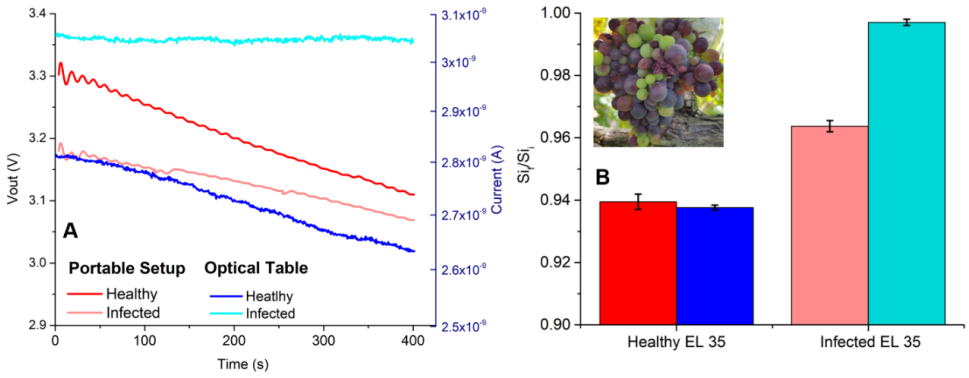

Figure 15.12: Real time acquisition of the assay output, the blue lines are the results obtained with the laboratory optical setup (to be read on the right axis), while the red and pink curves are obtained from the portable setup (voltage on the left axis) (A). A bar chart showing the value of the ratio of the averaging the last 30 s of each measurement (Sif) to the average of the initial 30 s (Sii) for healthy and infected grape at the EL35 maturation level (B). The photograph depicts the maturation stage at which these samples were tested.

being a competitive inhibitor for the enzymatic reaction, thus producing less of the colored compound. It is expected that the healthy samples will also have some basal level of AzA, as it also serves other functions in the plant metabolism.

There is also the issue of slightly different levels of initial voltage output, this is due to inconsistencies in the packing of the beads in the microchannel, however these are not significant for the output of the assay. Despite the differences in signal ratios obtained for the infected sample, it is still possible to distinguish a healthy sample from an infected one. With this result, we demonstrate the possibility of making a truly portable system capable of detecting infections in plants at the point of need.

15.4 Conclusions

This chapter demonstrated the feasibility of making a simple, versatile and user friendly portable read-out system for microfluidic devices to be used at the point-of-need. As a proof of concept, the prototype was used for the detection of Azelaic Acid, a plant health biomarker.

By including 4 driving and 4 amplification circuits one can perform multiplexed analysis as well as include functions such as heating or cooling and pumping of liquids in the microfluidic device.

The system works by optical transduction of a transmission measurement using thin-film amorphous silicon photodiodes and demonstrated the feasibility in reading out currents as low as 10^{-13} A in a portable setup. The prototype is designed to allow for the sensor read-out to be adapted to both high and low light levels by changing a few, easy to replace, resistors in the system. The system also allows the control of an LED light source as well as a peristaltic pump for liquid handling inside the channel.

As a proof of concept the prototype was applied to bioassay for the portable detection of fungal infections in plants. The results produced by the portable prototype was shown to be similar to those obtained using a laboratory bench setup, confirming the potential of the prototype.

Chapter 16

Final Remarks - A Truly Portable Microfluidic System for the Multiplexed Detection of Plant Health

This portion of the doctoral thesis was the main focus of my work during my years at INESC-MN and it was the one that required the largest skill set to accomplish.

I demonstrated the development of three different biosensing assays, which have three very different working mechanisms, the necessary sample integration and multiplexed detection in a single microfluidic chip.

In addition to that, a portable platform for the microfluidic chip was developed with this multiplexed measurement in mind, however was only demonstrated for the single assay of AzA detection. The primary reason for this, was the miss judgment in regards to the JA detection assay, as I didn't think I would need a laser for the excitation of the fluorophore, hence the system was designed only with LEDs in mind.

As for future work, I would enjoy having access to a wider panel of samples to test both in terms of plant variety as well as infections in order to consolidate the registered metabolite patterns.

Given more time, also the portable system could be redesigned with all the assays in mind, allowing for a portable system capable of detecting all the metabolites. Another add-onto the portable device would be the microfluidic chip insertion and automatic sample insertion. We would need to work on a user friendly method for the farmer to extract the sample, dilute it and then insert the sample into the system.

I think that, although a far cry from a perfect system, significant advances were made in terms of a portable system for precision agriculture.

Part V

Microfluidic Applications for Colorectal Cancer Research

Highlights

- Multiple cell lines, both primary and immortalized, were successfully cultured in different types of microfluidic chips
- A microfluidic chip for the screening of antibody fragments through a phage display-like approach was successfully developed
- A module for the assessment of cell viability through the detection of Adenylate Kinase was developed
- An ex vivo model, based on co-culture of two primary cell lines, for combinatorial treatment screening was developed

Roles and Colaborations

- In this portion of the work, I was mainly in charge of the microfluidic chip development as well as setting the initial protocols for cell culture. In addition to this, I developed in tandem with Pedro Monteiro the image analysis scripts required for data processing as well as experimental design and performed all calculations regarding phage kinetics. I also developed the biosensing assay for the detection of AK. All experiments concerning the nanovaccince therapy were done in tandme by myself and Dr. Ana Matos.
- **Pedro Monteiro, MSc.** was responsible for optimizing all experimental conditions regarding the cell culture and phage display experiments. He was also the front man in the development of the multi cell culture chip and heavily involved in the experimental design and execution of all three approaches.
- **Dr. Ana I. Matos** was responsible for maintaining the biological material necessary for the nanovaccine experiments, as well as the experimental design and execution. In addition to this, the nanovaccines used and animal treatment and sacrifice was all executed by her.
- **Pedro Fontes, MSc.** was responsible for producing the necessary phages for the phage display experiments as well as maintaining the biological materials and experiment execution.
- **Vanda Marques, MSc. and Dr. Marta B. Afonso** were responsible for maintaining the biological materials and experiment execution in terms of the drug screening chip. They were also responsible for experimental planning in this regard and execution of benchmark assays.

Scientific Output

MSc. Thesis Supervised

- Ricardo Serrão, *Monitoring cell cultures in real time in a biochip*, 2019
- Benjamin Heidt, *Multielectrode array integration into microfluidic systems for rapid screening of excitable cells*, 2017

Publications

- Matos, Ana I. et al. *"A microfluidic device for the screening of anti-cancer immune therapeutic strategies: a proof of concept comparison to in vivo"*, to be submitted
- Condelipes, Pedro, et al. *"Development and Characterization of a Microfluidic Phage Display Platform for Colorectal Cancer Treatment."*, to be Submitted.

Conference Presentations - Poster

- *"Development of a Microfluidic Platform for Targeted Phage Selection: in Pursuit of Personalized Colorectal Cancer Treatments"*, 23rd International Conference on Miniaturized Systems for Chemistry and Life Sciences (MicroTAS), Basel, Switzerland, 2019

Chapter 17

Colorectal Cancer and Microfluidics

Cancer is among the leading causes of death worldwide. In 2019, it was estimated that there were 1.76M new cases and around 600k deaths in the USA alone. [392] While such increased burden largely results from an adoption of unhealthy lifestyles related to economic development, including smoking, unbalanced diet, and physical inactivity, it is exacerbated by demographic changes of a growing and aging population. Chemotherapy, based on a combination of anticancer drugs to target rapidly dividing cells or pathways that control normal cell growth and malignant transformation, are used as front line treatment. Nevertheless, anticancer drugs often lead to acute systemic toxicity due to poor selectivity between normal and malignant cells, and to a high minimum effective dose required for any therapeutic benefit.

Colorectal cancer (CRC) specifically is among the third most common cancer type in the world, representing 6% of all cancer diagnosis and the fourth most lethal. [393, 394]

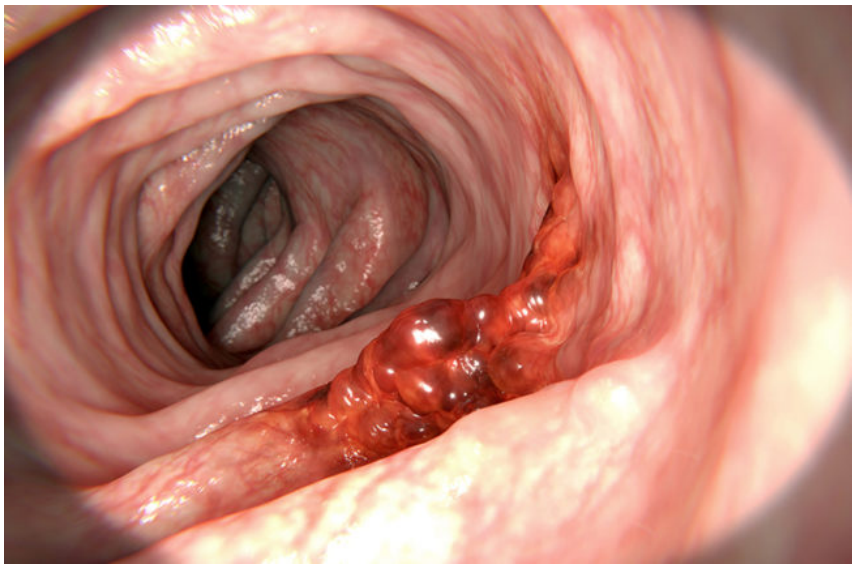

Figure 17.1: CRC tumor found during a colonoscopy. [395]

Significant advances in medical science has led the reduction of the CRC incidence rate in older populations. However, there is a high demand for the development of alternative and effective therapeutic

options to overcome advanced metastatic CRC (mCRC), while preventing disease recurrence.

CRC, also referred as bowel cancer, occurs when abnormal cells grow in the colon or rectum. [396] Approximately 96% of CRC are adenocarcinomas that result from the growth of precancerous polyps or adenomas, in the colon wall and rectum. [397] Among those, 10% tend to advance to be cancers. [398, 399] Once in place, those malignant cells can spread into the colorectum wall and invade blood or lymph vessels, leading to the spreading to other far away tissues, otherwise known as metastases.

In Portugal, there has been a large effort to tackle this issue through the POINT4PAC project. "The goal of POINT4PAC - PRECISION ONCOLOGY BY INNOVATIVE THERAPIES AND TECHNOLOGIES - is to build a platform for discovery and early-accelerated development of innovative technologies, therapies, and solutions for precise treatment, prevention and control of cancer. This will impact on health, society and economy at regional, national and international level, leading to advanced training, jobs and value creation in Portugal." - Taken from the POINT4PAC project description

Initially, this project was not predicted to play a role in my thesis, however after participating in the initial experiments, my interest and fondness for the project grew. This led me to take a very active role, namely in work package 8 of the project, led by Professors João Pedro Conde and João Gonçalves (FFUL), as well as creating a bridge to work package 10, led by Professor Helena Florindo (FFUL), through the collaboration with Dr. Ana Matos, which will be explored in Chapter 20.

17.1 Immunotherapies and phage display

Immunotherapies are therapeutic strategies where the patient's immune system is modulated in order to recognize and attack the cause of disease. There are two main approaches to this type of therapy, adoptive cell therapy, through the injection of T-cells that are capable of recognizing the antigen of choice, or through the injection of antibodies generated specifically for the antigen causing the disease. [400] Both strategies have been employed in the case of cancer treatment, from here on out, I will being focusing on the use of antibodies as the means of treatment. [401, 402]

Despite recent advances to these types of therapies, there is still a high rate of toxicity towards the patient. There is a wide variety of factors responsible for this toxicity, however it mainly stems from some cross recognition of healthy tissue by the therapeutic agents employed in these therapies. [403]

It is clear that one of the main challenges for immunotherapy strategies is to develop antibodies capable of recognizing cancerous tissue, without the cross reactivity to healthy tissue, as well as not triggering an immune response against the treatment. [404] Phage display technology may have an answer to this challenge.

Phage display technology relies on the capabilities of creating random genetic sequences through recombinant DNA strategies, creating a random assortment of phages with slight different genetic compositions. These differences are than *displayed* by the virus during the replication process as peptide sequences. [405] By creating random sequences of peptides, it is possible to create peptide sequences capable of recognizing cell membrane proteins that are selected through what is called cell panning. [406] These can than be retrieved and sequenced to produce artificial antibodies, which can than be

used in immunotherapy.

Despite the tedious and arduous processe involved in phage display technology, there are several reports concerning positive cases of peptide sequences that were than tested as potential CRC treatment. [407, 408] However several of the generated antibodies also present an affinity to the healthy tissue in that region, increasing the need for more stringent control assays. [409]

17.2 Drug development in cancer research

The pharmaceutical industry is facing increasing difficulties in new drug development, where the revenue generated with drug sales are not being able to cover the cost of development, leading to increases in the cost of treatment, which in turn limit its availability to the public.

The drugs that I am referring to are those that bring significant clinical advantages over drugs that are already available, in 2015 it was estimated that only 10% of drug candidates reach the market with an average development time of 13.5 years. [410] In some therapeutic classes this number of successful candidates can be as low as 3%, such as in the case of cardiovascular disease. [411] This low number of drugs reaching the market is in no small part due to the very low success rate during the screening of potential drug candidates. Compound libraries as large as 2 million molecules [412] are used in the initial screening studies to yield around 10's to 100's of candidates for clinical trials, which in turn, also have extremely low success rates. Taking the case of Alzheimer's Disease, between 2002 and 2012 there have been 413 clinical trials distributed between phases 1 to 3, however no new drug has been accepted since memantine in 2003! [413]

Methods currently employed for initial drug screening, typically, follow two types of avenue of thought. The first one relies on phenotypic screening assays, where the impact of the potential drug candidate on the cells that cause the disease, may these be bacteria or cancer tissue as examples, is observed. [414–416] The limitations of this approach will be better explored in the following section. The second approach, target-based drug discovery, relies on targeting specific pathways or proteins to inhibit their activity, however this requires a deep understanding of the mechanisms of the disease, which is not always possible. [417, 418] These methods ofter use *in silico* molecule design to play a very specific role to inhibit the disease causing agent. [419, 420] Both these methods are very specific and directed at the harmful tissue/pathogen, but rarely take into account the impact that the treatment will have on the remaining healthy tissue.

As for cancer treatments specifically, both these pathways are followed, however, there is a disproportional amount of drugs discovered through target-based approaches vs phenotypic approaches. [421] Although several drugs have been approved for treatment, they are never used alone, often combined with surgery or radiation therapy, and a large portion of the chemotherapy strategies takes an heavy toll on the patient leading to a grulling and painful therapy. [422, 423] This is due to the drugs used being extremely hazardous to healthy tissue, however are often the only approach for metastatic patients. [424, 425]

The urge for more efficient drug screening strategies is evident, in order to progress to more effective

treatments, cost-efficient methods of molecule screening must be developed, that take into consideration the impact on the harmful tissue or pathogen, but also on the remaining organs and tissues of the human body.

17.3 Limitations of biological models in cancer research

In the previous section, I made note of how the inefficiency of drug development is highly related to the biological model used to conduct the study. There are three groups of models, that can be classified in terms of there origin.

In vivo models rely on the use of animals to conduct the experimentation needed, with the prime animal candidate being the mouse, in the case of cancer research. This is not only due to its low economical burden, but also the successful comparison of drug effects to the human condition. [426] These models can be achieved through several methods: i) **ectopic xenografts**, where tumor derived cell lines are, for example, subcutaneously implanted into the animal; ii) **orthotopic models**, where the tumor derived cell lines are implanted into the respective organ; iii) **transgenic models**, where where the expression patterns of specific ocogenes are regulated; iv) **primary human tumorgrafts**, where primary cells from a human tumor are used; v) **carcinogen-induced models**, where known carcinogenic molecules are used to induce a tumor in the test subject. [427] *In vivo* models, despite being the most accepted model have severe limitations due to several reasons. One is the fact that, at the end of the day a mouse is not a human, there are metabolic differences between us and them, which may lead to poor treatment results once the jump to clinical trial is made. Another issue is the use of derived cell lines to induce the disease in the test subject, these cell lines present differences when compared to primary cells from patients. These models also present the highest cost and the highest ethical concerns as thousands of animals are slaughtered throughout the world. [428]

An alternative approach to th use of *in vivo* is the use of *in vitro* models. There models are defined as the use of biological material, typically immortalized cell lines, in man made vessels such as well plates and T-flasks. These systems can be further divided into two groups: i) **2D cell cultures**, where the cancer cell line is grown as a monolayer of cells; ii) **3D cell cultures**, where the cells have some degree of differentiation and are typically grown in what arecalled tumor spheroids. [429–431] The limitations of 2D cell culture models, in comparison to their 3D counterparts, stems from the fact that tumors located inside patients are three dimensional structures with numerous cell-cell interactions that a 2D culture is not able to mimic. [432] In addition to this, the 2D models fail to replicate the mass transport difficulties presented by the 3D models, as well as the actual culture conditions, such as the state of hypoxia registered inside the tumor itself. [433] In the case of 3D models, they present a better mimicry of a real tumor, however they still pale in comparison to *in vivo* models. This is due to the fact that the cell lines used to create 3D models lack the same metabolic responses than tumor cells grown within an animal. In addition to this, it is still not possible to reproduce accurately, the tumor microenvironment in these cell cultures. The tumor microenvironment (which will be further discussed in Chapter 20) inhibits the effect of the therapeutic agents on the main tumor cells, hence the difference often registered between

animal models and 3D cell cultures. [434–436] There is however a third option.

Ex vivo models present an attempt to meld together the advantage of both *in vitro* and *in vivo* models. They tend to be cheap to create in comparison to *in vivo* models however include the tumor microenvironment intricacies. These models are created by extracting primary cells from a patient, for instances through a biopsy or surgery, and are cultivated in *in vitro* systems. These models suffer from the fact that primary cell lines are extremely difficult to maintain in culture for extended periods of time, thus, when using this approach, researchers need to maximize the throughput of their testing protocols, which can be long and labor intensive. [437–439] Ex vivo models do present an innate advantage that non of the other models present, which is the capability for personalized medicine, if the tumor is accessible via biopsy, it can be possible to screen a library of compounds directly on the patients' cells, hence improving the probability of success. [440–442]

I believe that by improving the quality and robustness of *ex vivo* models, for instances through organ on a chip technology, we can improve the quality of treatment for cancer patients worldwide.

17.4 Potential of microfluidics

Microfluidics technology presents an array of interesting characteristics, such as, low sample volumes, the optimal control over chemical and physical properties within the devices and the possibility of instrumentation; which may be useful in addressing the problem posed by the increased rate of cancer patients. Several groups around the world have been working on different microfluidic approaches to tackle cancer patient treatment and diagnosis.

A large number of groups have focused their attention to the development of microfluidic biosensing assays for the early diagnosis of cancer. This detection has been performed through the detection of exosomes in ovarian cancer patients, [443] the capture of circulating tumor cells from lung cancer patients [444] as well as free DNA released from these circulating tumor cells [445].

Another microfluidic approach to cancer treatment is the development of ex vivo models in microfluidic systems that allow for a better understanding of disease progression, such as the work developed by Yankaskas et al. to study metastasis potential [446] or the modelling of cancer development in organ-on-a-chip devices [447].

One area where I believe that the full potential of microfluidic technology can be employed is in therapy screening. [448–450] These devices take advantage of the capacity for parallelization presented by the microfluidic platforms, however often rely on very complex tubing and valve schemes. [363]

Chapter 18

Microfluidic Based Phage Display

18.1 Introduction

In this portion of the POINT4PAC project, we aim at the development of a microfluidic-based, phage display system in order to screen peptide sequences capable of binding to colorectal cancer cells, while by-passing healthy cells. The end goal of this approach, would be to be able to collect both tumor and healthy cells from a patient, grow them in sequential chambers and flow a library of phages with a random peptide sequence in the recognition zone. The positive hits, in other words those that bind to the tumor cells but not to the healthy tissue would then be retrieved and amplified. These positive hits could then be subjected to another round of selection or be used as vehicles for drug delivery.

The initial part of this project was the design and optimization of the growth conditions for the cancer cells, as well as, the flow conditions for phage capture in order to avoid losing possible candidates due to them flowing through the chip without interacting with the cells at all.

To do this, the cancer cell line HCT116 and a genetically engineered M13 bacteriophage were used as a model system. The modified M13 bacteriophage displayed a VHH-based, anti-CXCR4 antibody peptide sequence, which is specific for the CXCR4 chemokine receptor expressed at the cell membrane of the tumor cells. [451, 452]

18.2 Materials and Methods

18.2.1 Reagents

The cell culture used for the *E. coli* culture for phage production was prepared by adding 0.5 g of NaCl (Nzytech), 20 g of tryptone (Oxoid), 5 g of yeast extract (Oxoid), to 950 mL of deionized water. When all the solids are dissolved, 10 mL of a KCl solution (0.25 M) and the pH is corrected to 7 using a NaOH solution (5 M), deionized water is added to a final volume of 1 L. After sterilization through autoclaving, 5 mL of a sterile $MgCl_2$ solution (2 M) is added to the medium, as well as the antibiotics ampicillin (Nzytech), tetracycline (Sigma), kanamycin (Merck).

For the complete growth medium used for the HCT116 cell culture, McCoy's 5a medium was purchased from Gibco while the the fetal bovine serum used for supplementation was acquired from Biowest; the trypsin used for cell detachment was purchased from Gibco.

18.2.2 Phage production and labeling

The mutated phage production is done according to the protocol described by Levisson *et al.*. [453] The initial part of the process is the bacterial transformation with a commercial pComb3XSS phagemid that will express the anti-CXCR4 peptide sequence. This is done through electroporation, which will create pores in the cell wall of the ER2738 *E. coli* cells (New England Biolabs) used, allowing for the incorporation og the phagemid into the cells. The next step is to infect the bacterial cell culture with the VCSM13 helper phage. During the infection process, the M13 phages will insert there DNA into the transformed cells, which will than be replicated and translated into the necessary proteins to form new phages. During this time, the phagemid will also be translated to a fusion of the surface g3p protein, natural to the phage, and the anti-CXCR4 peptide. The resulting fusion protein will be incorporated into the newly produced phages, making them infectious towards cells expressing the CXCR4 receptor. Phage concentration is then assessed through phage titration and the phages are then labeled with the BODIPY-FL fluorophore according to the manufacturer indication.

18.2.3 HCT116 cell culture - T-flask

The HCT116 cell line was maintained in T-flask culture until required for the microfluidic experiments as described by the National Cancer Institute. [454] Briefly, the cells are first thawed by gently heating the freezer vial at 37 °C for 2-3 min, then 1 mL of the thawed cell suspension is added to 9 mL of pre-heated (37 °C) complete growth medium (McCoy's 5a medium +10 % (v/v) of fetal bovine serum (FBS)). After gentle resuspension, the cells are centrifuged at 125 G for 10 min and the supernatant is exchanged for another 10 mL of the complete growth medium. From here, the concentration of viable cells are assessed using a Neubauer chamber and diluted/concentrated to a cell density of 10^5 cells/mL which are then transferred to a 25 cm^2 T-flask. The flasks are kept in an incubator at 37 °C with a 5 % CO_2 atmosphere. Cells are then checked daily to assess the need for transferring to a new T-flask by visual inspection of the flask surface area coverage (confluence) and medium renewal through observation of the culture medium color, which changes from red to orange/yellow due to the presence of phenol red in the medium. When there is a need to extract the cells from the T-flask, the supernatant is removed and replaced with a Trypsin solution (0.25 mg/mL) for 10 minutes. Cells are then pipetted and trypsin is neutralized by adding equal volume of fresh complete medium to avoid cell clumping. The cell suspension is than centrifuged and fresh medium added in order to count the viable cell number and dilute/ concentrate the cells according to the desired application. An easy assessment for cell viability is checking their morphology, healthy cells should look as presented in Figure 18.1.

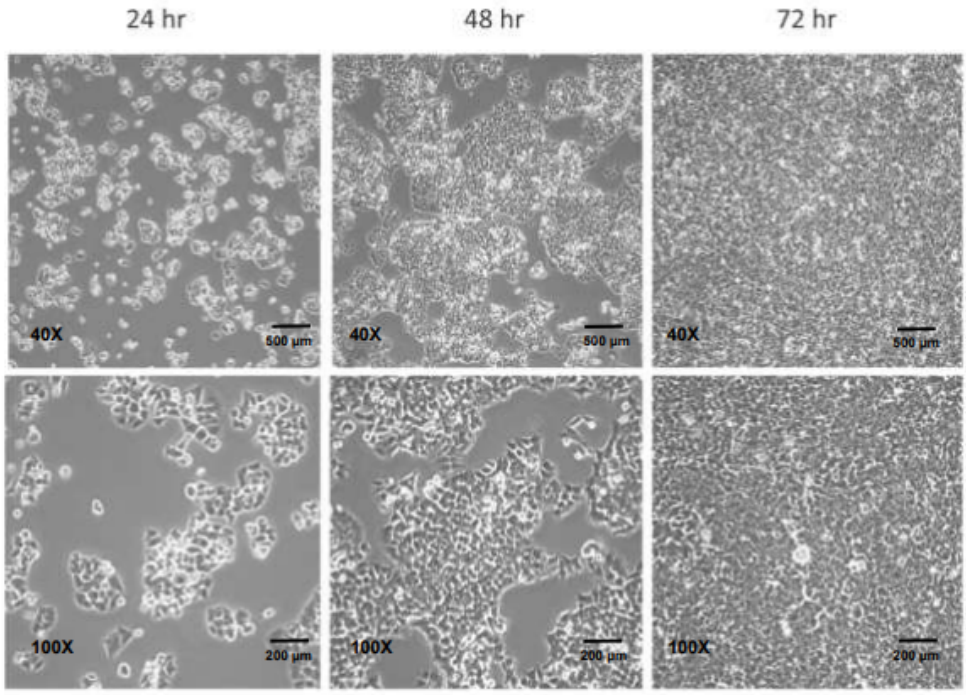

Figure 18.1: ”Healthy” morphology of the HCT116 cell line as presented by the manufacturer. Adapted from the SOP handbook. [454]

18.3 Results and Discussion

18.3.1 Microfluidic device design and experimental work flow

The design chosen for the microfluidic cell chip was a 1 cm x 1 cm PDMS-PS hybrid chip with a channel height of 20 μm. The design is presented in Figure 18.2-A. The cylindrical pillars presented in the device have a diameter of 100 μm and are placed in order to avoid the collapse of the structure under it's own weight. The height of 20 μm was chosen with the purpose of inhibiting the cell growth vertically. This was done in order to maintain a monolayer of cells to facilitate the modeling and capturing of the phages that were being injected into the microfluidic chip. The PDMS portion of the device was chemically sealed against PS-based 6 well plates to facilitate handling and incubator occupation. the device is comprised of two inlets, one lateral and one central, and a single lateral outlet. The central outlet is used for the cell seeding step in order to avoid potential clogging of the lateral inlet used for medium and phage injection.

As seen in Figure 18.2-B, the progression of the HCT116 cell growth undergoes different stages. Once the cells are inserted into the device, the cells are let to adhere to the base of the channel for 4 hours with no medium perfusion. In this time frame, some cells undergo some degree of morphology change as seen in the micrograph of Δt= 4 h of Figure 18.2-B. Incubation times of 2, 6 and 8 h were also tested, the 2 h incubation period was considered too short as most cells then were washed-out of the device and both the 6 h and 8 h incubation periods led to premature cell death. After the 4 h incubation period the culture medium is injected into the microfluidic device and the culture is monitored, as shown

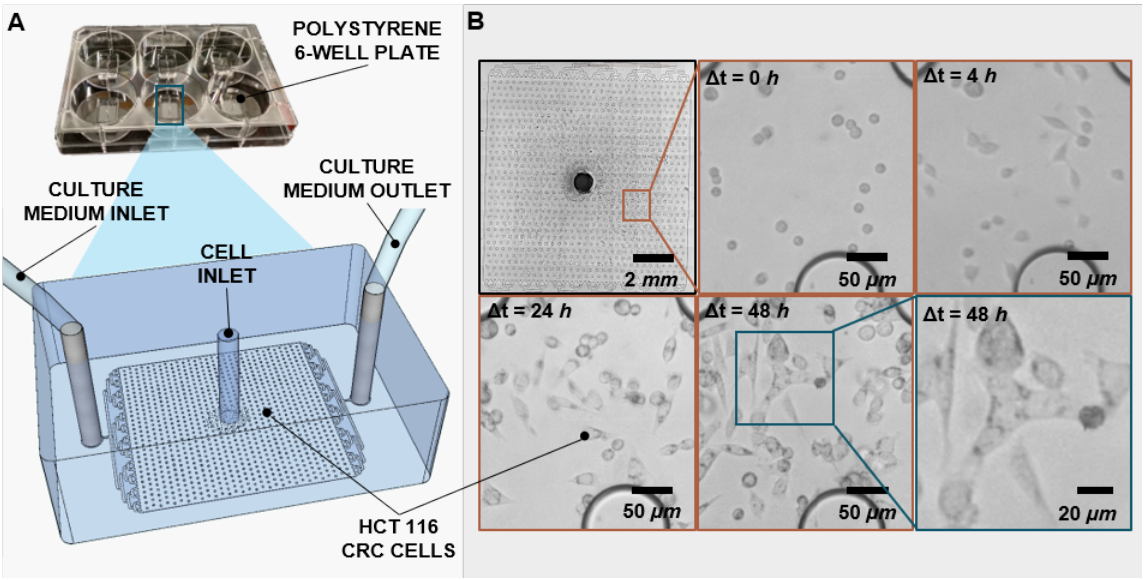

Figure 18.2: (A) Schematic representation of the microfluidic device used for the culturing of HCT116 cells. The device was chemically bonded to PS well plates to improve ease of use. (B) Total chip micrographs were taken using a well-plate scanner (Thermo-Fisher), which compiles several micrographs into a single composite image. Cells are maintained in culture for a total of 48 h.

in Figure 18.2-B, the cells eventually fully elongate and replicate.

In order to prepare the microfluidic chip for the cell seeding, the device is sterilized with UV light and coated with an extracellular matrix (ECM), in this case type I collagen was used, these steps are depicted in Figure 18.3-A. Once the cell culture is well established, which requires 48 h of medium perfusion, the phages are injected into the microfluidic device and captured by the cells, the data retrieved during this step allows for the calculation of the kinetic properties of the captured phages. After the phage injection, the cells are washed with PBS to remove any non-specific captured phages and then the phages that bind specifically to the cells are retrieved using trypsin, as depicted in Figure 18.3-A. These phages are then used to re-infect bacterias and amplified.

In Figure 18.3-B results for some of the culture conditions optimization is presented, namely the importance of the use of an ECM and the impact that the medium flowrate has on the cell culture. As seen in Figure 18.3-B the lack of an ECM allows for some degree of cell growth, however the cells eventually cluster up and die. When the collagen ECM is used, the cells grow to an elongated state, which is there typical phenotype, allowing for the subsequent steps of the experiment.

In Figure 18.3-B, it is also possible to evaluate the effects of the flowrate on the cell culture. In the first scenario, where no cell culture medium is perfused, cells quickly die, this is most likely due to nutrient depletion and/or waste accumulation, inducing apoptosis. On the opposite end of the spectrum, high flowrates tend to wash out the cells or induce enough shear stress that inhibits cell growth. The optimal flowrate was determined to be 0.2 μL/min, which results in a fluid linear velocity of approx. 16.7 mm/s. This value of cell culture medium speed, and thus shear stress, is similar to the speed of blood in the human body, to which these cells would naturally be exposed to, which averages between 16.1-9.3 mm/s depending on region and if arteries or veins are considered. [455]

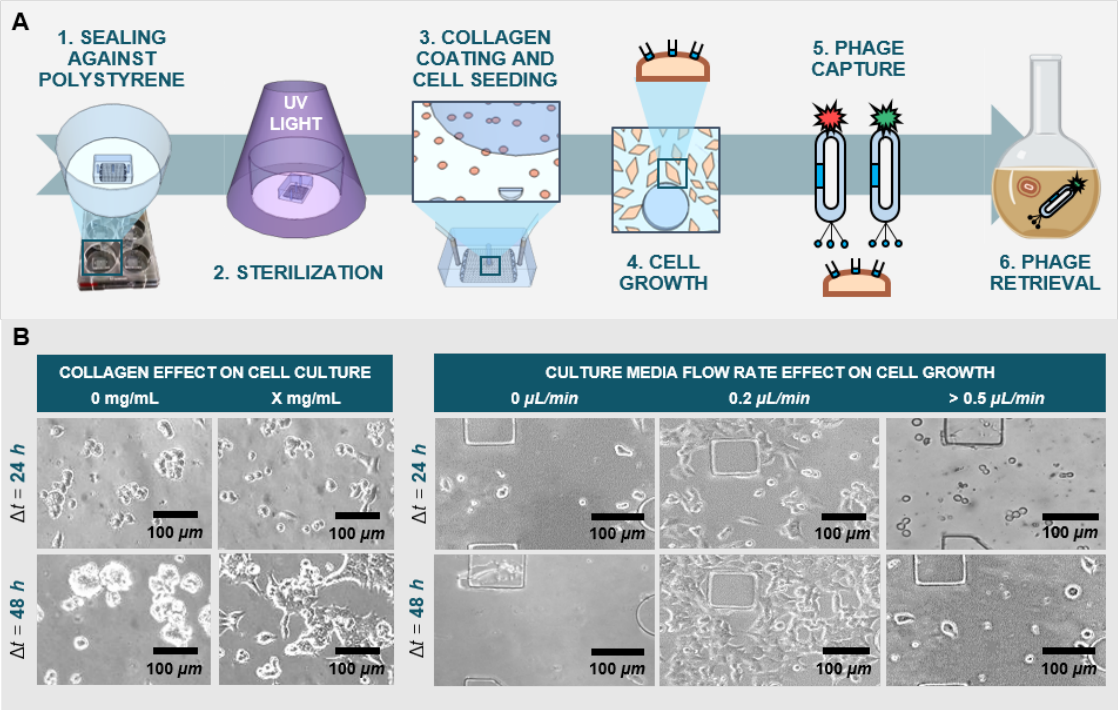

Figure 18.3: (A) Summary of the work flow followed in this experimental approach: 1) microfluidic devices are fabricated and sealed against the PS; 2) these are then sterilized using UV light for 20 min; 3) a layer of collagen is used as the ECM for the cell growth which is followed by cell seeding; 4) cells are grown under medium perfusion for 48 h; 5) phages are injected into the microfluidic device and are captured by the cells; 6) bound phages are collected for amplification. (B) Optimization of cell culture conditions, namely ECM concentration and flowrate for medium perfusion.

18.3.2 Phage capture and binding kinetics

Once the cell culture parameters were well defined, it was possible to move on to the phage capture experiments. As mentioned before, this consisted of the injection BODIPY-FL labeled phages capable of binding to the CXCR4 chemokine receptor. The phage solution had a concentration of 6 x 10^8 phages/μL and was injected at 2 μL/min for 45 min. The fluorescence signal of the chip was monitored and once a saturation of the fluorescent signal was achieved, PBS was injected into the microfluidic device to wash away phages that were non-specifically bound to the cells. The results of this experiment is presented in Figure 18.4.

By analyzing Figure 18.4, some expected conclusions can be immediately be made. The first is that the binding rate of the phages to the cells is higher in the first slice when compared to all the other slices and decreases as we move along the length of the microfluidic device. This is due to the fact that the concentration of phages in solution will decrease throughout the length of the microfluidic device, we will get into more details concerning this aspect latter in this work. Another ”easy to spot” phenomena is that during the wash the decrease in fluorescence signal is much higher in the initial slices than in the last slices of the microfluidic chip. There are two possible reasons, the first being that there are more non-specifically attached phages in the first portion of the microfluidic device then when compared to the following portions. The second reason is that, as phages are washed from the first portion and are dragged in solution, the equilibrium will change, decreasing the amount of phages released in the final

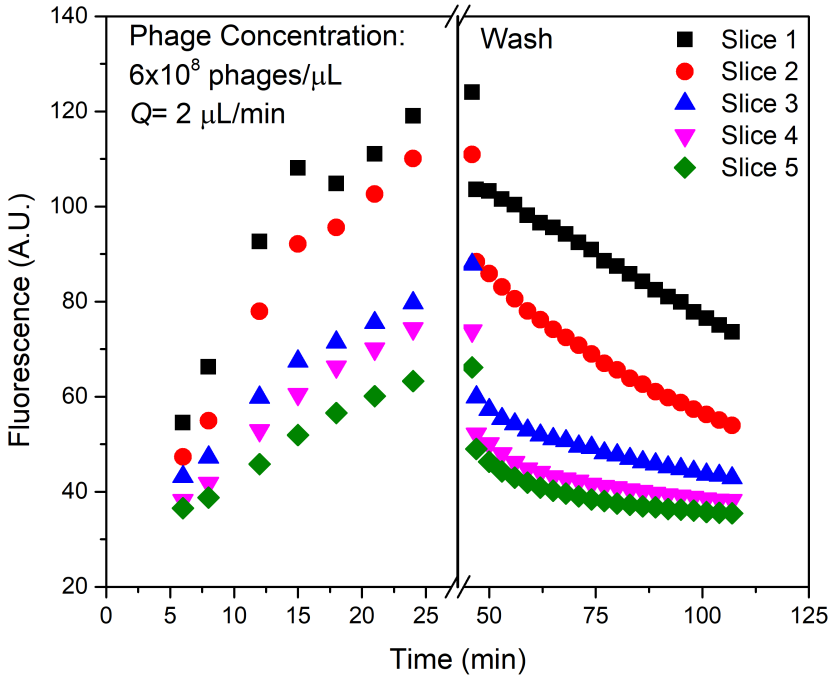

Figure 18.4: Fluorescent signal obtained form the injection of the anti-CXCR4 labeled phages. The intial moment of the experiment corresponds to the phage capture while the signal after the break refers to the washing of non-specific phages. The "Slices" in the legend refer to lengthwise cuts of the microfluidic device in order to better model the kinetic behavior of the phages. Each slice refers to a 2 mm long section of the microfluidic chip. Slice 1 is the channel portion closest to the inlet, while Slice 5 is the one closest to the outlet.

sections of the chamber, the most probable solution is a mix of both these phenomena.

As an example for future phages that could be discovered, the binding kinetics for this phage were determined in addition to the overall efficiency of the microfluidic chip. To model this interaction, the kinetics were assumed to be similar to affinity binding of proteins to a chromatography column as described by Pinto *et al.* [456] By considering the cells our "chromatography beads" we can relate the change of binding sites for a given slice i (b_i) over time to the k_{on} and k_{off} to the concentration of phages in solution in each slice (Cs_i) by using Equation 18.1. The k_{on} represents the binding kinetics of a given molecule, while the k_{off} represents the unbinding kinetics for said molecule.

$$\frac{\partial b_i}{\partial t} = k_{on} \times Cs_i \times (b_{max} - b_i) - k_{off} \times b_i \tag{18.1}$$

In Equation 18.1, b_{max} refers to the maximum amount of binding sites available on the cells. By considering the phage wash curve presented in Figure 18.4 for Slice 1, some assumptions can be made in order to obtain the k_{off}. As mentioned before, in order to wash the phages, PBS is being injected into the microfluidic device, thus Cs_1 during this experiment is 0, leading to the simplified version of Equation 18.1 presented below. By using Equation 18.2, a k_{off} of 8.5 x 10^{-4}s^{-1} was obtained.

$$\frac{\partial b_i}{\partial t} = -k_{off} \times b_i \tag{18.2}$$

In order to determine the k_{on}, more information is needed, it is commonly known that the dissociation constant, K_D is the ratio between the k_{off} and the k_{on} as presented in Equation 18.3. However, a less known relation is the one between the amount of available binding sites at equilibrium (b_{eq}) and b_{max}, presented in Equation 18.4.

$$K_D = \frac{k_{off}}{k_{on}} \tag{18.3}$$

$$\frac{b_{eq}}{b_{max}} = \frac{\frac{Cs_0}{K_D}}{1 + \frac{Cs_0}{K_D}} \tag{18.4}$$

By using the plateau value from the capture portion of the experiment as b_{eq} and by assuming that in the initial moments of the experiment ($b_{max} - b_i$) is approximately equal to b_{max}, one can derive Equation 18.5. By using the data from the phage capture in Slice 1, where Cs is known, both the k_{on} and K_D can be determined, resulting in values of k_{on} = 3.9 x 10^5 $M^{-1}.s^{-1}$ and K_D = 2.9 x 10^{-9} M.

$$k_{on} = \frac{1}{Cs_i}(\frac{\partial b_i}{\partial t} \times \frac{1}{b_{eq}} - k_{off}) \tag{18.5}$$

The value obtained for the K_D are in line for other antibodies (6.9x 10^{-9} M) antibody fragments (3.6 x 10^{-9} M) that have an affinity for the CXCR4 receptor reported in the literature. [457]

By calculating the affinity constants for the phage-HCT116 cell interaction it is now possible to better understand the efficiency of the microfluidic device. By resolving the mass balance for phages in solution as a function of space (Slice number) and time of the experiment, it is possible to monitor the evolution of phage concentration in solution for both the capture and the washing of the phages. At a given position i and a given time t, the phage concentration in solution will be the difference between the amount of phages in solution of the previous Slice and the amount of phages that were captured/released for that slice. This mass balance can be represented by Equation 18.6 and the results obtained for both the capture and wash experiments are presented in Figure 18.5. It is important to make note that for any given time, the Cs_1 will be 6 x 10^8 phages/μL for the capture portion of the assay and 0 phages/μL for the wash portion of the assay.

$$Cs_i(t) = Cs_{i-1}(t) - (b_{i-1}(t) - b_{i-1}(t-1)) \tag{18.6}$$

By analyzing the results presented in Figure 18.5-A it can be observed that in all sections of the microfluidic chip there is an increase of the phages in solution over time. This result is expected as once the cells become saturated, no more phages can interact with the cells and bind, so in principle all these curves should tend to the value of Cs_1 given a long enough time-frame. Another important aspect is the rate at which this happens throughout the length of the microfluidic chip, if we compare for instance Slice

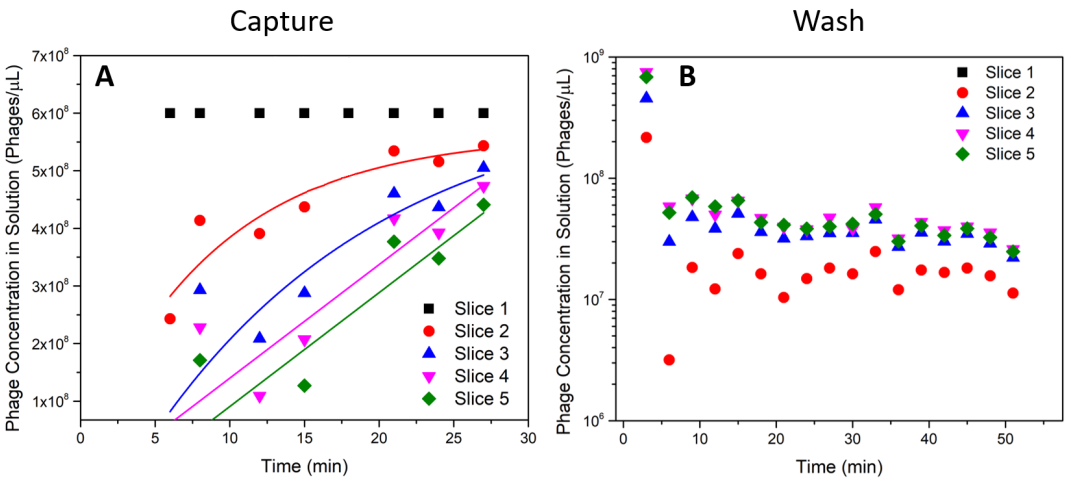

Figure 18.5: Evolution of phage concentration in solution at every Slice along the length of the microfluidic device in both the capture (A) and elution (B) of the phages.

2 to Slice 5, Slice 2 is already close to saturation while Slice 5 is still far away from this value. This is due to the depletion of the solution throughout the microfluidic chip through the attachment of the phages to the cells.

By observing the results presented in Figure 18.5-B, two different profiles can be identified, in the initial 5-10 minutes of the assay there is a very high amount of phages being washed away in the solution, which is more abrupt than the remainder of the experiment. We believe that this initial portion of the experiment are phages that are not specifically bound to the cells that are being washed away. These include phages that are bound not specifically to both PDMS and cells alike. Once this initial period has passed we can see an increasing gradient throughout the length of the microfluidic chip. This is expected due to two reasons, the first being that if we go to look back at Figure 18.4, there were more phages in the initial slices of the microfluidic device to be washed away. The second reason is that, as the phages are washed away the solution will accumulate these phages and increase the solution concentration leading to a shift in the chemical equilibrium. this second effect is also visible by analyzing the slopes of the elution portion of the experiment in Figure 18.4.

By using the data presented in Figure 18.5-A, it is also possible to calculate the phage capture yield as a function of time and position of the microfluidic device. These results are presented in Figure 18.6.

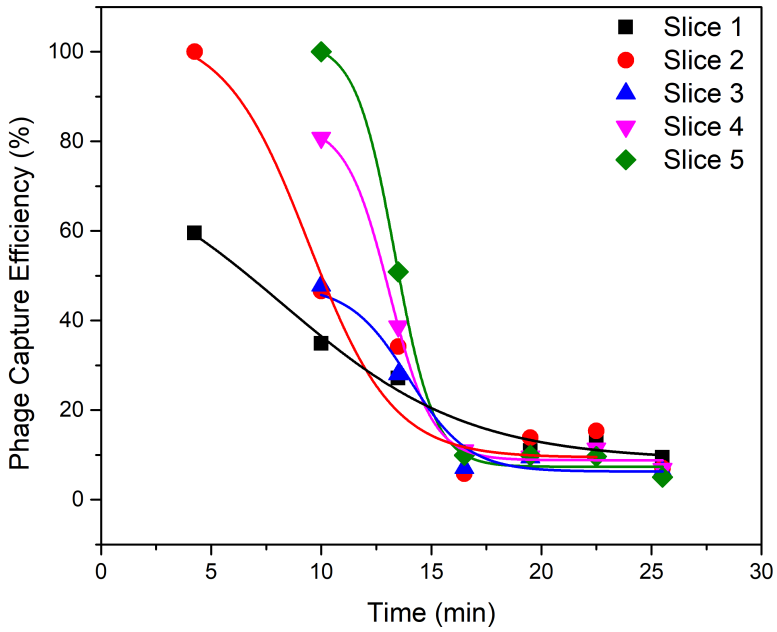

Figure 18.6: Phage capture efficiency as a function of time and position in the microchannel. The capture yield was defined as the ratio between the amount of phages captured and the amount of phages in solution for each time point. The curves presented in the plot are meant to be guides to the eyes and not true fits to the data.

The results presented in Figure 18.6 give us a good representation of what is happening in the microchannel. In the initial moments, the phage solution is completely depleted in the first portions of the microfluidic device. As these lines of cells become saturated, the capture efficiency of the first slices decreases and allow for the phages to move on and be captured at a later position in the microfluidic device. It can also be seen that in the middle of the experiment there is a increasing gradient of phage capture throughout the length of the microchannel. This gradient is due to the fact that there is a decreasing number of phages in solution capable of being captured. Eventually, the capture rate for all Slices in the microfluidic device tends to 0 %, this is expected as once all the number of occupied binding sites reaches the equilibrium, the phages simply pass through the channel. The average phage capture rate of the device, throughout the total length of the experiment was 25.8 ± 5.1 %. However, this number is not a fair assessment of the efficiency of the microfluidic device if used in the case of an actual random library of phages. Here, as a proof of concept, we are using a single phage variant which we know will bind to the target cells, while in the case of a random library the amount of phages that actually are capable of binding to the target cells may be even lower than 1 % of the total number of phages. By analyzing the initial moments of Figure 18.6 it can be observed that we are actually capturing 100 % of the phages that are being injected into the microfluidic chip, this leads us to believe that in the case of a random library we would be successful in capturing any positive phage type present in the library.

18.3.3 Phage retrieval

After running the phage library through the cell culture, it is necessary to retrieve the phages for posterior culture and amplification of the possible positive hits. To do this, first we need an efficient manner of retrieving the phages that are attached to the cells from the microfluidic device. In this portion of the work, we followed two different avenues of thought, a mechanical based process and a chemical one.

Mechanical extraction

The thought process behind this option was to maximize simplicity of the protocol. Due to the fragile nature of mammalian cell membranes it is relatively easy to collapse the microfluidic device and destroy the cells, releasing the captured phages.

The method employed for the mechanical lysis consisted of sealing off the lateral inlet and outlet of the microfluidic channel and apply a negative pressure at the central inlet using a syringe pump at a flowrate of 10 μL/min. This led to the collapse of the microfluidic device and subsequent cell lysis as shown in Figure 18.7. Using the recovered lysate, the number of phages presented was determined through phage titration. The mechanical lysis procedure had an estimated efficiency of 30%, this number seems low if we think about the number of positive hits present in an actual random library of phages. The low efficiency in tandem with a low reproducibility of the process led us to drop this as an option.

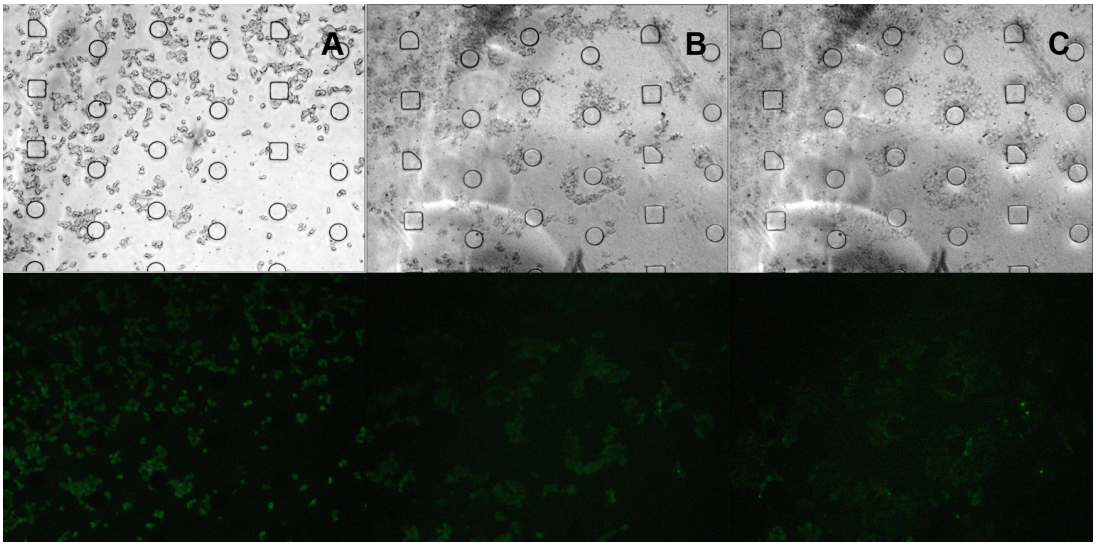

Figure 18.7: Mechanical cell lysis, by collapse of the microfluidic chip. Initially the cells are in their normal conformation (A), when pressure is applied the cells are seen to flatten out (B) and eventually rupture and release the attached fluorescent phages (C). The fluorescent micrographs demonstrate the captured phages dispersing and eventually being washed away in the process.

Chemical extraction

Due to the poor efficiency of the mechanical lysis, we tried to adapt the typical trypsin based protocol for the release of the HCT116 cells from the T-flask cultures. To do this, a trypsin solution (0.25 mg/mL) at 37 °C was injected into the microchannel, at a flowrate of 20 μL/min, until all the cells were detached ($<$

10 min). In Figure 18.8 a sequence of micrographs represent what is happening inside the microfluidic device. At the time of writing, we are still in the COVID-19 pandemic and thus all experimental activities on this topic have been interrupted. Hopefully at the time of the oral defense, more information on this topic may be presented.

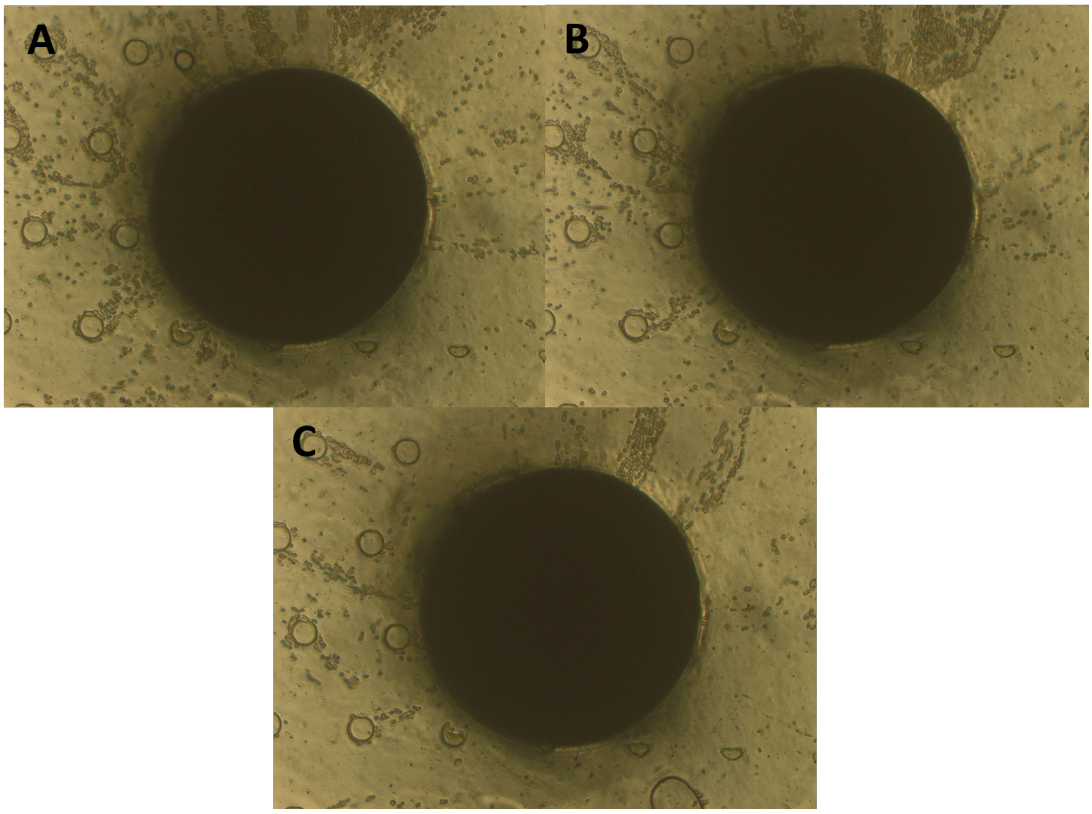

Figure 18.8: Micrographs depicting the cell extraction from the microfluidic chips. Cell density is different in the initial moments (A), the mid point (B) and the end of the extraction (C).

18.3.4 Pre-library and final experiments

As mentioned before, the conclusion of these experiments were caught in the midst of the COVID-19 pandemic and could not be completed at the time of writing. However, one can speculate what could be the next steps of the experiment.

Assuming that the efficiency for the chemical extraction of the phages was satisfactory ($>$50%) I think we are still not ready to move on to the experiments concerning a random library. To ensure that we are capable of capturing any positive hit that goes by the cells I would dilute the phage used up until this point with a solution of a phages which we know does not bind to these cells and check how low we could go, using dilution factors of 10x. Once that work is completed we are now ready to move on to the actual experiments with a random library.

A first screening could be performed using only one cell chamber, however to ensure that the chosen phages are specific to cancerous tissue and won't bind to healthy tissue, a second chamber has to be added to the microfluidic device in order to exclude any possible phage mutant that would bind to healthy

tissue, as this would be hazardous towards the patient.

18.4 Conclusions

In this chapter I showed the potential use of microfluidic devices as a vehicle for phage display assays, as a method to develop new colorectal cancer therapeutic agents. Sadly, this work is not complete due to external factors. However, I think that the results shown here demonstrate the potential of these devices in the future.

In this chapter, a successful culture of a cancer cell line was achieved, which was much more challenging than what is shown here. In addition to that, it was demonstrated how the design chosen for this microfluidic device should be capable of capturing any positive hit produced by a random genetic library of mutated phages.

One can envision this type of device to be used in personal therapy in situations where the tumor is accessible via biopsy, by culturing the tumor cells of the patient instead of an immortalized cell line, it is possible to screen a phage specific for that patient in a short period of time. This could allow the fabrication of patient tailored phages that can act as vehicles for drug delivery, or by analyzing the successful peptide sequence, generate antibodies that can identify the tumor as a form of immunotherapy.

It is with many regrets that this portion of th doctoral thesis is left incomplete.

Chapter 19

Biomarker Detection for Drug Screening

19.1 Introduction

Within work package 8 of the POINT4PAC project, there is another goal, which is the development of microfluidic devices that could aid in the screening of potential therapeutic agents for colorectal cancer. This part of the work was developed in collaboration with Vanda Marques and Dr Marta Afonso which work under the guidance of Professor Cecilia Rodrigues from the Faculty of Pharmacy of the University of Lisbon.

The rationale behind this part of the project is to use the cells chips, similar to the ones presented in the previous chapter of this thesis, to grow, not only the cancer cells such as the HCT116 cell line, but also some of the major body tissues to assess, not only the efficiency of the drug, but also, possible side effects.

Besides being able to culture these different cell lines, there is a technical challenge of monitoring the cell state over time during the drug screening. This can done through the instrumentation of the microfluidic chip by including for example, impedance sensors or photosensors for biomass monitoring, or pH sensors to try to account for metabolic changes to the pH of the chip outflow. Another approach is to include an integrated biosensing module at the chip exit to detect known viability markers such as adenylate kinase I (AK) or lactate dehydrogenase.

My role in this portion of the project was to develop a biosensing module for the detection of AK in the chip output. I will present the work done towards the development of a immunoassay-based, microfluidic module for the detection of AK in the cell supernatant. Sadly, in a similar fashion to the previous chapter this work was not completed, in part due to the impact of the COVID-19 pandemic. However, I will make note on how I would proceed in terms of future work for this project.

19.2 Materials and Methods

19.2.1 Cell culture and supernatant preparation

Cell culture conditions of the supernatants used in this portion of the work were the same as reported in the previous chapter.

RIPA buffer (Thermo Fisher) is added to each cell suspension according to the manufacturer, which is dependent on the suspension concentration. The mixture is left to incubate on ice for 30 minutes with manual agitation at t = 10, 20 and 30 min. After the 30 minutes incubation step, cell solutions are centrifuged for 30 minutes at 4 °C at 16 000 g. At the end of the centrifugation step, cell lysates are then resuspended in the complete culture medium.

19.2.2 Protein labeling

Two different fluorophore were used in this portion of the assay, Alexa430 and BODIPY FL, (Thermo Fisher), both were used according to the manufacturer's indications. Briefly, 50 μL of the target protein dissolved in a solution of 0.1 M of sodium bicarbonate was mixed with 5 μL of the fluorescent dye, dissolved in DMSO at 10 mg/mL and left to incubate under agitation in the dark and at room temperature for 1 h. Then, the excess dye was washed using a 10 kDa Amicon tube (Merck). This was done by using 500 μL of PBS at a time and centrifuging at 14000 g for 10 min until the permeate was not fluorescent.

19.2.3 Microfluidic detection assays

There were several iterations of these assays being performed, as will be described throughout the results section. The general architecture of the assay consisted of packing the microcolumn with the appropriate microbeads, by placing a pipette tip at the inlet containing 5 μL of the microbead suspension and applying a negative pressure at the outlet using a syringe pump, working in pull mode at a flowrate of 15 μL/min. Then the sample would be injected into the column using a syringe pump in push mode at the appropriate flowrate, followed by the antibody or washing buffer (PBS) depending on the experiment at hand. The fluorescent signal was monitored using a Leica microscope fitted with a 100 W mercury arc fluorescent lamp.

19.3 Results and Discussion

The direction I decided to follow for the detection of the AK in the cell supernatant was that of a direct immunoassay, where we capture the analyte and detect with a labeled, anti-ak antibody. There are some restrictions and assumptions that were made from the start of the work.

Since the goal is to have this module attached to a similar cell chip as the one presented in the previous chapter, the chip dimensions and working conditions for the culture of the HCT116 cell culture were used as a model. This translates to using a working flowrate for the supernatant of 0.2 μL/min and a detection range lower that 10000 cells in the microfluidic chip, or in other units, 10000 cells/μL, which

is the number of cells that fit in a completely filled microchip. However, the typical experiment can have a cell number varying between 2000 and 6000 cells in the chip. As in most cases, the more sensitive we are capable of being, the better.

19.3.1 Microbead screening

The initial challenge to develop a direct immunoassay is to be able to capture the analyte in solution and prevent its elution during the remainder of the steps used in the assay. To asses the capture of the AK in solution, pure AK was labeled with the BODIPY FL fluorophore and injected into similar microfluidic columns as the ones used by Pinto et al. [346] These microfluidic columns are 700 μm wide and 1 cm long, while having a height of 100 μm. These columns were packed with a variety of chromatography microbeads and the results are presented in Figure 19.1.

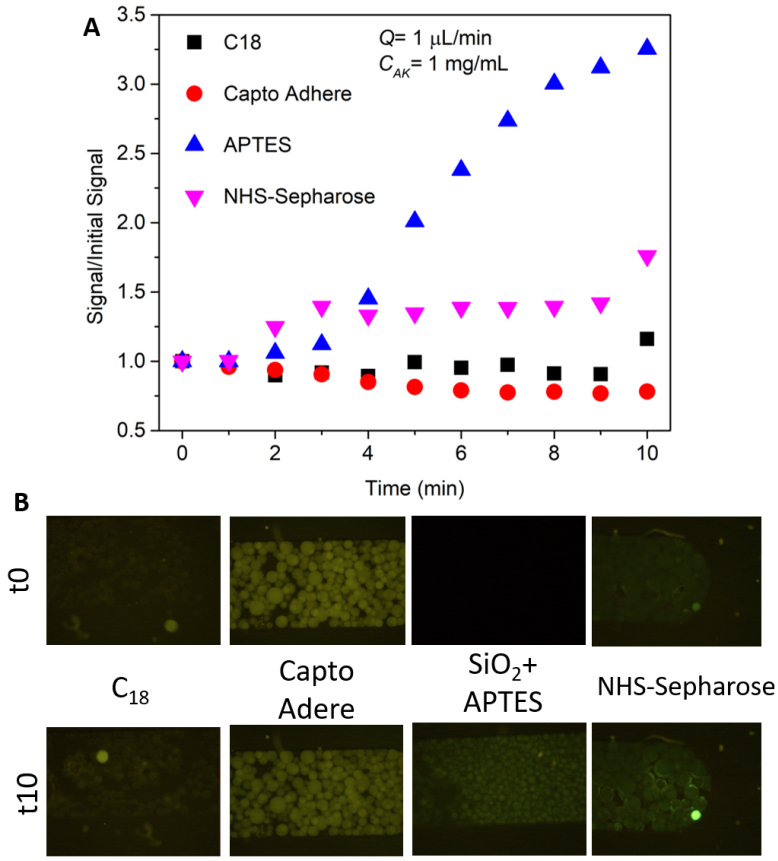

Figure 19.1: (A) Results obtained for the microbead screening to determine the optimal microbead for AK comparison. (B) Visual comparison of the microbead screening.

The results presented in Figure 19.1, show that there are two viable candidates for the capture of the AK molecules in the cell supernatant, the APTES beads, which have a positively charged primary amine as the functional group, while the NHS-Sepharose beads also have an amine as the functional group, in this case it promotes the formation of amide bonds with the proteins in solution. However it is important to note that it is unlikely that in the residence time of the molecules, a stable covalent bond is formed, as the manufacturer indicates a 16 h process time for this to occur.

To determine the best microbead between the two viable candidates, APTES functionalized SiO_2 and the NHS-Sepharose beads, a stringent was performed to determine the one with the strongest interatcion with the AK molecules. This was was done using PBS at a flowrate of 5 μL/min and the results are presented in Figure 19.2.

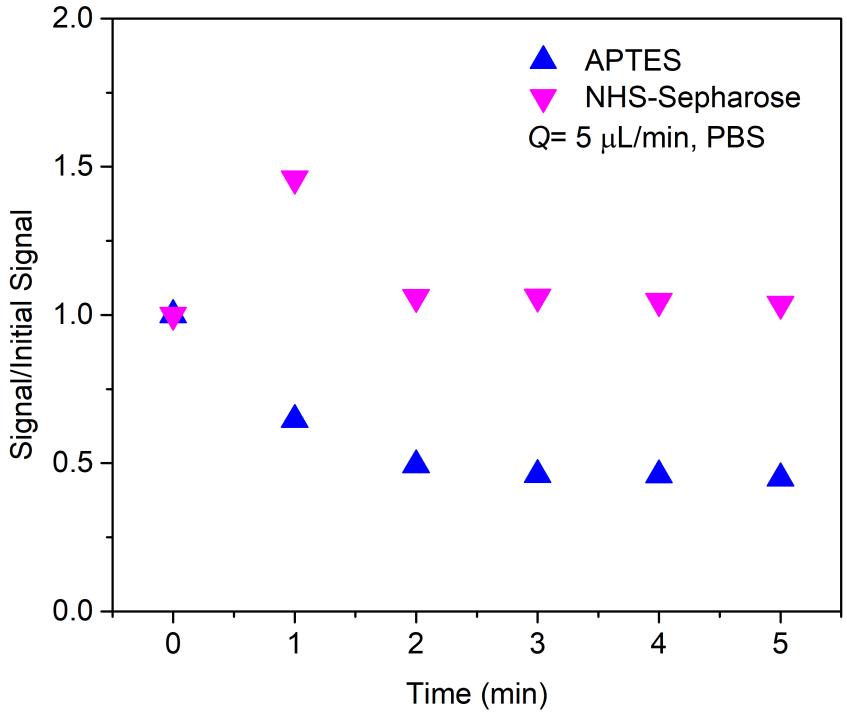

Figure 19.2: Results obtained to test the strength of the interaction between the captured AK and the microbeads packed in the microfluidic column.

As seen in Figure 19.2, the APTES beads lose fluorescence over time, meaning that there is elution of about 50-55% of the captured AK. In the case of the NHS-Sepharose beads, there is an initial peak in fluorescence, which is believed to be leftover antibody solution in the device inlet. Aside from that initial ”bump” in the signal, there is no variation in the fluorescence presented for these beads, meaning that there is no significant elution of the antibody during the washing step. These results led me to use the NHS-Sepharose beads as my capture element for these assays.

19.3.2 Immunoassay development

The next step in developing is assessing the antibody behavior, to do this, two assays were performed. The initial condition was to flow 100 mg/L of pure, unlabeled, AK into the microchannel, which was followed by an injection at 1 μ/min of the anti-AK antibody (50 mg/mL), which was labeled with the Alexa430 fluorophore. The signal obtained over time was compared to the signal obtained using a solution with no AK content. After the intial capture, the beads were washed using 5 μL/min of PBS. These results are presented in Figure 19.3.

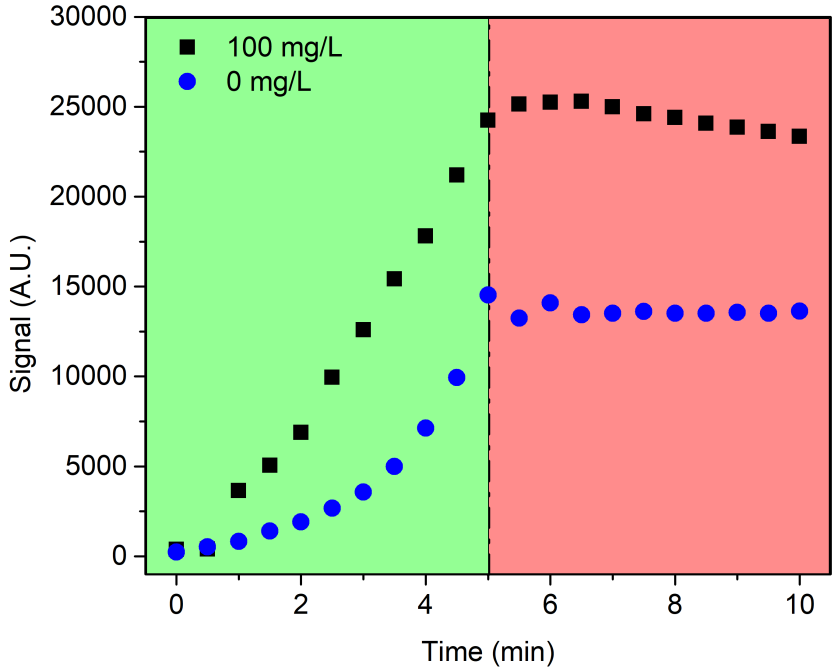

Figure 19.3: Comparison of the fluorescent signal obtained using 100 mg/mL of AK and a control with no AK in solution. In this assay the antibody was first captured (green) and then a wash with PBS at 5 μL/min was performed (red).

The results presented in Figure 19.3 gives us several relevant bits of information concerning our detection assay. The higher final signal and the higher slope presented by assay with AK indicates that the antibody is capable of recognizing the immobilized AK, while the lack of a significant decrease of signal during the wash tells us that the affinity of the antibody is reasonable and there is not a significant amount of non-specific interactions between the antibody and the other elements of the sensor. This wash experiment also shows us that the larger decrease in signal is obtained after 2 min of the washing procedure, which will be the washing time for the remaining experiments. The increase of signal in the absence of AK is to be expected. As mentioned before, these microbeads are optimal for establishing amide bonds with available proteins and peptides, so in the absence of blocking it is expected that the antibody would be captured

This is the point of the development where a series of experiments would be performed in buffered, model solutions, perhaps even spiked with some contaminants to emulate the experimental conditions. These experiments would serve to obtain the ideal blocking condition to prevent the non-specific capture of the antibody, followed by an optimization of the flow rate and other experimental conditions. However there are some things to take into consideration in this particular case.

The main goal of this device is to be capable of detecting cell death directly from the cell culture chamber after a potential drug was injected. Ideally we should keep the number of experimental steps to a minimum in order to have a reasonably functioning module to couple to the cell chip being used for the cell culture. When considering what the medium being used to grow these cells, we are using a cell culture medium that is being supplemented with FBS. FBS is very rich in proteins such as bovine serum albumin (BSA), which historically, are excellent blocking agents in immunoassays. With this in mind, I

attempted to simply flow the supernatant of a HCT116 cell culture that was lysed and the supernatant retrieved, followed by the injection of the antibody solution and a wash step. In order to confirm that the capture of the antibody was not due to the fluorescent label, a control assay, where the anti-JA acid antibody (50 mg/mL) labeled with the same Alexa430 was used instead. These results alongside micrographs of the antibodies being captured using the bare beads are presented in Figure 19.4.

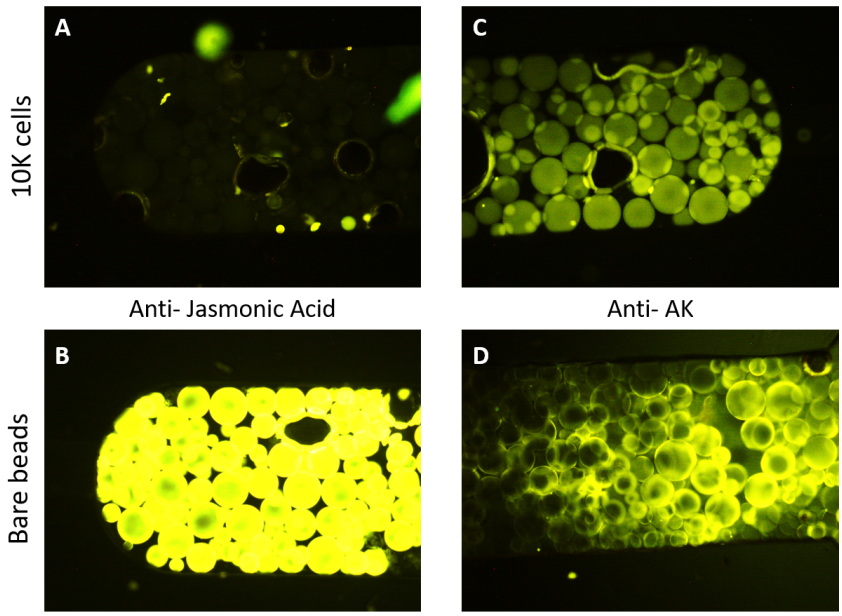

Figure 19.4: Comparison of the results obtained using an anti-JA (left) and an anti-AK (right) antibody on the detection of the AK presented in a supernatant that resulted from the lysis of a cell culture containing 10000 cells/ μL (top) and buffer (bottom). All micrographs, except the bottom left one, were enhanced for visualization purposes.

By observing the micrographs presented in Figure 19.4, it can be concluded that we are capturing the AK present in the cell supernatant, that we are still capable of detecting it using the anti-AK antibody and that the interaction is specific! Figure 19.4-B and D show us that the microbeads are capable of capturing both antibodies to a high degree, while Figure 19.4-A demonstrates that there is close to no non-specific interaction. This lack of capture of the anti-JA antibody in Figure 19.4-A indicates that there is a very efficient blocking of the microbead surface by the remaining components of the cell lysate supernatant. Figure 19.4-C demonstrates that the anti-AK antibody is still capable of detecting the bound AK released by the cells, despite the presence of several contaminants in solution.

At this point in time there are now two immediate questions: i) Is the blocking being done by the FBS proteins presented in the culture medium or is it the remaining proteins from the cell lysate? ii) How sensitive can we be using this approach?

To answer these questions, different cell lysates with different cell concentrations were used, with the results being presented in Figure 19.5. These lysates were injected into the column at 0.2 μL/min for 10 min.

In Figure 19.5 it can be observed that there is a dependence of the fluorescent signal obtained and the number of cells that were presented in the original cell suspension that was lysed. This is most likely due to the different amounts of AK released and presented in the supernatant.

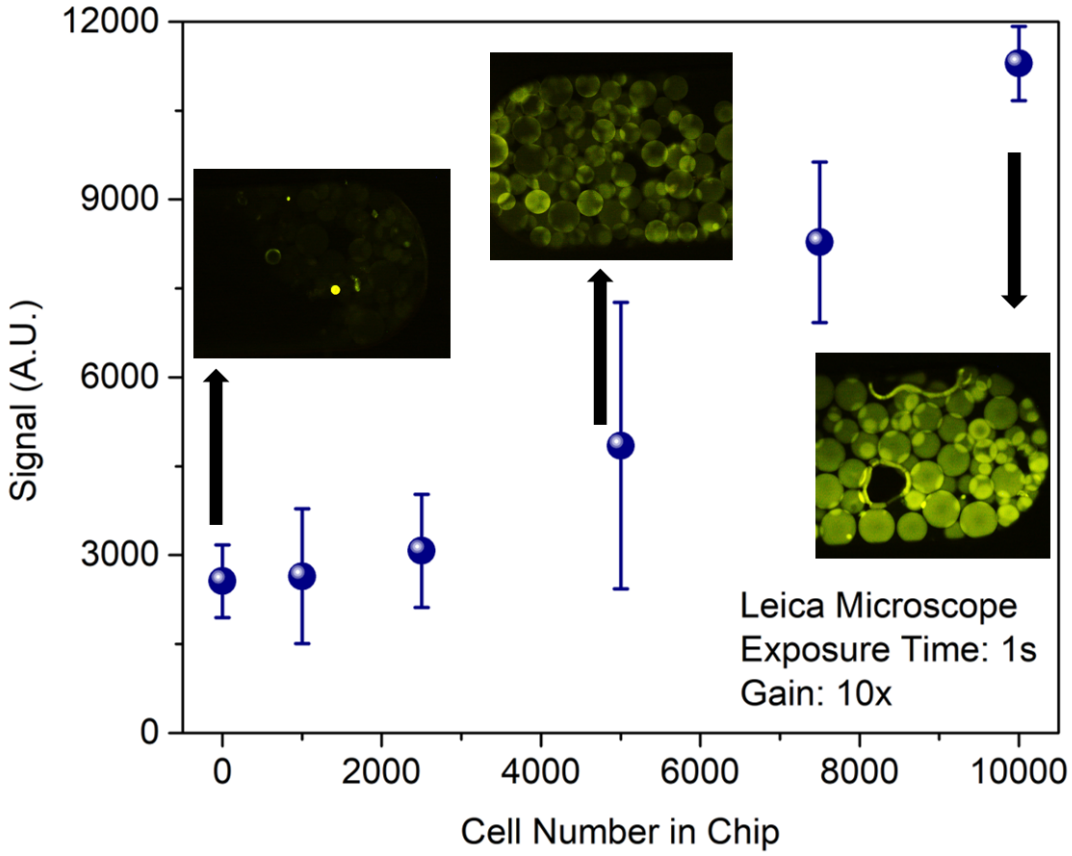

Figure 19.5: Results obtained for different concentrations lysates, presented as the equivalent number of cells that would be present in the microfluidic cell chip. Micrographs presented in the figure show the varying fluorescent signals obtained. The experimental points 10000, 7500 and 5000 are the result of the triplicate assays, while the others are the result of duplicates. The micrographs were enhanced for visualization purposes.

It was mentioned before that our typical cell experiment will have somewhere between 2000 and 6000, but can go up to 10000 cells in the microfluidic chip. This means that we are more or less at the upper limit of what would be needed for a sensitive biosensor. As it stands, the developed module can give us an indication of 100% cell death vs maybe 50-75% in a really well seeded chip vs 0% cell death.

19.3.3 Future Steps

Despite not achieving the desired sensibility for the assay, a basis which is not too far off was achieved. If more time was available the route I would attempt would be the following.

The initial step would be to test agarose based microbeads to confirm that the capture of the molecules is due to the activated NHS group and not the microbead matrix itself.

I would also consider the use of a longer microfluidic column. The reason behind this suggestion is that in some instances where the column was over-packed with the microbeads, there was a clear signal gradient along the microcolumn. This may be evidence of the microbeads being capable of depleting the supernatant solution. If this is true their might be the possibility of detecting different concentrations based on the ”fluorescent length” detected in the column.

Finally, the real test would be to test this with the actual microfluidic cell chip. There can also be the release of AK during the cell growth process which needs to be taken into account. In these experiments, the AK detected is what the cells had inside themselves at the moment of their death. So the relationship between the number of cells being cultivated and the AK that is released may actually be higher.

19.4 Conclusions

All in all this was a nice challenge to tackle in this PhD thesis. I was able to develop a very simple assay capable of detecting cell death in the upper limits of the required detection range of 5000-10000 cells/μL. Assuming the module is connected to the cell chip and is continuously capturing the chip output, the detection assay itself is performed in 7 min, which is quite fast.

The use of the actual cell medium as the blocking agent is an interesting approach for the development of an immunoassay as we can significantly reduce the complexity and time of the assay. Another interesting aspect is that we are (probably) capturing most if not all of the proteins released by the cells during their lysis process. This may open the door towards a multiplexed detection of different biomarkers such as lactate dehydrogenase or glyceraldehyde-3-phosphate dehydrogenase [458] by using a mixture of the appropriate antibodies with different fluorescent labels.

Another future development for this module would be to couple it to the a-Si:H photosensors, with the appropriate fluorescent filters to have an immediate response.

Chapter 20

A microfluidic device for the screening of anti-cancer immune therapeutic strategies: a proof of concept comparison to *in vivo*

20.1 Introduction

High mortality rates of cancer are usually attributed to metastasis. Usually, metastatic CRC patients are treated with chemotherapy, alone or in combination with biological agents, as most of metastases cannot be addressed surgically. However, these therapeutic combinations have presented a limited success, which may be explained by the "tumor immune microenvironment" (TIME). [459] In detail, TIME is constituted by a complex network of tumor, stromal and innate/adaptive immune cells, whose tumorigenic and suppressive phenotype further influence the growth, proliferation and tumor dissemination, being associated to the progress of adenomatous polyps to invasive CRC. [460]

The tumor-associated macrophages (TAM) infiltration seems to play a key role in CRC dissemination, being related with a poor outcome. Particularly, pro-tumoral M2-TAM (colony stimulating factor 1 receptor (CSF1R) dependent) are directly involved in the secretion of immune suppressive factors that trigger the prevention of effector functions of immune cells and induce their differentiation into immune regulatory and tumorigenic ones (such as, regulatory T (Treg) and dendritic cells (rDC)), thus acting as stimulators of immune suppression and tumor growth. [460]

The most explored and ongoing clinical trials in several solid tumor types and recently approved by Food and Drug Administration (FDA) for the treatment of tenosynovial giant cell tumors is Pexidartinib (PLX3397), an orally active and potent tyrosine kinase inhibitor of CSF1R, with activity to other kinases such as cKIT, mutant fms-like tyrosine kinase 3 (FLT3), and platelet-derived growth factor receptor (PDGFR)-β, which is safe and effective in depleting CSF1R+ TAM, reprogramming immune sup-

pressive myeloid cells towards an antigen-presenting and immune stimulatory phenotype, and restoring anti-tumoral T cell responses. [461–463]

In this work, we present a simple to use, microfluidic platform for the rapid assessment of potential cancer therapies.

As a model, the tumor microenvironment from colon cancer induced, C57BL/6J (10-12 weeks-old) mice was used, as well as spleenocytes which have a limited cytotoxic effect towards the TME. As a proof of concept, the effect of a nanoparticle based therapeutic vaccine, which increases the cytotoxic behavior of the spleenocytes, was assessed in the microfluidic device as well as the combined effect of the nanovaccine and a TAM inhibitor, Pexidartinib. The results obtained in the microfluidic device were then compared to the same treatments employed in an in vivo study, with both approaches resulting in similar conclusions, validating the use of the microfluidic platform approach for rapid screening of potential therapy strategies, while reducing the amount of sacrificed animals.

20.2 Materials and Methods

20.2.1 Reagents

Solutions were prepared from analytical grade reagents using Millipore Milli-Q ultra pure water and RNAse free water.

Poly(D,L-lactide-co-glycolide) (PLGA) Resomer® RG 502 (lactide:glycolide 50:50, molecular weight (M_w) range 7,000 – 17,000 g/mol) was purchased from Evonik (Frankfurt, Germany). Poly(2-butyl-2-oxazoline)-block-poly(2-methyl-2-oxazoline) (poly(2-oxazoline), POx) conjugated to mannosamine (POx-Man) was synthesized and kindly provided by Professor Rainer Jordan and Doctor Erik Wegener from Technische Universität Dresden (Dresden, Germany). Dichloromethane (DCM), (APTES), bovine serum albumin (BSA) and fluorescamine were purchased from Sigma-Aldrich (Darmstadt, Germany). N-butyl poly-L-arginine hydrochloride (pARG) with a Mw ranging 3,000 – 3,400 g/mol was purchased from Polypeptide Therapeutic Solutions (Valencia, Spain). Phosphate buffered saline (PBS, pH 7.4), Quant-iT^{TM} PicoGreen^{TM} dsDNA assay kit, Quant-iTTM OliGreen^{TM} ssDNA assay kit, RPMI 1640 + Glutamax^{TM}, heat inactivated fetal bovine serum (FBS), penicillin/streptomycin (PEST; Penicillin 10,000 U/mL and Streptomycin 10,000 mg/mL), HEPES buffer (1 M), sodium pyruvate (100 mM), β-mercaptoethanol (50 mM), trypsin-ethylenediaminetetraacetic acid (trypsin-EDTA, 0.25%), ACK lysing buffer, 4,6-diamidino-2-phenylindole (DAPI) and 7-Aminoactinomycin D (7AAD) were purchased from Thermo Fisher Scientific (Bremen, Germany). Tumor-associated peptides MHCI-restricted AdpgkR304M (MHCI-Adpgk): AM-9 (ASMTNMELM), MHCII-restricted AdpgkR304M (MHCII-Adpgk): GT-28 (GIPVHLELASMTNMELMSSIVHQQVFPT) were purchased from GeneCust (Dudelange, Luxembourg). CpG-ODN 1826 (TCCATGACGTTCCTGACGTT) and small interfering RNA (siRNA) anti-TGF-β1 (siTGF-β1) were purchased from Microsynth GmbH (Balgach, Switzerland). Poly(I:C) (High Mw) VacciGrade^{TM} was purchased from Invivogen (Toulouse, France). Pexidartinib was purchased from Selleckchem (Houston, TX, USA). Collagenase type II, neutral protease (dispase) and DNase I were purchased from Worthing-

ton Biochemical Corporation (Freehold, NJ, USA). Corning® collagen I (high concentration, rat tail) was supplied by Corning (New York, USA).

20.2.2 Nanoparticle synthesis and characterization

NP were prepared by a double emulsion (water-in-oil-in-water (w/o/w)) solvent evaporation method, as reported elsewhere. [464] Briefly, PLGA (80%) and POx-Man (20%) were dissolved in DCM at 50 mg/mL (organic phase). The internal aqueous phase was prepared by dissolving the TLR ligands (20 μg/mice for CpG-ODN and 40 μg/mice for Poly(I:C)), the antigens (500 μg of MHCI-Adpgk and MHCII-Adpgk CRC neoantigens), and the siRNA (16 mg/mL) against TGF-β1 previously complexed with pARG, in 8% (m/v) PVA aqueous solution. This aqueous phase was added to the organic phase containing the polymer blend previously dissolved. The single w/o emulsion was performed under continuous sonication at 20% of amplitude for 15 seconds, using a microprobe ultrasonic processor (Digital Sonifier® Cell Disruptor, Branson Ultrasonics, Emerson, USA). A second emulsion was performed with 2.5% (m/v) PVA aqueous solution under the same conditions. The w/o/w double emulsion was added dropwise into a 0.25% (m/v) PVA aqueous solution and left under magnetic stirring for 1 hour at room temperature, allowing for DCM evaporation and NP formation. NP were thereafter separated from the preparation media and washed with ultrapure water (to remove the excess of surfactant and/or non-entrapped biomolecules) by centrifugation at 22,000 g for 40 minutes, at 4 °C (Beckman J2MC super centrifuge, Beckman Instruments, Inc., USA), and finally resuspended in PBS for in vivo experiments.

NP mean diameter and polydispersity index (PdI) was determined by Dynamic Light Scattering (DLS) using a Zetasizer Nano ZS equipment (Malvern Instruments, Worcestershire, UK). The same equipment allowed for the determination of NP surface charge (ζ potential) by Laser Doppler Electrophoresis in combination with Phase Analysis Light Scattering. [464]

Antigens (MHCI-Adpgk and MHCII-Adpgk), siTGF-β1 and Poly(I:C), and CpG-ODN entrapped into NP were indirectly quantified with fluorescamine (360 nm absorbance and 460 nm emission wavelengths), Quant-iTTM PicoGreen^{TM} dsDNA and OliGreen^{TM} ssDNA Assay Kits (485 nm absorbance and 520 nm emission wavelengths), respectively, using the supernatants collected from centrifugation steps and a microplate reader (FLUOstar Omega, BMG Labtech, Durham, NY, USA), as previously reported. [464]

20.2.3 Animal Studies

C57BL/6J (10-12 weeks-old) mice were purchased from Instituto Gulbenkian de Ciência (Lisbon, Portugal), and housed in the animal facility of the Faculty of Pharmacy at the University of Lisbon. All animal procedures were completed in compliance with Faculty of Pharmacy, University of Lisbon guidelines. Protocols were reviewed and approved by the Direção-Geral de Alimentação e Veterinária (DGAV, Portugal). Animals were housed under a 12 hours light, 12 hours dark cycle, with food and water available ad libitum and handled in compliance with the National Institutes of Health (NIH) guidelines and the European Union rules for the care and handling of laboratory animals (Directive 2010/63/EU). Mice

body weight change was monitored 3 times a week. Mice were euthanized according to ethical protocol when showing signs of distress or with rapid weight loss (above 10% within a few days or 20% from the initial weight). For tumor-bearing mice, tumor size was monitored 3 times a week using a digital caliper. Animals were also euthanized in case the tumor size exceeded 1200 mm^3 or if the tumor was necrotic/ulcerative. Tumor volume (mm^3) was determined by $(d^2 \times D)/2$ where d and D are the shortest and longest diameter in mm, respectively.

Figure 20.1: Example of the C57BL/6J mice used for these experiments.

20.2.4 Therapeutic effect of nanovaccine alone or in combination with TAM modulator assays

On day 0, female C57BL/6J mice (10-12 weeks-old) were s.c. inoculated at the right flank with 5x10^5 (100 μL PBS) murine colon adenocarcinoma MC38 cells (kindly provided by Professor Diego Arango from the Vall d'Hebron Hospital Research Institute, Barcelona) previously cultured in RPMI 1640 + Glutamax supplemented with 10% (v/v) FBS and 1% (v/v) PEST, as reported by Luo et al. [398]. The right dorsal area was treated with depilatory cream before the inoculation. On day 10, mice were randomized into the following groups (N= 6) according to Table 20.1.

Table 20.1: Therapeutic groups and following administration routes. CpG: cytosine phosphorothioate-guanine motifs; i.p.: intraperitoneal; MHC: major histocompatibility complex; ODN: oligodeoxynucleotides; PBS: phosphate-buffered saline; Poly(I:C): polyinosinic:polycytidylic acid; s.c.: subcutaneous; siRNA: small interfering RNA; siTGF-β1: siRNA anti-TGF-β1; TLR: toll-like receptor. Nanovaccine siTGF-β1: NP loading MHCI-Adpgk + siTGF-β1/MHCII-Adpgk and TLR ligands (CpG-ODN, Poly (I:C)).

Group	**Treatment**	**Entrapped biomolecules**	**Route of administration**
G1	PBS		s.c.
G2	Nanovaccine	MHCI-Adpgk + siTGF-β1 + CpG-ODN + Poly(I:C) /MHCI-Adpgk + CpG-ODN + Poly(I:C)	s.c.
G3	Nanovaccine + Pexidartinib		s.c. + i.p.

PBS and nanovaccine treatments (200 μL) were s.c. administered by hock immunization, via injection proximal to inguinal LN (200 μL), on days 10, 17, and 24 following tumor inoculation (Figure 2A). Half dose was injected in the right side while the other half on left side. MHCI-Adpgk + siTGF-β1 and MHCII-Adpgk peptide antigens were administered at both sides of each mouse (groups 2-3). Each dose per mouse (50 μL per side) contained 100 μg of Adpgk antigen (50 μg of MHCI-Adpgk and 50 μg MHCII-Adpgk), 20 μg of siTGF-β1, 20 μg of CpG-ODN and 40 μg of Poly(I:C), entrapped into NP (10 – 20

mg/mL, according to MHCI/II-Adpgk loadings).

Pexidartinib (TAM inhibitor) was administered intraperitoneally (i.p.) at 10 mg/Kg [451]. Mice were treated with three doses, administered seven days apart, on the day of nanovaccine administration (Figure 2A).

On day 28 mice (N= 2-3) from each group were euthanized, and their tumors and spleens were isolated aseptically for microfluidic-based assays.

20.2.5 Tumor and spleen single cell suspension preparation

On day 28, PBS- and nanovaccine-treated mice (N= 3) (Table 20.1) were sacrificed, and their tumors and spleens were isolated aseptically and homogenized in a single cell suspension for characterizing the dynamics of immune-TIME interactions in microfluidic chips.

Tumor single cell suspensions were obtained by mechanical disruption and enzymatic digestion of the tumor tissues (0.5% (m/v) BSA, 0.1% (m/v) collagenase type II, 0.1% (m/v) neutral protease (dispase) and powders of DNAse I in RPMI 1640 + Glutamax) for 1 hour at 37 °C. After digestion, tumor single cell suspensions were depleted of erythrocytes using the ACK lysing buffer for 5 minutes at 37 °C and filtered through a 70 μm filter with cold PBS to remove the debris. Thereafter, tumor single cell suspensions were centrifuged at 300 g for 5 minutes at 4 °C and cultured in RPMI 1640 + Glutamax supplemented with 10% (v/v) FBS and 1% (v/v) PEST, in a humidified incubator equilibrated with 5% CO_2 at 37 °C. Cells were then recovered, counted to be loaded into microfluidic chip chamber (TIME chamber).

Spleens were also mechanically disrupted, and single cell suspensions depleted of erythrocytes and filtered as previously described. Cells were then centrifuged at 300 g for 5 minutes at 4 °C and cultured for 7 days in RPMI 1640 + Glutamax containing 10% (v/v) FBS, 1% (v/v) PEST, 1% (v/v) sodium pyruvate, 1% (v/v) HEPES buffer, 0.1% (v/v) β-mercaptoethanol only, or supplemented with MHCI/II-Adpgk (100 μg/mL, 50 μg/mL for MHCI-Adpgk and 50 μg/mL for MHCII-Adpgk) peptide solution and CD28 (2 μg/mL), in a humidified incubator equilibrated with 5% CO_2 at 37 °C. After 7 days, splenocytes were recovered and counted to be loaded into the microfluidic chip chamber (spleenocyte chamber).

20.2.6 Microfluidic cell chip material screening

MC38 CRC cells (1x10^5 per mL) were seeded in polystyrene petri dishes, or petri dishes covered with PDMS or Corning® glass (coverslip), previously treated with oxygen plasma functionalization (Harrick Plasma PDC-002-CE) for 10 minutes and sterilized using UV light of the laminar flow hood (BSB 4A, Gelaire Laminar Air Flow, Italy) for 15 minutes, and incubated overnight in a humidified incubator equilibrated with 5% CO_2 at 37 °C. Collagen (50 μg/mL, PBS) coating was also tested in the different materials. Images were obtained using an optical microscope (ULWCD 0.3 Olympus CK2, Japan) and a smartphone (WIKO U Feel Prime).

20.2.7 Microfluidic screening assays

Microfluidic cell chips were sterilized using the UV light of the laminar flow hood (BSB 4A, Gelaire Laminar Air Flow, Italy) for 20 minutes prior to experiments. Cell chips were then loaded with the TIME cells by placing 100 μL of the tumor cell suspension with a density of 4x10^6 cells/mL in the inlet of the TIME chamber and 100 μL of medium in the adjacent chamber inlet. Using a syringe pump (New Era Pump Systems, NE-1002X) at flow rate of 2 μL/minute, cells were pulled into the chamber by applying a negative pressure at the outlet. TIME cells were allowed to adhere for 4 hours, in a humidified incubator equilibrated with 5% CO2 at 37 $^\circ$C. Subsequently, the remaining cells in the inlet region were scraped out to avoid excessive medium depletion and the medium was renewed. Cells were allowed to grow in a static culture for 24 hours. Cell culture medium was then renewed with medium containing the cell death marker 7AAD (1:1000, 488 nm excitation and 647 nm emission wavelengths), to monitor the percentage of TIME cell death. Thereafter, spleenocytes (1:100) obtained from PBS- and nanovaccine-treated mice were loaded into the remaining spleenocyte chamber by the same method used in TIME chamber. For treatment condition of nanovaccine in combination with a TAM inhibitor, cell culture medium of spleenocytes from nanovaccine-treated mice was supplemented with Pexidartinib at 14.9 nM. [465] Cells were co-cultured for another 24 hours and the percentage of TIME cell death was evaluated. Microfluidic cell chips without spleenocytes were used as controls.

Cell culture viability was monitored using optical (ULWCD 0.3 Olympus CK2, Japan) and fluorescence (Rhodamine filter, 546 nm excitation and $>$590 nm emission wavelengths; Olympus AH-2, Japan). Fluorescent images were obtained using an AxioCam MRc coupled to the fluorescence microscope. The WCIF ImageJ Software was used for an automatic assessment of the fluorescent micrographs [450]. A threshold filter was applied, and the amount of fluorescent entities were counted.

20.3 Results and Discussion

20.3.1 Microfluidic Approach

As discussed briefly in the introduction, the development of successful treatment strategies is a highly time consuming and expensive endeavor. In this work we propose a different approach to overcome this issue, which will allow us to save more animal lives and to perform a larger amount of screening assays. This approach is summarized in Figure 20.2, using a theoretical exercise, for the screening of the synergistic effect of therapeutic vaccines in addition to a TIME inhibitor.

Taking into consideration the number of biological replicates needed for a successful treatment screening assay, the number of animals that will be sacrificed rise exponentially. Using our proposed approach, the number animals sacrificed is kept at a minimum. By extracting the whole tumor from mice, several microfluidic assays may be performed using the same biological material by assessing the effect of immune therapeutic approaches, such as nanovaccines alone or in combination with multiple inhibitors of the tumor-immune microenvironment (TIME), without the additional animal sacrifice. This approach also possesses advantages over the use of cell lines in vitro as the immortalized cell lines

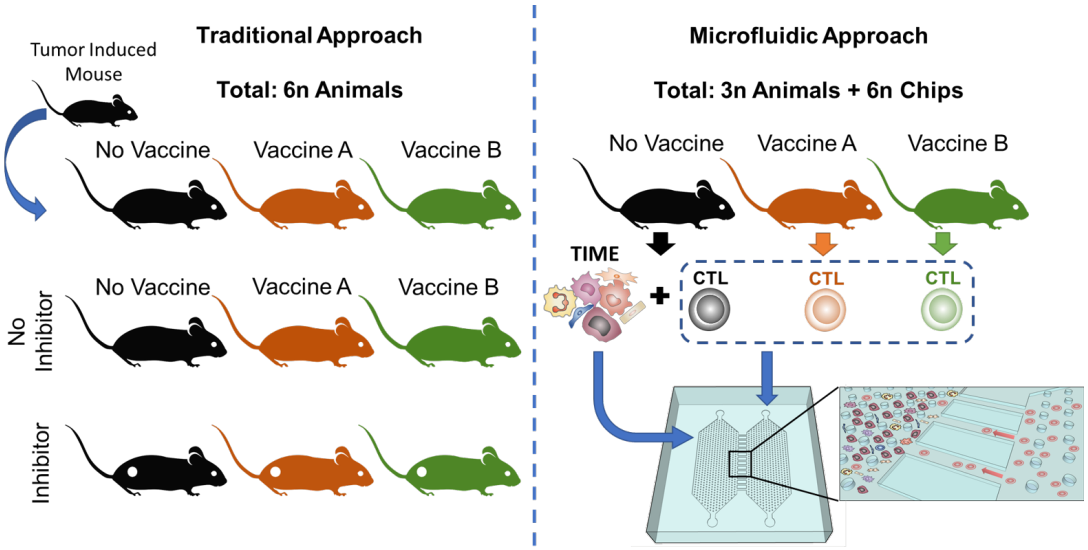

Figure 20.2: Schematic representation of the traditional approach towards treatment development studies (left) compared to the microfluidic-based approach proposed in this work (right). By using the microfluidic cell chips, more combinations of treatments can be tested at the expense of a lower number of animals, represented as mice.

often do not react in the same fashion as the primary cell lines. In addition, primary cell lines lack the immune suppressive factors expressed by the TIME. This approach could also be extended to cases of personalized medicine where a tumor biopsy from a patient could be collected and used as the screening material for an array of potential treatments.

In the following sections we report on a microfluidic cell-culture platform for exploring the tumor infiltrating lymphocyte (TIL)-mediated tumor killing in a static microenvironment, as a preclinical *ex vivo* complex model system alternative to *in vivo* studies.

As proof of concept, a preliminary experiment was designed to show how this platform can be used to screen the best anti-CRC therapy through the evaluation of the tumor cell death after the incubation of TIME cells with lymphocytes harvested from mice previously immunized with a nanovaccine alone or in combination with a TAM inhibiting agent.

20.3.2 Therapeutic nanovaccine alone or in combination with TAM blockade therapy restricts colorectal cancer growth in vivo

Previously explored by Matos et al. [464], an in vivo study was performed to evaluate the potential synergistic anti-tumor effect of a nanovaccine combined with modulatory therapies focused on blocking immune suppressive mechanisms involved in cancer progression, allowing the screening of the best anti-CRC therapy. Matos et al. [464] designed and prepared mannose-functionalized NP by using a modified state of the art double emulsion solvent evaporation method to deliver combinations of neoantigens (short MHCI- and long MHCII-Adpgk peptides) and TLR ligands (CpG-ODN and Poly(I:C) as agonists of the TLR9 and TLR3, respectively), in addition to the co-entrapment of siTGF-β1, to DC. Nanovaccine presented an average hydrodynamic diameter close to 200 nm, with low polydispersity index (PdI $<$0.2), near-neutral surface charge, and high loading levels for Adpgk peptides (EE $>$76.1 $\pm$ 4.1%, LC $>$38.1

$\pm$ 2.0 μg/mg) and TLR ligands (CpG-ODN: EE $>$98.2 $\pm$ 2.9%, LC $>$6.3 $\pm$ 0.1 μg/mg); and Poly(I:C): EE $>$98.2 $\pm$ 2.3% and LC $>$12.5 $\pm$ 0.1 μg/mg).

According to schedule in Figure 20.3-A, the nanovaccine co-entrapping the CRC neoantigens (MHCI- or MHCII-Adpgk), TLR ligands (CpG-ODN and Poly(I:C)) and siTGF-β1, was administered to these animals alone or in combination with an inhibitor of immune suppressive TAM, Pexidartinib, in the same day. The anti-tumor immune-mediated response was strongly enhanced with marked tumor growth inhibition (Figure 20.3-B, C) when mice were treated with the nanovaccine alone or in combination with TAM inhibitor, Pexidartinib.

At day 28 following tumor inoculation, animals treated with the nanovaccine alone or in combination with Pexidartinib, presented an average tumor volume significantly lower than those treated with PBS (P $<$0.0001) (Figure 20.3-B, C). Although different from PBS-treated group, the nanovaccine-treated groups also presented significantly different tumor volumes. Accordingly, mice treated with combinatorial treatment Nanovaccine + Pexidartinib presented significantly smaller average tumor volumes than those immunized with the nanovaccine (P = 0.0289) (Figure 20.3-B, C). Particularly, the combination Nanovaccine + Pexidartinib resulted in the most robust anti-tumor effect presenting an average tumor volume 2.8- and 6.6-fold significantly smaller than those obtained for nanovaccine and PBS-treated animals, respectively.

The important role of immune suppressive TAM in CRC dissemination and poor outcome have powered interest in therapeutically targeting these cells. The modulation of CSF1/CSF1R signaling, using CSF1R inhibitors (e.g. Pexidartinib) as monotherapy or in combination with other immune therapeutic strategies, have been reported to repolarize the pro-tumor phenotype of adaptive immune cells to an anti-tumor one, through the reduction of TAM infiltrate and promotion CD8+ effector T cells in CRC [459, 461-463, 493-495]. Moreover, pro-tumoral M2-TAM act as stimulators of immune suppressive cytokine TGF-β [46], which is involved in CRC metastasis and correlated with poor prognosis in CRC patients [144, 464]. Thus, the development of strategies to inhibit TGF-β pathway and TAM infiltration, in combination with other therapies including DC vaccination, have been stimulated in order to restore anti-cancer immunity associated to potent cytotoxic immune responses, control tumor homeostasis and prevention of metastatic CRC [465, 466]. Considering the important role of several tumor-infiltrating immune players with immune suppressive and pro-tumoral capacities in the dissemination and progression of CRC and other tumor subsets, and the drawbacks previously mentioned related to the *in vivo* studies, there is an urgent need in develop preclinical *ex vivo* models alternative to *in vivo* studies.

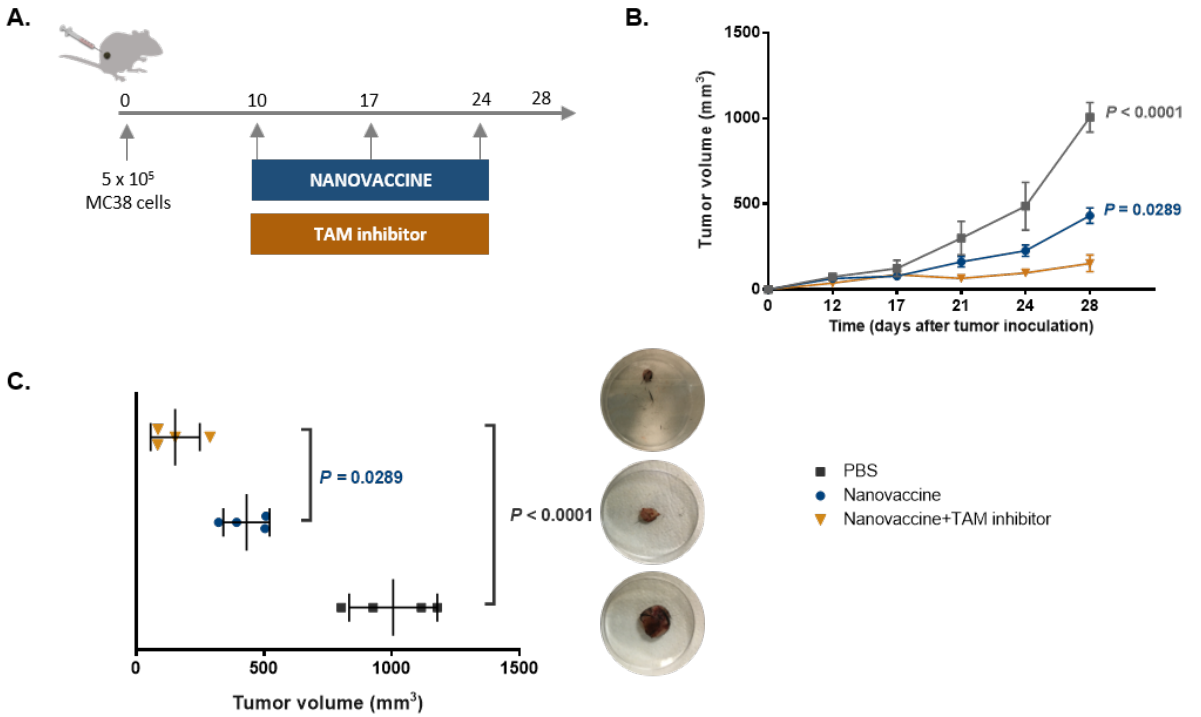

Figure 20.3: The co-delivery of antigens and adjuvants by our polymeric cancer nanovaccine showed a synergistic effect on the inhibition of tumor growth. (A) Timeline of tumor inoculation, immunizations, and immune modulatory therapy. (B) Tumor growth curve. (C) Tumor volume at day 28 following tumor inoculation. Data are presented as mean ± SEM (N= 6). One-way ANOVA followed by Tukey Post-Hoc test. P values regarding the tumor volume at day 28 after tumor inoculation relative to Nanovaccine + Pexidartinib group.

20.3.3 Co-culture microfluidic cell platform development for treatment screening

A microfluidic cell chip was developed as a preclinical *ex vivo* complex model system alternative to *in vivo* studies, to enable the rapid screening of the same anti-CRC treatments previously tested in vivo. Before the fabrication of the microfluidic chip, several substrate candidates were tested in order to determine the best material to promote cell growth. The materials tested were polydimethylsiloxane (PDMS), polystyrene (PS) and Corning Glass, which are common substrates among microfluidic fabrication procedures. MC38 CRC cells were seeded in the different sterile materials, previously coated with rat tail collagen type I, to test their ability to adhere. Cells seeded in a T-flask were used as control. Polystyrene was selected as the best material for the development of the microfluidic chip as MC38 CRC cells grew completely adherent with an elongated morphology (Figure 20.4-A). In contrast, PDMS seems to be the substrate less suitable for MC38 CRC cell culture, as it was observed cells in suspension, aggregated and with circular morphology typical of death cells (Figure 20.4-A).

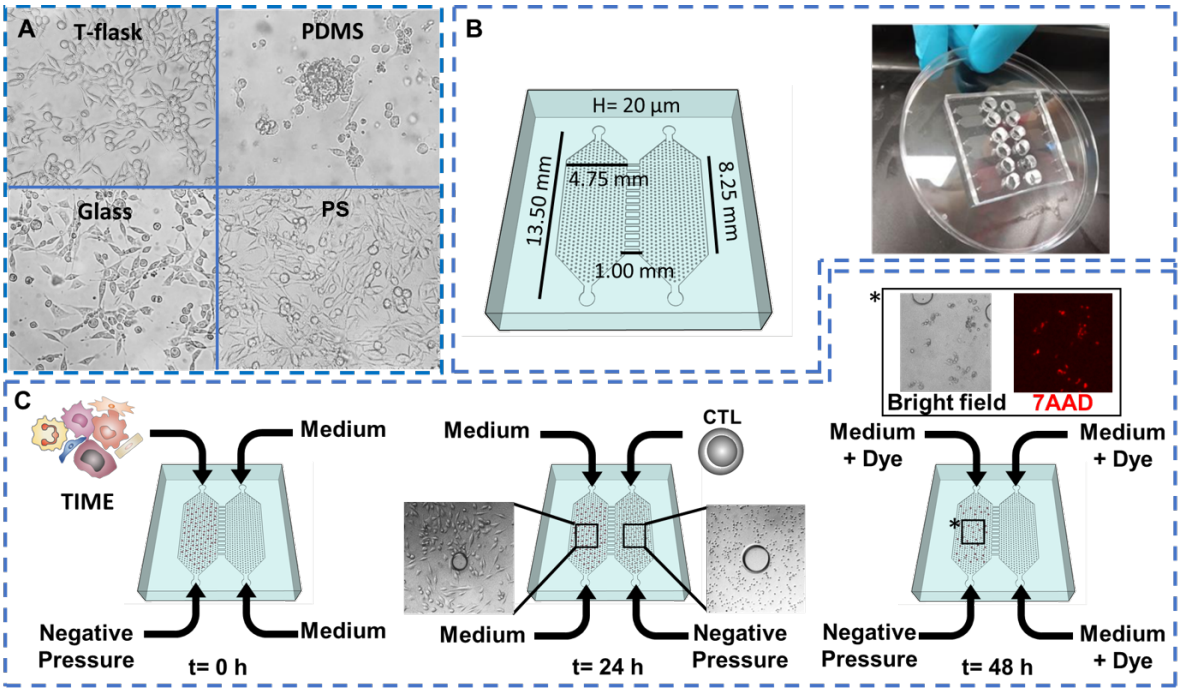

Figure 20.4: Schematic representation of the microfluidic cell chip is as a promising pre-clinical *ex vivo* alternative system to in vivo studies. (A) Substrate screening for the fabrication of microfluidic device. MC38 CRC cell seeding on PDMS, PS and Corning Glass, all coated with rat tail collagen, compared to the growth pattern in a typical T-flask. (B) Schematic representation of the PDMS-based microfluidic chip used in these experiments, as well as a photograph to show the use of large wells as a simple way for liquid insertion and pressure control of the system. (C) Schematic representation of the experimental sequence, following the chip preparation. TIME cells from tumors were seeded in the left chamber of the chip and allowed to adhere and grow. After 24 hours, the spleenocytes (Cytotoxic T Lymphocytes, CTL) from MC38-bearing C57BL/6J mice previously treated were introduced and co-cultured for another 24 hours. After this co-culture period the cell death was determined using 7AAD staining.

Having determined the best substrate to seal the PDMS-based device, the microfluidic structure was fabricated. The microfluidic device is composed of two parallel chambers connected by 10, 1 mm long, microchannels. The microfluidic devices were fabricated as arrays and chemically bonded to commercial Petri dishes as shown in Figure Figure 20.4-B.

The experimental procedure, depicted in Figure 20.4-C, consisted of chip sterilization and collagen coating followed by the loading of one of the microchambers with a cell suspension prepared with the tumor tissue harvested from MC38-bearing C57BL/6J mice. These cells are left in culture for 24 hours in order to allow the correct adhesion of the TIME cells as shown in the micrographs of Figure 20.4-C. After TIME cells adhere, the spleenocytes suspension obtained from the spleens of treated mice were loaded into the cell chip through a different inlet and maintained in co-culture for an additional 24 hours. The TIME cell death was inferred using fluorescence microscopy and the fluorescent death marker, 7AAD. To assess the potential synergistic effect between previously identified markers of the immune suppressive TIME and the nanovaccine, the growth medium was supplemented with the TAM inhibitor, Pexidartinib, at the time of spleen addition to the chip.

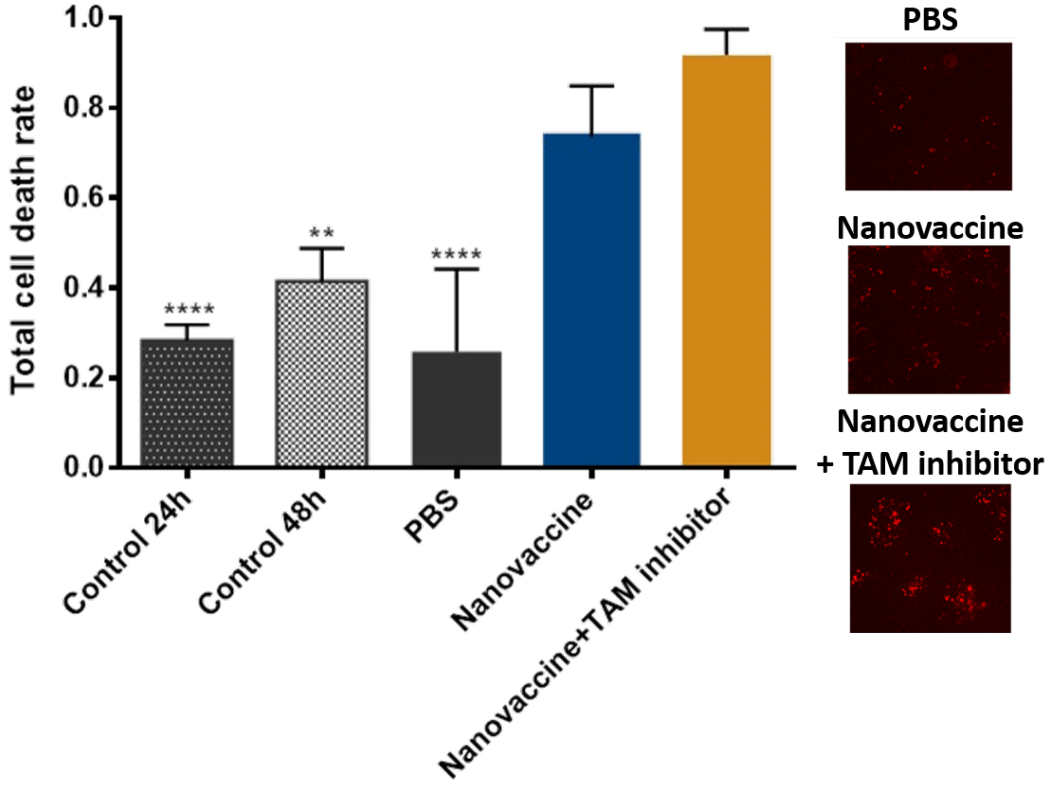

Figure 20.5: Microfluidic cell chip is a promising preclinical ex vivo alternative system to in vivo studies to screen the best anti-CRC treatment. Image J analysis of the percentage of TIME cell death in the microfluidic channel, following the incubation with medium, spleenocytes from PBS-treated MC38-bearing C57BL/6J mice, or spleenocytes obtained from MC38-bearing C57BL/6J mice previously immunized with nanovaccine, with or without the supplement of TAM inhibitor, Pexidartinib. Control 24 and Control 48 hours refers to the TIME cell dead, after the incubation with medium without the introduction of spleenocytes in the chip for the first and second days of culture, respectively. Data are presented as mean $\pm$ SD (N= 2, n = 2-3). Two-way ANOVA followed by Tukey Post-Hoc test. ****P $<$0.0001, **P $<$0.01. P values relative to Nanovaccine + Pexidartinib group. Micrographs represent an example of TIME dead cells in each of the treatment conditions tested. Micrograph contrast was enhanced for visualization purposes.

Figure 20.5 presents the results concerning TIME cell death in the microfluidic platform. During the initial 24 hours of cell culture, required for cell adhesion, where only TIME cells are presented in the chip, about 28% of the TIME cells are fluorescent. A relatively high TIME cell death is to be expected from primary cell cultures, which may be intensified by the shallowness of the microfluidic chip probably due to a lower nutrient availability when compared to the typical T-flask culture. Regarding the analogy between control assays at 24 and 48 hours, there is a higher variation of TIME cell death in the initial period of about 28% of cell death after 24 hours compared to 13% of cell death variation registered between the 24 and 48 hours of TIME culture in the microfluidic cell chip. This may suggest that the TIME cells may be adapting to the microfluidic culture environment. The co-culture assay of TIME cells and spleenocytes from PBS-treated MC38-bearing C57BL/6J mice for 24 hours, did not increase the TIME dead cell percentage. This indicates that these spleenocytes derived from mice treated with PBS do not present any or at least not significantly cytotoxic effect to the TIME, which is in line with the results of the in vivo study where the induced tumor grew to a significantly large size (Figure 20.3-B, C). On the

other hand, the co-culture of TIME cells with spleenocytes from vaccinated mice lead to stronger degree of TIME cell death (74%), compared to the co-culture assay with spleenocytes from PBS-treated mice (26%). These results are in line with the observations from the in vivo study (Figure 20.3), since the animals treated with the nanovaccine present an average tumor volume significantly lower than those presented by mice treated with PBS ($P < 0.0001$) (Figure 20.3-B, C). While the average tumor volume of the nanovaccine was 2.3-fold smaller than those obtained for PBS-treated mice for the in vivo assay (Figure 20.3-B, C), the TIME death percentage obtained from cytotoxic spleenocytes from vaccinated mice was 2.8-fold higher than the cell death obtained from the basal state spleenocytes in the microfluidic chip (Figure 20.4-D).

In addition, the main advantage of this microfluidic approach is to assess synergistic effects between different immune therapeutic approaches by targeting distinct biomarkers of tumor aggressiveness and related immune suppressive milieu. Accordingly, during the addition of spleenocytes from nanovaccine-treated mice the cell culture medium was supplemented with the TAM inhibitor, Pexidartinib. Also in line with the in vivo assay, the synergistic anti-tumor effect of therapeutic nanovaccine with the TAM blockade is highlighted as the TIME dead percentage increased with the addition of Pexidartinib (Figure 20.4-D). The modulation of CSF1/CSF1R signaling, which is involved in TAM survival, seems to be related to the reduction of immune suppressive TAM infiltrates and boosting of CD8+ effector T cell-mediated cytotoxic responses previously induced by vaccination [459, 461-463, 493-495].

Overall, this preclinical ex vivo complex model system based on a microfluidic cell chip was able to quantify increased levels of TIME cell death after incubation with spleenocytes collected from immunized mice, even in combination with Pexidartinib, being a suitable alternative to rapidly screen the potential synergistic effect between this nanovaccine and inhibitors of immune suppressive tumor immune evasion players, instead to considerably longer and expensive in vivo combinational studies.

20.4 Conclusions

In this work we report on the development of a microfluidic cell-culture platform as a preclinical ex vivo complex model system alternative to in vivo studies for the screening of potential immune therapeutic strategies using CRC as a model. As a proof of concept, this platform allowed for the successful culture of primary TIME cells, as well as, being a tool to screen the best anti-CRC therapy through the evaluation of the cell death after the co-culture of TIME cells with lymphocytes harvested from treated mice.

This system was able to quantify increased levels of TIME cell death under two different conditions: 1) co-culture of TIME cells and spleenocytes collected from immunized mice, and 2) co-culture of TIME cells and spleenocytes collected from immunized, in an environment supplemented with TAM inhibitor Pexidartinib; reproducing in vitro correlated results than the ones obtained in the in vivo study.

The similar conclusions concerning the efficiency of the treatment strategies demonstrate the potential of this microfluidic cell platform as a promising alternative to further rapidly screen the potential synergistic effect between this nanovaccine and inhibitors of the immune suppressive TIME, instead of longer and expensive in vivo combinational studies, using the same experimental conditions.

Chapter 21

Final Remarks - Microfluidic Applications for Colorectal Cancer Research

I believe the POINT4PAC project, was possibly the most interesting line of work I had the opportunity to participate in, as well as being the one with, in my opinion, the highest potential for a large impact in society.

Even though my role was more of a support role as an ”expert” in microfluidics, there was a huge time and effort investment. This led to three different methods which can have a positive contribution towards solving the cancer issue of the XXI century.

The phage display chip, proved to be a very interesting tool for the screening of possible therapeutic strategies, as well as to extract more fundamental information such as binding kinetics and internalization kinetics. The next step for this project would be the use of random libraries to perform a full on screening assay in pursuit of novel ligands, however this would require an alternative method of monitoring, in order to detect the limited number of successful hits. At the time of writing, there is one approach for this being developed at INESC-MN, through the use of impedance sensors, however the technology is not mature enough at this point in time. Another consideration for this approach is the inclusion of healthy cells as a negative control for the screening assay.

The basis for the assay to detect AK presented in this portion of the thesis may be used as thought of in the initial motivation, as a module to be coupled to the microfluidic cell culture chip presented in Chapter 18, or be used as a stand alone device to aid the typical culture of mammalian cells. It can also be adapted in future work for the multiplexed detection of several mammalian biomarkers in solution.

In regards to the nanovaccine screening, I believe that the use of primary cell lines directly from the animal provide a very interesting *ex vivo* approach to therapy development. In this work we only demonstrated one vaccine and one TAM inhibitor, however one can imagine the scaling of this process to include more drugs. Another potential addition to this work would be to co-culture the tumor cells with

cells from relevant tissues to assess toxicity during the screening.

Overall, I believe that once the hurdles presented by entities such as the FDA and other regulating authorities are overcome, there will be an increased interest of companies in this type of technology. This will not only expedite the development of novel therapies but also open future doors to a realistic approach for personalized medicine.

Part VI

Conclusions

Chapter 22

Conclusions

Finally we reach the end of the road, I will try to be brief as the road was long and tiring. Throughout this doctoral thesis I discussed a wide range of projects, where the full range of capabilities that microfluidic technology brings to the table are on display.

Microfluidics for bioprocess development

With the enzymatic platform I demonstrated that it was possible to not only optimize single step reactions using microfluidics technology, as well as the optimization of multi-step processes. It was possible to conduct production of L-DOPA for periods of over 50 h, however the best results were obtained in the initial 8 h of the process due to the reactor fouling. In addition to this, I showed the viability of the information obtained with the microfluidic device, by successfully increasing the scale to a bench-top system.

The results obtained in this portion of the thesis demonstrate the potential of microfluidic platforms for process optimization, however this is far from a complete system. To further develop this project, it would be interesting to include adequate forms of sensing for different process variables, in order to perform online monitoring of process conditions. Examples of this would be probes to measure pH and oxygen content in solution as these are important parameters in a wide variety of bioprocesses. Going back to the mention of dissolved oxygen, it would also be interesting to consider the possibility of other types of materials such as glass, plastics or some metals. The use of PDMS as a substrate has inherent advantages such as ease of prototyping, transparency and biological compatibility, however its' gas permeability and ease of adsorbing organic molecules may make it less than ideal in some cases. Once the chip is properly instrumented, one can consider the inclusion of controllers for an autonomous platform for rapid screening of production conditions.

Another interesting addition would be to use microfluidics to look into aspects of DSP. This has been heavily explored in the past by former colleagues of mine, Dr. Inês Pinto and Dr. Daniel Silva, as well with a minor contribution from myself. [185, 466, 467] But given the versatility of microfluidics technology, I believe it would be very interesting to be capable of looking at bioprocesses as a whole, instead of multiple puzzle fragments that are latter attempted to be fitted together.

Another interesting route to explore, is the possibility of scaling-out these devices, by having arrays of microreactors working in parallel as a means of production of valuable compounds in poor resource settings.

Portable biosensors for agricultural applications

Through the work developed for the grape biomarker measurements, I demonstrated the feasibility of multiplexing biochemical analysis on a single microfluidic platform, as well as including some sample preparation. This work encompasses the different types of assays that are possible to perform in a microfluidic environment by using enzyme activity, nanoparticle conjugation and an immunoassay on the same chip. If only there was a reason to include a nucleic acid based assay... By coupling the chip to thin-film photosensors and fabricating the necessary support system for the sensors I was able to create a portable lab-on-a-chip device capable of being used at the point of need.

To further explore this line of work, I would consider looking into performing this detection in the tree sap itself. Currently we are dependent on the tree to already have fruits of a reasonable sizes in order to extract juice for the analysis, by analyzing the tree sap it could be possible to have a year-round monitoring of the vine tree health. It would also be interesting to consider other infections and larger sample supplies, however this would require an industrial partner to achieve.

Other interesting avenues to improve on this work, would be to consider other plants beyond vine trees. Fruits like tomatoes or peas are not interesting targets in my opinion as the plants are seasonal and grow very quickly (¡6 months). However, there are other fruits such as oranges, apples, etc; where the tree takes several years to mature to the point of producing fruits. These types of plants are worth the cost of periodic testing as they are hard to replace. By changing the type of fruit, the sample treatment may have to be completely different, limiting the possibility of a generic chip for multi-plant assessment. However, it may be possible to group these into groups, for instance having a ”citrus chip”.

The portable prototype can also be improved as the coupling of the microfluidic chip to the platform is still manual. In addition to this, the optical setup inside the prototype can also be improved as well as the power management portion of the device. Overall the aesthetics of the device can also be improved.

Microfluidic devices in the fight against cancer

In the last part of this thesis I presented three different approaches where microfluidics technology can play a role in solving the cancer pandemic.

In the first approach I demonstrated the use of microfluidic technology as a screening device for random peptide sequences capable of recognizing, cancer specific, surface proteins. The device however is not complete, in order to truly identify specific cancer related proteins, a negative control has to be performed, either simultaneously with the first screening or afterwards with the positive hits of the first sample. This control sample will require the use of healthy cells, from at least the same tissue of the type of cancer, and probably with other cells from other body tissues depending on the administration strategy for the treatment, to exclude the possibility of the phages recognizing and damaging healthy

tissues of the patient. This will require the implementation of extra cell culture chambers. Another interesting approach to this project would be to conduct a study using primary cells obtained from mice or, ideally from human patients. This would discard any interferences that the tumor microenvironment may bring to the assay, as was done in Chapter 20.

Another avenue explored in this thesis, although very far from completion, is the detection of biomarkers for mammalian cell cultures. With the advent of organ-on-a-chip technology, these types of microfluidic modules have never been more necessary. Several groups around the world are working on these types of microfluidic chips for different tissue cultures, for different purposes such as disease modeling and drug discovery. [447] However, these devices suffer from low sample volumes, as well as, a very low number of cells, making traditional biochemical protocols difficult to employ. By adapting traditional bench-top protocols to microfluidic platforms, we are able to create very powerful tools for future health research. Further work to be done on this portion fo this thesis, besides fully optimizing the assay described in this work, would be the inclusion of other biomarker detection, as well as assays such as total protein detection, could be useful. The final step would be to instrument these microfluidic devices in a way that assays could be performed by pressing a button on a screen.

The final application for microfluidic technology explored in this thesis, was the use of primary cells to study the combinatorial effect of a nanoparticle vaccine and TME inhibitors to fight colorectal cancer. We successfully replicated the results obtained obtained using the tradition approach of *in vivo* assays, at a lesser cost of animal resources. This not only confirms the results obtained in the animal model, but also opens the possibility of being able to apply this approach to personalized medicine or even other diseases. By extracting a tissue sample from a patient, in the case of cancer, through a biopsy for example, one can directly assess the effect of different therapeutic combinations on the tumor cells and compare the results to healthy tissue. This type of approach would not only open the door to more efficient therapies, but also possibly diminishing some of the negative side effects. To improve on this line of work, it would be interesting to assess the effect for the Pexidartnib, or any other dug tested in the future on healthy tissue. I think it could also be interesting, in this case a 3 chamber chip with the CRC cells on one end, healthy tissue on the other and the spleenocytes in the middle to confirm that they migrate preferentially to the tumor cells chamber.

Final remarks on microfluidic technology

The diversity of these projects, as well as the rising numbers of microfluidic publications outside of journals entirely dedicated to the technology, are a testament to the versatility and power that microfluidics technology brings to the world. Hopefully, the contributions of microfluidics will increase in the future leading them to leave the lab bench and being used more frequently to solve problems in both industrial and clinical settings.

The advantages of microfluidic devices will be lost if we are not capable of providing the necessary instrumentation for the devices. It is hard to convince someone of using a microfluidic device for a given task if it is still necessary to have all the typical laboratory equipment and more to be capable of extracting information from the devices. Future applications should not only have the device, but also

the supporting apparatus in mind to convince the typical user of the utility of microfluidic technology.

When designing the aforementioned supporting apparatus and the assays as well, one should also take into consideration the number of steps a user will end up having to take. As an example if a microfluidic device for total protein determination involves 10 different steps, our colleagues will continue to perform the Bradford assay in a well plate.

All in all, I believe that microfluidic technology will continue to evolve at a rapid place and will soon become a common presence in different sectors of biotechnology, ranging from laboratory bench-top accessories for life science research, to point-of-need biosensors for the rapid diagnosis of diseases.

Bibliography

[1] E. K. Sackmann, A. L. Fulton, and D. J. Beebe. The present and future role of microfluidics in biomedical research. *Nature*, 507(7491):181–189, 2014.

[2] G. M. Whitesides. The origins and the future of microfluidics. *Nature*, 442(7101):368–373, 2006.

[3] C. Hansen and S. R. Quake. Microfluidics in structural biology: smaller, faster... better. *Current opinion in structural biology*, 13(5):538–544, 2003.

[4] J. Happel and H. Brenner. *Low Reynolds number hydrodynamics: with special applications to particulate media*, volume 1. Springer Science & Business Media, 2012.

[5] R. H. Pletcher, J. C. Tannehill, and D. Anderson. *Computational fluid mechanics and heat transfer*. CRC Press, 2012.

[6] C.-Y. Lee, W.-T. Wang, C.-C. Liu, and L.-M. Fu. Passive mixers in microfluidic systems: a review. *Chemical Engineering Journal*, 288:146–160, 2016.

[7] M. Hejazian and N.-T. Nguyen. A rapid magnetofluidic micromixer using diluted ferrofluid. *Micromachines*, 8(2):37, 2017.

[8] R. Soares, P. Novo, A. Azevedo, P. Fernandes, M. Aires-Barros, V. Chu, and J. Conde. On-chip sample preparation and analyte quantification using a microfluidic aqueous two-phase extraction coupled with an immunoassay. *Lab on a Chip*, 14(21):4284–4294, 2014.

[9] S. Hardt and T. Hahn. Microfluidics with aqueous two-phase systems. *Lab on a Chip*, 12(3): 434–442, 2012.

[10] C. W. Shields IV, C. D. Reyes, and G. P. López. Microfluidic cell sorting: a review of the advances in the separation of cells from debulking to rare cell isolation. *Lab on a Chip*, 15(5):1230–1249, 2015.

[11] Z. T. F. Yu, K. M. Aw Yong, and J. Fu. Microfluidic blood cell sorting: now and beyond. *Small*, 10 (9):1687–1703, 2014.

[12] A. Bussonnière, Y. Miron, M. Baudoin, O. B. Matar, M. Grandbois, P. Charette, and A. Renaudin. Cell detachment and label-free cell sorting using modulated surface acoustic waves (saws) in droplet-based microfluidics. *Lab on a Chip*, 14(18):3556–3563, 2014.

[13] L. Mazutis, J. Gilbert, W. L. Ung, D. A. Weitz, A. D. Griffiths, and J. A. Heyman. Single-cell analysis and sorting using droplet-based microfluidics. *Nature protocols*, 8(5):870–891, 2013.

[14] S. C. Shih, I. Barbulovic-Nad, X. Yang, R. Fobel, and A. R. Wheeler. Digital microfluidics with impedance sensing for integrated cell culture andanalysis. *Biosensors and Bioelectronics*, 42: 314–320, 2013.

[15] D. Witters, B. Sun, S. Begolo, J. Rodriguez-Manzano, W. Robles, and R. F. Ismagilov. Digital biology and chemistry. *Lab on a Chip*, 14(17):3225–3232, 2014.

[16] S. O. Rastegar and T. Gu. Empirical correlations for axial dispersion coefficient and peclet number in fixed-bed columns. *Journal of Chromatography A*, 1490:133–137, 2017.

[17] S. L. Anna. Droplets and bubbles in microfluidic devices. *Annual Review of Fluid Mechanics*, 48: 285–309, 2016.

[18] P. K. Mondal and S. Wongwises. Irreversibility analysis in a low peclet-number electroosmotic transport through an asymmetrically heated microchannel. *International Journal of Exergy*, 22(1): 29–53, 2017.

[19] S. G. Kandlikar, S. Colin, Y. Peles, S. Garimella, R. F. Pease, J. J. Brandner, and D. B. Tuckerman. Heat transfer in microchannels—2012 status and research needs. *Journal of Heat Transfer*, 135 (9):091001, 2013.

[20] R. Safavieh, A. Tamayol, and D. Juncker. Serpentine and leading-edge capillary pumps for microfluidic capillary systems. *Microfluidics and Nanofluidics*, 18(3):357–366, 2015.

[21] Y. Temiz and E. Delamarche. Capillary-driven microfluidic chips for miniaturized immunoassays: Efficient fabrication and sealing of chips using a “chip-olate” process. *Microchip Diagnostics: Methods and Protocols*, pages 25–36, 2017.

[22] P. Novo, F. Volpetti, V. Chu, and J. P. Conde. Control of sequential fluid delivery in a fully autonomous capillary microfluidic device. *Lab on a Chip*, 13(4):641–645, 2013.

[23] R. Safavieh and D. Juncker. Capillarics: pre-programmed, self-powered microfluidic circuits built from capillary elements. *Lab on a Chip*, 13(21):4180–4189, 2013.

[24] S.-J. Kim, X. Zhu, and S. Takayama. Gravity-driven fluid pumping and cell manipulation. In *Microtechnology for Cell Manipulation and Sorting*, pages 175–192. Springer, 2017.

[25] H. E. Abaci, K. Gledhill, Z. Guo, A. M. Christiano, and M. L. Shuler. Pumpless microfluidic platform for drug testing on human skin equivalents. *Lab on a Chip*, 15(3):882–888, 2015.

[26] E. Kondo, K.-I. Wada, K. Hosokawa, and M. Maeda. Microfluidic perfusion cell culture system confined in 35 mm culture dish for standard biological laboratories. *Journal of bioscience and bioengineering*, 118(3):356–358, 2014.

[27] A. Ishida, M. Fujii, T. Fujimoto, S. Sasaki, I. Yanagisawa, T. Hirofumi, and M. Tokeshi. A portable liquid chromatograph with a battery-operated compact electroosmotic pump and a microfluidic chip device with a reversed phase packed column. *Analytical Sciences*, 31(11):1163–1169, 2015.

[28] X. Wu, P. Ramiah Rajasekaran, and C. R. Martin. An alternating current electroosmotic pump based on conical nanopore membranes. *ACS nano*, 10(4):4637–4643, 2016.

[29] A. K. Au, N. Bhattacharjee, L. F. Horowitz, T. C. Chang, and A. Folch. 3d-printed microfluidic automation. *Lab on a chip*, 15(8):1934–1941, 2015.

[30] H.-H. Shen, S.-K. Fan, C.-J. Kim, and D.-J. Yao. Ewod microfluidic systems for biomedical applications. *Microfluidics and nanofluidics*, 16(5):965–987, 2014.

[31] M. La, S. J. Park, H. W. Kim, J. J. Park, K. T. Ahn, S. M. Ryew, and D. S. Kim. A centrifugal force-based serpentine micromixer (csm) on a plastic lab-on-a-disk for biochemical assays. *Microfluidics and nanofluidics*, 15(1):87–98, 2013.

[32] J. Loo, H. Kwok, C. Leung, S. Wu, I. Law, Y. Cheung, Y. Cheung, M. Chin, P. Kwan, M. Hui, et al. Sample-to-answer on molecular diagnosis of bacterial infection using integrated lab-on-a-disc. *Biosensors and Bioelectronics*, 93:212–219, 2017.

[33] E. Roy, G. Stewart, M. Mounier, L. Malic, R. Peytavi, L. Clime, M. Madou, M. Bossinot, M. G. Bergeron, and T. Veres. From cellular lysis to microarray detection, an integrated thermoplastic elastomer (tpe) point of care lab on a disc. *Lab on a Chip*, 15(2):406–416, 2015.

[34] K. Pitchaimani, B. C. Sapp, A. Winter, A. Gispanski, T. Nishida, and Z. H. Fan. Manufacturable plastic microfluidic valves using thermal actuation. *Lab on a Chip*, 9(21):3082–3087, 2009.

[35] J.-H. Kim, K.-H. Na, C. Kang, and Y.-S. Kim. A disposable thermopneumatic-actuated micropump stacked with pdms layers and ito-coated glass. *Sensors and Actuators A: Physical*, 120(2):365–369, 2005.

[36] C. Fu, Z. Rummler, and W. Schomburg. Magnetically driven micro ball valves fabricated by multilayer adhesive film bonding. *Journal of Micromechanics and microengineering*, 13(4):S96, 2003.

[37] H. Li, D. Roberts, J. Steyn, K. Turner, O. Yaglioglu, N. Hagood, S. Spearing, and M. Schmidt. Fabrication of a high frequency piezoelectric microvalve. *Sensors and Actuators A: Physical*, 111 (1):51–56, 2004.

[38] W. van der Wijngaart, H. Ask, P. Enoksson, and G. Stemme. A high-stroke, high-pressure electrostatic actuator for valve applications. *Sensors and Actuators A: Physical*, 100(2):264–271, 2002.

[39] X. Ma, W.-Y. Tseng, M. Eddings, P. Y. Keng, and R. M. Van Dam. A microreactor with phase-change microvalves for batch chemical synthesis at high temperatures and pressures. *Lab on a Chip*, 14(2):280–285, 2014.

[40] Y. Shiraki, K. Tsuruta, J. Morimoto, C. Ohba, A. Kawamura, R. Yoshida, R. Kawano, T. Uragami, and T. Miyata. Preparation of molecule-responsive microsized hydrogels via photopolymerization for smart microchannel microvalves. *Macromolecular rapid communications*, 36(6):515–519, 2015.

[41] E. Lee, H. Lee, S. I. Yoo, and J. Yoon. Photothermally triggered fast responding hydrogels incorporating a hydrophobic moiety for light-controlled microvalves. *ACS applied materials & interfaces*, 6(19):16949–16955, 2014.

[42] H. Bian, C. Shan, F. Chen, Q. Yang, Y. Li, and Q. Li. Miniaturized 3-d solenoid-type micro-heaters in coordination with 3-d microfluidics. *Journal of Microelectromechanical Systems*, 26(3):588–592, 2017.

[43] Y.-H. Chang, G.-B. Lee, F.-C. Huang, Y.-Y. Chen, and J.-L. Lin. Integrated polymerase chain reaction chips utilizing digital microfluidics. *Biomedical microdevices*, 8(3):215–225, 2006.

[44] J. Ditri, R. R. Pearson, R. Cadotte, J. W. Hahn, D. Fetterolf, M. McNulty, and D. Luppa. Gan unleashed: The benefits of microfluidic cooling. *IEEE Transactions on Semiconductor Manufacturing*, 29(4):376–383, 2016.

[45] P. Novo, G. Moulas, D. M. F. Prazeres, V. Chu, and J. P. Conde. Detection of ochratoxin a in wine and beer by chemiluminescence-based elisa in microfluidics with integrated photodiodes. *Sensors and Actuators B: Chemical*, 176:232–240, 2013.

[46] R. Soares, D. Santos, V. Chu, A. Azevedo, M. Aires-Barros, and J. Conde. A point-of-use microfluidic device with integrated photodetector array for immunoassay multiplexing: Detection of a panel of mycotoxins in multiple samples. *Biosensors and Bioelectronics*, 87:823–831, 2017.

[47] N. Luan and J. Yao. Surface plasmon resonance sensor based on exposed-core microstructured optical fiber placed with a silver wire. *IEEE Photonics Journal*, 8(1):1–8, 2016.

[48] D. Vercruysse, A. Dusa, R. Stahl, G. Vanmeerbeeck, K. de Wijs, C. Liu, D. Prodanov, P. Peumans, and L. Lagae. Three-part differential of unlabeled leukocytes with a compact lens-free imaging flow cytometer. *Lab on a Chip*, 15(4):1123–1132, 2015.

[49] A. I. Barbosa, P. Gehlot, K. Sidapra, A. D. Edwards, and N. M. Reis. Portable smartphone quantitation of prostate specific antigen (psa) in a fluoropolymer microfluidic device. *Biosensors and Bioelectronics*, 70:5–14, 2015.

[50] J. Yang, J.-H. Yu, J. R. Strickler, W.-J. Chang, and S. Gunasekaran. Nickel nanoparticle–chitosan-reduced graphene oxide-modified screen-printed electrodes for enzyme-free glucose sensing in portable microfluidic devices. *Biosensors and Bioelectronics*, 47:530–538, 2013.

[51] R. Liu, C. Zhang, and M. Liu. Open bipolar electrode-electrochemiluminescence imaging sensing using paper-based microfluidics. *Sensors and Actuators B: Chemical*, 216:255–262, 2015.

[52] T. A. Nguyen, T.-I. Yin, D. Reyes, and G. A. Urban. Microfluidic chip with integrated electrical cell-impedance sensing for monitoring single cancer cell migration in three-dimensional matrixes. *Analytical chemistry*, 85(22):11068–11076, 2013.

[53] M. Frankowski, P. Simon, N. Bock, A. El-Hasni, U. Schnakenberg, and J. Neukammer. Simultaneous optical and impedance analysis of single cells: A comparison of two microfluidic sensors with sheath flow focusing. *Engineering in Life Sciences*, 15(3):286–296, 2015.

[54] E. Albisetti, D. Petti, F. Damin, M. Cretich, A. Torti, M. Chiari, and R. Bertacco. Photolithographic bio-patterning of magnetic sensors for biomolecular recognition. *Sensors and Actuators B: Chemical*, 200:39–46, 2014.

[55] C. E. Krause, B. A. Otieno, G. W. Bishop, G. Phadke, L. Choquette, R. V. Lalla, D. E. Peterson, and J. F. Rusling. Ultrasensitive microfluidic array for serum pro-inflammatory cytokines and c-reactive protein to assess oral mucositis risk in cancer patients. *Analytical and bioanalytical chemistry*, 407(23):7239, 2015.

[56] J. Devkota, G. Kokkinis, T. Berris, M. Jamalieh, S. Cardoso, F. Cardoso, H. Srikanth, M. Phan, and I. Giouroudi. A novel approach for detection and quantification of magnetic nanomarkers using a spin valve gmr-integrated microfluidic sensor. *RSC Adv.*, 5(63):51169–51175, 2015.

[57] E. J. Brás, V. Chu, M. R. Aires-Barros, J. P. Conde, and P. Fernandes. A microfluidic platform for physical entrapment of yeast cells with continuous production of invertase. *Journal of Chemical Technology and Biotechnology*, 92(2):334–341, 2017.

[58] L. D. Garza-García, E. García-López, S. Camacho-León, M. del Refugio Rocha-Pizaña, F. López-Pacheco, J. López-Meza, D. Araiz-Hernández, E. J. Tapia-Mejía, G. Trujillo-de Santiago, C. A. Rodríguez-González, et al. Continuous flow micro-bioreactors for the production of biopharmaceuticals: the effect of geometry, surface texture, and flow rate. *Lab on a Chip*, 14(7):1320–1329, 2014.

[59] S. Rameez, S. S. Mostafa, C. Miller, and A. A. Shukla. High-throughput miniaturized bioreactors for cell culture process development: Reproducibility, scalability, and control. *Biotechnology progress*, 30(3):718–727, 2014.

[60] P. Žnidaršič-Plazl. The promises and the challenges of biotransformations in microflow. *Biotechnology journal*, 14(8):1800580, 2019.

[61] L. Tamborini, P. Fernandes, F. Paradisi, and F. Molinari. Flow bioreactors as complementary tools for biocatalytic process intensification. *Trends in biotechnology*, 36(1):73–88, 2018.

[62] A. Giannakopoulou, E. Gkantzou, A. Polydera, and H. Stamatis. Multienzymatic nanoassemblies: Recent progress and applications. *Trends in biotechnology*, 38(2):202–216, 2020.

[63] T. Honda, H. Yamaguchi, and M. Miyazaki. Development of enzymatic reactions in miniaturized reactors. *Applied Bioengineering: Innovations and Future Directions*, 5, 2017.

[64] M. Hartmann and X. Kostrov. Immobilization of enzymes on porous silicas–benefits and challenges. *Chemical Society Reviews*, 42(15):6277–6289, 2013.

[65] A. Küchler, J. Adamcik, R. Mezzenga, A. D. Schlüter, and P. Walde. Enzyme immobilization on silicate glass through simple adsorption of dendronized polymer–enzyme conjugates for localized enzymatic cascade reactions. *RSC Advances*, 5(55):44530–44544, 2015.

[66] S. Akay, R. Heils, H. K. Trieu, I. Smirnova, and O. Yesil-Celiktas. An injectable alginate-based hydrogel for microfluidic applications. *Carbohydrate Polymers*, 2017.

[67] C. Altinkaynak, S. Tavlasoglu, I. Ocsoy, et al. A new generation approach in enzyme immobilization: Organic-inorganic hybrid nanoflowers with enhanced catalytic activity and stability. *Enzyme and Microbial Technology*, 93:105–112, 2016.

[68] X. Wu, M. Hou, and J. Ge. Metal–organic frameworks and inorganic nanoflowers: a type of emerging inorganic crystal nanocarrier for enzyme immobilization. *Catalysis Science & Technology*, 5 (12):5077–5085, 2015.

[69] D. Valikhani, J. M. Bolivar, M. Viefhues, D. N. McIlroy, E. X. Vrouwe, and B. Nidetzky. A spring in performance: silica nanosprings boost enzyme immobilization in microfluidic channels. *ACS applied materials & interfaces*, 9(40):34641–34649, 2017.

[70] C. Timm and C. M. Niemeyer. Assembly and purification of enzyme-functionalized dna origami structures. *Angewandte Chemie International Edition*, 54(23):6745–6750, 2015.

[71] F. Kazenwadel, M. Franzreb, and B. Rapp. Synthetic enzyme supercomplexes: co-immobilization of enzyme cascades. *Analytical Methods*, 7(10):4030–4037, 2015.

[72] C. Cui, H. Chen, B. Chen, and T. Tan. Genipin cross-linked glucose oxidase and catalase multienzyme for gluconic acid synthesis. *Applied biochemistry and biotechnology*, 181(2):526–535, 2017.

[73] Y. Bi, H. Zhou, H. Jia, and P. Wei. Polydopamine-mediated preparation of an enzyme-immobilized microreactor for the rapid production of wax ester. *RSC Advances*, 7(20):12283–12291, 2017.

[74] H. R. Luckarift, B. S. Ku, J. S. Dordick, and J. C. Spain. Silica-immobilized enzymes for multi-step synthesis in microfluidic devices. *Biotechnology and bioengineering*, 98(3):701–705, 2007.

[75] R. A. Luz, A. R. Pereira, J. C. de Souza, F. C. Sales, and F. N. Crespilho. Enzyme biofuel cells: thermodynamics, kinetics and challenges in applicability. *ChemElectroChem*, 1(11):1751–1777, 2014.

[76] R. A. Escalona-Villalpando, R. C. Reid, R. D. Milton, L. Arriaga, S. D. Minteer, and J. Ledesma-García. Improving the performance of lactate/oxygen biofuel cells using a microfluidic design. *Journal of Power Sources*, 342:546–552, 2017.

[77] D. Desmaële, L. Renaud, and S. Tingry. A wireless sensor powered by a flexible stack of membraneless enzymatic biofuel cells. *Sensors and Actuators B: Chemical*, 220:583–589, 2015.

[78] R. C. Lo. Application of microfluidics in chemical engineering. *Chem Eng Process Technol*, 442: 368–373, 2013.

[79] X. Li, W. Chen, G. Liu, W. Lu, and J. Fu. Continuous-flow microfluidic blood cell sorting for unprocessed whole blood using surface-micromachined microfiltration membranes. *Lab on a Chip*, 14 (14):2565–2575, 2014.

[80] L. Schmid, D. A. Weitz, and T. Franke. Sorting drops and cells with acoustics: acoustic microfluidic fluorescence-activated cell sorter. *Lab on a Chip*, 14(19):3710–3718, 2014.

[81] T. M. Geislinger and T. Franke. Hydrodynamic lift of vesicles and red blood cells in flow—from fåhræus & lindqvist to microfluidic cell sorting. *Advances in colloid and interface science*, 208: 161–176, 2014.

[82] P. A. Levkin, S. Eeltink, T. R. Stratton, R. Brennen, K. Robotti, H. Yin, K. Killeen, F. Svec, and J. M. Fréchet. Monolithic porous polymer stationary phases in polyimide chips for the fast high-performance liquid chromatography separation of proteins and peptides. *Journal of Chromatography A*, 1200(1):55–61, 2008.

[83] R. Knob, V. Sahore, M. Sonker, and A. T. Woolley. Advances in monoliths and related porous materials for microfluidics. *Biomicrofluidics*, 10(3):032901, 2016.

[84] T. Yasui, S. Rahong, K. Motoyama, T. Yanagida, Q. Wu, N. Kaji, M. Kanai, K. Doi, K. Nagashima, M. Tokeshi, et al. Dna manipulation and separation in sublithographic-scale nanowire array. *ACS nano*, 7(4):3029–3035, 2013.

[85] C. R. Reedy, J. M. Bienvenue, L. Coletta, B. C. Strachan, N. Bhatri, S. Greenspoon, and J. P. Landers. Volume reduction solid phase extraction of dna from dilute, large-volume biological samples. *Forensic science international: genetics*, 4(3):206–212, 2010.

[86] A. S. Chan, M. K. Danquah, D. Agyei, P. G. Hartley, and Y. Zhu. A parametric study of a monolithic microfluidic system for on-chip biomolecular separation. *Separation Science and Technology*, 49 (6):854–860, 2014.

[87] I. F. Pinto, R. R. Soares, S. A. Rosa, M. R. Aires-Barros, V. Chu, J. P. Conde, and A. M. Azevedo. High-throughput nanoliter-scale analysis and optimization of multimodal chromatography for the capture of monoclonal antibodies. *Analytical chemistry*, 88(16):7959–7967, 2016.

[88] A. G. Deshpande, N. J. Darton, K. Yunus, A. C. Fisher, and N. K. Slater. In situ fabrication of a microfluidic device for immobilised metal affinity sensing. *New biotechnology*, 29(4):494–501, 2012.

[89] M. He, Y. Zeng, A. B. Jemere, and D. J. Harrison. Tunable thick polymer coatings for on-chip electrophoretic protein and peptide separation. *Journal of Chromatography A*, 1241:112–116, 2012.

[90] M. Jacinto, R. Soares, A. Azevedo, V. Chu, A. Tover, J. Conde, and M. Aires-Barros. Optimization and miniaturization of aqueous two phase systems for the purification of recombinant human immunodeficiency virus-like particles from a cho cell supernatant. *Separation and Purification Technology*, 154:27–35, 2015.

[91] U. Novak, M. Lakner, I. Plazl, and P. Nidarsic-plazl. Experimental studies and modeling of [alpha]-amylase aqueous two-phase extraction within a microfluidic device. *Microfluidics and Nanofluidics*, 19(1):75, 2015.

[92] E. Espitia-Saloma, P. Vázquez-Villegas, O. Aguilar, and M. Rito-Palomares. Continuous aqueous two-phase systems devices for the recovery of biological products. *Food and Bioproducts Processing*, 92(2):101–112, 2014.

[93] V. Sahore, S. Kumar, C. Rogers, J. Jensen, M. Sonker, and A. Woolley. Pressure-actuated microfluidic devices for electrophoretic separation of pre-term birth biomarkers. *Analytical and bioanalytical chemistry*, 408(2):599–607, 2016.

[94] L. Ge, S. Wang, S. Ge, J. Yu, M. Yan, N. Li, and J. Huang. Electrophoretic separation in a microfluidic paper-based analytical device with an on-column wireless electrogenerated chemiluminescence detector. *Chemical Communications*, 50(43):5699–5702, 2014.

[95] T.-C. Chao and N. Hansmeier. Microfluidic devices for high-throughput proteome analyses. *Proteomics*, 13(3-4):467–479, 2013.

[96] M. Safdar, J. Sproß, and J. Jänis. Microscale immobilized enzyme reactors in proteomics: latest developments. *Journal of Chromatography A*, 1324:1–10, 2014.

[97] H. Yamaguchi and M. Miyazaki. Enzyme-immobilized reactors for rapid and efficient sample preparation in ms-based proteomic studies. *Proteomics*, 13(3-4):457–466, 2013.

[98] A. Kecskemeti and A. Gaspar. Preparation and characterization of a packed bead immobilized trypsin reactor integrated into a pdms microfluidic chip for rapid protein digestion. *Talanta*, 166: 275–283, 2017.

[99] Y. Li, L. Yan, Y. Liu, K. Qian, B. Liu, P. Yang, and B. Liu. High-efficiency nano/micro-reactors for protein analysis. *Rsc Advances*, 5(2):1331–1342, 2015.

[100] F.-G. Banica. *Chemical sensors and biosensors: fundamentals and applications*. John Wiley & Sons, 2012.

[101] D. Mark, S. Haeberle, G. Roth, F. Von Stetten, and R. Zengerle. Microfluidic lab-on-a-chip platforms: requirements, characteristics and applications. In *Microfluidics Based Microsystems*, pages 305–376. Springer, 2010.

[102] T.-H. Kim, J. Park, C.-J. Kim, and Y.-K. Cho. Fully integrated lab-on-a-disc for nucleic acid analysis of food-borne pathogens. *Analytical chemistry*, 86(8):3841–3848, 2014.

[103] R. Prakash, K. Pabbaraju, S. Wong, A. Wong, R. Tellier, and K. Kaler. Droplet microfluidic chip based nucleic acid amplification and real-time detection of influenza viruses. *Journal of The Electrochemical Society*, 161(2):B3083–B3093, 2014.

[104] M. H. Shamsi and H.-B. Kraatz. The effects of oligonucleotide overhangs on the surface hybridization in dna films: an impedance study. *Analyst*, 136(15):3107–3112, 2011.

[105] D. Berdat, A. C. M. Rodríguez, F. Herrera, and M. A. Gijs. Label-free detection of dna with interdigitated micro-electrodes in a fluidic cell. *Lab on a Chip*, 8(2):302–308, 2008.

[106] J. W. Parks, M. A. Olson, J. Kim, D. Ozcelik, H. Cai, R. Carrion Jr, J. Patterson, R. Mathies, A. Hawkins, and H. Schmidt. Integration of programmable microfluidics and on-chip fluorescence detection for biosensing applications. *Biomicrofluidics*, 8(5):054111, 2014.

[107] R. M. Umek, S. W. Lin, J. Vielmetter, R. H. Terbrueggen, B. Irvine, C. Yu, J. F. Kayyem, H. Yowanto, G. F. Blackburn, D. H. Farkas, et al. Electronic detection of nucleic acids: a versatile platform for molecular diagnostics. *The Journal of Molecular Diagnostics*, 3(2):74–84, 2001.

[108] H. Tachibana, M. Saito, K. Tsuji, K. Yamanaka, E. Tamiya, et al. Self-propelled continuous-flow pcr in capillary-driven microfluidic device: microfluidic behavior and dna amplification. *Sensors and Actuators B: Chemical*, 206:303–310, 2015.

[109] D. Moschou, N. Vourdas, G. Kokkoris, G. Papadakis, J. Parthenios, S. Chatzandroulis, and A. Tserepi. All-plastic, low-power, disposable, continuous-flow pcr chip with integrated microheaters for rapid dna amplification. *Sensors and Actuators B: Chemical*, 199:470–478, 2014.

[110] J. Das, K. B. Cederquist, A. A. Zaragoza, P. E. Lee, E. H. Sargent, and S. O. Kelley. An ultrasensitive universal detector based on neutralizer displacement. *Nature chemistry*, 4(8):642–648, 2012.

[111] S. R. Shin, Y. S. Zhang, D.-J. Kim, A. Manbohi, H. Avci, A. Silvestri, J. Aleman, N. Hu, T. Kilic, W. Keung, et al. Aptamer-based microfluidic electrochemical biosensor for monitoring cell-secreted trace cardiac biomarkers. *Analytical chemistry*, 88(20):10019–10027, 2016.

[112] P. He, V. Oncescu, S. Lee, I. Choi, and D. Erickson. Label-free electrochemical monitoring of vasopressin in aptamer-based microfluidic biosensors. *Analytica chimica acta*, 759:74–80, 2013.

[113] X. Weng and S. Neethirajan. A microfluidic biosensor using graphene oxide and aptamer-functionalized quantum dots for peanut allergen detection. *Biosensors and Bioelectronics*, 85: 649–656, 2016.

[114] P. Zuo, X. Li, D. C. Dominguez, and B.-C. Ye. A pdms/paper/glass hybrid microfluidic biochip integrated with aptamer-functionalized graphene oxide nano-biosensors for one-step multiplexed pathogen detection. *Lab on a Chip*, 13(19):3921–3928, 2013.

[115] R. Soares, D. Ramadas, V. Chu, M. Aires-Barros, J. Conde, A. Viana, and A. Cascalheira. An ultrarapid and regenerable microfluidic immunoassay coupled with integrated photosensors for point-of-use detection of ochratoxin a. *Sensors and Actuators B: Chemical*, 235:554–562, 2016.

[116] J. C. Vidal, L. Bonel, P. Duato, and J. R. Castillo. Improved electrochemical competitive immunosensor for ochratoxin a with a biotinylated monoclonal antibody capture probe and colloidal gold nanostructuring. *Analytical Methods*, 3(4):977–984, 2011.

[117] N. Madaboosi, R. R. Soares, V. Chu, and J. P. Conde. A microfluidic immunoassay platform for the detection of free prostate specific antigen: a systematic and quantitative approach. *Analyst*, 140(13):4423–4433, 2015.

[118] Y.-S. Fang, S.-Y. Chen, X.-J. Huang, L.-S. Wang, H.-Y. Wang, and J.-F. Wang. Simple approach for ultrasensitive electrochemical immunoassay of clostridium difficile toxin b detection. *Biosensors and Bioelectronics*, 53:238–244, 2014.

[119] S. Viswanathan, L.-c. Wu, M.-R. Huang, and J.-a. A. Ho. Electrochemical immunosensor for cholera toxin using liposomes and poly (3, 4-ethylenedioxythiophene)-coated carbon nanotubes. *Analytical chemistry*, 78(4):1115–1121, 2006.

[120] C. Chai and P. Takhistov. Label-free toxin detection by means of time-resolved electrochemical impedance spectroscopy. *Sensors*, 10(1):655–669, 2010.

[121] C. Chai, J. Lee, and P. Takhistov. Direct detection of the biological toxin in acidic environment by electrochemical impedimetric immunosensor. *Sensors*, 10(12):11414–11427, 2010.

[122] J. Heo and R. M. Crooks. Microfluidic biosensor based on an array of hydrogel-entrapped enzymes. *Analytical chemistry*, 77(21):6843–6851, 2005.

[123] D. Agustini, M. F. Bergamini, and L. H. Marcolino-Junior. Tear glucose detection combining microfluidic thread based device, amperometric biosensor and micro flow injection analysis. *Biosensors and Bioelectronics*, 2017.

[124] S. Xu, H. Qi, S. Zhou, X. Zhang, and C. Zhang. Mediatorless amperometric bienzyme glucose biosensor based on horseradish peroxidase and glucose oxidase cross-linked to multiwall carbon nanotubes. *Microchimica Acta*, 181(5-6):535–541, 2014.

[125] J. Wang. Glucose biosensors: 40 years of advances and challenges. *Electroanalysis*, 13(12):983, 2001.

[126] D. Itoh, F. Sassa, T. Nishi, Y. Kani, M. Murata, and H. Suzuki. Droplet-based microfluidic sensing system for rapid fish freshness determination. *Sensors and Actuators B: chemical*, 171:619–626, 2012.

[127] F. Liu, Y. Piao, J. S. Choi, and T. S. Seo. Three-dimensional graphene micropillar based electrochemical sensor for phenol detection. *Biosensors and Bioelectronics*, 50:387–392, 2013.

[128] J. Horak, C. Dincer, H. Bakirci, and G. Urban. A disposable dry film photoresist-based microcapillary immunosensor chip for rapid detection of epstein–barr virus infection. *Sensors and Actuators B: Chemical*, 191:813–820, 2014.

[129] M. A. Ali, P. R. Solanki, M. K. Patel, H. Dhayani, V. V. Agrawal, R. John, and B. D. Malhotra. A highly efficient microfluidic nano biochip based on nanostructured nickel oxide. *Nanoscale*, 5(7): 2883–2891, 2013.

[130] M. A. Ali, S. Srivastava, K. Mondal, P. M. Chavhan, V. V. Agrawal, R. John, A. Sharma, and B. D. Malhotra. A surface functionalized nanoporous titania integrated microfluidic biochip. *Nanoscale*, 6(22):13958–13969, 2014.

[131] M. Bäcker, D. Rakowski, A. Poghossian, M. Biselli, P. Wagner, and M. J. Schöning. Chip-based amperometric enzyme sensor system for monitoring of bioprocesses by flow-injection analysis. *Journal of biotechnology*, 163(4):371–376, 2013.

[132] F. Bettazzi, E. Hamid-Asl, C. L. Esposito, C. Quintavalle, N. Formisano, S. Laschi, S. Catuogno, M. Iaboni, G. Marrazza, M. Mascini, et al. Electrochemical detection of mirna-222 by use of a magnetic bead-based bioassay. *Analytical and bioanalytical chemistry*, 405(2-3):1025–1034, 2013.

[133] Y.-J. Yoon, K. H. H. Li, Y. Z. Low, J. Yoon, and S. H. Ng. Microfluidics biosensor chip with integrated screen-printed electrodes for amperometric detection of nerve agent. *Sensors and Actuators B: Chemical*, 198:233–238, 2014.

[134] M. Mehling and S. Tay. Microfluidic cell culture. *Current opinion in biotechnology*, 25:95–102, 2014.

[135] H. Tazawa, K. Sato, A. Tsutiya, M. Tokeshi, and R. Ohtani-Kaneko. A microfluidic cell culture system for monitoring of sequential changes in endothelial cells after heat stress. *Thrombosis research*, 136(2):328–334, 2015.

[136] S. Giulitti, E. Magrofuoco, L. Prevedello, and N. Elvassore. Optimal periodic perfusion strategy for robust long-term microfluidic cell culture. *Lab on a Chip*, 13(22):4430–4441, 2013.

[137] J. T. S. Fernandes, S. Tenreiro, A. Gameiro, V. Chu, T. F. Outeiro, and J. P. Conde. Modulation of alpha-synuclein toxicity in yeast using a novel microfluidic-based gradient generator. *Lab on a Chip*, 14(20):3949–3957, 2014.

[138] M. Junkin and S. Tay. Microfluidic single-cell analysis for systems immunology. *Lab on a Chip*, 14 (7):1246–1260, 2014.

[139] A. E. Fischer, S. K. Wu, J. B. Proescher, A. Rotem, C. B. Chang, H. Zhang, Y. Tao, T. S. Mehoke, P. M. Thielen, A. O. Kolawole, et al. A high-throughput drop microfluidic system for virus culture and analysis. *Journal of virological methods*, 213:111–117, 2015.

[140] E. W. Esch, A. Bahinski, and D. Huh. Organs-on-chips at the frontiers of drug discovery. *Nature reviews Drug discovery*, 14(4):248–260, 2015.

[141] A. Polini, L. Prodanov, N. S. Bhise, V. Manoharan, M. R. Dokmeci, and A. Khademhosseini. Organs-on-a-chip: a new tool for drug discovery. *Expert opinion on drug discovery*, 9(4):335–352, 2014.

[142] Š. Selimović, M. R. Dokmeci, and A. Khademhosseini. Organs-on-a-chip for drug discovery. *Current opinion in pharmacology*, 13(5):829–833, 2013.

[143] A. Marsano, C. Conficconi, M. Lemme, P. Occhetta, E. Gaudiello, E. Votta, G. Cerino, A. Redaelli, and M. Rasponi. Beating heart on a chip: a novel microfluidic platform to generate functional 3d cardiac microtissues. *Lab on a Chip*, 16(3):599–610, 2016.

[144] N. S. Bhise, V. Manoharan, S. Massa, A. Tamayol, M. Ghaderi, M. Miscuglio, Q. Lang, Y. S. Zhang, S. R. Shin, G. Calzone, et al. A liver-on-a-chip platform with bioprinted hepatic spheroids. *Biofabrication*, 8(1):014101, 2016.

[145] S. Kim, S. C. LesherPerez, C. Yamanishi, J. M. Labuz, B. Leung, S. Takayama, et al. Pharmacokinetic profile that reduces nephrotoxicity of gentamicin in a perfused kidney-on-a-chip. *Biofabrication*, 8(1):015021, 2016.

[146] G. T. Kovacs, N. I. Maluf, and K. E. Petersen. Bulk micromachining of silicon. *Proceedings of the IEEE*, 86(8):1536–1551, 1998.

[147] R. Antonello and R. Oboe. *MEMS gyroscopes for consumer and industrial applications.* InTech, 2011.

[148] T. Rehg and B. Higgins. Evaporative convection in spin coating. 03 2014.

[149] D. B. Hall, P. Underhill, and J. M. Torkelson. Spin coating of thin and ultrathin polymer films. *Polymer Engineering & Science*, 38(12):2039–2045, 1998.

[150] C. F. Powell, J. H. Oxley, J. M. Blocher, and J. Klerer. Vapor deposition. *Journal of The Electrochemical Society*, 113(10):266C–269C, 1966.

[151] G. Sáfrán, C. Reinhard, A. Ehiasarian, P. Barna, L. Székely, O. Geszti, and P. E. Hovsepian. Influence of the bias voltage on the structure and mechanical performance of nanoscale multilayer cr al yn/ cr n physical vapor deposition coatings. *Journal of Vacuum Science & Technology A: Vacuum, Surfaces, and Films*, 27(2):174–182, 2009.

[152] Y. Purandare, A. Ehiasarian, and P. E. Hovsepian. Deposition of nanoscale multilayer crn/nbn physical vapor deposition coatings by high power impulse magnetron sputtering. *Journal of Vacuum Science & Technology A: Vacuum, Surfaces, and Films*, 26(2):288–296, 2008.

[153] D. Mattox. Fundamentals of ion plating. *Journal of Vacuum Science and Technology*, 10(1):47–52, 1973.

[154] S. Aisenberg and R. Chabot. Physics of ion plating and ion beam deposition. *Journal of Vacuum Science and Technology*, 10(1):104–107, 1973.

[155] W. Ensinger, J. Klein, P. Usedom, and B. Rauschenbach. Characteristic features of an apparatus for plasma immersion ion implantation and physical vapour deposition. *Surface and Coatings Technology*, 93(2-3):175–180, 1997.

[156] A. Rocket. Lecture notes: Sputter deposition of thin films, 1998.

[157] A. Baptista, F. Silva, J. Porteiro, J. Míguez, and G. Pinto. Sputtering physical vapour deposition (pvd) coatings: A critical review on process improvement and market trend demands. *Coatings*, 8 (11):402, 2018.

[158] P. O'Brien. Chemical vapor deposition. 2001.

[159] P. V. Pham. Atmospheric pressure chemical vapor deposition of graphene. *Chemical Vapor Deposition for Nanotechnology*, page 115, 2019.

[160] J.-O. Carlsson and P. M. Martin. Chemical vapor deposition. In *Handbook of Deposition Technologies for Films and Coatings*, pages 314–363. Elsevier, 2010.

[161] N.-T. Nguyen. *Micromixers: fundamentals, design and fabrication*. William Andrew, 2011.

[162] R. Zaouk, B. Y. Park, and M. J. Madou. Introduction to microfabrication techniques. In *Microfluidic Techniques*, pages 5–15. Springer, 2006.

[163] J. P. Singh, R. Bhardwaj, A. Sharma, B. Kaur, S. O. Won, S. Gautam, and K. H. Chae. Fabrication of magnetic tunnel junctions. In *Advanced Applications in Manufacturing Enginering*, pages 53–77. Elsevier, 2019.

[164] Learn about every aspect of photoresist. URL `https://www.elinfor.com/knowledge/learn-about-every-aspect-of-photoresist-2-p-11067`.

[165] D. Qin, Y. Xia, and G. M. Whitesides. Soft lithography for micro-and nanoscale patterning. *Nature protocols*, 5(3):491, 2010.

[166] Machining recommendations for semi-finished engineering plastics, . URL `https://www.curbellplastics.com/Research-Solutions/Technical-Resources/Technical-Resources/Machining-Engineering-Plastics`.

[167] Y. Hou, D. Zhang, M. Luo, and B. Wu. A cutting parameters selection method in milling aero-engine parts based on process condition matching. *Advances in Mechanical Engineering*, 5: 157343, 2013.

[168] S. M. Sze and K. K. Ng. *Physics of semiconductor devices*. John wiley & sons, 2006.

[169] M. Arjmand and S. Sadeghi. Nitrogen-doped carbon nanotube/polymer nanocomposites towards thermoelectric applications. *Thermoelectrics for Power Generation: A Look at Trends in the Technology*, page 323, 2016.

[170] A. J. Flewitt. Hydrogenated amorphous silicon thin-film transistors (a-si: H tfts). *Handbook of Visual Display Technology*, pages 1–18, 2014.

[171] B. Van Zeghbroeck. Principles of semiconductor devices. *Colarado University*, 34, 2004.

[172] B. Lipovšek, A. Jóskowiak, J. Krč, M. Topič, D. Prazeres, V. Chu, and J. Conde. Characterisation of hydrogenated silicon–carbon alloy filters with different carbon composition for on-chip fluorescence detection of biomolecules. *Sensors and Actuators A: Physical*, 163(1):96–100, 2010.

[173] D. R. Santos, R. R. Soares, V. Chu, and J. P. Conde. Performance of hydrogenated amorphous silicon thin film photosensors at ultra-low light levels: towards attomole sensitivities in lab-on-chip biosensing applications. *IEEE Sensors Journal*, 17(21):6895–6903, 2017.

[174] Pn junctions. URL `http://gy.kimiq.com/energy-band-diagram-for-pn-junction-diode/`.

[175] A. Jameson, L. Martinelli, and N. Pierce. Optimum aerodynamic design using the navier–stokes equations. *Theoretical and computational fluid dynamics*, 10(1-4):213–237, 1998.

[176] A. Bader, J. Chhugani, P. Dubey, S. Junkins, S. Lyalin, T. Morrison, D. Ragozin, A. Ryzhova, S. Sidorov, A. Soupikov, et al. Game physics performance on the larrabee architecture. *Intel white paper*, 2008.

[177] Navier–stokes equation, . URL `https://www.claymath.org/millennium-problems/navier%E2%80%93stokes-equation`.

[178] S. Berg, A. Cense, J. Hofman, and R. Smits. Flow in porous media with slip boundary condition. *Society of Core Analysts, Calgary, Canada. SCA-2007-13*, 2007.

[179] E. Lauga, M. P. Brenner, and H. A. Stone. Microfluidics: the no-slip boundary condition. *arXiv preprint cond-mat/0501557*, 2005.

[180] J.-J. Shu, J. B. M. Teo, and W. K. Chan. A new model for fluid velocity slip on a solid surface. *Soft Matter*, 12(40):8388–8397, 2016.

[181] J. V. Sehy, J. J. Ackerman, and J. J. Neil. Apparent diffusion of water, ions, and small molecules in the xenopus oocyte is consistent with brownian displacement. *Magnetic Resonance in Medicine: An Official Journal of the International Society for Magnetic Resonance in Medicine*, 48(1):42–51, 2002.

[182] M. A. Eddings, M. A. Johnson, and B. K. Gale. Determining the optimal pdms–pdms bonding technique for microfluidic devices. *Journal of Micromechanics and Microengineering*, 18(6):067001, 2008.

[183] S. Bhattacharya, A. Datta, J. M. Berg, and S. Gangopadhyay. Studies on surface wettability of poly (dimethyl) siloxane (pdms) and glass under oxygen-plasma treatment and correlation with bond strength. *Journal of microelectromechanical systems*, 14(3):590–597, 2005.

[184] V. Sunkara, D.-K. Park, and Y.-K. Cho. Versatile method for bonding hard and soft materials. *Rsc Advances*, 2(24):9066–9070, 2012.

[185] E. J. Bras, R. R. Soares, A. M. Azevedo, P. Fernandes, M. Arévalo-Rodríguez, V. Chu, J. P. Conde, and M. R. Aires-Barros. A multiplexed microfluidic toolbox for the rapid optimization of affinity-driven partition in aqueous two phase systems. *Journal of Chromatography A*, 1515:252–259, 2017.

[186] A. Schmid, J. Dordick, B. Hauer, A. Kiener, M. Wubbolts, and B. Witholt. Industrial biocatalysis today and tomorrow. *nature*, 409(6817):258–268, 2001.

[187] A. S. Bommarius and B. R. Riebel-Bommarius. *Biocatalysis: fundamentals and applications*. John Wiley & Sons, 2004.

[188] J. Haseloff and W. L. Gerlach. Simple rna enzymes with new and highly specific endoribonuclease activities. *Nature*, 334(6183):585–591, 1988.

[189] M. Gama, M. Aires-Barros, and J. Cabral. Engenharia enzimática, 2003.

[190] O. S. College. Potential, kinetic, free, and activation energy.

[191] Biochemaniacs. URL `https://biochemanics.wordpress.com/2013/04/06/what-affects-enzyme-velocity/`.

[192] V. Sirisha, A. Jain, and A. Jain. Enzyme immobilization: an overview on methods, support material, and applications of immobilized enzymes. In *Advances in food and nutrition research*, volume 79, pages 179–211. Elsevier, 2016.

[193] B. Krajewska. Application of chitin-and chitosan-based materials for enzyme immobilizations: a review. *Enzyme and microbial technology*, 35(2):126–139, 2004.

[194] L. Hajba and A. Guttman. Continuous-flow biochemical reactors: Biocatalysis, bioconversion, and bioanalytical applications utilizing immobilized microfluidic enzyme reactors. *Journal of Flow Chemistry*, 6(1):8–12, 2016.

[195] J. M. Walker. Methods in biotechnology. 2006.

[196] B. R. Glick and C. L. Patten. *Molecular biotechnology: principles and applications of recombinant DNA*, volume 34. John Wiley & Sons, 2017.

[197] D. Zabriskie and E. Arcuri. Factors influencing productivity of fermentations employing recombinant microorganisms. *Enzyme and microbial technology*, 8(12):706–717, 1986.

[198] A. Nakagawa, C. Matsuzaki, E. Matsumura, T. Koyanagi, T. Katayama, K. Yamamoto, F. Sato, H. Kumagai, and H. Minami. (r, s)-tetrahydropapaveroline production by stepwise fermentation using engineered escherichia coli. *Scientific reports*, 4:6695, 2014.

[199] Y.-J. Son, K.-H. Park, S.-Y. Lee, S.-J. Oh, C.-K. Kim, B.-T. Choi, Y.-C. Park, and J.-H. Seo. Effects of temperature shift strategies on human preproinsulin production in the fed-batch fermentation of recombinant escherichia coli. *Biotechnology and Bioprocess Engineering*, 12(5):556, 2007.

[200] B. Lin and Y. Tao. Whole-cell biocatalysts by design. *Microbial cell factories*, 16(1):106, 2017.

[201] C. C. de Carvalho. Whole cell biocatalysts: essential workers from nature to the industry. *Microbial biotechnology*, 10(2):250–263, 2017.

[202] P. Tufvesson, J. Lima-Ramos, M. Nordblad, and J. M. Woodley. Guidelines and cost analysis for catalyst production in biocatalytic processes. *Organic Process Research & Development*, 15(1): 266–274, 2011.

[203] C. C. De Carvalho. Enzymatic and whole cell catalysis: finding new strategies for old processes. *Biotechnology advances*, 29(1):75–83, 2011.

[204] J. Wachtmeister and D. Rother. Recent advances in whole cell biocatalysis techniques bridging from investigative to industrial scale. *Current opinion in biotechnology*, 42:169–177, 2016.

[205] K. S. Egorova and V. P. Ananikov. Ionic liquids in whole-cell biocatalysis: a compromise between toxicity and efficiency. *Biophysical reviews*, 10(3):881–900, 2018.

[206] Y. Ni and R. R. Chen. Accelerating whole-cell biocatalysis by reducing outer membrane permeability barrier. *Biotechnology and bioengineering*, 87(6):804–811, 2004.

[207] R. R. Chen. Permeability issues in whole-cell bioprocesses and cellular membrane engineering. *Applied microbiology and biotechnology*, 74(4):730–738, 2007.

[208] E. M. Buque-Taboada, A. J. Straathof, J. J. Heijnen, and L. A. Van Der Wielen. In situ product recovery (ispr) by crystallization: basic principles, design, and potential applications in whole-cell biocatalysis. *Applied microbiology and biotechnology*, 71(1):1–12, 2006.

[209] J.-M. Choi, S.-S. Han, and H.-S. Kim. Industrial applications of enzyme biocatalysis: current status and future aspects. *Biotechnology advances*, 33(7):1443–1454, 2015.

[210] S. Liu. *Bioprocess engineering: kinetics, sustainability, and reactor design*. Elsevier, 2016.

[211] R. den Haan, E. van Rensburg, S. H. Rose, J. F. Görgens, and W. H. van Zyl. Progress and challenges in the engineering of non-cellulolytic microorganisms for consolidated bioprocessing. *Current opinion in biotechnology*, 33:32–38, 2015.

[212] J. Wang, Y. Zhang, H. Liu, Y. Shang, L. Zhou, P. Wei, W.-B. Yin, Z. Deng, X. Qu, and Q. Zhou. A biocatalytic hydroxylation-enabled unified approach to c19-hydroxylated steroids. *Nature communications*, 10(1):1–9, 2019.

[213] H. Sun, H. Zhang, E. L. Ang, and H. Zhao. Biocatalysis for the synthesis of pharmaceuticals and pharmaceutical intermediates. *Bioorganic & medicinal chemistry*, 26(7):1275–1284, 2018.

[214] M. Fuchs, J. E. Farnberger, and W. Kroutil. The industrial age of biocatalytic transamination. *European journal of organic chemistry*, 2015(32):6965–6982, 2015.

[215] C. Yan, F. Parmeggiani, E. A. Jones, E. Claude, S. A. Hussain, N. J. Turner, S. L. Flitsch, and P. E. Barran. Real-time screening of biocatalysts in live bacterial colonies. *Journal of the American Chemical Society*, 139(4):1408–1411, 2017.

[216] R. Molitor, A. Bollinger, S. Kubicki, A. Loeschcke, K.-E. Jaeger, and S. Thies. Agar plate-based screening methods for the identification of polyester hydrolysis by pseudomonas species. *Microbial biotechnology*, 13(1):274–284, 2020.

[217] A. M. A. Maitig, M. A. Alhoot, and K. Tiwari. Isolation and screening of extracellular protease enzyme from fungal isolates of soil. *Journal of Pure and Applied Microbiology*, 4:2059, 2018.

[218] X. Zhang, X. Hao, S. Huo, W. Lin, X. Xia, K. Liu, and B. Duan. Isolation and identification of the raoultella ornithinolytica-zk4 degrading pyrethroid pesticides within soil sediment from an abandoned pesticide plant. *Archives of microbiology*, 201(9):1207–1217, 2019.

[219] P. Sriyapai, K. Chansiri, and T. Sriyapai. Isolation and characterization of polyester-based plastics-degrading bacteria from compost soils. *Microbiology*, 87(2):290–300, 2018.

[220] R. Dhali, A. Dey, A. N. Chattopadhyay, P. Saha, S. K. Mukhopadhyay, P. Roy, and S. Chatterjee. Isolation, characterization and study of amylase activity of microorganisms from arctic soil sample. *AOBR*, 3:5–15, 2016.

[221] A. Alam, A. Prakash, A. K. Sharma, V. Sharma, J. Saxena, and B. Yadav. Partial purification and characterization of protease enzyme from soil-borne fungi. *Mycopath*, 14(1&2), 2018.

[222] F. Thomas, C. Lorgeoux, P. Faure, D. Billet, and A. Cébron. Isolation and substrate screening of polycyclic aromatic hydrocarbon degrading bacteria from soil with long history of contamination. *International Biodeterioration & Biodegradation*, 107:1–9, 2016.

[223] A. Jain and K. P. Krishnan. A glimpse of the diversity of complex polysaccharide-degrading culturable bacteria from kongsfjorden, arctic ocean. *Annals of microbiology*, 67(2):203–214, 2017.

[224] H. Wang, D. J. Hart, and Y. An. Functional metagenomic technologies for the discovery of novel enzymes for biomass degradation and biofuel production. *BioEnergy Research*, 12(3):457–470, 2019.

[225] F. Lan, B. Demaree, N. Ahmed, and A. R. Abate. Single-cell genome sequencing at ultra-high-throughput with microfluidic droplet barcoding. *Nature biotechnology*, 35(7):640–646, 2017.

[226] M. Girault, T. Beneyton, D. Pekin, L. Buisson, S. Bichon, C. Charbonnier, Y. del Amo, and J.-C. Baret. High-content screening of plankton alkaline phosphatase activity in microfluidics. *Analytical chemistry*, 90(6):4174–4181, 2018.

[227] J. Cao, F. Kalensee, P. Günther, and J. Köhler. Microsegmented flow-assisted miniaturized culturing for isolation and characterization of heavy metal-tolerant bacteria. *International Journal of Environmental Science and Technology*, 17(1):1–16, 2020.

[228] J. Huang, D.-F. Xie, and Y. Feng. Engineering thermostable (r)-selective amine transaminase from aspergillus terreus through in silico design employing b-factor and folding free energy calculations. *Biochemical and biophysical research communications*, 483(1):397–402, 2017.

[229] Y. Zhang, A. N. Aryee, and B. K. Simpson. Current role of in silico approaches for food enzymes. *Current Opinion in Food Science*, 2019.

[230] A. Baccouche, S. Okumura, R. Sieskind, E. Henry, N. Aubert-Kato, N. Bredeche, J.-F. Bartolo, V. Taly, Y. Rondelez, T. Fujii, et al. Massively parallel and multiparameter titration of biochemical assays with droplet microfluidics. *nature protocols*, 12(9):1912, 2017.

[231] J. L. Porter, R. A. Rusli, and D. L. Ollis. Directed evolution of enzymes for industrial biocatalysis. *ChemBioChem*, 17(3):197–203, 2016.

[232] S. C. Hammer, A. M. Knight, and F. H. Arnold. Design and evolution of enzymes for non-natural chemistry. *Current Opinion in Green and Sustainable Chemistry*, 7:23–30, 2017.

[233] C. Zeymer and D. Hilvert. Directed evolution of protein catalysts. *Annual review of biochemistry*, 87:131–157, 2018.

[234] F. W. Chiu and S. Stavrakis. High-throughput droplet-based microfluidics for directed evolution of enzymes. *Electrophoresis*, 40(21):2860–2872, 2019.

[235] H. Goto, Y. Kanai, A. Yotsui, S. Shimokihara, S. Shitara, R. Oyobiki, K. Fujiwara, T. Watanabe, Y. Einaga, Y. Matsumoto, et al. Microfluidic screening system based on boron-doped diamond electrodes and dielectrophoretic sorting for directed evolution of nad (p)-dependent oxidoreductases. *Lab on a Chip*, 20(4):852–861, 2020.

[236] K. M. Sharma, R. Kumar, S. Panwar, and A. Kumar. Microbial alkaline proteases: Optimization of production parameters and their properties. *Journal of Genetic Engineering and Biotechnology*, 15(1):115–126, 2017.

[237] F. Gu, F. Xu, L. Tan, H. Wu, Z. Chu, and Q. Wang. Optimization of enzymatic process for vanillin extraction using response surface methodology. *Molecules*, 17(8):8753–8761, 2012.

[238] U. Krühne, S. Heintz, R. Ringborg, I. P. Rosinha, P. Tufvesson, K. V. Gernaey, and J. M. Woodley. Biocatalytic process development using microfluidic miniaturized systems. *Green Processing and Synthesis*, 3(1):23–31, 2014.

[239] P. Fernandes. Miniaturization in biocatalysis. *International journal of molecular sciences*, 11(3): 858–879, 2010.

[240] A. Bossi, L. Guizzardi, M. D'Acunto, and P. Righetti. Controlled enzyme-immobilisation on capillaries for microreactors for peptide mapping. *Analytical and bioanalytical chemistry*, 378(7):1722–1728, 2004.

[241] J. Čech, W. Schrott, Z. Slouka, M. Přibyl, M. Brož, G. Kuncová, and D. Šnita. Enzyme hydrolysis of soybean oil in a slug flow microsystem. *Biochemical engineering journal*, 67:194–202, 2012.

[242] B. O'Sullivan, H. Al-Bahrani, J. Lawrence, M. Campos, A. Cázares, F. Baganz, R. Wohlgemuth, H. C. Hailes, and N. Szita. Modular microfluidic reactor and inline filtration system for the biocatalytic synthesis of chiral metabolites. *Journal of Molecular Catalysis B: Enzymatic*, 77:1–8, 2012.

[243] S. Talaei, O. Frey, S. Psoma, P. Van Der Wal, and N. De Rooij. Smart su-8 pillars implemented in a microfluidic bioreactor for continuous measurement of glucose. *Procedia Engineering*, 5:448–451, 2010.

[244] S. T. Retterer, P. Siuti, C.-K. Choi, D. K. Thomas, and M. J. Doktycz. Development and fabrication of nanoporous silicon-based bioreactors within a microfluidic chip. *Lab on a Chip*, 10(9):1174–1181, 2010.

[245] E. Peris, O. Okafor, E. Kulcinskaja, R. Goodridge, S. V. Luis, E. Garcia-Verdugo, E. O'Reilly, and V. Sans. Tuneable 3d printed bioreactors for transaminations under continuous-flow. *Green Chemistry*, 19(22):5345–5349, 2017.

[246] J. J. Virgen-Ortíz, J. C. dos Santos, Á. Berenguer-Murcia, O. Barbosa, R. C. Rodrigues, and R. Fernandez-Lafuente. Polyethylenimine: a very useful ionic polymer in the design of immobilized enzyme biocatalysts. *Journal of Materials Chemistry B*, 5(36):7461–7490, 2017.

[247] X. Xiao, T. Siepenkoetter, R. Whelan, U. Salaj-Kosla, and E. Magner. A continuous fluidic bioreactor utilising electrodeposited silica for lipase immobilisation onto nanoporous gold. *Journal of Electroanalytical Chemistry*, 812:180–185, 2018.

[248] P. Mazurek, P. M. Zelisko, A. L. Skov, and M. A. Brook. Enzyme encapsulation in glycerol-silicone membranes for bioreactions and biosensors. *ACS Applied Polymer Materials*, 2020.

[249] A. Asthana, K. H. Lee, S.-J. Shin, J. Perumal, L. Butler, S.-H. Lee, and D.-P. Kim. Bromo-oxidation reaction in enzyme-entrapped alginate hollow microfibers. *Biomicrofluidics*, 5(2):024117, 2011.

[250] D. S. Peterson, T. Rohr, F. Svec, and J. M. Fréchet. Enzymatic microreactor-on-a-chip: protein mapping using trypsin immobilized on porous polymer monoliths molded in channels of microfluidic devices. *Analytical chemistry*, 74(16):4081–4088, 2002.

[251] E. Gkantzou, M. Patila, and H. Stamatis. Magnetic microreactors with immobilized enzymes—from assemblage to contemporary applications. *Catalysts*, 8(7):282, 2018.

[252] T. Honda, M. Miyazaki, H. Nakamura, and H. Maeda. Facile preparation of an enzyme-immobilized microreactor using a cross-linking enzyme membrane on a microchannel surface. *Advanced Synthesis & Catalysis*, 348(15):2163–2171, 2006.

[253] M. Bajić, I. Plazl, R. Stloukal, and P. Žnidaršič-Plazl. Development of a miniaturized packed bed reactor with ω-transaminase immobilized in lentikats®. *Process Biochemistry*, 52:63–72, 2017.

[254] N. Kockmann. Modular equipment for chemical process development and small-scale production in multipurpose plants. *ChemBioEng Reviews*, 3(1):5–15, 2016.

[255] J. Hemmerich, S. Noack, W. Wiechert, and M. Oldiges. Microbioreactor systems for accelerated bioprocess development. *Biotechnology journal*, 13(4):1700141, 2018.

[256] K. Min, G. W. Park, Y. J. Yoo, and J.-S. Lee. A perspective on the biotechnological applications of the versatile tyrosinase. *Bioresource technology*, page 121730, 2019.

[257] K. Min, K. Park, D.-H. Park, and Y. J. Yoo. Overview on the biotechnological production of l-dopa. *Applied microbiology and biotechnology*, 99(2):575–584, 2015.

[258] M. Bertoldi. Mammalian dopa decarboxylase: structure, catalytic activity and inhibition. *Archives of biochemistry and biophysics*, 546:1–7, 2014.

[259] M. R. Hormozi-Nezhad, A. Moslehipour, and A. Bigdeli. Simple and rapid detection of l-dopa based on in situ formation of polylevodopa nanoparticles. *Sensors and Actuators B: Chemical*, 243:715–720, 2017.

[260] R. Heacock. The chemistry of adrenochrome and related compounds. *Chemical Reviews*, 59(2): 181–237, 1959.

[261] G. Hermanson. Bioconjugate techniques, ; pierce biotechnology. *Thermo Fisher Scientific: Rockford, IL*, 2008.

[262] C. Mateo, J. M. Palomo, G. Fernandez-Lorente, J. M. Guisan, and R. Fernandez-Lafuente. Improvement of enzyme activity, stability and selectivity via immobilization techniques. *Enzyme and microbial technology*, 40(6):1451–1463, 2007.

[263] R. C. Rodrigues, C. Ortiz, Á. Berenguer-Murcia, R. Torres, and R. Fernández-Lafuente. Modifying enzyme activity and selectivity by immobilization. *Chemical Society Reviews*, 42(15):6290–6307, 2013.

[264] H. B. Yildiz, S. Caliskan, M. Kamaci, A. Caliskan, and H. Yilmaz. l-dopa synthesis catalyzed by tyrosinase immobilized in poly (ethyleneoxide) conducting polymers. *International journal of biological macromolecules*, 56:34–40, 2013.

[265] J. L. Muñoz-Muñoz, F. Garcia-Molina, R. Varon, P. A. Garcia-Ruíz, J. Tudela, F. Garcia-Cánovas, and J. N. Rodríguez-López. Suicide inactivation of the diphenolase and monophenolase activities of tyrosinase. *IUBMB life*, 62(7):539–547, 2010.

[266] E. Vilanova, A. Manjon, and J. Iborra. Tyrosine hydroxylase activity of immobilized tyrosinase on enzacryl-aa and cpg-aa supports: Stabilization and properties. *Biotechnology and bioengineering*, 26(11):1306–1312, 1984.

[267] F. Carvalho and P. Fernandes. Packed bed enzyme microreactor: Application in sucrose hydrolysis as proof-of-concept. *Biochemical Engineering Journal*, 104:74–81, 2015.

[268] H. Mickley, K. Smith, and E. Korchak. Fluid flow in packed beds. *Chemical Engineering Science*, 20(3):237–246, 1965.

[269] D.-Y. Xu, J.-Y. Chen, and Z. Yang. Use of cross-linked tyrosinase aggregates as catalyst for synthesis of l-dopa. *Biochemical engineering journal*, 63:88–94, 2012.

[270] M. J. Osland, N. M. Enwright, R. H. Day, C. A. Gabler, C. L. Stagg, and J. B. Grace. Beyond just sea-level rise: Considering macroclimatic drivers within coastal wetland vulnerability assessments to climate change. *Global Change Biology*, 22(1):1–11, 2016.

[271] K. Skogen, H. Helland, and B. Kaltenborn. Concern about climate change, biodiversity loss, habitat degradation and landscape change: Embedded in different packages of environmental concern? *Journal for nature conservation*, 44:12–20, 2018.

[272] S. E. Eikenberry and A. B. Gumel. Mathematical modeling of climate change and malaria transmission dynamics: a historical review. *Journal of mathematical biology*, 77(4):857–933, 2018.

[273] S. Stoll-Kleemann and U. J. Schmidt. Reducing meat consumption in developed and transition countries to counter climate change and biodiversity loss: a review of influence factors. *Regional Environmental Change*, 17(5):1261–1277, 2017.

[274] F. C. Moore, U. L. C. Baldos, and T. Hertel. Economic impacts of climate change on agriculture: a comparison of process-based and statistical yield models. *Environmental Research Letters*, 12 (6):065008, 2017.

[275] S. S. Myers, M. R. Smith, S. Guth, C. D. Golden, B. Vaitla, N. D. Mueller, A. D. Dangour, and P. Huybers. Climate change and global food systems: potential impacts on food security and undernutrition. *Annual review of public health*, 38:259–277, 2017.

[276] P. Zhang, J. Zhang, and M. Chen. Economic impacts of climate change on agriculture: The importance of additional climatic variables other than temperature and precipitation. *Journal of Environmental Economics and Management*, 83:8–31, 2017.

[277] A. Kaurin, R. Mihelič, D. Kastelec, H. Grčman, D. Bru, L. Philippot, and M. Suhadolc. Resilience of bacteria, archaea, fungi and n-cycling microbial guilds under plough and conservation tillage, to agricultural drought. *Soil Biology and Biochemistry*, 120:233–245, 2018.

[278] R. R. M. Paterson, A. Venâncio, N. Lima, M. Guilloux-Bénatier, and S. Rousseaux. Predominant mycotoxins, mycotoxigenic fungi and climate change related to wine. *Food research international*, 103:478–491, 2018.

[279] M. E. Requena, C. Egea-Gilabert, and M. E. C. Castillo. Effect of climate change on growth, development and pathogenicity of phytopathogenic telluric fungi. *Advanced Intelligent Systems for Sustainable Development (AI2SD'2018): Vol 1: Advanced Intelligent Systems Applied to Agriculture*, 911:14, 2019.

[280] H. Van der Fels-Klerx, C. Liu, and P. Battilani. Modelling climate change impacts on mycotoxin contamination. *World Mycotoxin Journal*, 9(5):717–726, 2016.

[281] F. Almeida, M. L. Rodrigues, and C. Coelho. The still underestimated problem of fungal diseases worldwide. *Frontiers in microbiology*, 10, 2019.

[282] D. S. Perlin, R. Rautemaa-Richardson, and A. Alastruey-Izquierdo. The global problem of antifungal resistance: prevalence, mechanisms, and management. *The Lancet infectious diseases*, 17 (12):e383–e392, 2017.

[283] S. V. Avery, I. Singleton, N. Magan, and G. H. Goldman. The fungal threat to global food security. *Fungal biology*, 123(8):555–557, 2019.

[284] B. Whelan, A. McBratney, and B. Boydell. The impact of precision agriculture. proceedings of the abare outlook conference. *The Future of Cropping in NW NSW, Moree, UK*, page 5, 1997.

[285] N. Zhang, M. Wang, and N. Wang. Precision agriculture—a worldwide overview. *Computers and electronics in agriculture*, 36(2-3):113–132, 2002.

[286] M. A. Córdoba, C. I. Bruno, J. L. Costa, N. R. Peralta, and M. G. Balzarini. Protocol for multivariate homogeneous zone delineation in precision agriculture. *biosystems engineering*, 143:95–107, 2016.

[287] F. Brubeck-Hernandez, T. Vladimirova, M. Pooley, R. Thompson, and B. Knight. Zone management in precision agriculture using satellite imagery. In *2019 NASA/ESA Conference on Adaptive Hardware and Systems (AHS)*, pages 65–71. IEEE, 2019.

[288] C. Yang. High resolution satellite imaging sensors for precision agriculture. *Frontiers of Agricultural Science and Engineering*, 5(4):393–405, 2018.

[289] T.-X. Zhang, J.-Y. Su, C.-J. Liu, and W.-H. Chen. Potential bands of sentinel-2a satellite for classification problems in precision agriculture. *International Journal of Automation and Computing*, 16 (1):16–26, 2019.

[290] J. Siegfried, L. Longchamps, and R. Khosla. Multispectral satellite imagery to quantify in-field soil moisture variability. *Journal of Soil and Water Conservation*, 74(1):33–40, 2019.

[291] N. Dercas, N. V. Spyropoulos, N. R. Dalezios, E. Psomiadis, A. Stefopoulou, G. Madonanakis, and N. Tserlikakis. Cotton evapotranspiration using very high spatial resolution wv-2 satellite data and ground measurements for precision agriculture. *WIT Trans Ecol Environ*, 220:101–107, 2017.

[292] A. Bchir, D. Mulla, A. B. Dhiab, F. B. Meriem, W. Bousetta, and M. Braham. Assessing spatial and temporal variability in evapotranspiration for olive orchards in tunisia using satellite remote sensing. In *Precision agriculture'19*, pages 61–72. Wageningen Academic Publishers, 2019.

[293] L. Comba, A. Biglia, D. R. Aimonino, and P. Gay. Unsupervised detection of vineyards by 3d point-cloud uav photogrammetry for precision agriculture. *Computers and Electronics in Agriculture*, 155:84–95, 2018.

[294] E. R. Hunt, D. A. Horneck, C. B. Spinelli, R. W. Turner, A. E. Bruce, D. J. Gadler, J. J. Brungardt, and P. B. Hamm. Monitoring nitrogen status of potatoes using small unmanned aerial vehicles. *Precision agriculture*, 19(2):314–333, 2018.

[295] W. H. Maes and K. Steppe. Perspectives for remote sensing with unmanned aerial vehicles in precision agriculture. *Trends in plant science*, 24(2):152–164, 2019.

[296] F. Castaldi, F. Pelosi, S. Pascucci, and R. Casa. Assessing the potential of images from unmanned aerial vehicles (uav) to support herbicide patch spraying in maize. *Precision Agriculture*, 18(1): 76–94, 2017.

[297] L. J. Méndez-Vázquez, A. Lira-Noriega, R. Lasa-Covarrubias, and S. Cerdeira-Estrada. Delineation of site-specific management zones for pest control purposes: Exploring precision agriculture and species distribution modeling approaches. *Computers and Electronics in Agriculture*, 167:105101, 2019.

[298] Y. Shi, J. A. Thomasson, S. C. Murray, N. A. Pugh, W. L. Rooney, S. Shafian, N. Rajan, G. Rouze, C. L. Morgan, H. L. Neely, et al. Unmanned aerial vehicles for high-throughput phenotyping and agronomic research. *PloS one*, 11(7), 2016.

[299] S. Khanal, J. Fulton, and S. Shearer. An overview of current and potential applications of thermal remote sensing in precision agriculture. *Computers and Electronics in Agriculture*, 139:22–32, 2017.

[300] Y. Ge, J. A. Thomasson, and R. Sui. Remote sensing of soil properties in precision agriculture: A review. *Frontiers of Earth Science*, 5(3):229–238, 2011.

[301] M. Davoodi, J. Mohammadpour Velni, and C. Li. Coverage control with multiple ground robots for precision agriculture. *Mechanical Engineering*, 140(06):S4–S8, 2018.

[302] M. C. Vuran, A. Salam, R. Wong, and S. Irmak. Internet of underground things in precision agriculture: Architecture and technology aspects. *Ad Hoc Networks*, 81:160–173, 2018.

[303] Y. Fang and R. P. Ramasamy. Detection of p-ethylphenol, a major plant volatile organic compound, by tyrosinase-based electrochemical biosensor. *ECS Journal of Solid State Science and Technology*, 5(8):M3054, 2016.

[304] H. Wang, P. Ramnani, T. Pham, C. C. Villarreal, X. Yu, G. Liu, and A. Mulchandani. Gas biosensor arrays based on single-stranded dna-functionalized single-walled carbon nanotubes for the detection of volatile organic compound biomarkers released by huanglongbing disease-infected citrus trees. *Sensors*, 19(21):4795, 2019.

[305] H. Y. Lau, H. Wu, E. J. Wee, M. Trau, Y. Wang, and J. R. Botella. Specific and sensitive isothermal electrochemical biosensor for plant pathogen dna detection with colloidal gold nanoparticles as probes. *Scientific reports*, 7(1):1–7, 2017.

[306] Q. Chen, D. Wang, G. Cai, and Y. Xiong. Catalysis and microfluidics, biosensors and bioelectronic. 2016.

[307] M. Ray, A. Ray, S. Dash, A. Mishra, K. G. Achary, S. Nayak, and S. Singh. Fungal disease detection in plants: Traditional assays, novel diagnostic techniques and biosensors. *Biosensors and Bioelectronics*, 87:708–723, 2017.

[308] G. Kim, J. Lim, C. Mo, et al. Applications of microfluidics in the agro-food sector: A review. *Journal of Biosystems Engineering*, 41(2):116–125, 2016.

[309] B. Xu, J. Guo, Y. Fu, X. Chen, and J. Guo. A review on microfluidics in the detection of food pesticide residues. *Electrophoresis*, 2019.

[310] S. Vasantham, S. Nagabooshanam, S. Wadhwa, and A. Mathur. Microfluidic devices and their application in modern agriculture system. In *Nanoscience for Sustainable Agriculture*, pages 659–681. Springer, 2019.

[311] M. L. Braunger, F. M. Shimizu, M. J. Jimenez, L. R. Amaral, M. H. Piazzetta, Â. L. Gobbi, P. S. Magalhães, V. Rodrigues, O. N. Oliveira, and A. Riul. Microfluidic electronic tongue applied to soil analysis. *Chemosensors*, 5(2):14, 2017.

[312] Z. Xu, X. Wang, R. J. Weber, R. Kumar, and L. Dong. Microfluidic eletrophoretic ion nutrient sensor. In *2016 IEEE SENSORS*, pages 1–3. IEEE, 2016.

[313] J. Marshall, X. Qiao, J. Baumbach, J. Xie, L. Dong, and M. K. Bhattacharyya. Microfluidic device enabled quantitative time-lapse microscopic-photography for phenotyping vegetative and reproductive phases in fusarium virguliforme, which is pathogenic to soybean. *Scientific reports*, 7: 44365, 2017.

[314] C. S. Bascom, S.-Z. Wu, K. Nelson, J. Oakey, and M. Bezanilla. Long-term growth of moss in microfluidic devices enables subcellular studies in development. *Plant Physiology*, 172(1):28–37, 2016.

[315] X. Qu, M. Li, H. Zhang, C. Lin, F. Wang, M. Xiao, Y. Zhou, J. Shi, A. Aldalbahi, H. Pei, et al. Real-time continuous identification of greenhouse plant pathogens based on recyclable microfluidic bioassay system. *ACS applied materials & interfaces*, 9(37):31568–31575, 2017.

[316] N. J. Vickers. Animal communication: When i'm calling you, will you answer too? *Current Biology*, 27(14):R713–R715, 2017.

[317] B. Kashyap and R. Kumar. Salicylic acid (sa) detection using bi-enzyme microfluidic electrochemical sensor. In *Smart Biomedical and Physiological Sensor Technology XV*, volume 10662, page 106620K. International Society for Optics and Photonics, 2018.

[318] P. Bhatnagar-Mathur, S. Sunkara, M. Bhatnagar-Panwar, F. Waliyar, and K. K. Sharma. Biotechnological advances for combating aspergillus flavus and aflatoxin contamination in crops. *Plant science*, 234:119–132, 2015.

[319] D. Fourie. Distribution and severity of bacterial diseases on dry beans (phaseolus vulgaris l.) in south africa. *Journal of Phytopathology*, 150(4-5):220–226, 2002.

[320] M. Khater, A. de la Escosura-Muñiz, and A. Merkoçi. Biosensors for plant pathogen detection. *Biosensors and Bioelectronics*, 93:72–86, 2017.

[321] A.-K. Mahlein. Plant disease detection by imaging sensors–parallels and specific demands for precision agriculture and plant phenotyping. *Plant disease*, 100(2):241–251, 2016.

[322] H. Bouwmeester, G. Heuvelink, and J. Stoorvogel. Mapping crop diseases using survey data: The case of bacterial wilt in bananas in the east african highlands. *European Journal of Agronomy*, 74:173–184, 2016.

[323] A. Panebianco, I. Castello, G. Cirvilleri, G. Perrone, F. Epifani, M. Ferrara, G. Polizzi, D. R. Walters, and A. Vitale. Detection of botrytis cinerea field isolates with multiple fungicide resistance from table grape in sicily. *Crop Protection*, 77:65–73, 2015.

[324] A. K. Vidaver. Uses of antimicrobials in plant agriculture. *Clinical infectious diseases*, 34 (Supplement_3):S107–S110, 2002.

[325] S. Neethirajan, K. Ragavan, and X. Weng. Agro-defense: Biosensors for food from healthy crops and animals. *Trends in Food Science & Technology*, 73:25–44, 2018.

[326] C. Wang, M. El-Shetehy, M. Shine, K. Yu, D. Navarre, D. Wendehenne, A. Kachroo, and P. Kachroo. Free radicals mediate systemic acquired resistance. *Cell Reports*, 7(2):348–355, 2014.

[327] K. Yu, J. M. Soares, M. K. Mandal, C. Wang, B. Chanda, A. N. Gifford, J. S. Fowler, D. Navarre, A. Kachroo, and P. Kachroo. A feedback regulatory loop between g3p and lipid transfer proteins dir1 and azi1 mediates azelaic-acid-induced systemic immunity. *Cell Reports*, 3(4):1266–1278, 2013.

[328] P. Agudelo-Romero, A. Erban, C. Rego, P. Carbonell-Bejerano, T. Nascimento, L. Sousa, J. M. Martínez-Zapater, J. Kopka, and A. M. Fortes. Transcriptome and metabolome reprogramming in vitis vinifera cv. trincadeira berries upon infection with botrytis cinerea. *Journal of Experimental Botany*, 66(7):1769–1785, 2015.

[329] F. Wittek, T. Hoffmann, B. Kanawati, M. Bichlmeier, C. Knappe, M. Wenig, P. Schmitt-Kopplin, J. E. Parker, W. Schwab, and A. C. Vlot. Arabidopsis enhanced disease susceptibility1 promotes systemic acquired resistance via azelaic acid and its precursor 9-oxo nonanoic acid. *Journal of experimental botany*, 65(20):5919–5931, 2014.

[330] Z. Á. Nagy, G. Kátay, G. Gullner, L. Király, and A. L. Ádám. Azelaic acid accumulates in phloem exudates of tmv-infected tobacco leaves, but its application does not induce local or systemic resistance against selected viral and bacterial pathogens. *Acta Physiologiae Plantarum*, 39(1):9, 2017.

[331] H. W. Jung, T. J. Tschaplinski, L. Wang, J. Glazebrook, and J. T. Greenberg. Priming in systemic plant immunity. *Science*, 324(5923):89–91, 2009.

[332] D. Malik and G. Kaur. A validated stability-indicating rp-hplc method for analysis of azelaic acid in pharmaceuticals. *Indian Journal of Pharmaceutical Sciences*, 80(3):503–509, 2018.

[333] I. Surowiec, I. Kaml, and E. Kenndler. Analysis of drying oils used as binding media for objects of art by capillary electrophoresis with indirect uv and conductivity detection. *Journal of Chromatography A*, 1024(1-2):245–254, 2004.

[334] R. Epifania, R. R. Soares, I. F. Pinto, V. Chu, and J. P. Conde. Capillary-driven microfluidic device with integrated nanoporous microbeads for ultrarapid biosensing assays. *Sensors and Actuators B: Chemical*, 265:452–458, 2018.

[335] X. Yu, Y. Xia, Y. Tang, W.-L. Zhang, Y.-T. Yeh, H. Lu, and S.-Y. Zheng. A nanostructured microfluidic immunoassay platform for highly sensitive infectious pathogen detection. *Small*, 13(24):1700425, 2017.

[336] S. Mross, S. Pierrat, T. Zimmermann, and M. Kraft. Microfluidic enzymatic biosensing systems: A review. *Biosensors and Bioelectronics*, 70:376–391, 2015.

[337] P. Rattanarat, P. Teengam, W. Siangproh, R. Ishimatsu, K. Nakano, O. Chailapakul, and T. Imato. An electrochemical compact disk-type microfluidics platform for use as an enzymatic biosensor. *Electroanalysis*, 27(3):703–712, 2015.

[338] J.-C. Chou, J.-S. Chen, Y.-H. Liao, C.-H. Lai, S.-J. Yan, M.-S. Huang, and T.-Y. Wu. Fabrication and characteristic analysis for enzymatic glucose biosensor modified by graphene oxide and magnetic beads based on microfluidic framework. *IEEE Sensors Journal*, 17(6):1741–1748, 2017.

[339] A.-M. Pappa, V. F. Curto, M. Braendlein, X. Strakosas, M. J. Donahue, M. Fiocchi, G. G. Malliaras, and R. M. Owens. Organic transistor arrays integrated with finger-powered microfluidics for multianalyte saliva testing. *Advanced Healthcare Materials*, 5(17):2295–2302, 2016.

[340] M. Medina-Sánchez, C. C. Mayorga-Martinez, T. Watanabe, T. A. Ivandini, Y. Honda, F. Pino, K. Nakata, A. Fujishima, Y. Einaga, and A. Merkoçi. Microfluidic platform for environmental con-

taminants sensing and degradation based on boron-doped diamond electrodes. *Biosensors and Bioelectronics*, 75:365–374, 2016.

[341] R. Tang, H. Yang, Y. Gong, M. You, Z. Liu, J. R. Choi, T. Wen, Z. Qu, Q. Mei, and F. Xu. A fully disposable and integrated paper-based device for nucleic acid extraction, amplification and detection. *Lab on a Chip*, 17(7):1270–1279, 2017.

[342] X. Zhang, X. Li, Q. Liu, S. Ke, Y. Ji, S. Liu, and G. Sui. Rapid and semiquantitative detection of staphylococcus epidermidis in humor samples by microfluidic platform. *Sensors and Actuators B: Chemical*, 278:8–14, 2019.

[343] M. C. Young and P. M. Zito. Azelaic acid in acne vulgaris. *Journal of the Dermatology Nurses Association*, 10(3):152–153, 2018.

[344] Á. Sánchez-Ferrer, J. N. Rodríguez-López, F. García-Cánovas, and F. García-Carmona. Tyrosinase: a comprehensive review of its mechanism. *Biochimica et Biophysica Acta (BBA)-Protein Structure and Molecular Enzymology*, 1247(1):1–11, 1995.

[345] M. Hassan, Z. Ashraf, Q. Abbas, H. Raza, and S.-Y. Seo. Exploration of novel human tyrosinase inhibitors by molecular modeling, docking and simulation studies. *Interdisciplinary Sciences: Computational Life Sciences*, 10(1):68–80, 2018.

[346] I. Pinto, C. Caneira, R. Soares, N. Madaboosi, M. Aires-Barros, J. Conde, A. Azevedo, and V. Chu. The application of microbeads to microfluidic systems for enhanced detection and purification of biomolecules. *Methods*, 116:112–124, 2017.

[347] Y. Yilmaz, Z. Göksel, S. S. Erdoğan, A. Öztürk, A. Atak, and C. Özer. Antioxidant activity and phenolic content of seed, skin and pulp parts of 22 grape (v itis vinifera l.) cultivars (4 common and 18 registered or candidate for registration). *Journal of Food Processing and Preservation*, 39 (6):1682–1691, 2015.

[348] B. Coombe. Growth stages of the grapevine: adoption of a system for identifying grapevine growth stages. *Australian journal of grape and wine research*, 1(2):104–110, 1995.

[349] P.-J. Tseng, C.-Y. Wang, T.-Y. Huang, Y.-Y. Chuang, S.-F. Fu, and Y.-W. Lin. A facile colorimetric assay for determination of salicylic acid in tobacco leaves using titanium dioxide nanoparticles. *Analytical Methods*, 6(6):1759–1765, 2014.

[350] R. Arimboor, K. S. Kumar, and C. Arumughan. Simultaneous estimation of phenolic acids in sea buckthorn (hippophae rhamnoides) using rp-hplc with dad. *Journal of Pharmaceutical and Biomedical Analysis*, 47(1):31–38, 2008.

[351] C. M. Pieterse, A. Leon-Reyes, S. Van der Ent, and S. C. Van Wees. Networking by small-molecule hormones in plant immunity. *Nature chemical biology*, 5(5):308–316, 2009.

[352] E. Fedorenko, M. K. Behr, and N. Kanwisher. Functional specificity for high-level linguistic processing in the human brain. *Proceedings of the National Academy of Sciences*, 108(39):16428–16433, 2011.

[353] H. Hou, Q. Yan, X. Wang, and H. Xu. A sbp-box gene vpsbp5 from chinese wild vitis species responds to erysiphe necator and defense signaling molecules. *Plant molecular biology reporter*, 31(6):1261–1270, 2013.

[354] Z. Toth, P. Winterhagen, B. Kalapos, Y. Su, L. Kovacs, and E. Kiss. Expression of a grapevine nac transcription factor gene is induced in response to powdery mildew colonization in salicylic acid-independent manner. *Scientific reports*, 6:30825, 2016.

[355] S. Ferrari, R. Galletti, C. Denoux, G. De Lorenzo, F. M. Ausubel, and J. Dewdney. Resistance to botrytis cinerea induced in arabidopsis by elicitors is independent of salicylic acid, ethylene, or jasmonate signaling but requires phytoalexin deficient3. *Plant physiology*, 144(1):367–379, 2007.

[356] K. Audenaert, G. B. De Meyer, and M. M. Höfte. Abscisic acid determines basal susceptibility of tomato tobotrytis cinerea and suppresses salicylic acid-dependent signaling mechanisms. *Plant physiology*, 128(2):491–501, 2002.

[357] D. Giavarina. Understanding bland altman analysis. *Biochemia medica: Biochemia medica*, 25 (2):141–151, 2015.

[358] H.-I. Lee, J. León, and I. Raskin. Biosynthesis and metabolism of salicylic acid. *Proceedings of the national academy of sciences*, 92(10):4076–4079, 1995.

[359] S.-W. Park, E. Kaimoyo, D. Kumar, S. Mosher, and D. F. Klessig. Methyl salicylate is a critical mobile signal for plant systemic acquired resistance. *Science*, 318(5847):113–116, 2007.

[360] M. L. Campos, J.-H. Kang, and G. A. Howe. Jasmonate-triggered plant immunity. *Journal of chemical ecology*, 40(7):657–675, 2014.

[361] K. Rodogiannis, J. T. Duong, and M. L. Kovarik. Microfluidic single-cell analysis of oxidative stress in dictyostelium discoideum. *Analyst*, 143(15):3643–3650, 2018.

[362] C. Kim, J. Kasuya, J. Jeon, S. Chung, and R. D. Kamm. A quantitative microfluidic angiogenesis screen for studying anti-angiogenic therapeutic drugs. *Lab on a chip*, 15(1):301–310, 2015.

[363] F. Eduati, R. Utharala, D. Madhavan, U. P. Neumann, T. Longerich, T. Cramer, J. Saez-Rodriguez, and C. A. Merten. A microfluidics platform for combinatorial drug screening on cancer biopsies. *Nature communications*, 9(1):1–13, 2018.

[364] T.-E. Park, N. Mustafaoglu, A. Herland, R. Hasselkus, R. Mannix, E. A. FitzGerald, R. Prantil-Baun, A. Watters, O. Henry, M. Benz, et al. Hypoxia-enhanced blood-brain barrier chip recapitulates human barrier function and shuttling of drugs and antibodies. *Nature communications*, 10(1): 1–12, 2019.

[365] J. Mairhofer, K. Roppert, and P. Ertl. Microfluidic systems for pathogen sensing: a review. *Sensors*, 9(6):4804–4823, 2009.

[366] T. Akyazi, L. Basabe-Desmonts, and F. Benito-Lopez. Review on microfluidic paper-based analytical devices towards commercialisation. *Analytica chimica acta*, 1001:1–17, 2018.

[367] Z. Liao, Y. Zhang, Y. Li, Y. Miao, S. Gao, F. Lin, Y. Deng, and L. Geng. Microfluidic chip coupled with optical biosensors for simultaneous detection of multiple analytes: A review. *Biosensors and Bioelectronics*, 126:697–706, 2019.

[368] T. Hoshino and F. Inagaki. Molecular quantification of environmental dna using microfluidics and digital pcr. *Systematic and Applied Microbiology*, 35(6):390–395, 2012.

[369] R. R. Soares, D. R. Santos, I. F. Pinto, A. M. Azevedo, M. R. Aires-Barros, V. Chu, and J. P. Conde. Multiplexed microfluidic fluorescence immunoassay with photodiode array signal acquisition for sub-minute and point-of-need detection of mycotoxins. *Lab on a Chip*, 18(11):1569–1580, 2018.

[370] A. J. Reyes, K. Ramcharan, P. Harnarayan, and J. Mooteeram. Symmetrical digital gangrene after a high dose intravenous infusion of epinephrine and dopamine following resuscitation from cardiac arrest. *Case Reports*, 2016:bcr2016217977, 2016.

[371] N. Pires, T. Dong, U. Hanke, and N. Hoivik. Integrated optical microfluidic biosensor using a polycarbazole photodetector for point-of-care detection of hormonal compounds. *Journal of biomedical optics*, 18(9):097001, 2013.

[372] M. Safavieh, M. U. Ahmed, M. Tolba, and M. Zourob. Microfluidic electrochemical assay for rapid detection and quantification of escherichia coli. *Biosensors and Bioelectronics*, 31(1):523–528, 2012.

[373] H. Jiang, X. Weng, and D. Li. Microfluidic whole-blood immunoassays. *Microfluidics and nanofluidics*, 10(5):941–964, 2011.

[374] J. Kim, M. Johnson, P. Hill, and B. K. Gale. Microfluidic sample preparation: cell lysis and nucleic acid purification. *Integrative Biology*, 1(10):574–586, 2009.

[375] X. Ge, A. M. Asiri, D. Du, W. Wen, S. Wang, and Y. Lin. Nanomaterial-enhanced paper-based biosensors. *TrAC Trends in Analytical Chemistry*, 58:31–39, 2014.

[376] J. Yu, L. Ge, J. Huang, S. Wang, and S. Ge. Microfluidic paper-based chemiluminescence biosensor for simultaneous determination of glucose and uric acid. *Lab on a Chip*, 11(7):1286–1291, 2011.

[377] J. Xie, J. Shih, Q. Lin, B. Yang, and Y.-C. Tai. Surface micromachined electrostatically actuated micro peristaltic pump. *Lab on a Chip*, 4(5):495–501, 2004.

[378] P. Skafte-Pedersen, D. Sabourin, M. Dufva, and D. Snakenborg. Multi-channel peristaltic pump for microfluidic applications featuring monolithic pdms inlay. *Lab on a Chip*, 9(20):3003–3006, 2009.

[379] S. Kumar, S. Kumar, M. A. Ali, P. Anand, V. V. Agrawal, R. John, S. Maji, and B. D. Malhotra. Microfluidic-integrated biosensors: Prospects for point-of-care diagnostics. *Biotechnology journal*, 8(11):1267–1279, 2013.

[380] D. R. Santos, R. R. Soares, I. F. Pinto, C. R. Caneira, R. M. Pinto, V. Chu, and J. P. Conde. Label-free detection of biomolecules in microfluidic systems using on-chip uv and impedimetric sensors. *IEEE Sensors Journal*, 19(18):7803–7812, 2019.

[381] E. J. Brás, A. M. Fortes, V. Chu, P. Fernandes, and J. P. Conde. Microfluidic device for the point of need detection of a pathogen infection biomarker in grapes. *Analyst*, 144(16):4871–4879, 2019.

[382] G. Kokkinis, M. Jamalieh, F. Cardoso, S. Cardoso, F. Keplinger, and I. Giouroudi. Magnetic-based biomolecule detection using giant magnetoresistance sensors. *Journal of Applied Physics*, 117 (17):17B731, 2015.

[383] J. Lum, R. Wang, B. Hargis, S. Tung, W. Bottje, H. Lu, and Y. Li. An impedance aptasensor with microfluidic chips for specific detection of h5n1 avian influenza virus. *Sensors*, 15(8):18565–18578, 2015.

[384] C.-J. Huang, Y.-H. Chen, C.-H. Wang, T.-C. Chou, and G.-B. Lee. Integrated microfluidic systems for automatic glucose sensing and insulin injection. *Sensors and Actuators B: Chemical*, 122(2): 461–468, 2007.

[385] D. Stern, D. Pauly, M. Zydek, C. Müller, M. A. Avondet, S. Worbs, F. Lisdat, M. B. Dorner, and B. G. Dorner. Simultaneous differentiation and quantification of ricin and agglutinin by an antibody-sandwich surface plasmon resonance sensor. *Biosensors and bioelectronics*, 78:111–117, 2016.

[386] N. Talukder, A. Furniturewalla, T. Le, M. Chan, S. Hirday, X. Cao, P. Xie, Z. Lin, A. Gholizadeh, S. Orbine, et al. A portable battery powered microfluidic impedance cytometer with smartphone readout: towards personal health monitoring. *Biomedical microdevices*, 19(2):36, 2017.

[387] J. Guo. Smartphone-powered electrochemical dongle for point-of-care monitoring of blood β-ketone. *Analytical chemistry*, 89(17):8609–8613, 2017.

[388] D. Zhang and Q. Liu. Biosensors and bioelectronics on smartphone for portable biochemical detection. *Biosensors and Bioelectronics*, 75:273–284, 2016.

[389] O. Tokel, U. H. Yildiz, F. Inci, N. G. Durmus, O. O. Ekiz, B. Turker, C. Cetin, S. Rao, K. Sridhar, N. Natarajan, et al. Portable microfluidic integrated plasmonic platform for pathogen detection. *Scientific reports*, 5(1):1–9, 2015.

[390] B. Bottazzi, L. Fornasari, A. Frangolho, S. Giudicatti, A. Mantovani, F. Marabelli, G. Marchesini, P. Pellacani, R. Therisod, and A. Valsesia. Multiplexed label-free optical biosensor for medical diagnostics. *Journal of biomedical optics*, 19(1):017006, 2014.

[391] C. L. Martin. i-stat–combining chemistry and haematology in poct. *The Clinical Biochemist Reviews*, 31(3):81, 2010.

[392] R. L. Siegel, K. D. Miller, and A. Jemal. Cancer statistics, 2019. *CA: a cancer journal for clinicians*, 69(1):7–34, 2019.

[393] R. L. Siegel, K. D. Miller, S. A. Fedewa, D. J. Ahnen, R. G. Meester, A. Barzi, and A. Jemal. Colorectal cancer statistics, 2017. *CA: a cancer journal for clinicians*, 67(3):177–193, 2017.

[394] P. Favoriti, G. Carbone, M. Greco, F. Pirozzi, R. E. M. Pirozzi, and F. Corcione. Worldwide burden of colorectal cancer: a review. *Updates in surgery*, 68(1):7–11, 2016.

[395] What you can do to catch colon cancer early. URL `https://health.clevelandclinic.org/what-you-can-do-to-catch-colon-cancer-early/`.

[396] Colorectal cancer facts and figures 2017-2019. URL `https://www.cancer.org`.

[397] P. J. Pickhardt, D. H. Kim, B. D. Pooler, J. L. Hinshaw, D. Barlow, D. Jensen, M. Reichelderfer, and B. D. Cash. Assessment of volumetric growth rates of small colorectal polyps with ct colonography: a longitudinal study of natural history. *The lancet oncology*, 14(8):711–720, 2013.

[398] J. S. Levine and D. J. Ahnen. Adenomatous polyps of the colon. *New England Journal of Medicine*, 355(24):2551–2557, 2006.

[399] M. Risio. Reprint of: the natural history of adenomas. *Best practice & research Clinical gastroenterology*, 24(4):397–406, 2010.

[400] T. A. Waldmann. Immunotherapy: past, present and future. *Nature medicine*, 9(3):269–277, 2003.

[401] S. A. Rosenberg and N. P. Restifo. Adoptive cell transfer as personalized immunotherapy for human cancer. *Science*, 348(6230):62–68, 2015.

[402] P. Sharma and J. P. Allison. The future of immune checkpoint therapy. *Science*, 348(6230):56–61, 2015.

[403] L. Milling, Y. Zhang, and D. J. Irvine. Delivering safer immunotherapies for cancer. *Advanced drug delivery reviews*, 114:79–101, 2017.

[404] B. Kwong, H. Liu, and D. J. Irvine. Induction of potent anti-tumor responses while eliminating systemic side effects via liposome-anchored combinatorial immunotherapy. *Biomaterials*, 32(22): 5134–5147, 2011.

[405] G. P. Smith and V. A. Petrenko. Phage display. *Chemical reviews*, 97(2):391–410, 1997.

[406] H. R. Hoogenboom, J. T. Lutgerink, M. M. Pelsers, M. J. Rousch, J. Coote, N. van Neer, A. de Bruïne, F. A. van Nieuwenhoven, J. F. Glatz, and J.-W. Arends. Selection-dominant and nonaccessible epitopes on cell-surface receptors revealed by cell-panning with a large phage antibody library. *European journal of biochemistry*, 260(3):774–784, 1999.

[407] S. Khajeh, M. R. Tohidkia, A. Aghanejad, T. Mehdipour, F. Fathi, and Y. Omidi. Phage display selection of fully human antibody fragments to inhibit growth-promoting effects of glycine-extended gastrin 17 on human colorectal cancer cells. *Artificial cells, nanomedicine, and biotechnology*, 46 (sup2):1082–1090, 2018.

[408] P. Murgas, N. Bustamante, N. Araya, S. Cruz-Gómez, E. Durán, D. Gaete, C. Oyarce, E. López, A. A. Herrada, N. Ferreira, et al. A filamentous bacteriophage targeted to carcinoembryonic antigen induces tumor regression in mouse models of colorectal cancer. *Cancer Immunology, Immunotherapy*, 67(2):183–193, 2018.

[409] P. Murer, L. Plüss, and D. Neri. A novel human monoclonal antibody specific to the a33 glycoprotein recognizes colorectal cancer and inhibits metastasis. In *mAbs*, number just-accepted, page 1714371. Taylor & Francis, 2020.

[410] H. Naci, A. W. Carter, and E. Mossialos. Why the drug development pipeline is not delivering better medicines. *BMJ*, 351:h5542, 2015.

[411] J. DiMasi. Feldman l, seckler a, wilson a. *Trends in Risks Associated With New Drug Development: Success Rates for Investigational Drugs, Clinical Pharmacology & Therapeutics*, 87(3):272–277, 2010.

[412] W. Zheng, N. Thorne, and J. C. McKew. Phenotypic screens as a renewed approach for drug discovery. *Drug discovery today*, 18(21-22):1067–1073, 2013.

[413] J. L. Cummings, T. Morstorf, and K. Zhong. Alzheimer's disease drug-development pipeline: few candidates, frequent failures. *Alzheimer's research & therapy*, 6(4):37, 2014.

[414] E. Chatelain and J.-R. Ioset. Phenotypic screening approaches for chagas disease drug discovery. *Expert opinion on drug discovery*, 13(2):141–153, 2018.

[415] M. T. Dinday and S. C. Baraban. Large-scale phenotype-based antiepileptic drug screening in a zebrafish model of dravet syndrome. *ENeuro*, 2(4), 2015.

[416] A. Griffin, K. R. Hamling, S. Hong, M. Anvar, L. P. Lee, and S. C. Baraban. Preclinical animal models for dravet syndrome: seizure phenotypes, comorbidities and drug screening. *Frontiers in pharmacology*, 9:573, 2018.

[417] D. Drewry, B. King, C. Wells, and W. Zuercher. New screening approaches for kinases. In *Kinase Drug Discovery*, pages 9–33. 2018.

[418] Y. E. Karapetyan, G. F. Sferrazza, M. Zhou, G. Ottenberg, T. Spicer, P. Chase, M. Fallahi, P. Hodder, C. Weissmann, and C. I. Lasmézas. Unique drug screening approach for prion diseases identifies tacrolimus and astemizole as antiprion agents. *Proceedings of the National Academy of Sciences*, 110(17):7044–7049, 2013.

[419] Z. Y. Pessetto, B. Chen, H. Alturkmani, S. Hyter, C. A. Flynn, M. Baltezor, Y. Ma, H. G. Rosenthal, K. A. Neville, S. J. Weir, et al. In silico and in vitro drug screening identifies new therapeutic approaches for ewing sarcoma. *Oncotarget*, 8(3):4079, 2017.

[420] S. Roberts. High-throughput screening approaches for investigating drug metabolism and pharmacokinetics. *Xenobiotica*, 31(8-9):557–589, 2001.

[421] J. G. Moffat, J. Rudolph, and D. Bailey. Phenotypic screening in cancer drug discovery—past, present and future. *Nature reviews Drug discovery*, 13(8):588–602, 2014.

[422] M. P. Menden, D. Wang, M. J. Mason, B. Szalai, K. C. Bulusu, Y. Guan, T. Yu, J. Kang, M. Jeon, R. Wolfinger, et al. Community assessment to advance computational prediction of cancer drug combinations in a pharmacogenomic screen. *Nature communications*, 10(1):1–17, 2019.

[423] M. Suggitt and M. C. Bibby. 50 years of preclinical anticancer drug screening: empirical to target-driven approaches. *Clinical Cancer Research*, 11(3):971–981, 2005.

[424] J. Mattina, B. Carlisle, Y. Hachem, D. Fergusson, and J. Kimmelman. Inefficiencies and patient burdens in the development of the targeted cancer drug sorafenib: a systematic review. *PLoS biology*, 15(2), 2017.

[425] S. Balasubramaniam, G. S. Kim, A. E. McKee, and R. Pazdur. Regulatory considerations on endpoints in ovarian cancer drug development. *Cancer*, 123(14):2604–2608, 2017.

[426] N. Cook, D. I. Jodrell, and D. A. Tuveson. Predictive in vivo animal models and translation to clinical trials. *Drug discovery today*, 17(5-6):253–260, 2012.

[427] B. A. Ruggeri, F. Camp, and S. Miknyoczki. Animal models of disease: pre-clinical animal models of cancer and their applications and utility in drug discovery. *Biochemical pharmacology*, 87(1): 150–161, 2014.

[428] A. L. Kung. Practices and pitfalls of mouse cancer models in drug discovery. *Advances in cancer research*, 96:191–212, 2006.

[429] M. Kim, H. Mun, C. O. Sung, E. J. Cho, H.-J. Jeon, S.-M. Chun, T. H. Shin, G. S. Jeong, D. K. Kim, E. K. Choi, et al. Patient-derived lung cancer organoids as in vitro cancer models for therapeutic screening. *Nature communications*, 10(1):1–15, 2019.

[430] C. Pauli, B. D. Hopkins, D. Prandi, R. Shaw, T. Fedrizzi, A. Sboner, V. Sailer, M. Augello, L. Puca, R. Rosati, et al. Personalized in vitro and in vivo cancer models to guide precision medicine. *Cancer discovery*, 7(5):462–477, 2017.

[431] S. Samavedi and N. Joy. 3d printing for the development of in vitro cancer models. *Current Opinion in Biomedical Engineering*, 2:35–42, 2017.

[432] A. Nyga, U. Cheema, and M. Loizidou. 3d tumour models: novel in vitro approaches to cancer studies. *Journal of cell communication and signaling*, 5(3):239, 2011.

[433] I. Godet, Y. J. Shin, J. A. Ju, I. C. Ye, G. Wang, and D. M. Gilkes. Fate-mapping post-hypoxic tumor cells reveals a ros-resistant phenotype that promotes metastasis. *Nature communications*, 10(1): 1–18, 2019.

[434] B. R. Seo, P. DelNero, and C. Fischbach. In vitro models of tumor vessels and matrix: engineering approaches to investigate transport limitations and drug delivery in cancer. *Advanced drug delivery reviews*, 69:205–216, 2014.

[435] J. B. Kim, R. Stein, and M. J. O'hare. Three-dimensional in vitro tissue culture models of breast cancer—a review. *Breast cancer research and treatment*, 85(3):281–291, 2004.

[436] J. Kondo and M. Inoue. Application of cancer organoid model for drug screening and personalized therapy. *Cells*, 8(5):470, 2019.

[437] S. Rockwell. In vivo-in vitro tumour cell lines: characteristics and limitations as models for human cancer. *The British journal of cancer. Supplement*, 4:118, 1980.

[438] J. A. Hickman, R. Graeser, R. de Hoogt, S. Vidic, C. Brito, M. Gutekunst, and H. van der Kuip. Three-dimensional models of cancer for pharmacology and cancer cell biology: capturing tumor complexity in vitro/ex vivo. *Biotechnology journal*, 9(9):1115–1128, 2014.

[439] M. M. Centenera, G. V. Raj, K. E. Knudsen, W. D. Tilley, and L. M. Butler. Ex vivo culture of human prostate tissue and drug development. *Nature reviews Urology*, 10(8):483–487, 2013.

[440] D. Caballero, S. Kaushik, V. Correlo, J. M. Oliveira, R. Reis, and S. Kundu. Organ-on-chip models of cancer metastasis for future personalized medicine: From chip to the patient. *Biomaterials*, 149:98–115, 2017.

[441] M. Astolfi, B. Peant, M. Lateef, N. Rousset, J. Kendall-Dupont, E. Carmona, F. Monet, F. Saad, D. Provencher, A.-M. Mes-Masson, et al. Micro-dissected tumor tissues on chip: an ex vivo method for drug testing and personalized therapy. *Lab on a Chip*, 16(2):312–325, 2016.

[442] M. Yu, A. Bardia, N. Aceto, F. Bersani, M. W. Madden, M. C. Donaldson, R. Desai, H. Zhu, V. Comaills, Z. Zheng, et al. Ex vivo culture of circulating breast tumor cells for individualized testing of drug susceptibility. *science*, 345(6193):216–220, 2014.

[443] Z. Zhao, Y. Yang, Y. Zeng, and M. He. A microfluidic exosearch chip for multiplexed exosome detection towards blood-based ovarian cancer diagnosis. *Lab on a Chip*, 16(3):489–496, 2016.

[444] L. Zhao, C. Tang, L. Xu, Z. Zhang, X. Li, H. Hu, S. Cheng, W. Zhou, M. Huang, A. Fong, et al. Enhanced and differential capture of circulating tumor cells from lung cancer patients by microfluidic assays using aptamer cocktail. *Small*, 12(8):1072–1081, 2016.

[445] J. C. Wan, C. Massie, J. Garcia-Corbacho, F. Mouliere, J. D. Brenton, C. Caldas, S. Pacey, R. Baird, and N. Rosenfeld. Liquid biopsies come of age: towards implementation of circulating tumour dna. *Nature Reviews Cancer*, 17(4):223, 2017.

[446] C. L. Yankaskas, K. N. Thompson, C. D. Paul, M. I. Vitolo, P. Mistriotis, A. Mahendra, V. K. Bajpai, D. J. Shea, K. M. Manto, A. C. Chai, et al. A microfluidic assay for the quantification of the metastatic propensity of breast cancer specimens. *Nature biomedical engineering*, 3(6):452–465, 2019.

[447] A. Sontheimer-Phelps, B. A. Hassell, and D. E. Ingber. Modelling cancer in microfluidic human organs-on-chips. *Nature Reviews Cancer*, 19(2):65–81, 2019.

[448] N. V. Menon, S. B. Lim, and C. T. Lim. Microfluidics for personalized drug screening of cancer. *Current opinion in pharmacology*, 48:155–161, 2019.

[449] H. L. Lanz, A. Saleh, B. Kramer, J. Cairns, C. P. Ng, J. Yu, S. J. Trietsch, T. Hankemeier, J. Joore, P. Vulto, et al. Therapy response testing of breast cancer in a 3d high-throughput perfused microfluidic platform. *BMC cancer*, 17(1):709, 2017.

[450] N. Dhiman, P. Kingshott, H. Sumer, C. S. Sharma, and S. N. Rath. On-chip anticancer drug screening–recent progress in microfluidic platforms to address challenges in chemotherapy. *Biosensors and Bioelectronics*, 137:236–254, 2019.

[451] J. Kim, H. Takeuchi, S. T. Lam, R. R. Turner, H.-J. Wang, C. Kuo, L. Foshag, A. J. Bilchik, and D. S. Hoon. Chemokine receptor cxcr4 expression in colorectal cancer patients increases the risk for recurrence and for poor survival. *Journal of Clinical Oncology*, 23(12):2744–2753, 2005.

[452] C. C. Schimanski, S. Schwald, N. Simiantonaki, C. Jayasinghe, U. Gönner, V. Wilsberg, T. Junginger, M. R. Berger, P. R. Galle, and M. Moehler. Effect of chemokine receptors cxcr4 and ccr7 on the metastatic behavior of human colorectal cancer. *Clinical Cancer Research*, 11(5):1743–1750, 2005.

[453] M. Levisson, R. B. Spruijt, I. N. Winkel, S. W. Kengen, and J. van der Oost. Phage display of engineered binding proteins. In *Protein Downstream Processing*, pages 211–229. Springer, 2014.

[454] *SOP: Thawing, Propagation and Cryopreservation of NCI-PBCF-CCL 247 (HCT116) Colorectal Carcinoma*. National Cancer Institute, 2012.

[455] P. J. Lee and G. A. Peyman. Visualization of the retinal and choroidal microvasculature by fluorescent liposomes. In *Methods in enzymology*, volume 373, pages 214–233. Elsevier, 2003.

[456] I. F. Pinto, D. R. Santos, C. R. Caneira, R. R. Soares, A. M. Azevedo, V. Chu, and J. P. Conde. Optical biosensing in microfluidics using nanoporous microbeads and amorphous silicon thin-film photodiodes: Quantitative analysis of molecular recognition and signal transduction. *Journal of Micromechanics and Microengineering*, 28(9):094004, 2018.

[457] M. K. Kashyap, C. I. Amaya-Chanaga, D. Kumar, B. Simmons, N. Huser, Y. Gu, M. Hallin, K. Lindquist, R. Yafawi, M. Y. Choi, et al. Targeting the cxcr4 pathway using a novel anti-cxcr4 igg1 antibody (pf-06747143) in chronic lymphocytic leukemia. *Journal of hematology & oncology*, 10(1):112, 2017.

[458] M.-H. Cho, A. Niles, R. Huang, J. Inglese, C. P. Austin, T. Riss, and M. Xia. A bioluminescent cytotoxicity assay for assessment of membrane integrity using a proteolytic biomarker. *Toxicology in vitro*, 22(4):1099–1106, 2008.

[459] T. Colangelo, G. Polcaro, L. Muccillo, G. D'Agostino, V. Rosato, P. Ziccardi, A. Lupo, G. Mazzoccoli, L. Sabatino, and V. Colantuoni. Friend or foe?: The tumour microenvironment dilemma in colorectal cancer. *Biochimica et Biophysica Acta (BBA)-Reviews on Cancer*, 1867(1):1–18, 2017.

[460] A. I. Matos, B. Carreira, C. Peres, L. I. Moura, J. Conniot, T. Fourniols, A. Scomparin, Á. Martínez-Barriocanal, D. Arango, J. P. Conde, et al. Nanotechnology is an important strategy for combinational innovative chemo-immunotherapies against colorectal cancer. *Journal of Controlled Release*, 307:108–138, 2019.

[461] D. Gyori, E. L. Lim, F. M. Grant, D. Spensberger, R. Roychoudhuri, S. J. Shuttleworth, K. Okkenhaug, L. R. Stephens, and P. T. Hawkins. Compensation between csf1r+ macrophages and foxp3+ treg cells drives resistance to tumor immunotherapy. *JCI insight*, 3(11), 2018.

[462] M. Sluijter, T. C. van der Sluis, P. A. van der Velden, M. Versluis, B. L. West, S. H. van der Burg, and T. van Hall. Inhibition of csf-1r supports t-cell mediated melanoma therapy. *PloS one*, 9(8), 2014.

[463] F. Dammeijer, L. A. Lievense, M. E. Kaijen-Lambers, M. van Nimwegen, K. Bezemer, J. P. Hegmans, T. van Hall, R. W. Hendriks, and J. G. Aerts. Depletion of tumor-associated macrophages with a csf-1r kinase inhibitor enhances antitumor immunity and survival induced by dc immunotherapy. *Cancer immunology research*, 5(7):535–546, 2017.

[464] A. I. Matos. *COMBI-CRC: COMBINATORIAL MULTIVALENT NANOPLATFORM FOR COLORECTAL CANCER TREATMENT*. PhD thesis, Instituto Superior Técnico, Universidade de Lisboa, 2020.

[465] Y.-Q. Liu, Y.-N. Wang, X.-Y. Lu, L.-J. Tong, Y. Li, T. Zhang, Q.-J. Xun, F. Feng, Y.-Z. Chen, Y. Su, et al. Identification of compound d2923 as a novel anti-tumor agent targeting csf1r. *Acta Pharmacologica Sinica*, 39(11):1768–1776, 2018.

[466] D. Silva, A. Azevedo, P. Fernandes, V. Chu, J. Conde, and M. Aires-Barros. Determination of partition coefficients of biomolecules in a microfluidic aqueous two phase system platform using fluorescence microscopy. *Journal of Chromatography A*, 1487:242–247, 2017.

[467] I. F. Pinto, R. R. Soares, M. R. Aires-Barros, V. Chu, J. P. Conde, and A. M. Azevedo. Optimizing the performance of chromatographic separations using microfluidics: multiplexed and quantitative screening of ligands and target molecules. *Biotechnology journal*, 14(10):1800593, 2019.

Appendix A

Mentored Students

In this section I will present a brief overview of the MSc. thesis I mentored during my PhD. In addition to these students there were also times where I accompanied summer interns and visiting PhD students (for example in the case of the MIT Portugal lab rotations).

Rafaela Pereira (IST) - Development of a miniaturized chip for personalized therapy of Cystic Fibrosis

In this work, the main goal was to cultivate a cystic fibrosis cell line model in the microfluidic chip in order to screen possible treatment combinations. The multiple inlets of the microfluidic device are used to inject the different components of the experiment, as well as to allow for different combinations of potential drugs through flow rate manipulation.

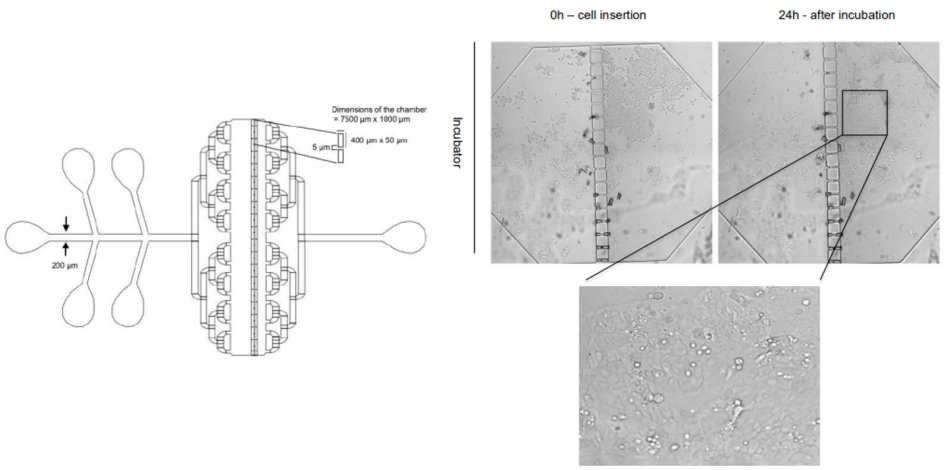

Figure A.1: (Left) Microfluidic structure for the physical entrapment of the cystic fibrosis cells. (Right) Micrographs of the cell culture.

Benjamin Heidt (Hochschule Kaiserslautern) - Multielectrode array integration into microfluidic systems for rapid screening of excitable cells

The goal of this work was to create a reusable microfluidic system that allowed for animal cell culture followed by potential difference measurements for neuron cell assessment. Despite the end-goal being neurons, the initial steps of this experiments used the HCT116 cell line from the POINT4PAC project, with the hope of transferring the knowledge built in these experiments to the neuron cells once Benjamin returned to Germany.

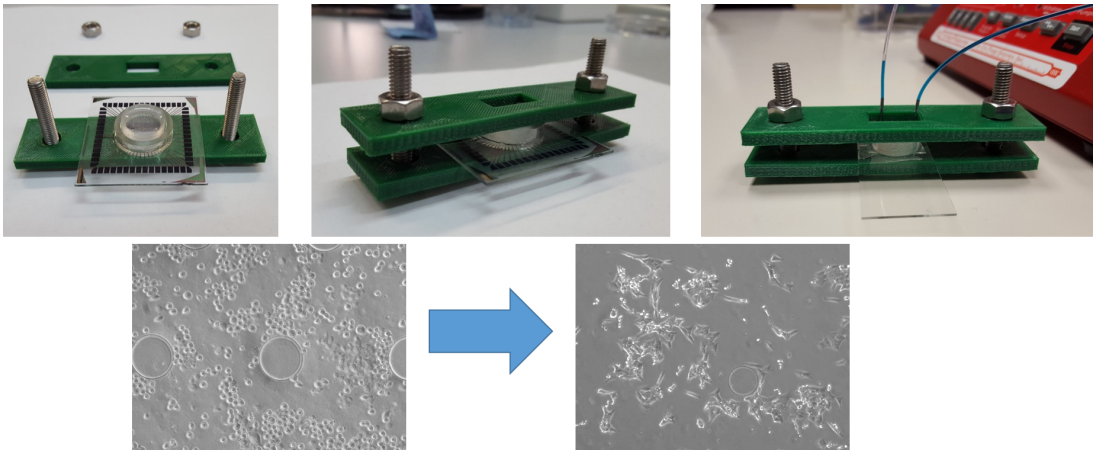

Figure A.2: Initial microfluidic structure developed in the context of the POINT4PAC project, before moving to a chemical bonding of the chip. Here the substrate was patterned with electrodes in order to interact with the cells. Micrographs depict the cell growth overtime.

Pedro Monteiro (IST) - Breakthrough curves in microfluidic chromatography columns

In this thesis, the main goal was to develop a robust method of characterizing microfluidic packed beds. This work was in line with an on-going project revolving around chromatography, however it produced very important results for the enzymatic production of L-DOPA as well. In the end, photosensors were used to quantify the breakthrough curves.

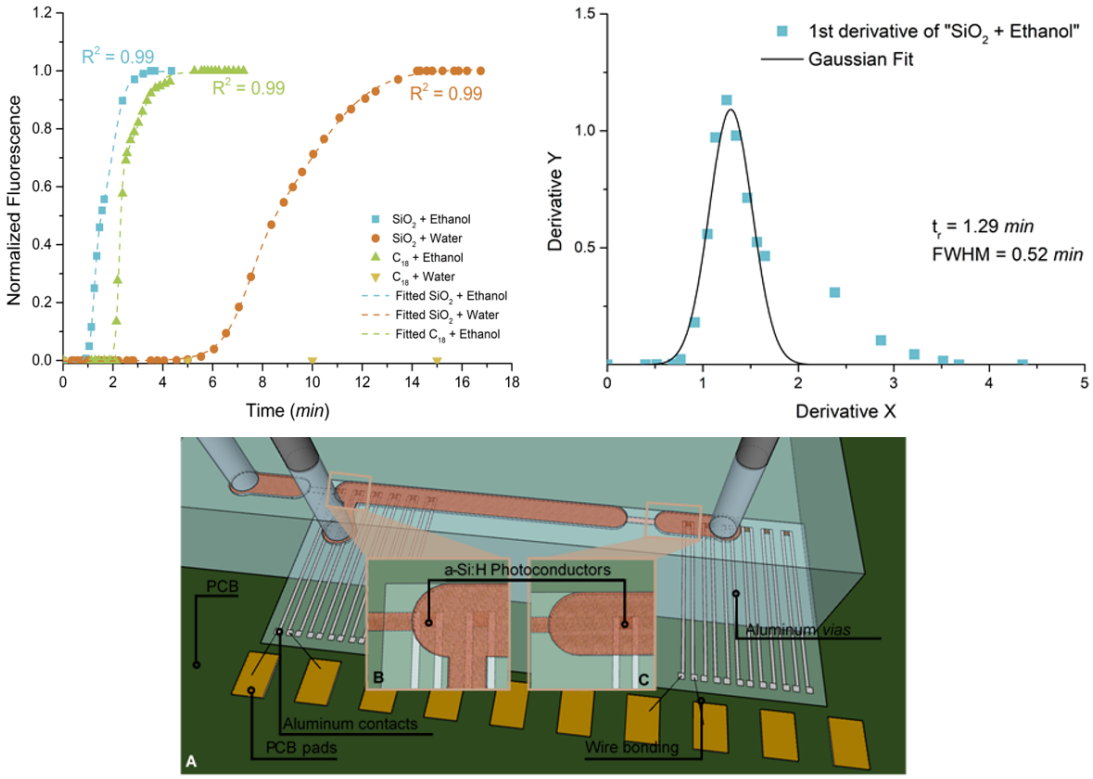

Figure A.3: (Top) Example of some of the breakthrough curves obtained. (Bottom) Experimental setup using the photosensors.

Niklas Floto (Hochschule Kaiserslautern) - Improvement and characterisation of a PDMS hybrid peristaltic pump

In this work, the objective was to develop a reusable, PDMS-PMMA peristaltic pumping system that could be used for different microfluidic chips, without changing the design of the pump itself.

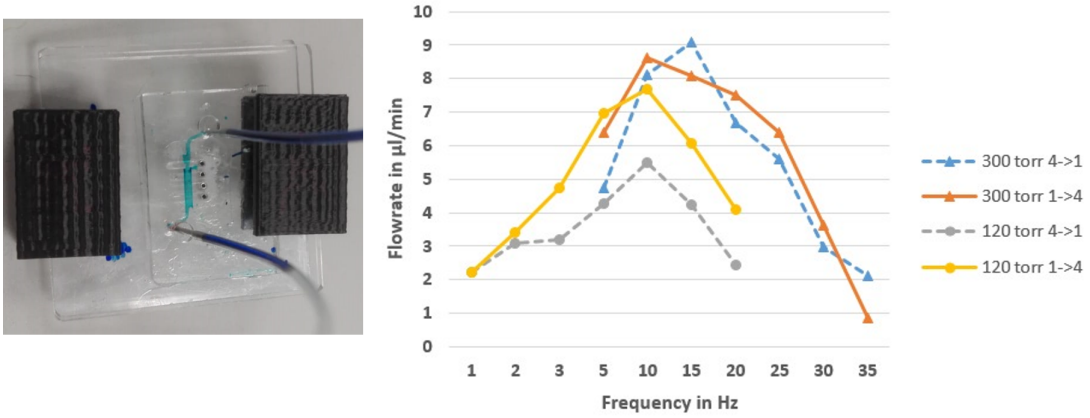

Figure A.4: Clamping system developed for a reusable peristaltic pumping module (left) and flowrate characterization as a function of membrane deflection frequency (right).

Cristiana Domingues (IST) - Immobilization of tyrosinase in porous micro beads for extended continuous production of L-DOPA

As described before, Cristiana played a very active role in the enzymatic production portion of this doctoral thesis. Having proposed her thesis topic myself, it was possible to align it within my thesis main goals.

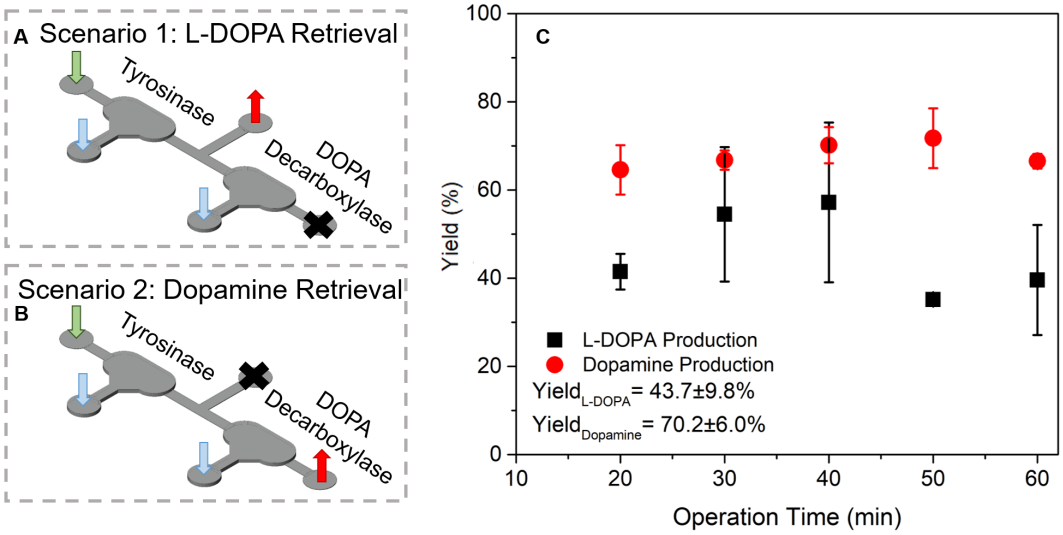

Figure A.5: Sequential production of both L-DOPA and dopamine in a single integrated microfluidic system. The reaction medium is injected at 1 μL/min and is composed of 100 μM of tyrosine and 100 μM of ascorbic acid. For the monitoring of L-DOPA production, the outlet is sealed off and the middle outlet is used for sample retrieval (A). For the detection of dopamine, the middle outlet is sealed off and the sample is collected at the outlet (B). Productivity for both reaction steps (C). n=2.

Ricardo Serrão (FCT-NOVA) - Monitoring cell cultures in real time in a biochip

The last MSc. student I mentored was Ricardo, the main goal of his thesis was the initial steps concerning the cell viability assay through the ADK I detection. this work was also performed within the landscape of the POINT4PAC project.

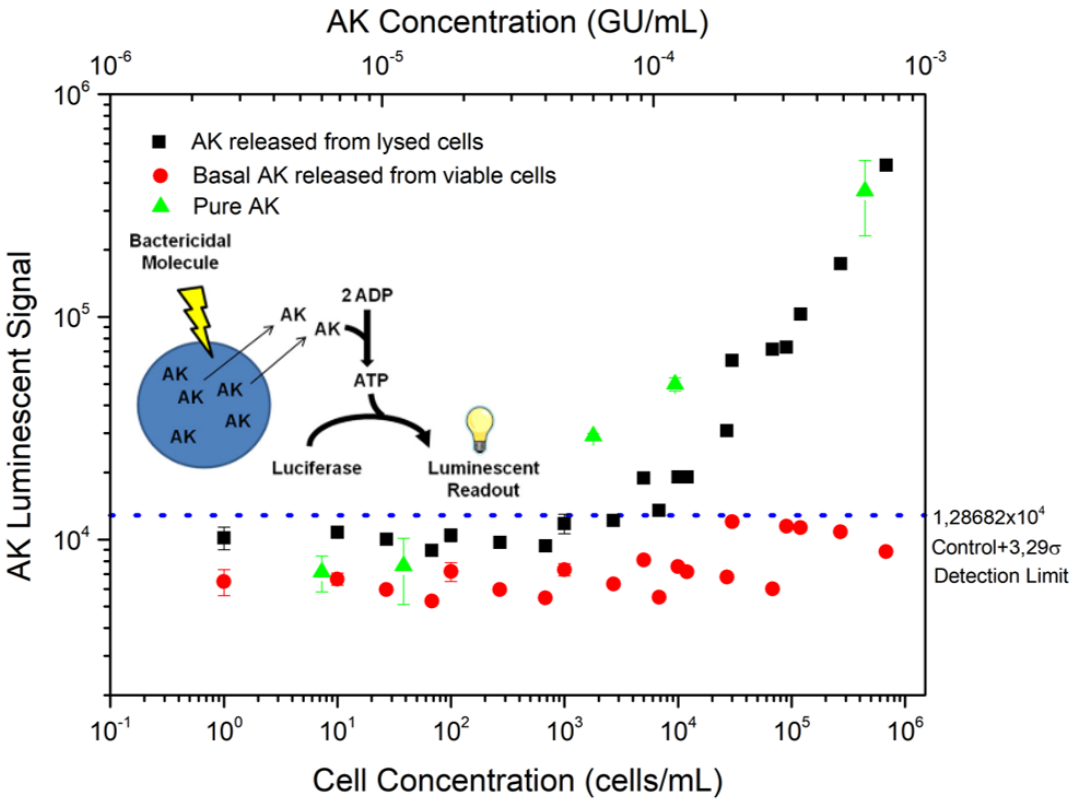

Figure A.6: Calibration curve for the release of ADK I vs the number of dead HCT116 cells.

Appendix B

Process Runsheets

B.1 Photoconductors

Expected process duration 3-4 weeks

1- Substrate Cleaning

Equipment and Materials

- Ultrasound Bath
- Alconox Solution
- DI Water
- Corning Glass Substrate
- IPA

Steps

- Rinse back of substrate with IPA to remove glue residue from dicing film
- Rinse with DI water to remove dust
- Submerge for 30 min in Alconox solution in ultrasound hot bath at 65°C
- Rinse with DI water and dry using compressed air
- Visual inspection

2- Bottom Aluminium Electrode Deposition (200 nm)

Equipment and Materials

- Sample
- Nordiko 7000 Magnetron Sputterer
- Kapton tape

Steps

- Place sample on metallic holder, remember that deposition is from the bottom-up
- Load the sample, run ”Al 200 nm, no etch” process sequence
- Visual inspection of film uniformity

3- Photoresist coat + Electrode definition + Development

Equipment and Materials

- Sample
- SVG resist coater and developer
- Heidelberg Instruments Direct Write Laser Lithography System (DWL)
- PFR7790G positive photoresist
- Optical Microscope
- Kapton tape

Steps

- Place sample on carrier wafer using minimal amount of Kapton tape to not affect PR coating thickness, load wafer in SVG track 2
- Run process sequence 6/2, this should produce a uniform coating of 1.5 μm thick layer of PR, if sample seems non-uniform, remove PR with acetone/microstrip followed by IPA rinse and start again
- Remove Kapton tape and load wafer on DWL stage, substrate alignment using manual alignment
- Exposure according to CAD file using latest calibrated laser condtions
- Unload sample, place new Kapton and load sample on SVG track 1 for development using process sequence 6/2
- Visual inspection of patterning using optical microscope with green filter, if underdeveloped, manual develop again in 10s intervals

4- Bottom Electrodes Wet Etching and Resist Strip

Equipment and Materials

- Sample
- Aluminum etchant
- Microstrip
- IPA

- DI Water

Steps

- Submerge sample in commercial etching solution, with gentle agitation until exposed aluminum is completely removed, microscope confirmation should be used
- Rinse with DI water, followed by a vigorous drying
- Submerge in microstrip solution until photoresist is removed
- Rinse with IPA and DI water, dry with compressed air

5- i-a-Si:H Deposition (Old CVD, 500 nm)

Equipment and Materials

- Sample
- rf-PECVD

Steps

- Isolating both deposition chambers, Load lock is brought to atmospheric pressure through N_2 injection, sample is loaded on sample carrier, load lock is brought to 10^{-7} Torr
- Silicon deposition is approx. 45 min, calibration is required some days before actual deposition, deposition conditions: V= 0 V; P= 0.1 Torr; P_{RF}= 5 W; Q SiH_4= 10 sccm, T= 250 $^{\circ}$C
- Sample unload and visual inspection for film uniformity

6- Photoresist coat + Sensor definition + Development

Equipment and Materials

- Sample
- SVG resist coater and developer
- Heidelberg Instruments Direct Write Laser Lithography System (DWL)
- PFR7790G positive photoresist
- Optical Microscope
- Kapton tape

Steps

- Place sample on carrier wafer using minimal amount of Kapton tape to not affect PR coating thickness, load wafer in SVG track 2
- Run process sequence 6/2, this should produce a uniform coating of 1.5 μm thick layer of PR, if sample seems non-uniform, remove PR with acetone/microstrip followed by IPA rinse and start again

- Remove Kapton tape and load wafer on DWL stage, substrate alignment using manual alignment
- Exposure according to CAD file using latest calibrated laser condtions
- Unload sample, place new Kapton and load sample on SVG track 1 for development using process sequence 6/2
- Visual inspection of patterning using optical microscope with green filter, if underdeveloped, manual develop again in 10s intervals

7- i-a-Si:H island etch via Reactive Ion Etching (LAM)

Equipment and Materials

- Sample
- LAM Research Rainbow Plasma Etcher
- Microstrip
- IPA
- DI water

Steps

- A carrier wafer should be coated with a protective layer of PR, then the sample is placed on this wafer and loaded to the machine
- Processing conditions are SF_6+CHF_3; P= 100 mTorr; P= 200 W; Q(SF_6)= 50 sccm; Q(CHF_3)= 50 sccm, Δt= 200 s
- Sample unload and visual inspection
- Submerge sample in hot Microstrip, this resist strip is longer then usual due to hardening of the resist during the RIE step
- Wash sample with IPA and DI water, visual inspection

8- Photoresist coat + Pad definition + Development

Equipment and Materials

- Sample
- SVG resist coater and developer
- Heidelberg Instruments Direct Write Laser Lithography System (DWL)
- PFR7790G positive photoresist
- Optical Microscope
- Kapton tape

Steps

- Place sample on carrier wafer using minimal amount of Kapton tape to not affect PR coating thickness, load wafer in SVG track 2
- Run process sequence 6/2, this should produce a uniform coating of 1.5 μm thick layer of PR, if sample seems non-uniform, remove PR with acetone/microstrip followed by IPA rinse and start again
- Remove Kapton tape and load wafer on DWL stage, substrate alignment using manual alignment
- Exposure according to CAD file using latest calibrated laser condtions
- Unload sample, place new Kapton and load sample on SVG track 1 for development using process sequence 6/2
- Visual inspection of patterning using optical microscope with green filter, if underdeveloped, manual develop again in 10s intervals

9- SiN$_x$ Passivation Layer Deposition (Old CVD, 100 nm)

Equipment and Materials

- Sample
- rf-PECVD

Steps

- Isolating both deposition chambers, Load lock is brought to atmospheric pressure through N_2 injection, sample is loaded on sample carrier, load lock is brought to 10^{-7} Torr
- Silicon Nitride deposition is approx. 45 min, calibration is required some days before actual deposition, deposition conditions: V= 0 V; P= 0.1 Torr; P_{RF}= 10 W; Q (SiH_4)= 5 sccm; Q(H_2)= 35 sccm; Q(NH_3)= 10 sccm; T= 100 °C
- Sample unload and visual inspection for film uniformity

10- SiN$_x$ Passivation Layer Lift-off

Equipment and Materials

- Microstrip
- Ultrasound Bath
- DI Water
- IPA

Steps

- Submerge sample in hot Microstrip, this step is much longer then any other (¿24h) due to the microstrip having to penetrate the film
- Wash with IPA and SI water, visual inspection under the optical microscope

At this point the sample may be diced and wire bonded, in the case of Si:C fluorescence filters, extra steps are needed.

11- Photoresist coat + Filter definition + Development

Equipment and Materials

- Sample
- SVG resist coater and developer
- Heidelberg Instruments Direct Write Laser Lithography System (DWL)
- PFR7790G positive photoresist
- Optical Microscope
- Kapton tape

Steps

- Place sample on carrier wafer using minimal amount of Kapton tape to not affect PR coating thickness, load wafer in SVG track 2
- Run process sequence 6/2, this should produce a uniform coating of 1.5 μm thick layer of PR, if sample seems non-uniform, remove PR with acetone/microstrip followed by IPA rinse and start again
- Remove Kapton tape and load wafer on DWL stage, substrate alignment using manual alignment
- Exposure according to CAD file using latest calibrated laser condtions
- Unload sample, place new Kapton and load sample on SVG track 1 for development using process sequence 6/2
- Visual inspection of patterning using optical microscope with green filter, if underdeveloped, manual develop again in 10s intervals

12- SiC Filter Deposition (Old CVD, 1.5 μm)

Equipment and Materials

- Sample
- rf-PECVD

Steps

- Isolating both deposition chambers, Load lock is brought to atmospheric pressure through N_2 injection, sample is loaded on sample carrier, load lock is brought to 10^{-7} Torr
- Silicon Carbide deposition is approx. 4 h, calibration is required some days before actual deposition, deposition conditions: V= 0 V; P= 0.1 Torr; P_{RF}= 10 W; Q (SiH_4)= 10.6 sccm; Q(C_2H_6)= 2.5 sccm; T= 100 °C, note that flow rates depend on fluorophore
- Sample unload and visual inspection for film uniformity

13- SiC Filter Lift-off

Equipment and Materials

- Microstrip
- Ultrasound Bath
- DI Water
- IPA

Steps

- Submerge sample in hot Microstrip, this step is much longer then any other (¿24h) due to the microstrip having to penetrate the film
- Wash with IPA and SI water, visual inspection under the optical microscope

B.2 Photodiodes

Expected process duration 1-2 weeks

1- Substrate Cleaning

Equipment and Materials

- Ultrasound Bath
- Alconox Solution
- DI Water
- Corning Glass Substrate
- IPA

Steps

- Rinse back of substrate with IPA to remove glue residue from dicing film
- Rinse with DI water to remove dust
- Submerge for 30 min in Alconox solution in ultrasound hot bath at 65°C
- Rinse with DI water and dry using compressed air
- Visual inspection

2- Bottom Aluminium Electrode Deposition (200 nm)

Equipment and Materials

- Sample
- Nordiko 7000 Magnetron Sputterer
- Kapton tape

Steps

- Place sample on metallic holder, remember that deposition is from the bottom-up
- Load the sample, run ”Al 200 nm, no etch” process sequence
- Visual inspection of film uniformity

3- Photoresist coat + Electrode definition + Development

Equipment and Materials

- Sample
- SVG resist coater and developer
- Heidelberg Instruments Direct Write Laser Lithography System (DWL)

- PFR7790G positive photoresist
- Optical Microscope
- Kapton tape

Steps

- Place sample on carrier wafer using minimal amount of Kapton tape to not affect PR coating thickness, load wafer in SVG track 2
- Run process sequence 6/2, this should produce a uniform coating of 1.5 μm thick layer of PR, if sample seems non-uniform, remove PR with acetone/microstrip followed by IPA rinse and start again
- Remove Kapton tape and load wafer on DWL stage, substrate alignment using manual alignment
- Exposure according to CAD file using latest calibrated laser condtions
- Unload sample, place new Kapton and load sample on SVG track 1 for development using process sequence 6/2
- Visual inspection of patterning using optical microscope with green filter, if underdeveloped, manual develop again in 10s intervals

4- Bottom Electrodes Wet Etching and Resist Strip
Equipment and Materials

- Sample
- Aluminum etchant
- Microstrip
- IPA
- DI Water

Steps

- Submerge sample in commercial etching solution, with gentle agitation until exposed aluminum is completely removed, microscope confirmation should be used
- Rinse with DI water, followed by a vigorous drying
- Submerge in microstrip solution until photoresist is removed
- Rinse with IPA and DI water, dry with compressed air

5- p-i-n-a-Si:H stack Deposition (Old CVD, 10nm + 500 nm + 10 nm)
Equipment and Materials

- Sample
- rf-PECVD

Steps

- Isolating both deposition chambers, Load lock is brought to atmospheric pressure through N_2 injection, sample is loaded on sample carrier, load lock is brought to 10^{-7} Torr
- n^+-layer deposition is approx. 1 min 40 s, calibration is required some days before actual deposition, deposition conditions: V= 0 V; P= 0.1 Torr; P_{RF}= 5 W; Q(SiH_4)= 10 sccm, Q(PH_3)= 5 sccm, T= 250 °C
- i-layer deposition is approx. 45 min, calibration is required some days before actual deposition, deposition conditions: V= 0 V; P= 0.1 Torr; P_{RF}= 5 W; Q(SiH_4)= 10 sccm, T= 250 °C
- p^+-layer deposition is approx. 1 min 40 s, calibration is required some days before actual deposition, deposition conditions: V= 0 V; P= 0.1 Torr; P_{RF}= 5 W; Q(SiH_4)= 10 sccm, Q(B_2H_6)= 5 sccm, T= 250 °C
- Sample unload and visual inspection for film uniformity

From this point onward, sample should be protected form the light as much as possible to avoid voltage stress.

6- Photoresist coat + Sensor definition + Development

Equipment and Materials

- Sample
- SVG resist coater and developer
- Heidelberg Instruments Direct Write Laser Lithography System (DWL)
- PFR7790G positive photoresist
- Optical Microscope
- Kapton tape

Steps

- Place sample on carrier wafer using minimal amount of Kapton tape to not affect PR coating thickness, load wafer in SVG track 2
- Run process sequence 6/2, this should produce a uniform coating of 1.5 μm thick layer of PR, if sample seems non-uniform, remove PR with acetone/microstrip followed by IPA rinse and start again
- Remove Kapton tape and load wafer on DWL stage, substrate alignment using manual alignment

- Exposure according to CAD file using latest calibrated laser condtions
- Unload sample, place new Kapton and load sample on SVG track 1 for development using process sequence 6/2
- Visual inspection of patterning using optical microscope with green filter, if underdeveloped, manual develop again in 10s intervals

7- p-i-n-a-Si:H island etch via Reactive Ion Etching (LAM)

Equipment and Materials

- Sample
- LAM Research Rainbow Plasma Etcher
- Microstrip
- IPA
- DI water

Steps

- A carrier wafer should be coated with a protective layer of PR, then the sample is placed on this wafer and loaded to the machine
- Processing conditions are SF_6+CHF_3; P= 100 mTorr; P= 200 W; Q(SF_6)= 50 sccm; Q(CHF_3)= 50 sccm, Δt= 200 s
- Sample unload and visual inspection
- Submerge sample in hot Microstrip, this resist strip is longer then usual due to hardening of the resist during the RIE step
- Wash sample with IPA and DI water, visual inspection

8- Photoresist coat + Side wall definition + Development

Equipment and Materials

- Sample
- SVG resist coater and developer
- Heidelberg Instruments Direct Write Laser Lithography System (DWL)
- PFR7790G positive photoresist
- Optical Microscope
- Kapton tape

Steps

- Place sample on carrier wafer using minimal amount of Kapton tape to not affect PR coating thickness, load wafer in SVG track 2
- Run process sequence 6/2, this should produce a uniform coating of 1.5 μm thick layer of PR, if sample seems non-uniform, remove PR with acetone/microstrip followed by IPA rinse and start again
- Remove Kapton tape and load wafer on DWL stage, substrate alignment using manual alignment
- Exposure according to CAD file using latest calibrated laser condtions
- Unload sample, place new Kapton and load sample on SVG track 1 for development using process sequence 6/2
- Visual inspection of patterning using optical microscope with green filter, if underdeveloped, manual develop again in 10s intervals

9- SiN$_x$ Side Wall Passivation Layer Deposition (Old CVD, 100 nm)

Equipment and Materials

- Sample
- rf-PECVD

Steps

- Isolating both deposition chambers, Load lock is brought to atmospheric pressure through N_2 injection, sample is loaded on sample carrier, load lock is brought to 10^{-7} Torr
- Silicon Nitride deposition is approx. 45 min, calibration is required some days before actual deposition, deposition conditions: V= 0 V; P= 0.1 Torr; P_{RF}= 10 W; Q (SiH_4)= 5 sccm; Q(H_2)= 35 sccm; Q(NH_3)= 10 sccm; T= 100 °C
- Sample unload and visual inspection for film uniformity

10- SiN$_x$ Passivation Layer Lift-off

Equipment and Materials

- Microstrip
- Ultrasound Bath
- DI Water
- IPA

Steps

- Submerge sample in hot Microstrip, this step is much longer then any other (¿24h) due to the microstrip having to penetrate the film

- Wash with IPA and DI water, visual inspection under the optical microscope

11- Photoresist coat + ITO top contact definition + Development

Equipment and Materials

- Sample
- SVG resist coater and developer
- Heidelberg Instruments Direct Write Laser Lithography System (DWL)
- PFR7790G positive photoresist
- Optical Microscope
- Kapton tape

Steps

- Place sample on carrier wafer using minimal amount of Kapton tape to not affect PR coating thickness, load wafer in SVG track 2
- Run process sequence 6/2, this should produce a uniform coating of 1.5 μm thick layer of PR, if sample seems non-uniform, remove PR with acetone/microstrip followed by IPA rinse and start again
- Remove Kapton tape and load wafer on DWL stage, substrate alignment using manual alignment
- Exposure according to CAD file using latest calibrated laser condtions
- Unload sample, place new Kapton and load sample on SVG track 1 for development using process sequence 6/2
- Visual inspection of patterning using optical microscope with green filter, if underdeveloped, manual develop again in 10s intervals

12- ITO top contact deposition (50 nm)

Equipment and Materials

- Alcatel PVD

Steps

- Sample must be loaded the previous evening for deposition chamber to reach the adequate working pressure
- Run ITO deposition protocol

13- ITO Layer Lift-off

Equipment and Materials

- Microstrip
- Ultrasound Bath
- DI Water
- IPA

Steps

- Submerge sample in hot Microstrip, this step is much longer then any other (¿24h) due to the microstrip having to penetrate the film
- Wash with IPA and SI water, visual inspection under the optical microscope

14- Photoresist coat + Aluminum top contact definition + Development
Equipment and Materials

- Sample
- SVG resist coater and developer
- Heidelberg Instruments Direct Write Laser Lithography System (DWL)
- PFR7790G positive photoresist
- Optical Microscope
- Kapton tape

Steps

- Place sample on carrier wafer using minimal amount of Kapton tape to not affect PR coating thickness, load wafer in SVG track 2
- Run process sequence 6/2, this should produce a uniform coating of 1.5 μm thick layer of PR, if sample seems non-uniform, remove PR with acetone/microstrip followed by IPA rinse and start again
- Remove Kapton tape and load wafer on DWL stage, substrate alignment using manual alignment
- Exposure according to CAD file using latest calibrated laser condtions
- Unload sample, place new Kapton and load sample on SVG track 1 for development using process sequence 6/2
- Visual inspection of patterning using optical microscope with green filter, if underdeveloped, manual develop again in 10s intervals

15- Aluminium Deposition (200 nm)
Equipment and Materials

- Sample
- Nordiko 7000 Magnetron Sputterer
- Kapton tape

Steps

- Place sample on metallic holder, remember that deposition is from the bottom-up
- Load the sample, run ”Al 200 nm, no etch” process sequence
- Visual inspection of film uniformity

16- Aluminum Layer Lift-off

Equipment and Materials

- Microstrip
- Ultrasound Bath
- DI Water
- IPA

Steps

- Submerge sample in hot Microstrip, this step is much longer then any other (¿24h) due to the microstrip having to penetrate the film
- Wash with IPA and SI water, visual inspection under the optical microscope

17- Photoresist coat + Pad definition + Development

Equipment and Materials

- Sample
- SVG resist coater and developer
- Heidelberg Instruments Direct Write Laser Lithography System (DWL)
- PFR7790G positive photoresist
- Optical Microscope
- Kapton tape

Steps

- Place sample on carrier wafer using minimal amount of Kapton tape to not affect PR coating thickness, load wafer in SVG track 2

- Run process sequence 6/2, this should produce a uniform coating of 1.5 μm thick layer of PR, if sample seems non-uniform, remove PR with acetone/microstrip followed by IPA rinse and start again
- Remove Kapton tape and load wafer on DWL stage, substrate alignment using manual alignment
- Exposure according to CAD file using latest calibrated laser condtions
- Unload sample, place new Kapton and load sample on SVG track 1 for development using process sequence 6/2
- Visual inspection of patterning using optical microscope with green filter, if underdeveloped, manual develop again in 10s intervals

18- SiN$_x$ Passivation Layer Deposition (Old CVD, 100 nm)

Equipment and Materials

- Sample
- rf-PECVD

Steps

- Isolating both deposition chambers, Load lock is brought to atmospheric pressure through N_2 injection, sample is loaded on sample carrier, load lock is brought to 10^{-7} Torr
- Silicon Nitride deposition is approx. 45 min, calibration is required some days before actual deposition, deposition conditions: V= 0 V; P= 0.1 Torr; P_{RF}= 10 W; Q (SiH_4)= 5 sccm; Q(H_2)= 35 sccm; Q(NH_3)= 10 sccm; T= 100 °C
- Sample unload and visual inspection for film uniformity

19- SiN$_x$ Passivation Layer Lift-off

Equipment and Materials

- Microstrip
- Ultrasound Bath
- DI Water
- IPA

Steps

- Submerge sample in hot Microstrip, this step is much longer then any other (¿24h) due to the microstrip having to penetrate the film
- Wash with IPA and SI water, visual inspection under the optical microscope

At this point the sample may be diced and wire bonded, in the case of Si:C fluorescence filters, extra steps are needed.

B.3 Microfluidic Hard Masks

Expected process duration 1-2 weeks

1- Substrate Cleaning

Equipment and Materials

- Ultrasound Bath
- Alconox Solution
- DI Water
- Corning Glass Substrate
- IPA

Steps

- Rinse back of substrate with IPA to remove glue residue from dicing film
- Rinse with DI water to remove dust
- Submerge for 30 min in Alconox solution in ultrasound hot bath at 65°C
- Rinse with DI water and dry using compressed air
- Visual inspection

2- Aluminium Deposition (200 nm)

Equipment and Materials

- Sample
- Nordiko 7000 Magnetron Sputterer
- Kapton tape

Steps

- Place sample on metallic holder, remember that deposition is from the bottom-up
- Load the sample, run ”Al 200 nm, no etch” process sequence
- Visual inspection of film uniformity

3- Photoresist coat + Patterning + Development

Equipment and Materials

- Sample
- SVG resist coater and developer
- Heidelberg Instruments Direct Write Laser Lithography System (DWL)

- PFR7790G positive photoresist
- Optical Microscope
- Kapton tape

Steps

- Place sample on carrier wafer using minimal amount of Kapton tape to not affect PR coating thickness, load wafer in SVG track 2
- Run process sequence 6/2, this should produce a uniform coating of 1.5 μm thick layer of PR, if sample seems non-uniform, remove PR with acetone/microstrip followed by IPA rinse and start again
- Remove Kapton tape and load wafer on DWL stage, substrate alignment using manual alignment
- Exposure according to CAD file using latest calibrated laser condtions
- Unload sample, place new Kapton and load sample on SVG track 1 for development using process sequence 6/2
- Visual inspection of patterning using optical microscope with green filter, if underdeveloped, manual develop again in 10s intervals

4- Wet Etching and Resist Strip

Equipment and Materials

- Sample
- Aluminum etchant
- Microstrip
- IPA
- DI Water

Steps

- Submerge sample in commercial etching solution, with gentle agitation until exposed aluminum is completely removed, microscope confirmation should be used
- Rinse with DI water, followed by a vigorous drying
- Submerge in microstrip solution until photoresist is removed
- Rinse with IPA and DI water, dry with compressed air

B.4 Microfluidic Mold - 20 μm high

1- Substrate Cleaning

Equipment and Materials

- Ultrasound Bath
- Alconox Solution
- DI Water
- Silicon Substrate
- IPA

Steps

- Rinse back of substrate with IPA to remove glue residue from dicing film
- Rinse with DI water to remove dust
- Submerge for 30 min in Alconox solution in ultrasound hot bath at 65°C
- Rinse with DI water and dry using compressed air
- Visual inspection

2- SU-8 Spin Coating

Equipment and Materials

- Laminar Flow Hood
- SU-8 2015
- Spinner

Steps

- Center substrate in the spinner and pour a reasonable amount of SU-8 in the center of the substrate
- Rotate substrate in 2 steps, first: 10 s, 500 rpm, 100 rpm/s; second step: 34 s, 1700 rpm, 300 rpm/s
- Release vacuum and retrieve sample avoiding any spillage from spinner walls
- Visual inspection

3- Pre-exposure bake

Equipment and Materials

- Laminar Flow Hood

- Hot plate

Steps

- Heat the substrate for 4 min at 95 °C, this will evaporate the SU-8 solvent
- Visual inspection

4- UV Exposure

Equipment and Materials

- UV Lamp
- Kapton tape
- Hard mask

Steps

- Center the substrate on the holder and place the hard mask on top of the SU-8 covered sample, aluminum faced down
- Expose for 30 s

5- Post-exposure bake

Equipment and Materials

- Laminar Flow Hood
- Hot plate

Steps

- Heat the substrate for 5 min at 95 °C, this will accelerate the photo induced reticulation of the SU-8
- Visual inspection

6- Development

Equipment and Materials

- Glass tin
- Propylene glycol methyl ether acetate (PGMEA)
- IPA

Steps

- Submerge the sample in PGMEA, under gentle agitation
- Development confirmation can be performed by spraying with IPA and check for white precipitate formation, this should be done in a non crucial area as the white precipitate is hard to remove

- Visual inspection

7- Hard Bake

Equipment and Materials

- Laminar Flow Hood
- Hot plate

Steps

- Heat the substrate for 45 min at 150 °C, this will harden the mold
- Visual inspection

B.5 Microfluidic Mold - 100 μm high

1- Substrate Cleaning

Equipment and Materials

- Ultrasound Bath
- Alconox Solution
- DI Water
- Silicon Substrate
- IPA

Steps

- Rinse back of substrate with IPA to remove glue residue from dicing film
- Rinse with DI water to remove dust
- Submerge for 30 min in Alconox solution in ultrasound hot bath at 65°C
- Rinse with DI water and dry using compressed air
- Visual inspection

2- SU-8 Spin Coating

Equipment and Materials

- Laminar Flow Hood
- SU-8 50
- Spinner

Steps

- Center substrate in the spinner and pour a reasonable amount of SU-8 in the center of the substrate
- Rotate substrate in 2 steps, first: 10 s, 500 rpm, 100 rpm/s; second step: 30 s, 1000 rpm, 300 rpm/s
- Release vacuum and retrieve sample avoiding any spillage from spinner walls
- Visual inspection

3- Pre-exposure bake

Equipment and Materials

- Laminar Flow Hood

- Hot plate

Steps

- Heat the substrate for 10 min at 65 °C, ramp temperature to 95 °C, followed by 30 min bake, this will evaporate the SU-8 solvent slowly
- Visual inspection

4- UV Exposure

Equipment and Materials

- UV Lamp
- Kapton tape
- Hard mask

Steps

- Center the substrate on the holder and place the hard mask on top of the SU-8 covered sample, aluminum faced down
- Expose for 70 s

5- Post-exposure bake

Equipment and Materials

- Laminar Flow Hood
- Hot plate

Steps

- Heat the substrate for 1 min at 65 °C, ramp temperature to 95 °C, followed by 10 min bake, this will accelerate the photo induced reticulation of the SU-8
- Visual inspection

6- Development

Equipment and Materials

- Glass tin
- Propylene glycol methyl ether acetate (PGMEA)
- IPA

Steps

- Submerge the sample in PGMEA, under gentle agitation

- Development confirmation can be performed by spraying with IPA and check for white precipitate formation, this should be done in a non crucial area as the white precipitate is hard to remove
- Visual inspection

7- Hard Bake

Equipment and Materials

- Laminar Flow Hood
- Hot plate

Steps

- Heat the substrate for 45 min at 150 °C, this will harden the mold
- Visual inspection

Appendix C

Arduino Coding For Portable Prototype

```
  //HVir// Included Libraries:

#include <SD.h>
#include <Adafruit_GFX.h>              // Graphics library
#include <SPI.h>                       // SPI protocol library to interface with the LCD
    chip and the SD card
#include <Adafruit_ILI9341.h>          // Graphics library
#include "TouchScreen.h"               // Resistive touch screen library

#include <Fonts/FreeSans9pt7b.h>       // Font libraries
#include <Fonts/FreeSans12pt7b.h>
#include <Fonts/FreeSans18pt7b.h>
#include <Fonts/FreeSerif18pt7b.h>

// These are the four touchscreen analog pins
#define YP A9   // must be an analog pin, use "An" notation!
#define XM A12  // must be an analog pin, use "An" notation!
#define YM 24   // can be a digital pin
#define XP 9    // can be a digital pin

// This is calibration data for the raw touch data to the screen coordinates
#define TS_MINX 125
#define TS_MINY 65
#define TS_MAXX 920
#define TS_MAXY 920

#define MINPRESSURE 5
#define MAXPRESSURE 1000

// The display uses hardware SPI
#define TFT_DC 9
```

```
#define TFT_CS 10
#define TFT_MOSI 11
#define TFT_CLK 13
#define TFT_RST 12
#define TFT_MISO 12

// Coordinates for text printing
unsigned int x00 = 0;
unsigned int y00 = 100;
unsigned int x;
unsigned int y;
int          xx1, yy1;
unsigned int w, h;

// Buttons for the menu
int butwidth = 180;       // Width of the buttons
int butheight = 40;       // Height of the buttons
int startY = 65;

// Color definitions
#define BLACK               0x0000
#define BLUE                0x001F
#define RED                 0xF800
#define GREEN               0x07E0
#define CYAN                0x07FF
#define MAGENTA             0xF81F
#define YELLOW              0xFFE0
#define WHITE               0xFFFF
#define ILI9341_BLACK       0x0000      /*   0,   0,   0 */
#define ILI9341_NAVY        0x000F      /*   0,   0, 128 */
#define ILI9341_DARKGREEN   0x03E0      /*   0, 128,   0 */
#define ILI9341_DARKCYAN    0x03EF      /*   0, 128, 128 */
#define ILI9341_MAROON      0x7800      /* 128,   0,   0 */
#define ILI9341_PURPLE      0x780F      /* 128,   0, 128 */
#define ILI9341_OLIVE       0x7BE0      /* 128, 128,   0 */
#define ILI9341_LIGHTGREY   0xC618      /* 192, 192, 192 */
#define ILI9341_DARKGREY    0x7BEF      /* 128, 128, 128 */
#define ILI9341_BLUE        0x001F      /*   0,   0, 255 */
#define ILI9341_GREEN       0x07E0      /*   0, 255,   0 */
#define ILI9341_CYAN        0x07FF      /*   0, 255, 255 */
#define ILI9341_RED         0xF800      /* 255,   0,   0 */
#define ILI9341_MAGENTA     0xF81F      /* 255,   0, 255 */
#define ILI9341_YELLOW      0xFFE0      /* 255, 255,   0 */
#define ILI9341_WHITE       0xFFFF      /* 255, 255, 255 */
#define ILI9341_ORANGE      0xFD20      /* 255, 165,   0 */
#define ILI9341_GREENYELLOW 0xAFE5      /* 173, 255,  47 */
#define ILI9341_PINK        0xF81F
int chipSelect = BUILTIN_SDCARD;
// If using the breakout, change pins as desired
```

```
Adafruit_ILI9341 tft = Adafruit_ILI9341(TFT_CS, TFT_DC, TFT_MOSI, TFT_CLK, TFT_RST,
    TFT_MISO);

// For better pressure precision, we need to know the resistance
// between X+ and X- Use any multimeter to read it
// For the one we're using, its 300 ohms across the X plate
TouchScreen ts = TouchScreen(XP, YP, XM, YM, 301);


void setup() {
  //
  tft.begin();


  // Define Screen Orientation
  tft.setRotation(0);

  // Welcome Screen
  tft.fillScreen(ILI9341_LIGHTGREY);
  tft.fillScreen(ILI9341_DARKGREY);
  tft.fillScreen(ILI9341_BLACK);
  tft.setFont(&FreeSerif18pt7b);
  tft.setCursor(13, 80);
  tft.setTextColor(WHITE);
  tft.println("    Portable");
  tft.println("       Grape");
  tft.println("     Analyser");
  tft.setFont(&FreeSans12pt7b);
  tft.setTextColor(RED);
  tft.setCursor(50, 240);
  tft.println("EB&RMRP");
  tft.setTextColor(GREEN);
  tft.println("");
  tft.println("         INESC MN");
  delay(3000);
  Serial.begin(9600);
  //while (!Serial) {
  // ; // wait for serial port to connect. Needed for Leonardo only
  //}
  tft.fillScreen(BLACK);
  tft.setFont(&FreeSans12pt7b);
  tft.setTextColor(WHITE);
  tft.setCursor(0, 40);
  tft.println("Initializing SD card...");

  // see if the card is present and can be initialized:
  if (!SD.begin(chipSelect)) {
    delay(2500);
    tft.fillScreen(BLACK);
```

```
    tft.setFont(&FreeSans12pt7b);
    tft.setTextColor(WHITE);
    tft.setCursor(0, 40);
    tft.println("Card failed, or not present");
    // don't do anything more:
    return;
  }
  delay(2500);
  tft.fillScreen(BLACK);
  tft.setFont(&FreeSans12pt7b);
  tft.setTextColor(WHITE);
  tft.setCursor(0, 40);
  tft.println("card initialized.");
  delay(3000);
  tft.fillScreen(BLACK);
  tft.setFont(&FreeSans12pt7b);
  tft.setTextColor(WHITE);
  tft.setCursor(0, 40);
  tft.println("         MENU");

  tft.fillRect((tft.width() - butwidth) / 2, startY, butwidth, butheight, CYAN);
  tft.setTextColor(BLACK);
  tft.setFont(&FreeSans9pt7b);
  tft.setCursor(55, startY + 25);
  tft.println("Sensor Check");

  tft.fillRect((tft.width() - butwidth) / 2, startY + butheight + 10, butwidth, butheight
    , CYAN);
  tft.setCursor(55, startY + butheight + 10 + 25);
  tft.println("Measurements");

  tft.fillRect((tft.width() - butwidth * 0.7) / 2, startY + butheight * 4 + 50, butwidth
    * 0.7, butheight * 0.8, RED);
  tft.setFont(&FreeSans9pt7b);
  tft.setTextColor(WHITE);
  tft.setCursor(tft.width() / 2 - 53, startY + butheight * 4 + 40 + 32);
  tft.println("SHUTDOWN");


}

void loop()
{
  // Retrieve a point
  TSPoint p = ts.getPoint();

  // we have some minimum pressure we consider 'valid'
  // pressure of 0 means no pressing!
  if (p.z < MINPRESSURE || p.z > MAXPRESSURE) {
```

```
    return;
}

// Scale from ~0->1000 to tft.width using the calibration #'s
p.x = map(p.x, TS_MINX, TS_MAXX, 0, tft.width());
p.y = map(p.y, TS_MINY, TS_MAXY, 0, tft.height());

/* If pressure is adequate, see if the user pressed inside any of the buttons */
if (p.x > 30  && p.x < 210)
{
  if (p.y > 65 && p.y < 105) /* Option 1 - Print submenu 1 */
  {
    tft.fillScreen(BLACK);
    tft.setFont(&FreeSans12pt7b);
    tft.setTextColor(WHITE);
    tft.setCursor(0, 40);
    tft.println("         MENU");

    tft.fillRect((tft.width() - butwidth) / 2, startY, butwidth, butheight, CYAN);
    tft.setTextColor(BLACK);
    tft.setFont(&FreeSans9pt7b);
    tft.setCursor(55, startY + 25);
    tft.println("PhotoDiodes");

    tft.fillRect((tft.width() - butwidth) / 2, startY + butheight + 10, butwidth,
  butheight, CYAN);
    tft.setCursor(55, startY + butheight + 10 + 25);
    tft.println("PhotoConductors");

    tft.fillRect((tft.width() - butwidth * 0.7) / 2, startY + butheight * 4 + 50,
  butwidth * 0.7, butheight * 0.8, RED);
    tft.setFont(&FreeSans9pt7b);
    tft.setTextColor(WHITE);
    tft.setCursor(tft.width() / 2 - 53, startY + butheight * 4 + 40 + 32);
    tft.println("Menu");

    while (1) {
      // Retrieve a point
      TSPoint p = ts.getPoint();
      if (p.z > MINPRESSURE && p.z < MAXPRESSURE) {
        // Scale from ~0->1000 to tft.width using the calibration #'s
        p.x = map(p.x, TS_MINX, TS_MAXX, 0, tft.width());
        p.y = map(p.y, TS_MINY, TS_MAXY, 0, tft.height());
        if (p.x > 30  && p.x < 210)
        {
          if (p.y > 65 && p.y < 105)
          {
            tft.fillScreen(BLACK);
            tft.setFont(&FreeSans12pt7b);
```

```
222             tft.setTextColor(ILI9341_ORANGE);
223             tft.setCursor(0, 40);
224             tft.println("  Jumper 2 and 3 ");
225             delay(3000);
226             tft.fillScreen(BLACK);
227             tft.setFont(&FreeSans12pt7b);
228             tft.setTextColor(ILI9341_ORANGE);
229             tft.setCursor(0, 40);
230             tft.println("  Sensor Check ");
231
232             int BlueLED = A21;
233             int UvLED = A1;
234             int Pump = A22;
235             int SensorValueDark1;
236             int SensorValueDark2;
237             int SensorValueDark3;
238             int SensorValueDark4;
239             int SensorValue1;
240             int SensorValue2;
241             int SensorValue3;
242             int SensorValue4;
243             pinMode(BlueLED, OUTPUT);
244             pinMode(UvLED, OUTPUT);
245             pinMode(Pump, OUTPUT);
246            // elapsedMillis tim;
247             tft.println("Dark Acquisition");
248             delay(250);
249             SensorValueDark1 = analogRead(A7);
250             SensorValueDark2 = analogRead(A6);
251             delay (250);
252
253             //while (tim < 5000) {
254
255               //SensorValueDark1 = analogRead(A7);
256               //SensorValueDark2 = analogRead(A6);
257               //delay (250);
258
259             //}
260             //tft.println ("Light Acquisition");
261            // while (tim < 10000) {
262               digitalWrite(UvLED, HIGH);
263
264               delay (3000);
265               SensorValue1 = analogRead(A7);
266               digitalWrite(UvLED, LOW);
267               delay (250);
268               analogWrite(BlueLED, 8000);
269               delay(3000);
270               SensorValue2 = analogRead(A6);
```

```
271               analogWrite(BlueLED, 0);
272               delay (250);
273
274             //}
275
276             //digitalWrite(BlueLED, LOW);
277             //digitalWrite(UvLED, LOW);
278
279
280             if (SensorValue1 / SensorValueDark1 > 2)
281             { tft.println("Sensor1 Ok");
282             }
283             else
284             { tft.println("Sensor1 Fail");
285             }
286             if (SensorValue2 / SensorValueDark2 > 2)
287             { tft.println("Sensor2 Ok");
288             }
289             else
290             { tft.println("Sensor2 Fail");
291             }
292
293
294             delay(3000);                                  // Wait 3 seconds
295             break;
296
297
298           }
299
300           if (p.y > startY + butheight + 10 && p.y < startY + butheight * 2 + 10) /*
    Option 2 */
301           { tft.fillScreen(BLACK);
302             tft.setFont(&FreeSans12pt7b);
303             tft.setTextColor(ILI9341_ORANGE);
304             tft.setCursor(0, 40);
305             tft.println("  Jumper 1 and 2 ");
306             delay(3000);
307             tft.fillScreen(BLACK);
308             tft.setFont(&FreeSans12pt7b);
309             tft.setTextColor(ILI9341_ORANGE);
310             tft.setCursor(0, 40);
311             tft.println("  PhotoConductor Test ");
312             int BlueLED = A1;
313             int UvLED = A0;
314             int Pump = A21;
315             int Heater = A22;
316             int SensorValueDark1;
317             int SensorValueDark2;
318             int SensorValueDark3;
```

```
              int SensorValueDark4;
              int SensorValue1;
              int SensorValue2;
              int SensorValue3;
              int SensorValue4;
              pinMode(BlueLED, OUTPUT);
              pinMode(UvLED, OUTPUT);
              pinMode(Pump, OUTPUT);//
              elapsedMillis tim;
              while (tim < 5000) {
                tft.println ("Dark Acquisition");
                SensorValueDark1 = analogRead(A8);
                SensorValueDark2 = analogRead(A7);

              }

              digitalWrite(BlueLED, HIGH);
              digitalWrite(UvLED, HIGH);
              while (tim < 10000) {
                tft.println ("Light Acquisition");
                SensorValue1 = analogRead(A8);
                SensorValue2 = analogRead(A7);
                delay (250);

              }
              digitalWrite(BlueLED, LOW);
              digitalWrite(UvLED, LOW);

              if (SensorValue1 / SensorValueDark1 > 10)
              { tft.println("Sensor1 Ok");
              }
              else
              { tft.println("Sensor1 Fail");
              }
              if (SensorValue2 / SensorValueDark2 > 10)
              { tft.println("Sensor2 Ok");
              }
              else
              { tft.println("Sensor2 Fail");
              }

              delay(3000);                                  // Wait 3 seconds
              break;
            }


            if (p.x > (tft.width() - butwidth * 0.7) / 2 && p.x < (tft.width() - (tft.
    width() - butwidth * 0.7) / 2) && p.y > startY + butheight * 4 + 50 && p.y < startY +
```

```
 butheight * 4 + 50 + butheight * 0.8) /* Option 5 Shutdown*/
367            {
368              break;
369            }
370
371          }
372
373
374        }
375
376
377
378      }
379      tft.fillScreen(BLACK);
380      tft.setFont(&FreeSans12pt7b);
381      tft.setTextColor(WHITE);
382      tft.setCursor(0, 40);
383      tft.println("         MENU");
384
385      tft.fillRect((tft.width() - butwidth) / 2, startY, butwidth, butheight, CYAN);
386      tft.setTextColor(BLACK);
387      tft.setFont(&FreeSans9pt7b);
388      tft.setCursor(55, startY + 25);
389      tft.println("Sensor Check");
390
391      tft.fillRect((tft.width() - butwidth) / 2, startY + butheight + 10, butwidth,
    butheight, CYAN);
392      tft.setCursor(55, startY + butheight + 10 + 25);
393      tft.println("Measurements");
394
395      tft.fillRect((tft.width() - butwidth * 0.7) / 2, startY + butheight * 4 + 50,
    butwidth * 0.7, butheight * 0.8, RED);
396      tft.setFont(&FreeSans9pt7b);
397      tft.setTextColor(WHITE);
398      tft.setCursor(tft.width() / 2 - 53, startY + butheight * 4 + 40 + 32);
399      tft.println("SHUTDOWN");
400
401    }
402    //Measurement Menu Options
403    if (p.y > startY + butheight + 10 && p.y < startY + butheight * 2 + 10) /* Option 2
    */
404    { tft.fillScreen(BLACK);
405      tft.setFont(&FreeSans12pt7b);
406      tft.setTextColor(WHITE);
407      tft.setCursor(0, 40);
408      tft.println("         MENU");
409
410      tft.fillRect((tft.width() - butwidth) / 2, startY, butwidth, butheight, CYAN);
411      tft.setTextColor(BLACK);
```

```
412       tft.setFont(&FreeSans9pt7b);
413       tft.setCursor(55, startY + 25);
414       tft.println("End Point");
415
416       tft.fillRect((tft.width() - butwidth) / 2, startY + butheight + 10, butwidth,
      butheight, CYAN);
417       tft.setCursor(55, startY + butheight + 10 + 25);
418       tft.println("Continuous");
419
420       tft.fillRect((tft.width() - butwidth * 0.7) / 2, startY + butheight * 4 + 50,
      butwidth * 0.7, butheight * 0.8, RED);
421       tft.setFont(&FreeSans9pt7b);
422       tft.setTextColor(WHITE);
423       tft.setCursor(tft.width() / 2 - 53, startY + butheight * 4 + 40 + 32);
424       tft.println("Menu");
425
426       while (1) {
427         // Retrieve a point
428         TSPoint p = ts.getPoint();
429         if (p.z > MINPRESSURE && p.z < MAXPRESSURE) {
430           // Scale from ~0->1000 to tft.width using the calibration #'s
431           p.x = map(p.x, TS_MINX, TS_MAXX, 0, tft.width());
432           p.y = map(p.y, TS_MINY, TS_MAXY, 0, tft.height());
433           if (p.x > 30  && p.x < 210)
434           { // Endpoint measurement
435             if (p.y > 65 && p.y < 105)
436             {
437               tft.fillScreen(BLACK);
438               tft.setFont(&FreeSans12pt7b);
439               tft.setTextColor(ILI9341_ORANGE);
440               tft.setCursor(0, 40);
441               tft.println("  EndPoint Measurement ");
442               delay (1500);
443               int BlueLED = A21;
444               int UvLED = A1;
445               int Pump = A0;
446              //int Heater = A22;
447               int SensorValueDark1;
448               int SensorValueDark2;
449
450               int SensorValue1;
451               int SensorValue2;
452               int PumpValue;
453               int HeaterValue;
454               int T0Blue;
455               int T1Blue;
456               int T0UV;
457               int T1UV;
458               pinMode(BlueLED, OUTPUT);
```

```
459             pinMode(UvLED, OUTPUT);
460             pinMode(Pump, OUTPUT);//
461             elapsedMillis tim;
462             while (tim < 10000) {
463               tft.fillScreen(BLACK);
464               tft.setFont(&FreeSans12pt7b);
465               tft.setTextColor(ILI9341_ORANGE);
466               tft.setCursor(0, 40);
467               tft.println("BaseLine Check");
468               for (int i = 0; i < 100; i++) {
469                 analogWrite(BlueLED, 8000);
470                 SensorValueDark1 = (SensorValueDark1 + analogRead(A7));
471                 T0Blue = SensorValueDark1 / 100;
472                 delay (50);
473                 analogWrite(BlueLED, 0);
474                 delay (50);
475                 digitalWrite(UvLED, HIGH);
476                 SensorValueDark2 = (SensorValueDark2 + analogRead(A6));
477                 T0UV = SensorValueDark2 / 100;
478                 delay(50);
479                 digitalWrite(UvLED, LOW);
480               }
481
482
483               while (tim < 40000) {
484                 analogWrite(Pump, 8000);
485                 tft.fillScreen(BLACK);
486                 tft.setFont(&FreeSans12pt7b);
487                 tft.setTextColor(ILI9341_ORANGE);
488                 tft.setCursor(0, 40);
489                 tft.println("Pumping");
490                 delay(250);
491                 //for (int i = 0; i < 100; i++) {
492                   analogWrite(Pump, 400);
493                 //}
494               }
495
496
497               while (tim < 50000) {
498                 tft.fillScreen(BLACK);
499                 tft.setFont(&FreeSans12pt7b);
500                 tft.setTextColor(ILI9341_ORANGE);
501                 tft.setCursor(0, 40);
502                 tft.println("Signal Acquisition");
503                 analogWrite(Pump, 0);
504                 for (int i = 0; i < 100; i++) {
505                   analogWrite(BlueLED, 8000);
506                   SensorValue1 = (SensorValue1 + analogRead(A7));
507                   T1Blue = SensorValue1 / 100;
```

```
                    delay(50);
                    analogWrite(BlueLED, 0);
                    delay (50);
                    digitalWrite(UvLED, HIGH);
                    SensorValue2 = (SensorValue2 + analogRead(A6));
                    T1UV = SensorValue2 / 100;
                    delay(250);
                    digitalWrite(UvLED, LOW);
                  }
                }
                delay (3000);
                File dataFile;
                char fileName[] = "EP00.csv";  // Base filename for logging.
                for (byte i = 1; i <= 99; i++)
                {
                  // check before modifying target filename.
                  if (SD.exists(fileName))
                  {
                    // the filename exists so increment the 2 digit filename index.
                    fileName[2] = i / 10 + '0';
                    fileName[3] = i % 10 + '0';
                  } else {
                    break;  // the filename doesn't exist so break out of the for loop.
                  }
                }
                Serial.print("Init. Sig. - B");
                Serial.print(",");
                Serial.println("Fina. Sig. - B");
                Serial.print("Init. Sig. - UV");
                Serial.print(",");
                Serial.println("Fina. Sig. - UV");
                dataFile = SD.open(fileName, FILE_WRITE);
                Serial.print(fileName);
                dataFile.print("Init. Sig. - B");
                dataFile.print(",");
                int initsigB = float (T0Blue);
                dataFile.println(initsigB, DEC);
                dataFile.println("Final Sig. - B");
                dataFile.print(",");
                int finsigB = float (T1Blue);
                dataFile.println(finsigB, DEC);
                dataFile.print("Init. Sig. - UV");
                dataFile.print(",");
                int initsigUV = float (T0UV);
                dataFile.println(initsigUV, DEC);
                dataFile.println("Final Sig. - UV");
                dataFile.print(",");
                int finsigUV = float (T1UV);
                dataFile.println(finsigUV, DEC);
```

```
                dataFile.close();
                
                
                
                tft.fillScreen(BLACK);
                tft.setFont();
                tft.setTextSize(1);
                tft.setCursor(0, 40);
                tft.println( "Init. Sig. - B");
                tft.println(T0Blue);
                tft.println( "Init. Sig. - UV");
                tft.println(T0UV);
                tft.println( "Final Sig. - B");
                tft.println(T1Blue);
                tft.println( "Final Sig. - UV");
                tft.println(T1UV);
                tft.println( "Sig. Ratio - B");
                int ratioBlue;
                ratioBlue = T1Blue / T0Blue;
                int ratioUV;
                ratioUV = T1UV / T0UV;
                tft.println(ratioBlue);
                tft.println( "Sig. Ratio - UV");
                tft.println(ratioUV);
                
                
                
                
                
                delay(5000);
                tft.fillScreen(BLACK);
                tft.setFont(&FreeSans12pt7b);
                tft.setTextColor(WHITE);
                tft.setCursor(0, 40);
                tft.println("         MENU");
                
                tft.fillRect((tft.width() - butwidth) / 2, startY, butwidth, butheight,
    CYAN);
                tft.setTextColor(BLACK);
                tft.setFont(&FreeSans9pt7b);
                tft.setCursor(55, startY + 25);
                tft.println("End Point");
                
                tft.fillRect((tft.width() - butwidth) / 2, startY + butheight + 10,
    butwidth, butheight, CYAN);
                tft.setCursor(55, startY + butheight + 10 + 25);
                tft.println("Continuous");
                
                tft.fillRect((tft.width() - butwidth * 0.7) / 2, startY + butheight * 4 +
```

```
 50, butwidth * 0.7, butheight * 0.8, RED);
604             tft.setFont(&FreeSans9pt7b);
605             tft.setTextColor(WHITE);
606             tft.setCursor(tft.width() / 2 - 53, startY + butheight * 4 + 40 + 32);
607             tft.println("Menu");
608             // tft.fillScreen(BLACK);
609             // tft.setFont(&FreeSans12pt7b);
610             // tft.setTextColor(WHITE);
611             // tft.setCursor(0, 40);
612             // tft.println("         MENU");
613 
614             //   tft.fillRect((tft.width() - butwidth) / 2, startY, butwidth,
    butheight, CYAN);
615             // tft.setTextColor(BLACK);
616             //  tft.setFont(&FreeSans9pt7b);
617             // tft.setCursor(55, startY + 25);
618             // tft.println("Sensor Check");
619 
620             // tft.fillRect((tft.width() - butwidth) / 2, startY + butheight + 10,
    butwidth, butheight, CYAN);
621             // tft.setCursor(55, startY + butheight + 10 + 25);
622             // tft.println("Measurements");
623 
624             // tft.fillRect((tft.width() - butwidth * 0.7) / 2, startY + butheight *
    4 + 50, butwidth * 0.7, butheight * 0.8, RED);
625             // tft.setFont(&FreeSans9pt7b);
626             // tft.setTextColor(WHITE);
627             // tft.setCursor(tft.width() / 2 - 53, startY + butheight * 4 + 40 + 32);
628             // tft.println("SHUTDOWN");
629             // Wait 3 seconds
630             break;
631 
632 
633           }
634         }
635 
636         if (p.y > startY + butheight + 10 && p.y < startY + butheight * 2 + 10) /*
    Option 2 */
637         {
638           tft.fillScreen(BLACK);
639           tft.setFont(&FreeSans12pt7b);
640           tft.setTextColor(ILI9341_ORANGE);
641           tft.setCursor(0, 40);
642           tft.println("  Continuous Assay ");
643           delay (1500);
644           int BlueLED = A21;
645           int UvLED = A1;
646           int Pump = A0;
647         //  int Heater = A22;
```

```
int SensorValueDark1;
int SensorValueDark2;
int SensorValue1 = 0;

int SensorValue11;
int SensorValue2 = 0;
int SensorValue22;
int PumpValue;
int HeaterValue;
int T0Blue;
int T1Blue;
int T0UV;
int T1UV;
int redline = 0xF800;
File dataFile;
char fileName[] = "CM00.csv";  // Base filename for logging.
for (byte i = 1; i <= 99; i++)
{
  // check before modifying target filename.
  if (SD.exists(fileName))
  {
    // the filename exists so increment the 2 digit filename index.
    fileName[2] = i / 10 + '0';
    fileName[3] = i % 10 + '0';
  } else {
    break;  // the filename doesn't exist so break out of the for loop.
  }
}
pinMode(BlueLED, OUTPUT);
pinMode(UvLED, OUTPUT);
pinMode(Pump, OUTPUT);//
elapsedMillis tim;
while (tim < 5000) {
  tft.fillScreen(BLACK);
  tft.setFont(&FreeSans12pt7b);
  tft.setTextColor(ILI9341_ORANGE);
  tft.setCursor(0, 40);
  tft.println("BaseLine Check");
  for (int i = 0; i < 100; i++) {
    analogWrite(BlueLED, 8000);
    SensorValueDark2 = (SensorValueDark2 + analogRead(A6));
    T0UV = SensorValueDark2 / 100;
    delay(50);
    analogWrite(BlueLED, 00);

  }

}
Serial.print("Baseline");
```

```
                Serial.print(",");
                dataFile = SD.open(fileName, FILE_WRITE);
                Serial.print(fileName);
                dataFile.print("Baseline");
                dataFile.print(",");
                int baseline = float (TOUV);
                dataFile.println(baseline, DEC);
                dataFile.close();

                tft.fillScreen(BLACK);
                tft.setFont(&FreeSans12pt7b);
                tft.setTextColor(ILI9341_ORANGE);
                tft.setCursor(0, 40);
                tft.println("Measurement");
                analogWrite(BlueLED, 8000);
                SensorValue1 = analogRead (A7);
                SensorValue1 = map(SensorValue1, 0, 1023, 300, 110);
                tft.drawLine(20, 300, 239, 300, WHITE);
                tft.drawLine(235, 297, 239, 300, WHITE);
                tft.drawLine(235, 303, 239, 300, WHITE);
                tft.drawLine(20, 300, 20, 110, WHITE);
                tft.drawLine(17, 114, 20, 110, WHITE);
                tft.drawLine(23, 114, 20, 110, WHITE);
                tft.setFont();
                tft.setTextSize(1);
                tft.setCursor(0, 115);
                tft.setTextColor(WHITE);
                tft.print("100");
                tft.setCursor(10, 310);
                tft.setTextColor(WHITE);
                tft.print("0");
                tft.setCursor(0, 158);
                tft.setTextColor(WHITE);
                tft.print("75");
                tft.drawLine(18, 160, 22, 160, WHITE);
                tft.setCursor(0, 205);
                tft.setTextColor(WHITE);
                tft.print("50");
                tft.drawLine(18, 207, 22, 207, WHITE);
                tft.setCursor(0, 253);
                tft.setTextColor(WHITE);
                tft.print("25");
                tft.drawLine(18, 255, 22, 255, WHITE);
                tft.setCursor(100, 310);
                tft.setTextColor(WHITE);
                tft.print("Time (min)");
                analogWrite(Pump, 000);

                while (tim < 1000000) {
```

```
                for (int x = 0; x < 300; x++) {
                  delay(200);
                  analogWrite(Pump, 000);
                  //tft.setFont();
                  // tft.setTextSize(1);
                  // tft.setCursor(0, 180);
                  // tft.setTextColor(WHITE);
                  // tft.print (analogRead(A8));
                  // tft.print ("         ");
                  analogWrite(BlueLED, 8000);
                  SensorValue11 = map(analogRead(A6), 0, 1023, 300, 110);
                  // tft.setFont();
                  //tft.setTextSize(1);
                  //tft.setCursor(0, 200);
                  //tft.setTextColor(WHITE);
                  //tft.print (SensorValue11);
                  //tft.print ("     ");
                  // SensorValue22 = map(analogRead(A7), 0, 1023, 0, 320);
                  tft.drawLine(x - 1 + 20, SensorValue1, x + 20, SensorValue11, redline);
                  SensorValue1 = SensorValue11;
                  int timme = float (x);
                  Serial.print("Signal");
                  Serial.print(",");
                  dataFile = SD.open(fileName, FILE_WRITE);
                  Serial.print(fileName);
                  dataFile.print(timme);
                  dataFile.print(",");
                  int signal1 = float (SensorValue1);
                  dataFile.println(SensorValue1, DEC);
                  dataFile.close();
                }

                delay(5000);
                tft.fillScreen(BLACK);
                tft.setFont(&FreeSans12pt7b);
                tft.setTextColor(WHITE);
                tft.setCursor(0, 40);
                tft.println("         MENU");

                tft.fillRect((tft.width() - butwidth) / 2, startY, butwidth, butheight,
    CYAN);
                tft.setTextColor(BLACK);
                tft.setFont(&FreeSans9pt7b);
                tft.setCursor(55, startY + 25);
                tft.println("Sensor Check");

                tft.fillRect((tft.width() - butwidth) / 2, startY + butheight + 10,
    butwidth, butheight, CYAN);
                tft.setCursor(55, startY + butheight + 10 + 25);
```

```
                tft.println("Signal Acquisition");

                tft.fillRect((tft.width() - butwidth * 0.7) / 2, startY + butheight * 4 +
    50, butwidth * 0.7, butheight * 0.8, RED);
                tft.setFont(&FreeSans9pt7b);
                tft.setTextColor(WHITE);
                tft.setCursor(tft.width() / 2 - 53, startY + butheight * 4 + 40 + 32);
                tft.println("SHUTDOWN");
                break;
              }
              analogWrite(BlueLED, 00);
              analogWrite(Pump, 0);

            }
            if (p.x > (tft.width() - butwidth * 0.7) / 2 && p.x < (tft.width() - (tft.
   width() - butwidth * 0.7) / 2) && p.y > startY + butheight * 4 + 50 && p.y < startY +
    butheight * 4 + 50 + butheight * 0.8) /* Option 5 Shutdown*/
            { delay(3000);
              break;
            }
          }
        }

        if (p.x > (tft.width() - butwidth * 0.7) / 2 && p.x < (tft.width() - (tft.width()
    - butwidth * 0.7) / 2) && p.y > startY + butheight * 4 + 50 && p.y < startY +
   butheight * 4 + 50 + butheight * 0.8) /* Option 5 Shutdown*/
        {

          tft.fillScreen(BLACK);
          tft.setFont(&FreeSans18pt7b);
          tft.setTextColor(RED);
          tft.setCursor(0, 90);
          tft.println("    YOU MAY");
          tft.println("   TURN THE");
          tft.println("        MAIN");
          tft.println("     SWITCH");
          tft.println("         OFF");
          while (1) {}; /* Wait forever here */
        }
      }
    }
  }
}
```

Appendix D

Bradford Calibration Curves

In this Annex the calibration curves for the protein detection are presented.

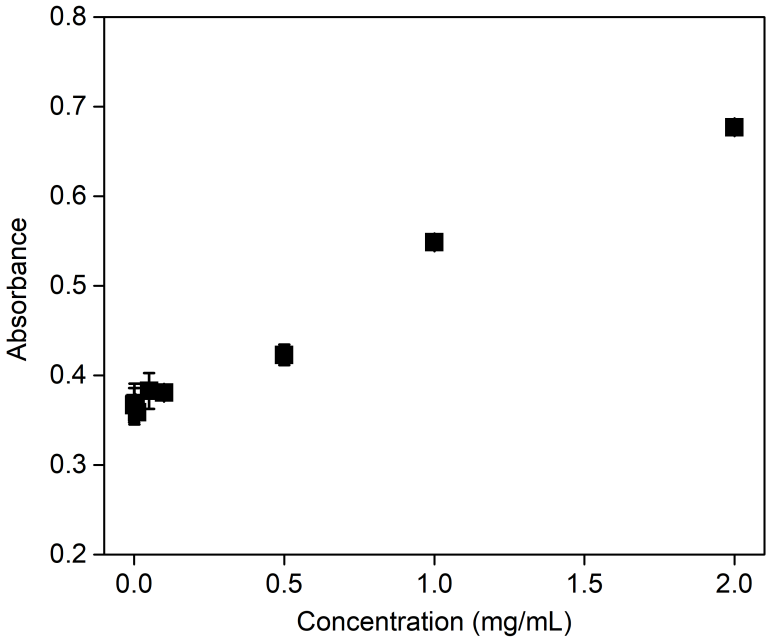

Figure D.1: Calibration curve for Tyrosinase determination using the Bradford assay.

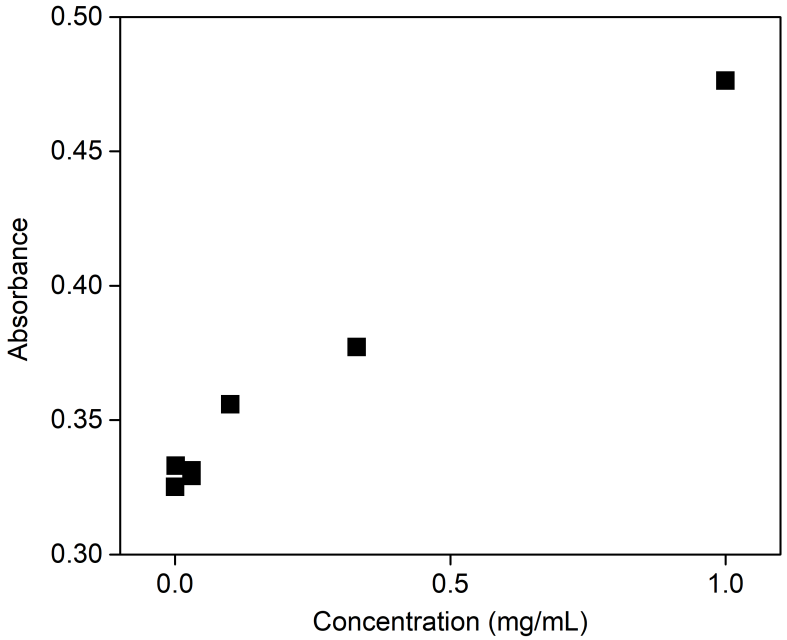

Figure D.2: Calibration curve for DOPA-decarboxylase determination using the Bradford assay.

Appendix E

qPCR for Grape Pathogen Confirmation

Table E.1: qPCR results of the infected grape samples. The Actin gene was used as a reference, as its expression was not impacted by the presence of the fungal infection. Fungal biomass accumulation and infection level was determined by qPCR amplification of the B. cinerea polygalacturonase 1 (PG1)

Sample ID	CtCDSBcPG1	CtActin	ΔCt (Cttarget- CtActin)	ΔΔCt (Healthy samples values were subtracted)	2-ΔΔCt
EL 32	29.00±2.41	22.00±0.86	7.00±1.56	-4.44±1.56	30.17±25.55
EL 35	27.16±0.56	21.49±0.12	5.67±0.50	-5.03±0.50	33.88±10.72
EL 38	27.01±1.93	23.62±2.04	3.40±1.56	-6.23±1.56	101.93±69.46